Calculations of Non-equilibrium Effects in Nano-conductors

Christensen, Rasmus Bjerregaard

Publication date:
2015

Document Version
Publisher's PDF, also known as Version of record

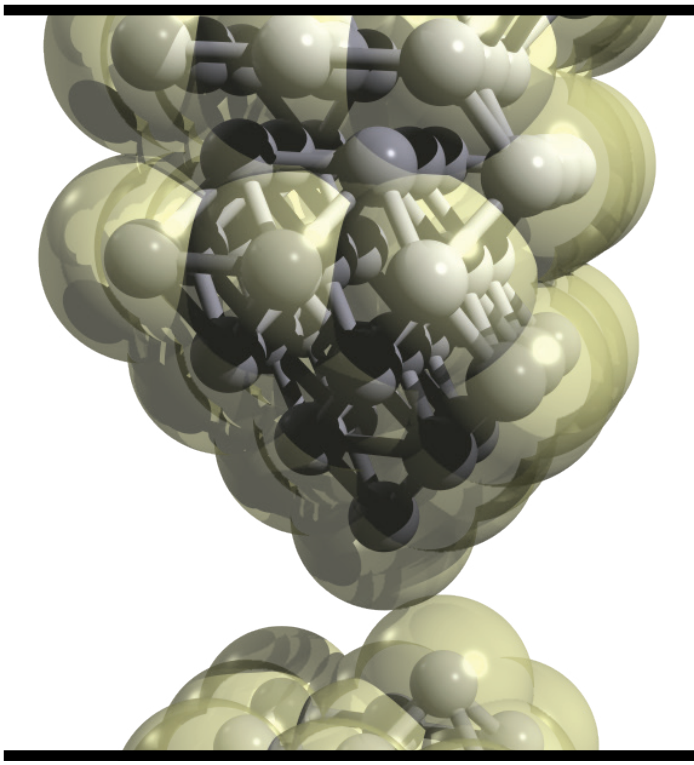

Calculations of Non-equilibrium Eects in Nano-conductors

Electrical Current and the Interplay with Vibrations and Plasmon

Rasmus Bjerregaard Christensen
PhD Thesis April 2015

DTU Nanotech
Department of Micro- and Nanotechnology

Calculations of Non-equilibrium Effects in Nano-conductors

Electrical Current and the Interplay with Vibrations and Plasmons

Rasmus Bjerregaard Christensen

Kongens Lyngby 2015
NTCH-PhD

Technical University of Denmark
DTU Nanotech
Department of Micro- and Nanotechnology
Ørsteds Plads, building 345E,
2800 Kongens Lyngby, Denmark
NTCH-PhD

Abstract

This thesis is concerned with the interplay between electrical current and vibrational and plasmonic excitations. The development of nano-scale devices for electronics relies on the ability to identify individual atoms and molecules as well as their geometry and electronic structure. In this thesis we show how measuring the **noise** can give information about the quantum nature of the device and relate the high frequency noise to **light-emission**. A first principle method is presented for calculating the light-emission and is utilized to calculate the light-emission from two STM experiments: An adatom on a Ag(111) surface and a C_{60} molecule on a Cu(111) surface. The calculated photon yield is found to agree with experiments for photons with energies below the applied bias ($\hbar\omega < eV$). Inelastic electron tunneling spectroscopy(**IETS**) serves as a powerful tool for non-destructive characterization. A new fast method for calculating the **energy dependent** IETS signal is presented, and applied to a one-level model revealing how a symmetric system can give rise to peak-dip features in the IETS. The new method is used to explain the IETS signal obtained for a 1,4-benzene-dithiol(BDT) molecule in a symmetric gold junction as a function of gate voltage. Gating molecules in 3D metal junctions is difficult due to screening effects. On the other hand, graphene devices are routinely gated. Thus, we study the IETS signal from gated **graphene nanoribbons** (GNR). We study pristine GNRs with both zigzag and armchair chirality, and related the IETS signal to the phononic band structure. For the spin-polarized zigzag GNRs the role of the spin-polarization is investigated, revealing IETS as an indirect measurement of spin-polarization. Further, the role of impurities is explored, revealing the possibility of detecting defects in the hydrogen passivisation by IETS. Lastly a preliminary study of the **heating** due to the electrical current is described, investigating the effect of the **deterministic current-induced forces**, treated within the framework of the **semi-classical**

generalized Langevin equation(SGLE). For a pristine zigzag ribbon the deterministic current-induced forces is seen to give rise to runaway modes. For an armchair ribbon with partly dehydrogenated edges the deterministic current-induced forces is seen to break the symmetry and increase the excess heating.

Summary (Danish)

Denne afhandling omhandler samspillet mellem elektrisk strøm og vibrationelle og plasmoniske excitationer. Udviklingen af nano-skala-enheder til elektronik er afhængig af evnen til at identificere de enkelte atomer og molekyler samt deres geometri og elektroniske struktur. I denne afhandling viser vi, hvordan måling af den elektroniske **støj** kan give oplysninger om kvante karakteren af systemet, og vi relatere den højfrekvente støj til **lys-emission**. Vi præsenterer en metode, baseret på tætheds-functional teori (DFT), til beregning af lys-emission. Vi anvender metoden til beregning af lys-emissionen fra to STM eksperimenter: Et adatom på en Ag(111) overflade og et C_{60} molekyle på en Cu(111) overflade. Det beregnede foton udbytte er i overensstemmelse med eksperimenter for fotoner med energier under den anvendte bias ($\hbar\omega < eV$). Uelastisk elektron tunneling spektroskopi (**IETS**) er et effektivt redskab til ikke destruktiv karakterisering. En ny hurtig metode til beregning af det **energi afhængige** IETS signal præsenteres. Den nye metode anvendes på en et-niveau model. Et-niveau modellen forklarer, hvordan et symmetrisk systemet kan give anledning til positiv-negativ signaler i IETS. Endvidere anvendes den nye metode til at forklare IETS signalet opnået for et 1,4-benzene-dithiol(BDT) molekyle i en symmetrisk atomar guld kontakt som en funktion af gate spænding. Gating af molekyler i 3D metal kontakter er vanskelig på grund af screening effekter. Derimod er graphene systemer rutinemæssigt gated. Således har vi studerer IETS signalet fra gated **graphene nanoribbons** (GNR). Vi studerer rene GNRs med både zigzag og armchair chiralitet og fortolker IETS signalet ved hjælp af den vibrationelle bånd struktur. Vi undersøger effekten af spin-polarisering for det rene zigzag GNR, og vi viser hvordan IETS kan bruges som en indirekte måling af spin-polarisering. Endvidere udforsker vi effekten af defekter, og viser hvordan defekter i brint passivisationen kan detekteres vedhjælp af IETS. Til sidst

præsenteres de indledende undersøgelse af **opvarmning** forsaget af den elektriske strøm. Vi undersøger effekten af de **deterministiske strøm inducerede kræfter** inden for rammerne af den **semi-klassiske generaliserede Langevin ligning** (SGLE). For et rent zigzag GNR giver de deterministiske strøm inducerede kræfter anledning til ustabile vibrationer. For et armchair GNR med delvis dehydrogenerede kanter bryder de deterministiske strøm inducerede kræfter symmetrien, hvilket resultere i en øget opvarmning.

Preface

This thesis is submitted for the Doctor of Philosophy degree at the Technical University of Denmark (DTU). The work was carried out between September 2011 and January 2015 at the Department of Micro- and Nanotechnology (DTU Nanotech). The project was financed by the Independent Research Council for Natural Science(FNU), FNU-10-083120. The project was supervised by Associate Prof. Mads Brandbyge. I would like to thank Mads for his participation in developing novel and inspiring ideas, which has made this project exciting work for me for the past three years, I would also like to thank Prof. Jing-Tao Lü for the fruitful collaboration and sharing of technical experience and knowledge and for generously hosting a short research stay at School of Physics, Huazhong University of Science and Technology, Wuhan, China. Likewise, I wish to thank Prof. Thomas Frederiksen for an inspiring collaboration and generously hosting a short research stay at the Donostia International Physics Center in Donostia-San Sebastián, Spain. I also thank Prof. Antti-Pekka Jauho for sharing his great knowledge and Prof. Per Hedegård for always asking the necessary questions, and Giuseppe Foti, Tue Gunst and Jian-Sheng Wang for previous and ongoing collaboration. It has been a great pleasure working in the Theoretical Nanoelectronics and Nanotechnology group, where many fruitful discussions have been invaluable in the progress of this project. Therefore, a great thanks to all the guys for creating a pleasant working environment and for assistance. In particular I would like to thank Nick P. Andersen for his patience assisting with programing and latex problems and for being and outstanding office mate. Several people have helped in the completion of this manuscript, Mattias Lau Nøhr Palsgaard, Nick Papior Andersen, Tue Gunst and Daniele Stradi. Finally I would like to thank my family and friends for their moral support.

Lyngby, 01-January-2015

Rasmus Bjerregaard Christensen

"What did you do before the iPad?"

Bertram Brix Bjerregaard (2010 -)

Contents

Chapter 1

Introduction

The memory card of my first digital camera, purchased in 2003, could store 16 MB while my current phone can hold 1000 times as much information; illustrating the exponential growth which most technology obey, but maybe best known from Moore's law stating that the exponential decline in the price per transistor or said with an other focus by his Intel colleague David House that integrated circuits would double in performance every 18 months[82].

Contrary to the laws of thermal and quantum physics Moore's law is not a law of nature, and in a not that distant future, heat dispersion and leakage will flatten the growth out.

At the end of 2014 Intel launched their new processor called the Core M, entering the 14 nm regime. Comparing to the lattice constant of unstrained silicon of 0.543 nm implies that less than thirty atoms would span the channel length, leading to substantial leakage. Thus, the silicon industry has already gone nano, necessitating the replacement, on the theoretical side, of an traditional statistical view, as the use of the Boltzmann equation, by an "ab initio" description such as Density functional theory(DFT) and noneequilibrium Green's functions(NEGF). The use of an "ab initio" description in the silicon industry have paved the way for the Danish company *QuantumWise* developing and selling commercial software based on DFT and NEGF.

The silicon industry have matured through several decades and refined and renewed itself, investing billions of dollars in research[1]. Thus, in any foreseeable future silicon based integrated circuits will maintain the position as the fundamental building block in our electronics, pushing the limits of size, price, and power consumption. However, to enable this evolution the fundamental question arise: are a few atoms of silicon still silicon? Thus, a fundamental understanding of the electron transport on the nanoscale is needed.

An alternative to the top down approach of modifying bulk silicon wafers by photo-lithography is to consider a bottom up approach such as self assembled molecular transistors. Molecules can be chemical synthesized in large quantities, at a low cost, with tailored electronic properties, and since only a few electrons needs to take part in the process, the power consumption is low. However the switching speeds are expected to be slow due to low transmission probability through contacts and interconnects, and due to charging effects[19]

Bridging lithographic techniques and chemical synthesis, nano-structured graphene has been the center of much attention in the last years as the basis of a new generation of electronics[98], and devices based on nanostructured graphene have been put forward. The most generic form of nanostructured graphene is graphene nanoribbons (GNR),[24] and other structures, such as graphene antidot lattices[93, 6], can be viewed as networks of them. GNRs are potential candidates for molecular wires with tailored conductance properties. For graphene-based nanostructures the edges and their passivation, as well as defects inside the structure, can play crucial roles for the transport properties,[130] and it is thus of interest to characterize these in well-controlled experiments compared to theory.

1.0.0.1 Information hidden in the current

The development of atomic-scale devices for nanoelectronics relies on the ability to identify individual atoms and molecules as well as their geometry and electronic structure. However, since the minimum size of a photon visible to the human eye is about 400 nm, other means are necessary to visualizing and gain information. Raman spectroscopy[27] can give information about large areas of the sample but does not yield local information and the importance for transport. For molecules on an conducting substrate scanning tunneling microscope (STM) can give information with an lateral resolution of 0.1 nm, as exemplified in Fig. 1.1 (a). However, if the molecule/nanostructure is utilized in a device external spectroscopic methods can be difficult to preform, especially if the device is sealed of by a top gate or a protecting insulating layer. In some instances the molecule can be investigated before the device fabrication, but the fabrication

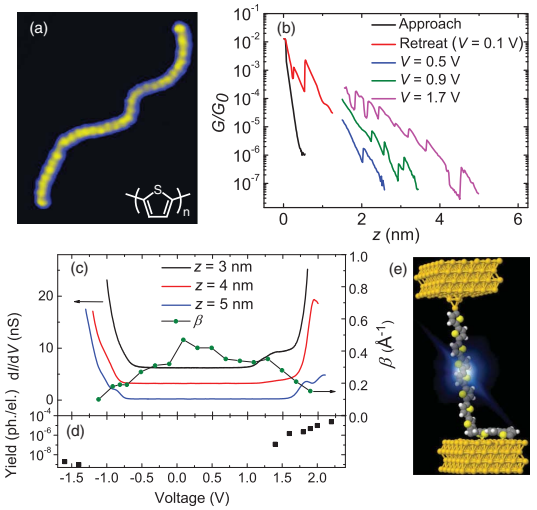

Figure 1.1: (Adopted from G. Reecht *et al.*[99]) (a) STM image ($9.0 \times 10.8\ nm^2$, $I = 2$ nA, $V = 0.1$ V) of a polythiophene wire (inset) polymerized on a Au(111) sample. (b) Normalized conductance G/G_0 vs tip-sample distance z for a polythiophene wire suspended in the junction for different voltages. The black curve corresponds to the initial approach of the clean STM tip to a wire extremity. The point of contact defines the origin of the abscissa. (c) Conductance dI/dV spectra (lines) acquired at different tip-sample distances and inverse decay length β (circles) as a function of V, for a given suspended wire. The spectra acquired at $z = 4$ nm and $z = 3$ nm are offset by 3 and 6 nS, respectively. (d) Light emission efficiency (squares) as a function of V. (e) Artistic view of a fluorescent polythiophene junction.

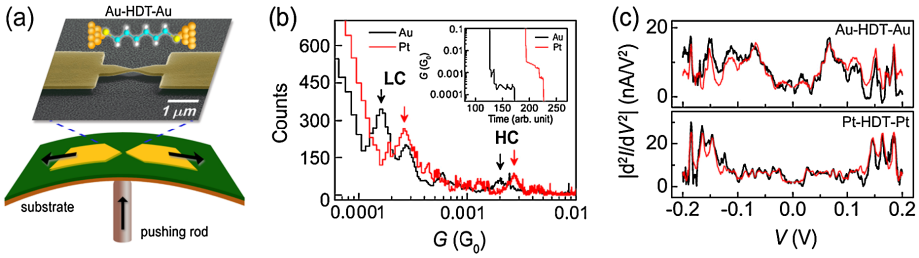

Figure 1.2: Adopted from Y. Kim *et al.*[57] (a) Schematic illustration of MCBJ system and scanning electron micrograph image of a sample with a scheme of a MJ. (b) Histograms of Au (black) and Pt (red) junctions, repeated 2000 and 300 times, respectively. Inset: Representative conductance traces. (c) IETS (black) of HDT connected with Au and Pt. For negative polarity, the sign of d^2I/dV^2 has been inverted for better illustration. The red lines are obtained by the simple formula $(y = [f(x) - f(-x)]/2)$ which applies for the symmetrization of point-symmetric functions.

method itself can alter the molecule.

Fortunately, information can be obtained just by measuring the current through the device, carefully. Besides the I-V characteristic itself and differential conductance, giving information about the total electronic transmission, measuring the time correlation in the current *i. e.* the electronic noise, can give information of how many transmission channels are involved, and thus the quantum nature of the device.

Further, measured finite frequency noise can be correlated to the light emission[110, 107]. Understanding the luminescence of a single molecule between metallic electrodes is an important step towards molecular optoelectronics[32]. Experimentally electroluminescence can be investigated in an STM setup as exemplified in Fig. 1.1 were G. Reecht *et al.*[99] reported the light emission from a Polythiophene molecular wire suspended between a Au(111) surface and a STM tip. The emitted light can both originate from excitations of surface plasmons or from LUMO-HOMO transition in the molecule. N. L. Schneider *et al.*[107] have shown how DFT in combination with NEGF calculations can help to understand the origin of the light and the dependence on the bias-polarity and non-equilibrium state of the system.

The correlation between finite frequency noise and light is due to the inelastic tunneling of the electrons by interacting with surface plasmons. The electrons can also tunnel inelastically by emitting or absorbing an vibrational quantum *i. e.* a phonon in the device. Scattering on an atomic vibration can either

open or close a transport channel and thereby raise or lower the differential conductance, thus giving rise to dips or peaks in the second derivative of the current with respect to the voltage. Measuring the second derivative of the current is also known as inelastic electron tunneling spectroscopy (IETS). The IETS signal gives a fingerprint of the vibrational modes of the system and can be used to investigate the contact geometry and molecular conformation as exemplified in Fig. 1.2, adopted from Y. Kim *et al.*[57], where the effect of strain on the contact geometry and molecular conformation is investigated for a 1,6-hexanedithiol in an Au and Pt break junction. Thus IETS serves as a way of performing non-destructive characterization yielding vibrational/phonon fingerprints of the atomic structure.

1.0.0.2 Dynamics

The IETS signal is due to the coupling between the current and vibrations. When the electrons scatter on an phonon, energy is transferred between the electrons and phonons. The heating due to random scattering with electrons is called Joule heating. Joule heating is an non-equilibrium effect, and are thought to be the activation mechanism for electromigration. Scaling down our electronic devices while keeping the voltage constant results in an increased current density which enhances the Joule heating and electromigration in the device, potentially leading to contact disrupture and thereby malfunction.

Thus, understanding of the mechanism behind heating on the nano-scale is an important issue in nano-scale electronics. While Joule heating is a random process, alternative deterministic current induced forces have been suggested as an alternative/addition to Joule heating responsible for the heating on the nano-scale. The deterministic force have four contributions: The non-conservative "wind" force (NC), a Lorentz-type force originating in the quantum-mechanical Berry phase (BP), the electronic friction force due to electron hole-pair excitations, and finally the renormalization force (RN) which acts as correction to the confining potential[23, 73, 11, 74]. The deterministic nature of the forces can in principle be utilized to make molecular scaled devices. Dundas *et al.*[23] have suggested how the NC force can be used to drive an molecular motor. However, a maybe more imminent/simple question is understanding the mechanisms behind the breaking of an metallic-chain[115]. If the nuclei preforms a closed loop through regions of varying current density, the NC force can continuously pump energy into the system increasing the kinetic energy of the nuclei leading to "runaway modes"[74]. Runaway modes can also be obtained through the non-equilibrium part of the electronic friction, which can turn positive if the probability of exiting an phonon exceeds the probability of absorbing a phonon[78, 39]. Experimentally, the coupling between the current and vibrations have been used

to make small devices as illustrated by C. Schirm *et al.*[105] in their report of a current-driven single atom memory. In the experiment they were able to switch between two stable atomic configuration in a aluminum break junction, by passing a high current. The resulting two distinct values of the conductance, are seen in Fig. 1.3. Afterwards the stored information/conductance could be read by passing a small current.

Thus, understanding the interplay between phonons and current can both be used for spectroscopic purposes, and for making more robust devices minimizing the heat generation or as the underling principle behind atomic size "mechanical" devices.

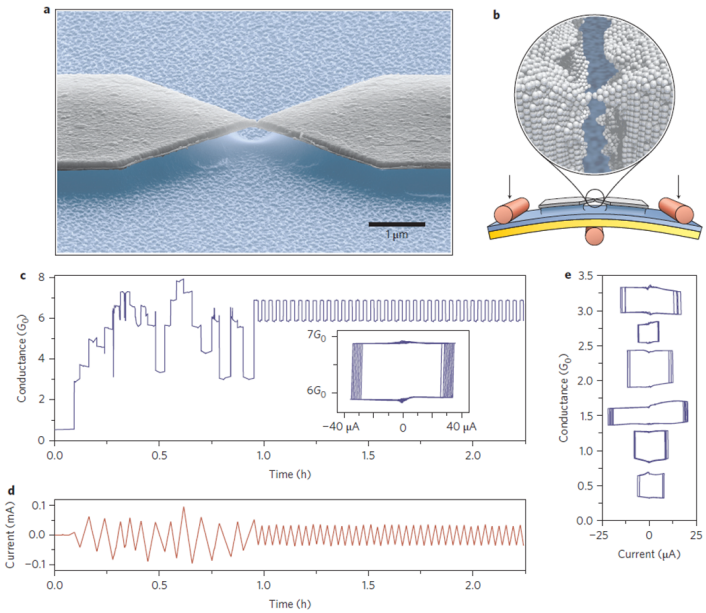

Figure 1.3: (Adopted from C. Schirm *et al.*[105]) Creation of a bistable atomic switch. a, Representative scanning electron microscope image (in false colours) of a break-junction sample. b, Principle of the break-junction set-up. A lithographically defined suspended nanobridge on a flexible substrate is elongated by bending the substrate in a three-point bending mechanism. The magnification represents an artist's view of the atomic arrangement when the nanobridge is stretched such that it forms a single-atom contact. c, Conductance of a break-junction structure made from aluminium as a function of time when applying the control current given in d. Inset: conductance versus control current for the bistable part. d, Control current applied for creating atomic rearrangements as a function of time. e, Examples of several bistable junctions plotted as a function of control current

1.1 Outline of the Thesis

The remaining of the thesis is organized as follows (with related papers in parentheses)

- In Chap. 2: We describe the basic methods and theoretical framework which will be used through out the rest of the thesis. We describe briefly the framework of density functional theory(DFT) and non-equilibrium Greens function (NEGF) theory of quantum transport for phonons and electrons.

- In Chap. 3(Paper1): We investigate the interplay between finite frequency noise and light emission. A first principle method is presented for calculating the light-emission and is utilized to calculate the light-emission from two STM experiments: An adatom on a Ag(111) surface[110] and a C_{60} on a Cu(111) surface[107]. The calculated photon yield is found to agree with experiments for photons with energies below the applied bias ($\hbar\omega < eV$).

- In Chap. 4(Paper2): A new fast method for calculating the energy dependent Inelastic electron tunneling spectroscopy(IETS) signal is presented, and applied to a one-level model revealing how a symmetric system can give rise to peak-dip features in the IETS. The new method is used to explain the IETS signal obtained for a BDT molecule in a symmetric gold junction[118] as a function of gate voltage.

- In Chap. 5(Paper3): We shortly review the lifting experiments by Koch *et al.*,[59] and the investigation of the vibrational structure of graphene nano-ribbons investigated in the Doktorarbeit of M. Koch [58]. Then the lifting experiment is modeled in a simplified manner as a gold-chain AGNR junction. Followed, by a more thorough treatment of the IETS originating from the bulk GNRs. The results for pristine AGNR and ZGNR are presented and discussed comparing transport and IETS with their phononic band structures. Then we turn to the defected systems where we consider examples of defects in the passivation, atomic structure, or by the presence of adatoms.

- In Chap. 6(Paper4) We presents the preliminary study of the heating due to the electrical current, investigating the effect of the deterministic current-induced forces, treated within the framework of the semi-classical generalized Langevin equation(SGLE). For a pristine zigzag ribbon the non-conservative and Berry forces is seen to give rise to runaway

modes. For an armchair ribbon with partly dehydrogenated edges the non-conservative and Berry forces is seen to break the symmetry and increase the excess heating.

- In Chap. 7: We evaluate the progress made in the thesis and summarize the main results. Furthermore, we discuss some possible next steps to take in the future.

Chapter 2

Method

To explain or predict the outcome of experiments a good fundamental theory is needed. Thus, this chapter describes the basic methods and theoretical framework which will be used through out the rest of the thesis. We take an atomistic approach, describing the system at hand from the viewpoint of individual atoms.

2.1 Dynamics of electrons and nuclei

The general problem of solving a many body quantum mechanical system consisting of N particles amounts to solving $3 \cdot N$ coupled differential equations. Considering a solid-state system consisting of N ions and n electrons the Hamiltonian describing the system can easily be written as:

$$H = \underbrace{-\sum_{I=1}^{N} \frac{\hbar^2}{2M_I}\nabla_I}_{T_n} \underbrace{-\sum_{i=1}^{n} \frac{\hbar^2}{2m_e}\nabla_i}_{T_e} + \underbrace{\frac{e^2}{2}\sum_{I=1}^{N}\sum_{J=1}^{N}\frac{Z_I Z_J}{|R_I - R_J|}}_{V_{nn}} + \underbrace{\frac{e^2}{2}\sum_{i=1}^{n}\sum_{j=1}^{n}\frac{1}{|r_i - r_J|}}_{U_{ee}} \underbrace{-\frac{e^2}{2}\sum_{I=1}^{N}\sum_{j=1}^{n}\frac{Z_I}{|R_I - r_j|}}_{V_{en}}. \tag{2.1}$$

where R is a set of N nuclear coordinates, r is a set of n electronic coordinates, M_I is the nuclear mass, m_e is the mass of the electron and Z_I is nuclear charge. The Hamiltonian above then give rise to the time independent Scrödinger equation

$$H\Psi(R, r) = E\Psi(R, r) \tag{2.2}$$

However, solving the Schrödinger equation in Eq. (2.2) is non trivial and can only be solved analytically for a very limited number of systems. A direct numerical solution, is out of reach for most relevant systems, due to the unrealistic amount of memory space necessary to store the state vectors.

2.1.1 The Born Oppenheimer Approximation

The first step, to reduce the number of coupled differential equations, is to realize that the ions are much heavier than the electrons, a single nuclei is about 2000 times heavier than a single electron. Thus, in a classical picture, the electrons move much faster than the ions. Hence, from an electron's point of view the electron moves in the background of a frozen ionic configuration. Thus motivating the following assumption:

When "the ions follow their dynamics the electrons instantaneously adjust their wave function according to the nuclear wavefunction" [60] and furthermore do not undergo transitions between stationary states; this is also known as the Born Oppenheimer Approximation[12].

The consequence of the Born Oppenheimer approximation is that the electronic and ionic degrees of freedom can be separated resulting in:

$$H\chi(R)\psi(r; R) = E\chi(R)\psi(r; R) \tag{2.3}$$

Where $\psi(r;R)$ only depend parametrically on R and is an eigenfunction of the electronic part of the Hamiltonian $(T_e + U_{ee} + V_{en})\psi(r;R) = E_e\psi(r;R)$. Similar $\chi(R)$ is an eigenfunction of the nuclear part of the Hamiltonian $H_n = T_n + V_{nn}$.

Separating the Hamiltonian in an electronic and nuclear part leads to the following wave-equation for the nuclei:

$$(H_n + E_e(R))\chi(R) = E\chi(R). \tag{2.4}$$

$E_e(R)$ is the electronic energy which acts as a potential energy for the nuclei, as seen from Eq. (2.4). Neglecting the nuclei kinetic energy[1] and treating the nuclei as classical particles, *i. e.* treating V_{nn} as a classical Coulomb interaction, gives a classical equation for the motion of the nuclei:

$$-\left(\frac{\partial}{\partial R}(V_{nn}(R) + E_e(R))\right) = Ma. \tag{2.5}$$

Thus the first step is to find the energy surface $E_e(R)$ if one wishes to find the equilibrium positions of the nuclei.

2.1.2 The Hohenberg-Kohn Theorem

The objective is now to find the potential energy surface ($E_e(R)$) of the system. However, we have still not circumvented the obstacle of solving $3n$ coupled differential equations. Walter Kohn and Pierre Hohenberg overcame this obstacle by identifying the electron density(ρ) as the essential quantity [61, 80], and thereby reducing the dimension of the problem from $3n$ to only 3 dimensions.

The 1. Hohenberg-Kohn theorem states that: "the external potential is unequivocally determined by the electronic density, besides a trivial additive constant". Furthermore since $\rho(r)$ determines v_{ext} it also determins the ground state wave function[47, 60]. This leads to the second part of the Hohenberg-Kohn theorem, which states that: the energy of the system can be expressed as a functional of the density,

$$E_v[\rho] = F[\rho] + \int \rho(r)v_{ext}(r)dr, \tag{2.6}$$

[1] The kinetic energy scales like $\frac{1}{m}$, when comparing electronic and nuclei kinetic energy, under the assumption that the electronic and nuclei momentum have the same magnitude; this assumption can be justified by considering a molecule, the molecule consists of nuclei and electrons. Both the electrons and nuclei are confind to the molecule; thus if one think of the molecule as a box and ignores all interactions they will have the same momentum.

where $F[\rho] = \langle \phi[\rho] | T + U_{ee} | \phi[\rho] \rangle$ and $\phi[\rho]$ is the ground state of the potential which has ρ as its ground state density. Thus the groundstate energy can be found by minimising the above functional. However, finding an expression for the functional $F[\rho]$ in Eq. (2.6) is nontrivial. The electron-electron interaction part of $F[\rho]$ can be divided into three part of decreasing contribution to the total energy: The largest contribution is the classical electrostatic energy which functional form is known exactly; the second contribution, the exchange term, originates from the fermionic nature, the Pauli principle, of the electrons and can be calculated exact; however, for computational reasons this term is often approximated; the last term consist of the energy missed by the two others when neglecting the true many body nature of the electronic wavefunction and is called the correlation term. the correlation term is unknown and has to be approximated. Often the exchange and correlation terms are collected in a single term $E_{XC}[\rho]$ called the exchange correlation term[60].

2.1.3 The Kohn-Sham equations

Besides finding and appropriate approximation for $E_{XC}[\rho]$ the remaining obstacle is the kinetic energy $T = \langle \phi[\rho] | T | \phi[\rho] \rangle$, because no functional dependence on the electron density is known. However, the kinetic energy can be found for a system of non-interacting particles. Thus the idea of Kohn and Sham was to consider a system of non-interacting electrons exposed to an external potential that reproduced the same electronic density, and thus the same ground state energy, as the interacting system; and then calculate the kinetic energy for the non-interacting system instead. Thus consider a reference system of N non-interacting particles described by the Hamiltonian and associated Schrödinger equation:

$$H_{ref} = \sum_{i=1}^{N} \left[-\frac{\hbar^2}{2m} \nabla_i^2 + v_{ref}(r_i) \right] \text{ and } H_{ref} \varphi_i(r) = \epsilon_i(r) \varphi_i(r) \tag{2.7}$$

The question now is: how should the reference potential, $v_{ref}(r_i)$, look to ensure that $\rho_{ref} = \rho$.

By minimizinge the energy functionals, under the constraint that the density integrates to N particles, both for the interacting and non-interacting systems the answer turns out to be:

$$v_{ref}(r_i) = v_{ext}(r) + \int \frac{\rho(r')}{|r - r'|} dr' + \frac{\delta E_{XC}[\rho]}{\delta \rho} \tag{2.8}$$

This leads to the Kohn-Sham equation[60]:

$$\left\{-\frac{\hbar}{2m}\nabla^2 + v_{ext}(r)\int\frac{\rho(r')}{|r-r'|}dr' + \frac{\delta E_{XC}\left[\rho\right]}{\delta\rho}\right\}\varphi_i(r) = \epsilon_i(r)\varphi_i(r) \tag{2.9}$$

where $\varphi_i(r)$ are the so called Kohn-Sham orbitals. The electron density ρ entering Eq. (2.8) is calculated from:

$$\rho(r) = \sum_i^N n_f^i \varphi_i(r)\varphi_i^*(r), \tag{2.10}$$

where n_f^i is the fermi-function and is included to ensure that only occupied orbitals are taking into account. Thus the Kohn-Sham equation has to be solved self-consistently. Note that the kinetic energy derived from the non-interacting system is not the exact kinetic energy because of the fact that the true many-body wave function is not a Slater determinant; the difference $T\left[\rho\right] - T_{ref}\left[\rho\right]$ are absorbed into the exchange correlation functional. Thus the Kohn-Sham functional becomes:

$$E_{ks}\left[\rho\right] = T_{ref}\left[\rho\right] + \int\rho(r)v_{ext}(r)dr + \frac{1}{2}\iint\frac{\rho(r)\rho(r')}{|r-r'|}drdr' + E_{XC}\left[\rho\right] \tag{2.11}$$

where now $E_{XC}\left[\rho\right]$ consists of an exchange part originating from the electron-electron interaction and a correlation part which has contributions both from the electron-electron interaction and the kinetic energy.

2.1.3.1 The SIESTA implementation

To solve Eq. (2.9) a specific boundary condition and exchange-correlation have to be chosen. In this thesis the academic code SIESTA is used[116]. In SIESTA the boundary conditions of Eq. (2.9) are chosen to be periodic in all directions. SIESTA offers a range of choices for the exhange-correlation functional, however in this thesis only the Perdew-Burke-Ernzerhof(PBE)[94] parametrization of the generalized gradient approximation (GGA) is used.

Furthermore, the Kohn-Sham orbitals needs to be expanded in a specific basis set. The quality of the basis set influence the accuracy of the DFT calculation; by choosing an infinity amount of plane waves this can be avoided, however in reality a finite basis is chosen. SIESTA uses a linear combination of atomic orbitals (LCAO). Because the basis is atom-centered the memory and cpu-time used on describing the vacuum is reduced. However, the basis of atomic or-

bitals are non orthogonal, thus Eq. (2.9) is replaced by a generalized eigenvalue problem:

$$\left\{-\frac{\hbar}{2m}\nabla^2 + v_{ext}(\mathbf{r}) \int \frac{\rho(\mathbf{r}')}{|\mathbf{r}-\mathbf{r}'|} d\mathbf{r}' + \frac{\delta E_{XC}\left[\rho\right]}{\delta\rho}\right\} \varphi_k(\mathbf{r}_i) = \epsilon_i \boldsymbol{S} \varphi_k(\mathbf{r}), \qquad (2.12)$$

where $\boldsymbol{S} = \sum_{i,j} \langle \varphi_i | \, \varphi_j \rangle$ is the overlap matrix; and $\varphi_{k\in[\{i,lmn\}]}(\mathbf{r}) = \phi_{i,nl}(r_i) Y_{lm}(\mathbf{r}_i)$ are the the atomic orbitals, for atom number i at position $\mathbf{R}_i$. $\phi_{i,nl}(r_i)$ is the radial component, labeled by atom (i), principal quantum number (n) and azimuthal quantum number (l); and $Y_{lm}(\mathbf{r}_i)$ is the angular component, labeled by the magnetic quantum number (m). The position are relative to the atomic position $(\mathbf{r}_i = \mathbf{r} - \mathbf{R}_i)$.

To further improve the basis set a "multiple-ζ" basis can be applied. In a "multiple-ζ" basis there are multiple orbitals, with the same quantum numbers n, l and m, but with different radial dependence, per atom.

The atomic orbitals are chosen to be confined inside a radius R, which can be chosen individually for the atomic orbitals. The confinement ensures a sparse Hamiltonian and overlap matrix. Finally the density and some of the Hamiltonian matrix elements are calculated on a real-space grid. The resolution of the grid is described by an energy "grid cutoff". Lastly, only the chemically active orbitals are taking into account; the core electrons are, instead described by a norm-conserving pseudo-potential[40, 125].

2.2 Transport and NEGF

The true many-body wave function is not the Slater determinant of Kohn-Sham orbitals, obtained above[60], however they have proven themselves as a reasonable approximation for ab-initio quantum transport[92, 135], thus in this thesis the Kohn-Sham orbitals are used as a mean field approximation for the states of the system. However, DFT calculations based on the LDA or the PBE EX-functional are known to underestimate the gap between valence and conduction band and the HOMO-LUMO separation, especially for poorly conducting molecules. More accurate results can be achieved with more advanced methods like time dependent DFT, the GW method or the Kubo formula[20, 21, 63, 122, 123]. But, the advanced methods are often considerable more time consuming and limited in system size. If the shape of the bands are well described with ordinary DFT good results can be achieved by the use of an scissor operator[53, 34].

The single particle nature of the Kohn-Sham orbitals opens op for the use of the unperturbed retarded single particle Green's function, as the central building block. The unperturbed retarded single particle Green's function is defined as:

$$\boldsymbol{G}^{0,r}(\epsilon) \equiv \left[(\epsilon + i\eta)\boldsymbol{S} - \mathbf{H}\right]^{-1}. \tag{2.13}$$

Because of the local basis used in SIESTA the electronic Hamiltonian $\mathbf{H}$ and overlap matrix $\boldsymbol{S}$ can be partitioned into a central device(D), a left(L) and a right (R) region, respectably, as in Fig. 2.1. To perform a transport calculation the central device region has to be chosen large enough that there is no direct overlap between the left and right part of the system. Furthermore, removing the periodic boundary conditions in the transport direction give rise to the following Hamiltonian and overlap matrix:

$$\mathbf{H} = \begin{bmatrix} \mathbf{H}_L & \mathbf{H}_{LD} & 0 \\ \mathbf{H}_{DL} & \mathbf{H}_D & \mathbf{H}_{DR} \\ 0 & \mathbf{H}_{RD} & \mathbf{H}_R \end{bmatrix} \tag{2.14}$$

$$\boldsymbol{S} = \begin{bmatrix} \boldsymbol{S}_L & \boldsymbol{S}_{LD} & 0 \\ \boldsymbol{S}_{DL} & \boldsymbol{S}_D & \boldsymbol{S}_{DR} \\ 0 & \boldsymbol{S}_{RD} & \boldsymbol{S}_R \end{bmatrix} \tag{2.15}$$

The retarded Green's function down folded to the device region then becomes

$$\boldsymbol{G}_D^{0,r}(\epsilon) = \left[(\epsilon + i\eta)\boldsymbol{S}_D - \mathbf{H}_D - \boldsymbol{\Sigma}_L^r(\epsilon) - \boldsymbol{\Sigma}_R^r(\epsilon)\right]^{-1}, \tag{2.16}$$

where $\Sigma_{L/R}$ is the left/right self-energy, originating from the coupling to the half infinite left/right electrode, see Fig. 2.1(c). The self-energies are obtained, from the surface Green's functions ($\boldsymbol{g}_{L/R}^r$) of the electrodes. The surface Green's function can be obtained by a recursive method[103]. Having obtained $\boldsymbol{g}_{L/R}^r$ the self-energy is given by:

$$\boldsymbol{\Sigma}_\alpha^r(\epsilon) = \left(\mathbf{H}_{D\alpha} - \epsilon\boldsymbol{S}_{D\alpha}\right)\boldsymbol{g}_\alpha^r(\epsilon)\left(\mathbf{H}_{\alpha D} - \epsilon\boldsymbol{S}_{\alpha D}\right) \tag{2.17}$$

In this thesis the self-energy above are obtained using the academic code TRANSIESTA[13]. Further, if an external bias voltage V is applied TRANSIESTA fully treats the potential drop between the semi-infinite leads within the self-consistent procedure taking into account charging and polarization effects.

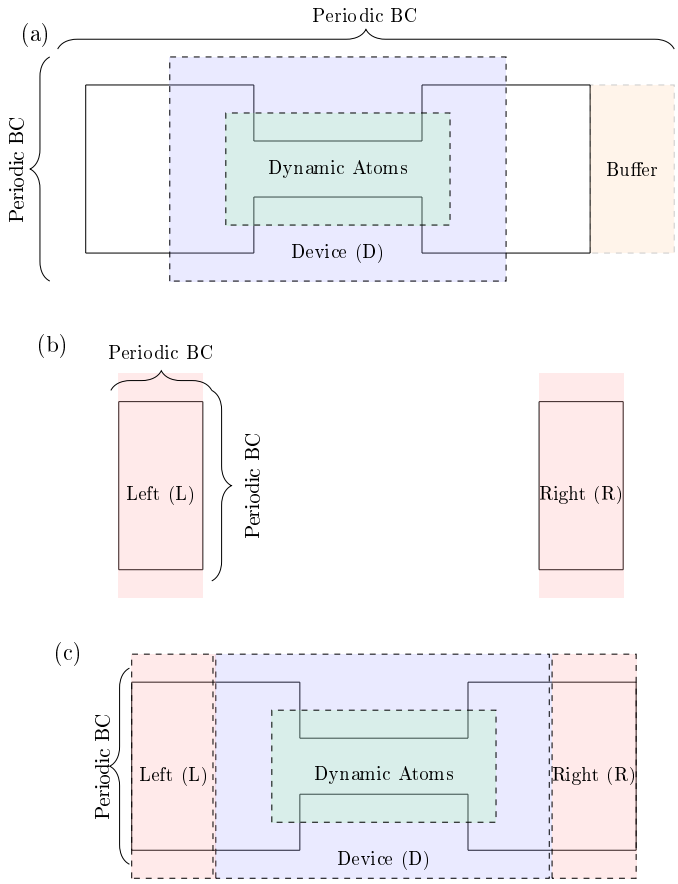

Figure 2.1: Three steps in making a Transport calculation. (a) Generic system setup for a SIESTA calculation. The system is periodic in all directions. The Dynamical matrix can be calculated for a subset of the system, denoted Dynamic Atoms. The coupling between the dynamical and electronic degrees of freedom, can be calculated in a finite Device region. Additional atom layers can be added, either to enforce periodicity or to ensure a better representation of bulk electrodes. (b) An independent SIESTA calculation is made for the electrodes. (c) In the TRANSIESTA scheme the device region are coupled to semi-infinite electrodes via self-energies, thus removing the periodicity along the transport direction.

2.2.1 The Current

In a real experiment the most common observable is the electronic current. The current is calculated by the Meir-Wingreen expression[42, 81], allowing for possible interactions in the device region. Thus, in lead α the current is given by:

$$I_\alpha = 2e\langle\dot{\hat{N}}_\alpha\rangle = -\frac{2e}{\hbar}\int_{-\infty}^{\infty}\frac{d\epsilon}{2\pi}T_\alpha, \tag{2.18}$$

$$T_\alpha(\epsilon) \equiv Tr\left[\mathbf{\Sigma}_\alpha^{<}(\epsilon)\mathbf{G}_D^{>}(\epsilon) - \mathbf{\Sigma}_\alpha^{>}(\epsilon)\mathbf{G}_D^{<}(\epsilon)\right]. \tag{2.19}$$

Here $\langle\dot{\hat{N}}_\alpha\rangle$ is the expectation value of the electronic particle number operator of lead α, $\mathbf{G}_D^{\lessgtr}(\epsilon)$ the full lesser/greater Green's function in the device region, including all relevant interactions, and $\mathbf{\Sigma}_\alpha^{\lessgtr}(\epsilon)$ the lesser/greater self-energy representing the rate of electrons scattering into/out of the states in the device region (D). Assuming the leads to be unaffected by the non-equilibrium conditions in the device region the self-energies can be written as[42]:

$$\mathbf{\Sigma}_\alpha^{<}(\epsilon) = in_F(\epsilon-\mu_\alpha)\mathbf{\Gamma}_\alpha(\epsilon) \tag{2.20}$$

$$\mathbf{\Sigma}_\alpha^{>}(\epsilon) = -i(1-n_F(\epsilon-\mu_\alpha))\mathbf{\Gamma}_\alpha(\epsilon), \tag{2.21}$$

where $n_F(\epsilon-\mu_\alpha) = 1/\left(\exp(\frac{\epsilon-\mu_\alpha}{k_bT})+1\right)$ is the Fermi-funciton, μ_α the chemical potential of lead α and,

$$\mathbf{\Gamma}_\alpha(\epsilon) = i(\mathbf{\Sigma}_\alpha^{r}(\epsilon) - \mathbf{\Sigma}_\alpha^{r\dagger}(\epsilon)) \tag{2.22}$$

is the broadening of the states inside the device region D due to the coupling to lead α.

The relation between the full Green's functions and the unperturbed is given by Dyson and Keldysh equations[42, 28]:

$$\mathbf{G}^r(\epsilon) = \mathbf{G}_0^r(\epsilon) + \mathbf{G}_0^r(\epsilon)\mathbf{\Sigma}_{\text{int}}^r(\epsilon)\mathbf{G}^r(\epsilon) \tag{2.23}$$

$$\mathbf{G}^<(\epsilon) = \mathbf{G}^r(\epsilon)[\mathbf{\Sigma}_L^<(\epsilon) + \mathbf{\Sigma}_R^<(\epsilon) + \mathbf{\Sigma}_{\text{int}}^<(\epsilon)]\mathbf{G}^a(\epsilon) \tag{2.24}$$

$$\mathbf{G}^>(\epsilon) = \mathbf{G}^r(\epsilon)[\mathbf{\Sigma}_L^>(\epsilon) + \mathbf{\Sigma}_R^>(\epsilon) + \mathbf{\Sigma}_{\text{int}}^>(\epsilon)]\mathbf{G}^a(\epsilon), \tag{2.25}$$

$$\tag{2.26}$$

here $\mathbf{\Sigma}_{int}^{\lessgtr r}(\epsilon)$ is a self-energy arising due to the interactions. Furthermore, if the system is in a steady-state the greater and advanced Green's function are related due to time reversal symmetry as: $\mathbf{G}^a = (\mathbf{G}^r)^\dagger$[42]

2.2.2 Phonons

In this thesis the dynamical matrix, describing the vibrational degrees of freedom, are obtained by the use of the frozen phonon method as implemented in the academic code Inelastica[90, 30, 28]. The Atomic forces are obtained by displacing, by turn, each atom by $\Delta_{i\nu} = 0.02$ Å in the $\nu \in \{x, y, z\}$ directions and performing a total energy calculation in SIESTA yielding the atomic forces directly. The force-constant matrix can be obtained as:

$$\mathbf{K}_{i\nu,j\mu} = \frac{\partial^2 E(\mathbf{R})}{\partial r_{i,\nu} \partial r_{j,\mu}}\Big|_{\mathbf{R}=\mathbf{R}^0} = -\frac{F_{i,\nu}(\Delta_{j\mu}) - F_{i,\nu}(-\Delta_{j\mu})}{2\Delta_{j\mu}}, \tag{2.27}$$

further, momentum conservation is enforced by correcting the diagonal. The dynamical matrix is obtained by normalizing with the mass:

$$\mathbf{W}_{i\nu,j\mu} = \frac{1}{\sqrt{M_i M_j}} \mathbf{K}_{\mathbf{i}\nu,\mathbf{j}\mu}. \tag{2.28}$$

The dynamical matrix $\mathbf{W}$ give rise to the following eigenvalue problem:

$$(\omega \mathbf{1} - \mathbf{W})\mathbf{v} = 0, \tag{2.29}$$

which have the set of solutions $\{\omega_\lambda, \mathbf{v}_\lambda\}$. Similar to the electronic degrees of freedom the dynamical matrix can be partitioned into a central device, left and right part:

$$\mathbf{W} = \begin{bmatrix} \mathbf{W}_L & \mathbf{W}_{LD} & 0 \\ \mathbf{W}_{DL} & \mathbf{W}_D & \mathbf{W}_{DR} \\ 0 & \mathbf{W}_{RD} & \mathbf{W}_R \end{bmatrix}, \tag{2.30}$$

and the phonon retarded Green's function can be defined for vibrational degrees of fredom as:

$$\boldsymbol{D}^{0,r}(\omega) \equiv \left[(\omega + i\eta)^2 \mathbf{1} - \mathbf{W}\right]^{-1}, \tag{2.31}$$

$$\boldsymbol{D}_D^{0,r}(\omega) \equiv \left[(\omega + i\eta)^2 \mathbf{1} - \mathbf{W} - \boldsymbol{\Pi}_L^r - \boldsymbol{\Pi}_R^r\right]^{-1}, \tag{2.32}$$

The phonon transmission then becomes

$$T_{ph}(\omega) \equiv Tr\left[\boldsymbol{\Pi}_\alpha^<(\omega)\mathbf{D}^>(\omega) - \boldsymbol{\Pi}_\alpha^>(\omega)\mathbf{D}^<(\omega)\right]. \tag{2.33}$$

2.2.3 Electron-Phonon interaction

A large part of this thesis concerns the interplay between the electronic and vibrational degrees of freedom. The electron-phonon interaction is calculated in the harmonic approximation by finite difference as implemented in Inelastica[90, 30, 28] and explained in Sec. 2.2.2. Expanding the Kohn-Sham Hamiltonian to lowest order with respect to the displacement gives:

$$\mathbf{M}_{ij}^{\lambda} = \sum_{I\nu} \langle \psi_i | \frac{\partial \mathbf{H}}{\partial r_{I\nu}} | \psi_j \rangle \Big|_{\mathbf{R}=\mathbf{R}^0} \mathbf{v}_{I\nu}^{\lambda} \sqrt{\frac{\hbar}{2M_I \omega_\lambda}} \tag{2.34}$$

When calculating the electron-phonon interaction, by finite difference, the Fermi-energy between the equilibrium- and the displaced structure can shift. However, ff the system at hand is connected to infinite metal leads which pins the Fermi-energy, the shift must be considered a finite size effect in the periodic SISTA calculation. Thus, to compensate for the finite size effect the default setting in Inelastica is to measure all energies with respect to the Fermi energy of the relaxed structure ϵ_F^0 [30]. Thus the displaced Hamiltonians are shifted as:

$$\overline{\mathbf{H}}(Q_{I\nu}) = \mathbf{H}(Q_{I\nu}) - \left[\epsilon_F(Q_{I\nu}) - \epsilon_F^0\right]. \tag{2.35}$$

However, care has to be taken if the leads are not metallic, then the Fermi-level needs not to be well defined. In this case the uncorrected Hamiltonian might give a better representation of the system.

2.3 Summary

In this chapter the basic concepts of DFT and the SIESTA implementation have been explained. It hase been shown how the local basis set enables transport calculations and the Green's function formalism have been introduced both for electrons and phonons.

The final model can be summarized as:

$$\hat{H}_{total} = \hat{H}_e^0 + \hat{H}_{ph}^0 \hat{H}_{e-ph}, \tag{2.36}$$

$$\hat{H}_e^0 = \sum_{ij} H_{ij}^0 \hat{c}_i^\dagger \hat{c}_j, \tag{2.37}$$

$$\hat{H}_{ph}^0 = \sum_{\lambda} \hbar\omega_\lambda \hat{b}_\lambda^\dagger \hat{b}_\lambda, \tag{2.38}$$

$$\hat{H}_{e-ph} = \sum_{\lambda} \sum_{ij} M_{ij}^\lambda \hat{c}_i^\dagger \hat{c}_j (\hat{b}_\lambda^\dagger + \hat{b}_\lambda), \tag{2.39}$$

were $\hat{c}_i$ and $\hat{b}_\lambda$ are the electron and phonon creation operators, respectively. Thus, $\hat{H}_e^0$ is the single-particle mean-field Hamiltonian given by the Kohn-Sham orbitals, $\hat{H}_{ph}^0$ is the uncoupled phonon/vibration Hamiltonian obtained by the frozen phonon method together with the coupling between the electrons and phonons $\hat{H}_{e-ph}$.

Chapter 3

Finite-Frequency Shot Noise and Light Emission

In this chapter we investigate the interplay between finite frequency noise and light emission. We take inspiration from two experiments probing light emission in a STM setup. The first experiment, by Schneider *et al.*[110], concerns light emission in a Ag-Ag(111) junction, where they measure the photon yield as a function of conductance. The conductance is varied by changing the tip surface distance. The obtained photon yield is interpreted in terms of current noise at optical frequencies, see Fig. 3.1. In the second experiment, by Schneider *et al.*[107], a similar setup is used, however now they probe a C_{60} on a Cu(111) surface. Here the photon yield depends on the bias polarity, indicating a non trivial effect of the bias polarity and the non-equilibrium electronic structure, see Fig. 3.2.

The chapter is organized as follows. First the basics of current noise is introduced, then the finite frequency noise is related to light emission and finally we calculate the finite frequency noise for a Ag-Ag(111) junction and a C_{60} on a Cu(111) surface. The results of this chapter were published in (paper 1) [77]

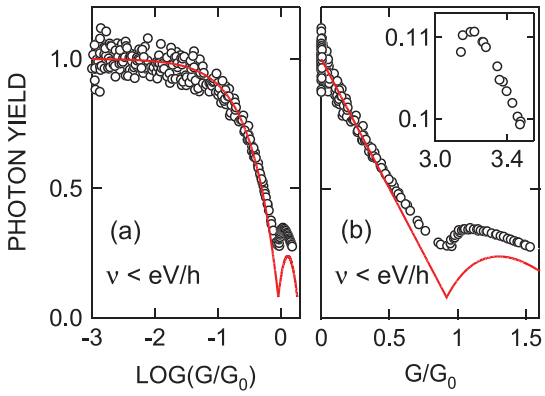

Figure 3.1: Adopted from Schneider *et al.*[110]. Yield of photons, originating from one-electron processes, (defined as intensity divided by the current, normalized to 1 at low conductance) vs conductance on (a) logarithmic and (b) linear scales. Dots, experimental data. Red line, Fano factor from Eq. (3.3) for a two channel model. A yield of 1 corresponds to an estimated quantum efficiency of 3×10^{-6}.

3.1 Noise

Generally, any electronic circuit will experience fluctuations in the electronic current, due to the quantized nature of the charge carriers. The fluctuations will have an equilibrium thermal noise contribution, also called Nyquist-Johnson noise[83, 55], and a non-equilibrium contribution denoted shot noise. The Nyquist-Johnson noise is given by $S_{thermal} = 4k_BTG$[83]; thus, proportional to the conductance G and the temperature T. Therefore, investigating the Nyquist-Johnson noise gives the same information as a conductance measurement. However, for low temperatures the Nyquist-Johnson noise is small and the shot noise becomes dominant ; the shot noise gives information complementary to conductance measurements about the non-equilibrium electronic state, and the number of transmission channels involved[127]. If the electrons are considered uncorrelated, the variation in the electron flow, is given by the Poisson distribution; meaning the time intervals between arrivals of carriers is Poissonian $P(\Delta t) = \tau^{-1}\exp(-\Delta T/\tau)$, with τ being the mean time interval[109]. Thus the Poisson value for shot noise is frequency independent and given by:

$$S_P = 2e\,|I| = \frac{2e^3}{\pi\hbar}\,|V| \sum_n T_n. \tag{3.1}$$

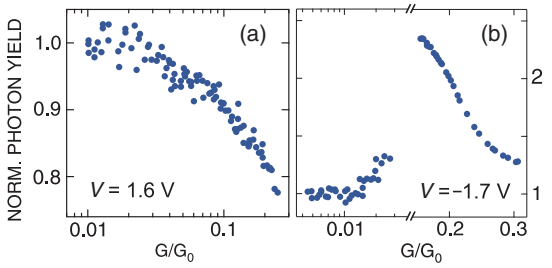

Figure 3.2: Adopted from Schneider *et al.*[107]. Yield of photons with energy $1.22 < h\nu < 1.57$ eV and $1.22 < h\nu < 1.62$ eV versus conductance at (a) positive and (b) negative sample voltage V, respectively.

Were V is the applied bias and T_n is the eigenchannel transmission probability for the n'th channel. However taking into account that the electrons obey Fermi-Dirac statistics, in the zero-frequency limit, the expression for the noise becomes

$$S = \frac{2e^3}{\pi\hbar}|V|\sum_n T_n(1-T_n), \tag{3.2}$$

which is suppressed compared to the Poisson value due to correlations[15]. The degree of suppression of the noise compared to the Poisson value is called the Fano factor[10]:

$$F = \frac{S}{S_P}. \tag{3.3}$$

3.1.1 Finite frequency noise

To describe the frequency dependence of the noise spectrum, observed in experiments, we define the finite frequency noise as:

$$S_{z,z'}(0,t) \equiv \langle\langle I_z(0)I_{z'}(t)\rangle\rangle = \langle(I_z(0) - \langle I_z(0)\rangle)(I_{z'}(t) - \langle I_{z'}(t)\rangle)\rangle, \tag{3.4}$$

where $I_z(t) = e^{iHt/\hbar}I_z e^{-iHt/\hbar}$ is the current operator, in the Heisenberg representation, through a surface normal to the transport direction at a point z. Hence, $S_{z,z'}(0,t)$ expresses the correlation between the current at a position z at $t = 0$ and the current at a position z' at a later time t The Fourier transform

of $S_{z,z'}(0,t)$ in Eq. (3.4) gives the noise spectrum,

$$S_{zz'}(\omega) = \int_{-\infty}^{+\infty} \langle\langle I_z(0) I_{z'}(t)\rangle\rangle e^{i\omega t} dt\,. \tag{3.5}$$

Following [35, 3] , inserting a complete set of eigenstates into Eq. (3.5), and doing the Fourier transform, we obtain a golden-rule-type expression for the current noise,

$$\begin{aligned} S_{zz'}(\omega) =& 2\pi\hbar \sum_{\substack{i,f \\ i\neq f}} \iint \langle\psi_i|I_z|\psi_f\rangle\langle\psi_f|I_{z'}|\psi_i\rangle \delta(\varepsilon_i - \varepsilon_f - \hbar\omega) \\ & \times n_F(\varepsilon_i - \mu_i)(1 - n_F(\varepsilon_f - \mu_f)) d\varepsilon_i d\varepsilon_f\,. \end{aligned} \tag{3.6}$$

The initial and final states are summed over scattering states from both electrodes. Equation (3.6) includes both the Nyquist-Johnson (thermal) and shot noise contributions. Since the energy of the emitted light is much larger than the thermal energy ($\hbar\omega \gg k_B T$), only the zero-temperature limit is considered. In this case, besides the zero-point fluctuations, the only contribution is the shot noise. Thus, considering a STM-tip surface junction and a applied bias $V = V_t - V_s > 0$, the current noise reduces to,

$$S_{zz'}(\omega) = 2\pi\hbar \sum_{s,t} \int_{\mu_s+\hbar\omega}^{\mu_t} \langle\psi_t|I_z|\psi_s\rangle\langle\psi_s|I_{z'}|\psi_t\rangle d\varepsilon_t, \tag{3.7}$$

with $\varepsilon_s = \varepsilon_t - \hbar\omega$. The "diagonal" correlation S_{zz} in Eq. (3.7) gives the sum of the transition rates between the initial filled tip scattering states ψ_t, and the final empty surface scattering states ψ_s, with energies ε_t and ε_s, respectively. We notice that if z and z' are located at the surface and tip electrode, respectively, then according to charge conservation,

$$I_d \equiv \dot{Q}_d = I_z - I_{z'}\,, \tag{3.8}$$

the charge fluctuation in the central molecule/"device" region(D) is given by

$$S_{dd} = S_{zz} + S_{z'z'} - S_{zz'} - S_{z'z}\,. \tag{3.9}$$

Similarly for the fluctuation of the average current $I_a = \frac{1}{2}(I_z + I_{z'})$ we have

$$S_{aa} = \frac{1}{4}\left(S_{zz} + S_{z'z'} + S_{zz'} + S_{z'z}\right). \tag{3.10}$$

3.2 Inelastic Transition due to Electron-plasmon Interaction

When a scanning tunneling microscope (STM) tip is brought towards a metal surface, strong localized plasmon modes develop between the tip and surface, in addition to the propagating surface mode at the metal interface[54]. Thus, in this section we will connect the finite frequency noise to the light emission experiments by Schneider *et al.*[110, 107] shown in Fig. 3.1 and Fig. 3.2. In the presence of an electric field, the electrons traversing the gap interacts with the plasmon modes opening the possibility for an electron to tunnel inelasticly by the emission/absorption of a plasmon.

As mentioned above the "diagonal" correlation S_{zz} in Eq. (3.7) gives the sum of the transition rates between the initial filled tip scattering states ψ_t, and the final empty surface scattering states ψ_s. Thus, the finite frequency shot noise can be viewed as inelastic electronic transitions between the tip and surface scattering states[77]. The positive frequency/energy part of the noise spectrum corresponds to the photon emission, relevant to the experiment, and the negative part to the absorption process. To further underline the connection between the shot noise and light emission we investigate the interactions of the electrical current with the plasmon field. Following the theory of light emission from STM[54, 96] and point contacts[65], the interaction of the electrical current with the plasmon field in the tip-surface cavity is described by the following Hamiltonian,

$$H_{int} = \frac{1}{c}\int j(r)A(r)d^3r\,, \tag{3.11}$$

where $j(r)$ is the electron current density operator at position r. The plasmon mode, with frequency, ω_p, and spatial distribution, $\xi(r)$, is represented by a vector potential,

$$A(r) = \sqrt{\frac{2\pi\hbar c^2}{V\omega_p}}\xi(r)\left(a + a^\dagger\right)\,. \tag{3.12}$$

Here $a(a^\dagger)$ is the annihilation (creation) operator of the plasmon mode, c is the speed of the light, $\hbar$ the reduced Planck constant, and V the normalization volume. In principle, the plasmon mode frequency and field distribution can be calculated for a given tip-surface distance. However, this is a daunting task for atomistic first principles theory and we do not consider this problem here. Instead, we focus only on the source of the light emission, and investigate the effect of the non-equilibrium electronic structure on the emission rate. We ignore the spatial distribution of the mode in the xy-plane transverse to the current, $\xi(r) = \xi(z)$, and perform the integration over these directions in Eq. (3.11) and

get

$$H_{int} = \frac{1}{c}\int I(z)A(z)dz, \tag{3.13}$$

$$= M(a + a^{\dagger}), \tag{3.14}$$

where $I(z)$ is the surface current evaluated at z, integrated over the transverse surface , and M is the coupling given by the integrated current and mode distribution. The emitted power from the junction is proportional to the inelastic transition probability due to the interaction between initial(ψ_i) and final(ψ_f) states originating from the tip (t) or surface (s) electrode,

$$P \sim \sum_{i,f} \iint |\langle \psi_f | M | \psi_i \rangle|^2 \delta(\varepsilon_i - \varepsilon_f - \hbar\omega_p) \times n_F(\varepsilon_i - \mu_i)(1 - n_F(\varepsilon_f - \mu_f)) d\varepsilon_i d\varepsilon_f \,. \tag{3.15}$$

We employ the normalization, $\langle \psi_i | \psi_j \rangle = \delta_{ij}\delta(\varepsilon_i - \varepsilon_j)$, and filling given by the Fermi-Dirac distribution n_F. Finally, we assume that the "diagonal" contributions in the z direction capture the main dependence of the emitted power on the electronic structure of the junction. Thus we get,

$$P \sim \int dz\, |\xi(z)|^2 \sum_{i,f} \iint |\langle \psi_f | I(z) | \psi_i \rangle|^2 \delta(\varepsilon_i - \varepsilon_f - \hbar\omega_p) \times n_F(\varepsilon_i - \mu_i)(1 - n_F(\varepsilon_f - \mu_f)) d\varepsilon_i d\varepsilon_f. \tag{3.16}$$

The "diagonal" assumption can not be justified without concrete knowledge about the spatial distribution of the mode along with the local current operator. However, it is computationally too expensive to include all of them. Thus, below we will use a first principles method in order to calculate without any fitting parameters the light emission using this approximation and compare with the experimental trends. Furthermore, we actually tried to include some of the cross terms and only saw slight changes of the final results.

Using equation Eq. (3.7), we can write Eq. (3.16) as

$$P(\omega_p) \sim \int dz\, |\xi(z)|^2 S_{zz}(\omega_p), \tag{3.17}$$

Equation Eq. (3.17) shows how the power of the emitted light are connected to the finite frequency noise. To achieve a direct relation between the emission rates and the intensity of light emission, the integral in Eq. (3.17) needs to be

performed, taking into account the spatial distribution of the plasmon mode, $\xi(z)$. However, since we do not have specific knowledge about the mode we will to do the simplest possible approximation by taking the equally-weighted average of all the surface layers (e.g., $\xi(z) = \text{Constant}$). In reality, the plasmon field distribution may change with the tip-surface distance. In the tunneling regime, we expect a high weighting-factor in the region between the tip-surface gap. On the other hand, upon contact, due to the high conductance, we expect the field distribution to spread out into both electrodes[111, 104].

3.3 Reformulation in Terms of NEGF

Calculating the shot noise $S_{zz'}$ in Eq. (3.7) involves the evaluation of matrix elements of the form:

$$\langle \psi_t | I_z | \psi_s \rangle. \tag{3.18}$$

The current matrix I_s, can be written as[89],

$$I_s = -\frac{ie}{\hbar}[P_s, H] = \frac{ie}{\hbar}(V_{ds} - V_{sd}), \tag{3.19}$$

where P_s denotes projection into the surface electrode subspace, H is the total Hamiltonian, V_{ds} is the coupling matrix between the device and surface electrode and V_{sd} is its complex conjugate. An orthogonal basis set is assumed; however, a generalization to the non-orthogonal case is straightforward by a Löwdin transformation[18]. Thus we need to express the current operator in a basis of scattering states in terms of quantities readily available in the DFT-NEGF calculation. This can be done by the use of the operator identity $I = P_s + P_d + P_t$ and the Lippmann-Schwinger equation[70] which connect the scattering states and the full retarded Greens functions:

$$|\psi_s(\varepsilon)\rangle = |\phi_s(\varepsilon)\rangle + G^r(\varepsilon) V_T |\phi_s(\varepsilon)\rangle \,, \tag{3.20}$$

were $|\psi_s(\varepsilon)\rangle$ and $|\phi_s(\varepsilon)\rangle$ are the scattering states from the semi-infinite surface electrode with and without coupling to the device, respectively. ϕ_s is non-zero only in the surface electrode, contrary to ψ_s which spans the whole region including both electrodes and the device; the coupling matrix, V_T, represent the coupling between the device and the two electrodes and $G^r(\varepsilon)$ is the retarded Green's function of the whole system including the effect of V_T. The desired matrix element is (see Lü *et al.*[77] for details.):

$$\langle \psi_t(\varepsilon) | I_s | \psi_s(\varepsilon_-) \rangle = \frac{ie}{\hbar} \langle \psi_t^d(\varepsilon) | W_s(\varepsilon_-, \varepsilon) | \psi_s^d(\varepsilon_-) \rangle \,, \tag{3.21}$$

where

$$W_i(\varepsilon_-, \varepsilon) \equiv (G_{dd}^r)^{-1}(\varepsilon_-) + \Sigma_i(\varepsilon_-) - \Sigma_i^\dagger(\varepsilon). \tag{3.22}$$

Note that all quantities are projected to the device region, ($G^r_{dd} = P_d G^r P_d$), and thus depend on the actual splitting into regions. Using the current matrix element, we can now write the surface current shot noise at zero temperature as,

$$S_{ss}(\omega) = \int_\theta \mathrm{Tr}\left[W_s(\varepsilon_-,\varepsilon)A_s(\varepsilon_-)W_s^\dagger(\varepsilon_-,\varepsilon)A_t(\varepsilon)\right] d\varepsilon\,,$$

where the integral is defined as,

$$\int_\theta \cdot\; d\varepsilon = \theta(|eV|-\hbar\omega)\frac{e^2}{2\pi\hbar}\int_{\hbar\omega-|eV|/2}^{|eV|/2} \cdot\; d\varepsilon, \tag{3.23}$$

with $\theta(x)$ being the Heaviside step function, $A_\alpha(\varepsilon) = G_d(\varepsilon)\Gamma_\alpha(\varepsilon)G_d^\dagger(\varepsilon) = 2\pi\sum_{i=\alpha}|\psi_i^d(\varepsilon)\rangle\langle\psi_i^d(\varepsilon)|$ is the device spectral function due to scattering states from the surface/tip electrode and $\Gamma_\alpha = i(\Sigma_\alpha - \Sigma_\alpha^\dagger)$, for α belonging to the surface (s) or tip (t). A similar derivation gives the tip current noise $S_{tt}(\omega)$ and their cross correlation $S_{st}(\omega) = S_{ts}^*(\omega)$:

$$S_{tt}(\omega) = \int_\theta \mathrm{Tr}\Big[W_t^\dagger(\varepsilon,\varepsilon_-)A_s(\varepsilon_-)W_t(\varepsilon,\varepsilon_-)A_t(\varepsilon)\Big] d\varepsilon\,, \tag{3.24}$$

$$S_{st}(\omega) = -\int_\theta \mathrm{Tr}\left[W_s(\varepsilon_-,\varepsilon)A_s(\varepsilon_-)W_t(\varepsilon,\varepsilon_-)A_t(\varepsilon)\right] d\varepsilon. \tag{3.25}$$

The difference between Eqs. (3.23) and (3.24) reveals the position dependence of finite frequency noise. Importantly, they both yield the standard result in the zero-frequency limit[10]. Assuming constant self-energies (Σ_s, Σ_t), and decoupled eigenchannel transmissions[89] at different energies, $T_n(\varepsilon)$, gives more physically transparent expressions,

$$S_{ss}(\omega) = \sum_n \int_\theta T_n(\varepsilon)(1-T_n(\varepsilon_-))\, d\varepsilon\,, \tag{3.26}$$

$$S_{tt}(\omega) = \sum_n \int_\theta T_n(\varepsilon_-)(1-T_n(\varepsilon))\, d\varepsilon\,, \tag{3.27}$$

valid for positive sample voltages, $V > 0$. The two expressions are exchanged for negative bias. Note that T_n are the channel transmissions calculated for the particular bias, V. Unfortunately, we are not able to write the cross correlations S_{st} and S_{ts} in terms of the eigentransmissions T_n. Equations (3.26-3.27) show that the finite frequency noise is related to the eigenchannel transmission and reflection coefficients at two energy windows. The first energy window corresponds to transmission in the energy range $[\hbar\omega-(eV/2); eV/2]$, the other window is shifted downwards by $\hbar\omega$, $[-eV/2; eV/2-\hbar\omega]$. We denote these as the active energy windows. The correlation, S_{ss}, corresponds to inelastic transitions taking place at the device-surface interface. For positive sample voltage, $V > 0$, it

is proportional to the transmission coefficient of the tip scattering state in the high energy window, and the reflection coefficient of the surface scattering state in the low energy window. The reverse is the case for S_{tt}. Schematic diagrams of these two processes are shown in Fig. 3.3.

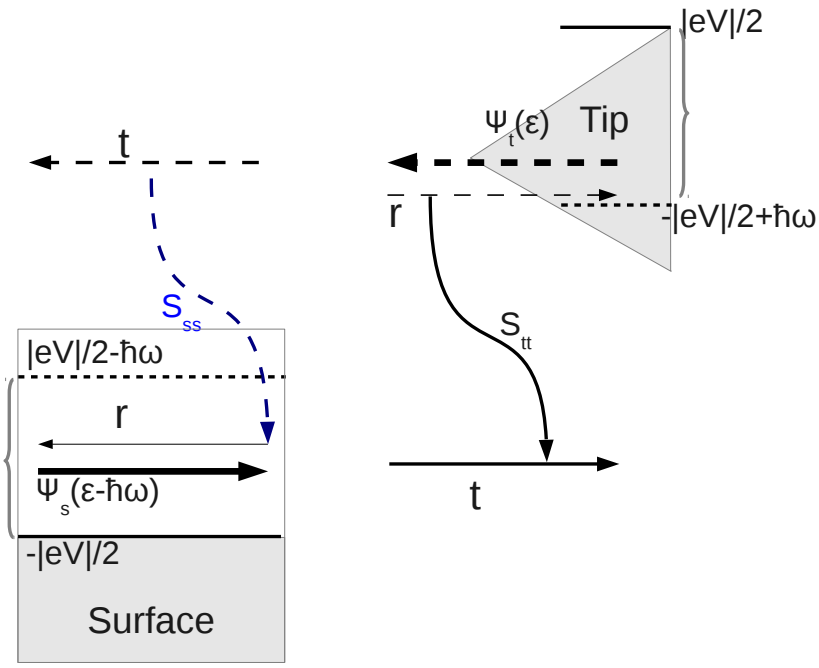

Figure 3.3: Schematic diagrams showing the two processes contributing to S_{tt} (solid black) and S_{ss} (dashed blue) for positive sample bias, $V > 0$. The curly brackets show two active energy windows for inelastic transitions. The correlation, S_{ss} corresponds to a transition from a tip transmitted scattering state to a surface reflected scattering state. The correlation, S_{tt} corresponds to a transition from a tip reflected scattering state to a surface transmitted scattering state.

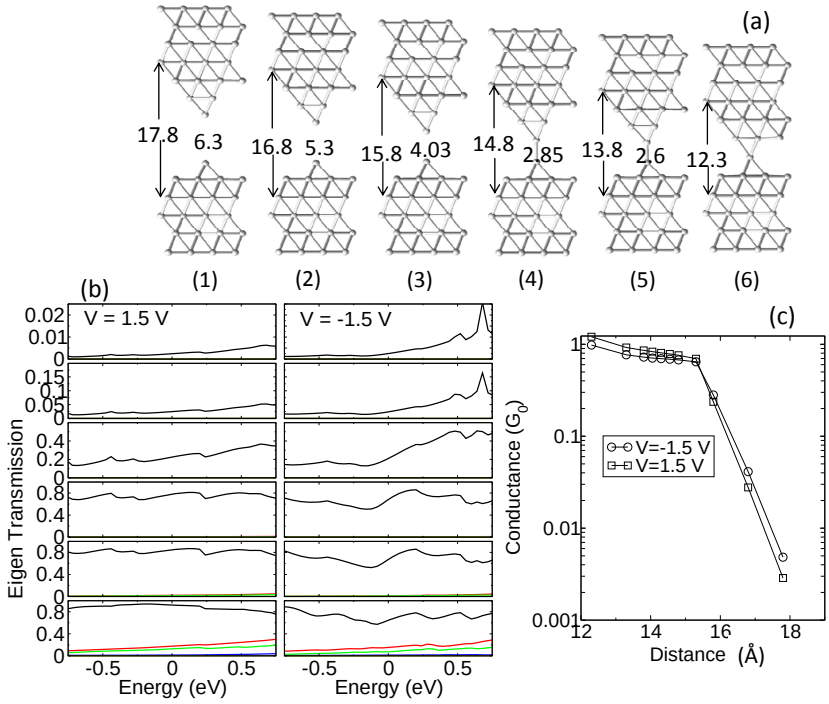

Figure 3.4: (a) A subset of structures used in the calculation, going from tunneling to contact. In the final structure, one tip atom is pushed aside when forming contact. The two surface layers, the tip and the adatom, are relaxed at zero bias for each structure. The numbers show the distance between the two fixed layers and between the tip-adatom in units of Å. (b) Transmission eigenchannels at $V = V_s - V_t = \pm 1.5$ V, going from tunneling to contact (top to bottom), for the structures shown in (a). (c) The average conductance as a function of surface layer separation, showing the transition from tunneling to contact.

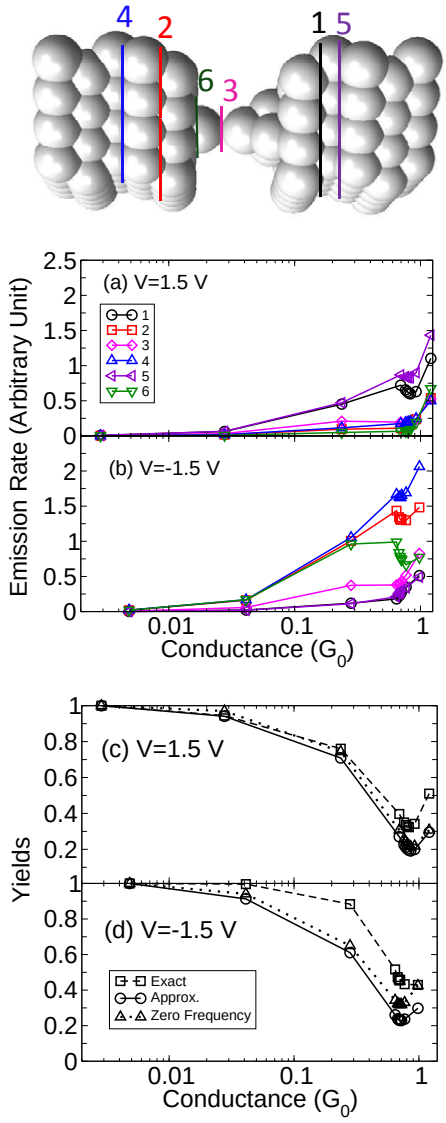

Figure 3.5: (a)-(b): Calculated noise power (or emission rate) S_{zz} from Eq. (3.7) for I_z defined through 6 different surfaces, shown above, for plasmon energy $\hbar\omega_p = 1.2$ eV. (c)-(d): Calculated yields $Y = P/\langle I\rangle$, normalized with respect to the first point. The power P is the averaged noise power over the 6 different surfaces (squares). Also shown are the results from average of S_{ss} and S_{tt} using the approximated expressions Eqs. (3.26-3.27) (circles), and from the zero-frequency noise calculation used in by Schneider *et al.*[110]. All of them give qualitatively similar results.

3.4 Calculated Light Emission in a STM Setup

3.4.1 Ag adatom on Ag(111)

Having achieved an expression for the power of the emitted light, in the DFT-NEGF approach, we now return to the experiment, mentioned in the introduction to this chapter. Schneider *et al.*. [110], studied STM-induced light emission from a Ag-Ag(111) junction. In the experiment, they probe from tunneling to the contact regime, see Fig. 3.1, measuring the photon yield (roughly emission probability per electron). The photon yield decrease linearly(plateau on log scale) going from tunneling towards contact, and has a kink just before reaching the conductance quantum. The photon yield is compared to the Fano factor (red line in Fig. 3.1), obtained from a simple two channel model. This suggest a possible correlation between photon emission and current shot noise. To simulate this experiment, we have studied a similar setup, consisting of a Ag adatom on Ag(111) surface. Fig. 3.4(a) shows a subset of the structures used in the calculations, going from tunneling to contact regime, (for the calculation details see paper1, Lü *et al.*). The transport calculations were done for a bias of $V = \pm 1.5$ V. As is evident from Fig. 3.4(c) the average conductance depends exponentially on the tip-atom distance, while it develops to a plateau upon contact as typically seen in experiments[110]. Except from the last structure in Fig. 3.4(a), the transmission is dominated by a single eigenchannel, as apparent from Fig. 3.4(b), and there is a small asymmetry for the two bias polarities.

The emission rate (proportional to the shot noise power) was evaluated for a plasmon energy of $\hbar\omega = \hbar\omega_p = 1.2$ eV using Eq. (3.7), or equivalently Eqs. (3.23-3.24). In order to map out the spatial distribution, the emission rate was calculated for the surface current defined at 6 different interfaces, shown in Fig. 3.5(a)-(b). From these calculations, we observe that the emission rate does not change significantly for interfaces in the same electrode, while they are quite different for the two electrodes, and for the tip-adatom interface. To relate the emission rates to the intensity of light emission, we need to evaluate the integral in Eq. (3.17). However, because we don't have specific knowledge about the spatial distribution of the plasmon mode, $\xi(z)$, we choose to evaluate the integral in the simplest possible way, by taking the equally-weighted average of all the surface layers (e.g., $\xi(z) = \text{Constant}$).

The final results for the photon yields $Y = P/\langle I \rangle$, using Eq. (3.17), are shown in Fig. 3.5(c)-(d), together with results from the approximate calculation using Eqs. (3.26-3.27), and from the zero-frequency noise in Eq. (3.2), corresponding to the red line in Fig. 3.1. We see that the qualitatively trends are similar for all three calculations: linear(plateau on log scale) in the tunneling regime, and

has a kink just before reaching the conductance quantum, consistent with the experiment[110] shown in Fig. 3.1.

The agreement between different approximations can be understood from the eigentransmission plotted in Fig. 3.4 (b): In the tunneling regime, the eigentransmission is rather small, hence, the photon yields is encoded in the reflection coefficient $R(\varepsilon) = 1 - T \approx 1$. Thus, the energy dependence of R is negligible, and in the contact regime, the eigentransmission is rather flat in the whole bias window. According to Eqs. (3.26-3.27) the finite frequency shot noise becomes similar to the zero frequency one, for a constant transmission.

3.4.2 C_{60} on Cu(111)

In case of the Ag-Ag junction mentioned above, the zero frequency expression for the shot noise gave an accurate description of the light emission due to the lack of features in the the electronic structure. Now we turn to another experiment studying, STM-induced light emission from a C_{60} molecule sitting on the reconstructed Cu(111) surface [107]. Contrary to the Ag-Ag junction, the non-equilibrium electronic structure and the C_{60} molecule modifies the photon yields drastically giving rise to a strong bias polarity dependence, indicating the effect of localized molecular resonance on the light emission property.

To simulate the experiment, we consider the five structures shown in Fig. 3.6(a)(for the calculation details see paper 1 [77]). Due to the surface reconstruction in the experiments[87, 107] the two first surface layers and tip were relaxed at zero bias to 0.02 eV/Å at different tip positions. Thus, we do not capture the abrupt jump-to-contact observed in the experiment at finite negative bias in our calculations. The transmission eigenchannels at $V = \pm 1.5$ V are displayed in Fig. 3.6. When making the contact, there are now mainly three contributing eigenchannels, contrary to the Ag system. As in the experiment, we observe different emission rates for the two bias polarities (Fig. 3.7(a)-(b)). For positive sample bias, the magnitude at 4 different surfaces is comparable. But for the negative bias, the fluctuations near the surface electrode are 4 times larger than that of the tip electrode. Consequently, the calculated yields show different trends at negative and positive bias when going from tunneling to contact, as shown in Fig. 3.7(c)-(d). These results can be explained as a consequence of the appearance of the HOMO level in the bias window, as discussed by Schneider *et al.*[107] . When the HOMO level enters the bias window, the occupied charge begins to fluctuate. This generates new available final states for inelastic transitions, which contribute to high frequency noise at the plasmon frequency. Since the molecule couples better to the surface than the tip, the charge fluctuations are compensated mainly by the surface-current fluctuations. This allows us to un-

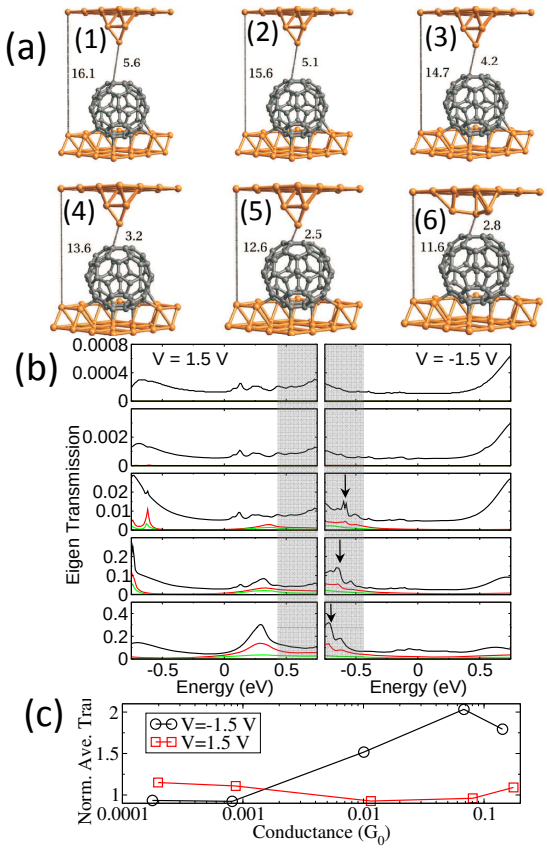

Figure 3.6: (a) All structures considered in the calculation. In structure 6 a deformation of the tip occurred and has been disregarded in the following. The two surface layers, C_{60} and the tip were relaxed at zero bias for each electrode separation. (b) Transmission eigenchannels at $V = \pm 1.5$ V for the structures shown above. The shaded areas are the active energy windows contributing to S_{ss}. (c) The average transmission in the active energy window (shaded areas in (b)), normalized over that in the whole bias window [-0.75 - 0.75] eV. The increase from tunneling to contact at $V = -1.5$ V is due to the appearance of the HOMO level (peak in the shaded region).

derstand the results qualitatively by looking at the surface current fluctuations. In the single channel, small transmission case, we can ignore the $1 - T$ term in Eqs. (3.26-3.27). So the photon yield due to surface current fluctuation can be characterized by the ratio of the average transmission in the active window (shaded region in Fig. 3.6) to that in the whole bias window. We plotted this normalized average transmission in Fig. 3.6 (c), and observed a sudden increase upon contact.

3.5 Summary

Comparing the Ag and C_{60} system, we see that the main difference is whether spatially localized molecular resonance participates in the light emission process or not. For the Ag system there are no such localized resonances and the transmission spectrum is weakly energy dependent. Thus the behavior of the finite frequency noise resembles the zero-frequency noise. This Explains why the experimental results can basically be understood by looking at the zero-frequency noise. Contrary, for the C_{60} system, at negative bias, the C_{60} HOMO level enters into the active window upon contact, modifying the transmission and enhances the shot noise power. From this study, we can see that molecular level engineering provides an efficient way to control the light emission property of STM junctions. Along these lines we note that very recent STM experiments using the photon-map technique indicate that individual molecular resonances can play a determining role ("gate") for the emission process[79].

In this chapter we have only considered below-threshold emission ($\hbar\omega > eV$). However, in the experiments[110, 112] above-threshold phonon emission, ($\hbar\omega > eV$), was also observed. The mechanism behind emission of phonons with energy exceeding the applied bias is still debated[134, 46, 124, 108, 56]. It can be attributed to hot electrons due to direct electron-electron interaction[108, 112], or alternative due to higher-order electron-plasmon scattering[56, 134].

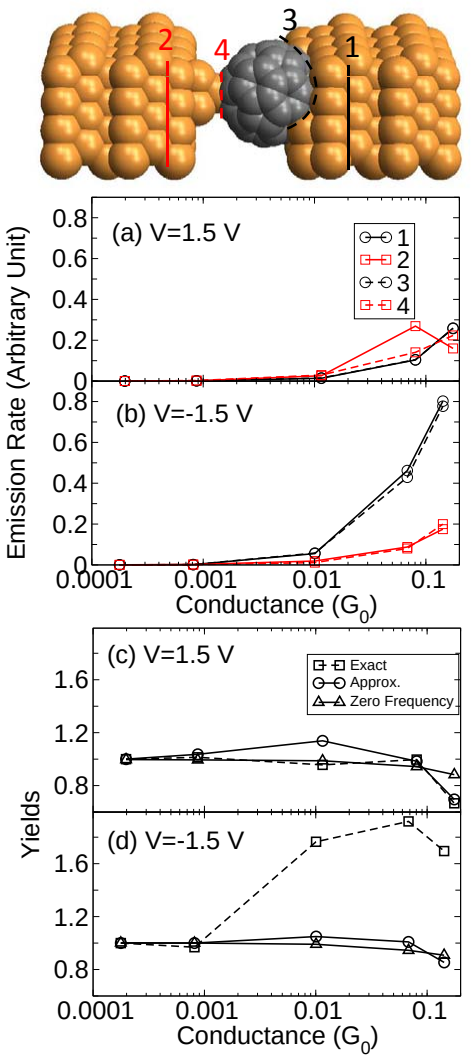

Figure 3.7: (a)-(b) Similar to Fig. 3.5(a)-(b), calculated emission rates at 4 different surfaces for the C_{60} system using $\hbar\omega_p = 1.2$ eV at $V = \pm 1.5$ V. (c)-(d) Similar to Fig. 3.5 (c)-(d).

Chapter 4

Inelastic Vibration Signals in Electron Transport

The previous chapter showed how electrons can tunnel inelastically through the emission of a plasmon. In this chapter inelastic scattering of the electronic current on atomic vibrations (phonons) is introduced. Inelastic electron tunneling spectroscopy (IETS) is a powerful tool for investigations of conductive atomic-scale junctions. IETS has been used to probe molecules on surfaces with scanning tunneling microscopy (STM) [120], and for junctions more symmetrically bonded between the electrodes [2, 114, 64, 138, 118, 84].

Typical IETS signals show up as dips or peaks in the second derivative of the current-voltage (I–V) curve [33]. The dips or peaks appear when the applied voltage matches the frequency of one of the vibrations ($eV_{applied} = \hbar\omega_\lambda$) of the system, which couples to the current. The dip/peak occurs because scattering on an atomic vibration can either open or close a transport channel. We define the IETS signal as the relative increase in differential conductance:

$$IETS = \frac{d^2I/dV^2}{dI/dI} \tag{4.1}$$

Thus the IETS signal gives a fingerprint of the vibrational modes of the system. Insight into the vibrational modes is important since, in many experiments, the bonding geometry, the nature of impurities or the passivisation is

unknown. Therefore, theoretical modeling of the vibrations and their coupling to the current can give important validation of experiments. This chapter introduces a scheme on the basis of DFT in combination with non-equilibrium Greens functions[113, 90, 51, 117, 30, 100], as introduced in chapter 2, to gain valuable insights into the atomistic structure and IETS.

4.1 Lowest Order expansion

Considering the usual two probe set up, as in Fig. 2.1, the current in the left lead, is given by the the Meir-Wingreen expression[42, 81],

$$I_L = 2e\langle \dot{\hat{N}}_L \rangle = -\frac{2e}{\hbar}\int_{-\infty}^{\infty}\frac{d\epsilon}{2\pi}\,\mathrm{Tr}\left[\mathbf{\Sigma}_L^<(\epsilon)\mathbf{G}_D^>(\epsilon) - \mathbf{\Sigma}_L^>(\epsilon)\mathbf{G}_D^<(\epsilon)\right], \tag{4.2}$$

where the electron-phonon (e-ph) coupling is included in the device Greens function $\mathbf{G}_D$ through the electronic self-energy, due to the atomic vibrations, in the Dyson equation:

$$\mathbf{G}^r(\epsilon) = \mathbf{G}_0^r(\epsilon) + \mathbf{G}_0^r(\epsilon)\mathbf{\Sigma}_{\mathrm{ph}}^r(\epsilon)\mathbf{G}^r(\epsilon) \tag{4.3}$$

Only the lowest order diagrams are included in the phonon contribution to the self-energies of the electrons. The greater and lesser Hartree terms are zero due to energy considerations, ($\boldsymbol{D}_0^{\lessgtr}(\epsilon = 0) = 0$), and the retarded Hartree term only gives a constant contribution which will be ignored. Thus, only the Fock diagram is left:

$$\mathbf{\Sigma}_{\mathrm{ph}}^<(\epsilon) = \sum_\lambda i\int\frac{d\omega}{2\pi}\mathbf{M}_\lambda\mathbf{D}_0^<(\omega)\mathbf{G}_0^<(\epsilon-\omega)\mathbf{M}_\lambda, \tag{4.4}$$

$$\mathbf{\Sigma}_{\mathrm{ph}}^>(\epsilon) = \sum_\lambda i\int\frac{d\omega}{2\pi}\mathbf{M}_\lambda\mathbf{D}_0^>(\omega)\mathbf{G}_0^>(\epsilon-\omega)\mathbf{M}_\lambda, \tag{4.5}$$

$$\mathbf{\Sigma}_{\mathrm{ph}}^r(\epsilon) = \frac{1}{2}\left(\mathbf{\Sigma}_{\mathrm{ph}}^>(\epsilon) - \mathbf{\Sigma}_{\mathrm{ph}}^<(\epsilon)\right) - \frac{i}{2}\mathcal{H}\left[\mathbf{\Sigma}_{\mathrm{ph}}^>(\epsilon) - \mathbf{\Sigma}_{\mathrm{ph}}^<(\epsilon)\right], \tag{4.6}$$

were $\mathcal{H}$ denotes the Hilbert transform.

Using $\mathbf{\Sigma}_{\mathrm{ph}}^r(\epsilon)$, Dyson's equation can be solved iteratively, this procedure is called the self-consistent Born approximation(SCBA). However, the SCBA approach is numerical heavy for systems containing more than a handful of atoms[28]. But, if the e-ph coupling is sufficiently weak, expanding the current in terms of the e-ph coupling, gives an adequate description. Furthermore if, the density of states (DOS) varies slowly with energy (compared to typical vibration

energies) the calculations can be greatly simplified by applying the LOE together with the wide band approximation LOE-WBA[90, 129]. Within the LOE-WBA the energy integral in Eq. (4.2) contains only Fermi-functions and their Hilbert transforms and can therefore be solved analytically. The LOE-WBA thus yields simple expressions for the inelastic signal in terms of quantities readily available in DFT-NEGF calculations. Importantly, the LOE-WBA can be applied to systems of considerable size. The LOE-WBA has been successfully applied in the study of *e. g.* atomic gold wires[29] and hydrocarbon molecules[88]. However, if the system contains sharp molecular resonances or a sharp band-onset, the assumption of constant electronic properties is not valid. Even off-resonance, high-frequency vibrations involving hydrogen can stretch the limit of the WBA[75, 86, 85]. Furthermore, knowing the energy dependence of the IETS signal can give substantial information of the underlying electronic structure[95, 25].

The need of an energy dependent theoretical modeling of the IETS signal have recently been stimulated by the reports of Song *et al.*[118] of IETS for a single benzene-dithiol (BDT) molecule in a Au electrochemical break junction. In the experiment they were able to tune the transport from off-resonance to close-to-resonance, by an external gate. The measured I–Vcurves, see Fig. 4.1, are symmetric indicating a symmetric coupling to the two Au-leads. Nonetheless, a change in the IETS signal from peak to peak-dip shape was observed upon gating the BDT molecule closer to resonance. Within LOE-WBA the peak-dip feature can only occur for a non-symmetric junction[90]. Illustrating the need to go beyond the WBA.

In the rest of this chapter a method is developed to restore the energy dependence of the LOE and the resulting method is used, first on a one-level model which can be solved analytically and then on a numerical DFT example: a BDT molecule between gold leads.

4.2 Energy Dependent LOE

Expanding the current in Eq. (4.2) to lowest order in the e-ph self-energies $\mathbf{\Sigma}_\lambda$ (2nd order in $\mathbf{M}_\lambda$) the current can be expressed as a sum of two terms, $I(V) = I_e + I_i$, using unperturbed Greens functions $\mathbf{G}^a = \mathbf{G}^{r\dagger}$ defined in region D [90, 129],

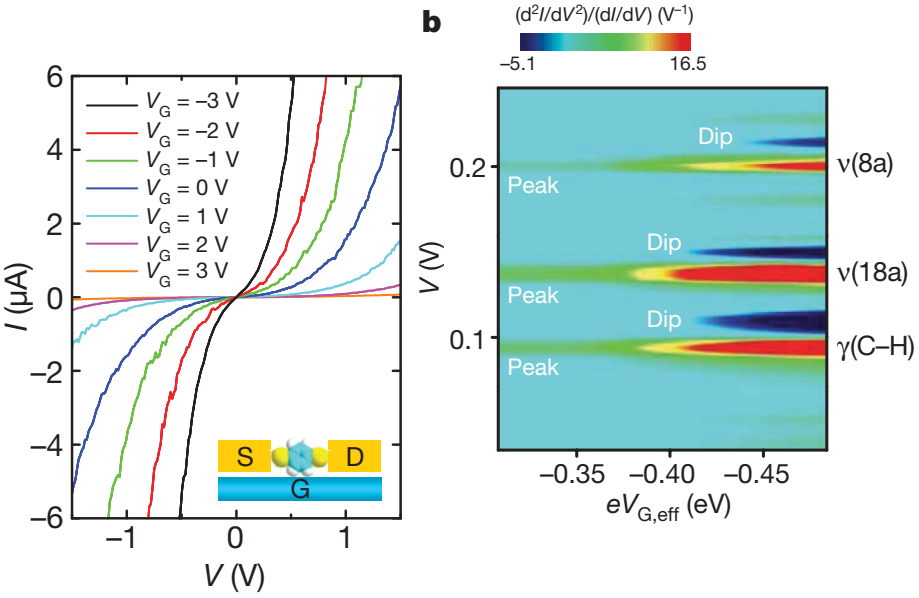

Figure 4.1: Adopted from Song *et al.*[118]. Left: I–V curves measured at 4.2 Kelvin for different gate values. Right:Two dimensional colour map of the gated IETS spectra, showing that IETS intensity and line shape vary significantly as functions of the, experimental determined, effective molecular $eV_{G,eff}$ orbital gating energy.

$$I_e = \frac{\mathrm{G}_0}{e}\int_{-\infty}^{\infty} \mathrm{d}\varepsilon \left\{ f_L(\varepsilon) - f_R(\varepsilon) \right\} \left\{ \mathrm{Tr}[\mathbf{G}^r \mathbf{\Gamma}_L \mathbf{G}^a \mathbf{\Gamma}_R](\varepsilon) \right. \\ \left. + 2\mathrm{Re}\,\mathrm{Tr}[\mathbf{G}^r \mathbf{\Sigma}_\lambda^r \mathbf{G}^r \mathbf{\Gamma}_L \mathbf{G}^a \mathbf{\Gamma}_R](\varepsilon) \right\}, \tag{4.7}$$

$$I_i = \frac{\mathrm{G}_0}{e}\int_{-\infty}^{\infty} \mathrm{d}\varepsilon \mathrm{Tr}[\mathbf{\Sigma}_\lambda^< \mathbf{G}^r \mathbf{\Sigma}_L^> \mathbf{G}^a - \mathbf{\Sigma}_\lambda^> \mathbf{G}^r \mathbf{\Sigma}_L^< \mathbf{G}^a](\varepsilon), \tag{4.8}$$

where $f_{L/R}(\varepsilon) = n_F(\varepsilon - \mu_{L/R})$ is the left/right reservoir Fermi-function and $\mathrm{G}_0 = 2e^2/h$ is the conductance quantum and summation over the vibration index λ is assumed ($\mathbf{\Sigma}_{ph} = \sum_\lambda \mathbf{\Sigma}_\lambda$). The contribution I_e consist of two terms, the Landauer-Büttiker term which dos not depend on $\mathbf{\Sigma}_{ph}$ and therefore dos not carry any signal and a term depending on the retarded phonon self-energy carrying a signal. Assuming the vibrations to be described by the unperturbed phonon Greens functions:

$$D_{0,\lambda}^<(\omega) = -2\pi i[n_b(\hbar\omega_\lambda)\delta(\omega - \omega_\lambda) + (1 + n_b(\hbar\omega_\lambda))\delta(\omega + \omega_\lambda)], \tag{4.9}$$

$$D_{0,\lambda}^>(\omega) = -2\pi i[n_b(\hbar\omega_\lambda)\delta(\omega + \omega_\lambda) + (1 + n_b(\hbar\omega_\lambda))\delta(\omega - \omega_\lambda)], \tag{4.10}$$

with bosonic occupations $n_b(\hbar\omega_\lambda)$, then the e-ph self-energies $\mathbf{\Sigma}_\lambda$ are expressed as

$$\mathbf{\Sigma}_\lambda^{\gtrless}(\varepsilon) = \mathbf{M}_\lambda \Big\{ (n_b(\hbar\omega_\lambda) + 1)\mathbf{G}^{\gtrless}(\varepsilon_\mp) + n_b(\hbar\omega_\lambda)\mathbf{G}^{\gtrless}(\varepsilon_\pm) \Big\} \mathbf{M}_\lambda, \tag{4.11}$$

$$\mathbf{\Sigma}_\lambda^{r,a}(\varepsilon) = \pm\frac{1}{2}\left\{ \mathbf{\Sigma}_\lambda^>(\varepsilon) - \mathbf{\Sigma}_\lambda^<(\varepsilon) \right\} - \frac{i}{2}\mathcal{H}\left[\mathbf{\Sigma}_\lambda^> - \mathbf{\Sigma}_\lambda^< \right](\varepsilon), \tag{4.12}$$

with $\varepsilon_\pm = \varepsilon \pm \hbar\omega_\lambda$.

Finally, the lesser/greater Greens functions $\mathbf{G}^{\lessgtr}$ describing the occupied/unoccupied states,

$$\mathbf{G}^{\gtrless}(\varepsilon) = \mp i \left\{ f_L(\mp\varepsilon)\mathbf{A}_L(\varepsilon) + f_R(\mp\varepsilon)\mathbf{A}_R(\varepsilon) \right\}, \tag{4.13}$$

are given by the spectral density matrices $\mathbf{A}_{L/R} = \mathbf{G}^r \mathbf{\Gamma}_{L/R} \mathbf{G}^a$ for left/right moving states with fillings according to the reservoir Fermi-functions.

4.2.0.1 Vibration-signal

Calculating the current directly from Eq. (4.7) and Eq. (4.8) is numerically demanding due to the energy integration over voltage-dependent traces. However, the coupling between electron current and phonons ideally show up at zero

temperature as a step discontinuity in the differential conductance when the inelastic phonon emission channel becomes energetically allowed, that is when the chemical potential difference exceeds the vibrational energy, $|\mu_L - \mu_R| > \hbar\omega_\lambda$. Thus, around the emission threshold the electronic states involved are those at μ_L and μ_R.

Abandoning information about the total current and focusing on the "vibration-signal", that is the change in the current close to the excitation threshold, $|\mu_L - \mu_R| = |eV| \approx \hbar\omega_\lambda$, further simplifications is possible without resorting to the WBA.

As IETS signals are obtained at low temperatures, the temperature is assumed to be the smallest energy scale, $k_BT \ll \hbar\omega_\lambda, \Gamma$, where Γ is the typical electronic resonance broadening.

The inelastic term I_i, in Eq. (4.8), then reduces to

$$I_i \approx \frac{\mathrm{G}_0}{2e}\sum_{\sigma=\pm}\left(\coth\frac{\hbar\omega_\lambda}{2k_BT} - \coth\frac{\hbar\omega_\lambda + \sigma eV}{2k_BT}\right) \times \int_{-\infty}^{\infty} d\varepsilon \mathrm{Tr}\left[\mathbf{M}_\lambda \tilde{\mathbf{A}}_L(\varepsilon)\mathbf{M}_\lambda \mathbf{A}_R(\varepsilon_\sigma)\right]\{f_L(\varepsilon) - f_R(\varepsilon_\sigma)\}, \tag{4.14}$$

where $\tilde{\mathbf{A}}_\alpha = \mathbf{G}^a\mathbf{\Gamma}_\alpha\mathbf{G}^r$ is the time-reversed of $\mathbf{A}_\alpha$. Assuming $T = 0$ and $\mu_L = -\mu_R = \frac{eV}{2}$, the 1st and 2nd derivative of I_i w.r.t. V reduces to:

$$\partial_V I_i = \frac{1}{2}\frac{\mathrm{G}_0}{2e}\Theta(eV - \hbar\omega_\lambda)\left(\tilde{\mathbf{A}}_L(\frac{eV}{2})\mathbf{M}\mathbf{A}_R(\frac{eV}{2} - \hbar\omega_\lambda)\mathbf{M} + \tilde{\mathbf{A}}_L(\hbar\omega_\lambda - \frac{eV}{2})\mathbf{M}\mathbf{A}_R(-\frac{eV}{2})\mathbf{M}\right) \tag{4.15}$$

$$\partial_V^2 I_i = \frac{\mathrm{G}_0}{2e}\delta(eV - \hbar\omega_\lambda)\tilde{\mathbf{A}}_L(\hbar\omega_\lambda/2)\mathbf{M}\mathbf{A}_R(-\hbar\omega_\lambda/2)\mathbf{M} \tag{4.16}$$

Thus, if the electronic structure ($\mathbf{A}_\alpha$) varies slowly on the k_BT scale, it can be replaced by a constant using $\varepsilon \approx \mu_L$ and $\varepsilon_\sigma \approx \mu_R = \mu_L + \sigma\hbar\omega_\lambda$. Therefore, around the vibration threshold the $\partial_V^2 I_i$ can be approximated as:

$$\partial_V^2 I_i \approx \gamma_{i,\lambda}\,\partial_V^2 \mathcal{I}^{\mathrm{sym}}, \tag{4.17}$$

$$\gamma_{i,\lambda} = \mathrm{Tr}\left[\mathbf{M}_\lambda \tilde{\mathbf{A}}_L(\mu_L)\mathbf{M}_\lambda \mathbf{A}_R(\mu_R)\right], \tag{4.18}$$

where $\mathcal{I}^{\mathrm{sym}}$ is the "universal" function also known from the LOE-WBA [30], see Fig. 4.2

$$\mathcal{I}^{\mathrm{sym}} \equiv \frac{\mathrm{G}_0}{2e}\sum_{\sigma=\pm}\sigma(\hbar\omega_\lambda + \sigma eV)\left(\coth\frac{\hbar\omega_\lambda}{2k_BT} - \coth\frac{\hbar\omega_\lambda + \sigma eV}{2k_BT}\right) \tag{4.19}$$

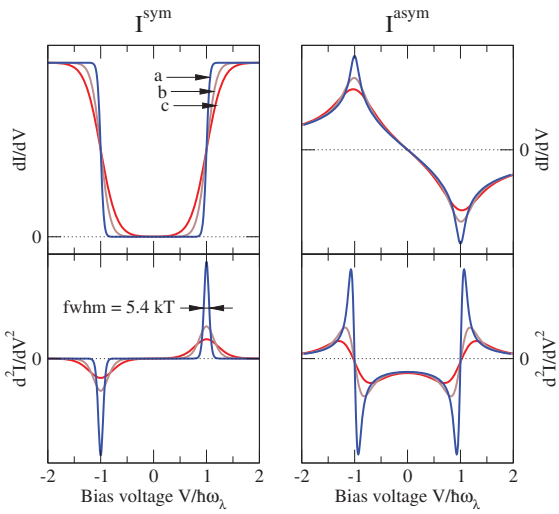

Figure 4.2: Adopted from T. Frederiksen *et al.*[30]. The first and second derivative of the universal functions in Eq. (4.19) and Eq. (4.31) are shown, for a single mode, with frequency $\hbar\omega_\lambda$, for three different temperatures: (a) $k_bT/\hbar\omega_\lambda = 0.02$, (b) $k_bT/\hbar\omega_\lambda = 0.06$ and (c) $k_bT/\hbar\omega_\lambda = 0.10$

The elastic term I_e, in Eq. (4.7), depends on the retarded part of the phonon self-energy ($\mathbf{\Sigma}^r_{\rm ph}(\epsilon)$). Defining $\mathbf{X} \equiv \frac{1}{2}(\mathbf{\Sigma}^>_{\rm ph} - \mathbf{\Sigma}^<_{\rm ph})$, which satisfies $\mathbf{X}^\dagger = -\mathbf{X}$, the retarded self-energy and its complex conjugate becomes:

$$\mathbf{\Sigma}^r_{\rm ph} = {\rm Re}(\mathbf{\Sigma}^r_{\rm ph}) + i\,{\rm Im}(\mathbf{\Sigma}^r_{\rm ph}), \tag{4.20}$$

$$= \mathbf{X} - i\mathcal{H}\left[\mathbf{X}\right], \tag{4.21}$$

$$\left(\mathbf{\Sigma}^r_{\rm ph}\right)^\dagger = -\mathbf{X} - i\mathcal{H}\left[\mathbf{X}\right]. \tag{4.22}$$

Therefore, $\mathbf{X}$ gives a Symmetric contribution and $\mathcal{H}\left[\mathbf{X}\right]$ gives an antisymmetric contribution to the differential conductance.

Thus, the elastic term I_e, in Eq. (4.7), can be divided in two parts, $I_e = I^n_e + I^h_e$, where I^n_e represents all the terms containing $\mathbf{X}$ and I^h_e represents all the terms with the Hilbert transform $\mathcal{H}\left[\mathbf{X}\right]$. The non-Hilbert part, I^n_e, yields a coth-factor and integral similar in form to the one for I_i. Both I_i and I^n_e thus yield an inelastic signal with a lineshape given by the function $\partial^2_V \mathcal{I}^{\rm sym}$ and the

sign/intensity governed by $\gamma_\lambda = \gamma_{i,\lambda} + \gamma_{e,\lambda}$, with $\gamma_{e,\lambda} \approx \mathrm{Im}B_\lambda$, and

$$B_\lambda \equiv \mathrm{Tr}[\mathbf{M}_\lambda \mathbf{A}_R(\mu_L)\mathbf{\Gamma}_L(\mu_L)\mathbf{G}^r(\mu_L)\mathbf{M}_\lambda \mathbf{A}_R(\mu_R) - \mathbf{M}_\lambda \mathbf{G}^a(\mu_R)\mathbf{\Gamma}_L(\mu_R)\mathbf{A}_R(\mu_R)\mathbf{M}_\lambda \mathbf{A}_L(\mu_L)]. \tag{4.23}$$

The Hilbert part, I_e^h, requires a bit more consideration. Besides terms which do not result in threshold signals [43], there are terms involving $\mathcal{H}[\mathbf{A}_\alpha f_\alpha]$, which at $T = 0$ can be written as:

$$\mathcal{H}\left[n_f(\epsilon')\mathbf{A}(\epsilon')\right](\epsilon) = \frac{1}{\pi}\lim_{\delta\to 0}\int_{-\infty}^{\mu} d\epsilon' \, \frac{\mathbf{A}(\epsilon')(\epsilon' - \epsilon)}{(\epsilon' - \epsilon)^2 + \delta^2}. \tag{4.24}$$

If the spectral-function varies on the scale of the phonon-frequencies then Eq. (4.24) becomes numerical difficult to solve. Thus, we choose to Taylor-expand the Spectral-function $\mathbf{A}(\epsilon')$ around ϵ,

$$\mathbf{A}(\epsilon') = \mathbf{A}(\epsilon) + \mathbf{A}'(\epsilon)(\epsilon' - \epsilon) + \frac{1}{2}\mathbf{A}''(\epsilon)(\epsilon' - \epsilon)^2 + \ldots, \tag{4.25}$$

here only the zero-order term is considered since only this term gives a divergent contribution. Thus Eq. (4.24) can be approximated as

$$\mathcal{H}\left[n_f(\epsilon')\mathbf{A}(\epsilon')\right](\epsilon) = \frac{1}{\pi}\mathrm{P}\int_{-\infty}^{\mu} d\epsilon' \, \frac{\mathbf{A}(\epsilon)}{(\epsilon' - \epsilon)} \tag{4.26}$$

$$= \frac{1}{\pi}\mathbf{A}(\epsilon)(\log(\mu - \epsilon) - B), \tag{4.27}$$

where P denotes the principal value and B is a boundary term stemming from the lower cutoff of $\mathbf{A}$, which is independent of the voltage and will therefore not give a contribution to the IETS. To include the broadening, due to the temperature we now write

$$\mathcal{H}\left[n_f(\epsilon')\mathbf{A}(\epsilon')\right](\epsilon) = \mathbf{A}(\epsilon)\mathcal{H}\left[n_f(\epsilon')\right](\epsilon) \tag{4.28}$$

the derivative of the Hilbert transformation of the Fermi function is strongly peaked at the chemical potential, and again the energy integration is preformed by evaluating all electronic structure functions $(\mathbf{A}_\alpha, \mathbf{G}^r, \mathbf{\Gamma}_\alpha)$ at the peak value, keeping only the energy dependence of the functions related to f_α inside the integral. In this approximation the result is

$$\partial_V^2 I_e^h \approx \kappa_\lambda \, \partial_V^2 \mathcal{I}^{\mathrm{asym}}, \tag{4.29}$$

with $\kappa_\lambda = 2\mathrm{Re}B_\lambda$ and, again as in the LOE-WBA, the "universal" function, see Fig. 4.2

$$\mathcal{I}^{\mathrm{asym}} \equiv \frac{\mathrm{G}_0}{2e}\int_{-\infty}^{+\infty} d\varepsilon \mathcal{H}\{f(\varepsilon'_-) - f(\varepsilon'_+)\}(\varepsilon)\,(f(\varepsilon - eV) - f(\varepsilon)) \tag{4.30}$$

$$= \quad -\frac{e}{\pi}k_bT\left(h(\frac{eV+\hbar\omega_\lambda}{2\pi k_bT}) - h(\frac{eV-\hbar\omega_\lambda}{2\pi k_bT}) - 2h(\frac{\hbar\omega_\lambda}{2\pi k_bT})\right) \tag{4.31}$$

where $h(x) \equiv x\,\mathrm{Re}\,\Psi(ix)$, and $\Psi(x)$ is the digamma function[8]. A more transparent expression is obtained for $k_BT = 0$, where $\mathcal{I}^{\mathrm{asym}}$ gives a divergent logarithmic contribution:

$$\mathcal{I}^{\mathrm{asym}} \approx -\frac{G_0}{2e\pi}\sum_{\sigma=\pm}\sigma|eV + \sigma\hbar\omega_\lambda|\ln\left|\frac{eV+\sigma\hbar\omega_\lambda}{\hbar\omega_\lambda}\right|. \tag{4.32}$$

To summarize, the signal due to the phonons have two contributions to the conductance. A symmetric contribution which gives a step with the amplitude γ_λ and an antisymmetric contribution with the amplitude κ_λ

$$\partial_V^2 I(V) = \gamma_\lambda\,\partial_V^2\mathcal{I}^{\mathrm{sym}}(V,\hbar\omega_\lambda,T,N_\lambda) + \kappa_\lambda\,\partial_V^2\mathcal{I}^{\mathrm{asym}}(V,\hbar\omega_\lambda,T), \tag{4.33}$$

$$\gamma_\lambda = \mathrm{Tr}[\mathbf{M}_\lambda\tilde{\mathbf{A}}_L(\mu_L)\mathbf{M}_\lambda\mathbf{A}_R(\mu_R)] + \mathrm{Im}B_\lambda, \tag{4.34}$$

$$\kappa_\lambda = 2\mathrm{Re}B_\lambda, \tag{4.35}$$

Equation (4.33) expresses the vibration signals in terms of the "universal" functions with amplitudes containing quantities which can be obtained from DFT-NEGF. Importantly, equation (4.33) is generalized to include,the effect of a finite vibration frequency $\hbar\omega_\lambda$, and thus the change in electronic structure over the excitation energy. However, the electronic properties are still assumed to be constant on the scale of k_bT, thus a delta like resonance or a very sharp band onset are not included in the above derivation. The LOE expressions for γ_λ and κ_λ above simply reduce to the LOE-WBA when $\mu_L = \mu_R = \mu_0$ or equivalent $\hbar\omega = 0$.

4.3 One level model

To understand the difference between the LOE and the LOE-WBA for a symmetric junction, and why the LOE can explain the transition from a peak to a

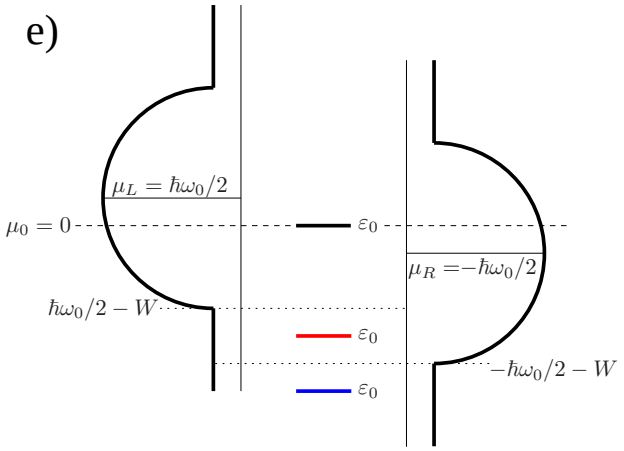

Figure 4.3: Adopted from Lü *et al.*[75]. Schematics of the one-level modes (shown for three different level positions) biased at the emmision threshold $V = \hbar\omega_0$

peak-dip signal it is illustrative to consider a one level model were γ_λ and κ_λ are reduced from a trace over matrices to products of complex functions.

We therefore, consider a system consisting of a single electronic level with energy ε_0 which is coupled symmetrically to the left and right leads. The coupling to the leads are described by an energy dependent function $\Gamma(\varepsilon)$. The model is illustrated in Fig. 4.3. Further, the electronic level interacts with a single vibrational mode of frequency $\hbar\omega_0$ with coupling M.

Thus, assuming a symmetrical potential drop, and defining $\Gamma_l = \Gamma_L(\mu_L) + \Gamma_R(\mu_L)$ and $\Gamma_r = \Gamma_L(\mu_R) + \Gamma_R(\mu_R)$, γ and κ are written as:

$$\gamma = -C\left\{\Gamma_l^2\Gamma_r^2 - (4\varepsilon_0^2 - \hbar\omega_0^2)^2\right\}, \tag{4.36}$$

$$\kappa = 4C\left(\delta\Gamma\,\varepsilon_0 + \bar{\Gamma}\,\hbar\omega_0\right)\left\{\Gamma_l\Gamma_r - \left(4\varepsilon_0^2 - \hbar^2\omega_0^2\right)\right\}, \tag{4.37}$$

where $\delta\Gamma = \Gamma_l - \Gamma_r$ and $\bar{\Gamma} = (\Gamma_l + \Gamma_r)/2$, and C is given by:

$$C = \frac{4\Gamma_l\Gamma_r}{\left(\Gamma_l^2 + (2\varepsilon_0 - \hbar^2\omega_0)^2\right)^2\left(\Gamma_r^2 + (2\varepsilon_0 + \hbar^2\omega_0)^2,\right)^2}. \tag{4.38}$$

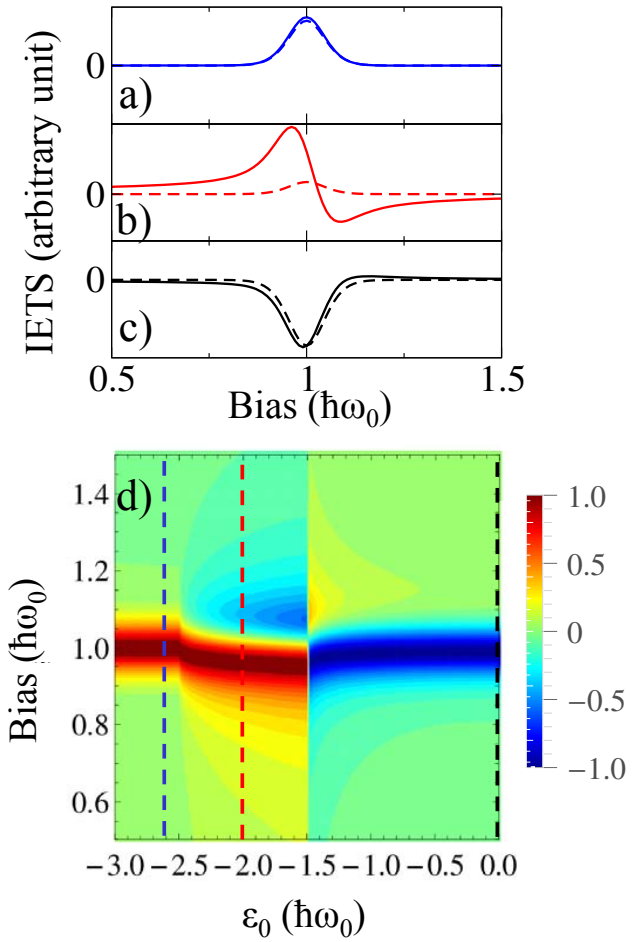

Figure 4.4: Adopted from Lü *et al.*[75]. (a-c) IETS spectrum from LOE (solid) and LOE-WBA (dashed) for three different position of an electronic level, coupling with a wide s band with constant density of states, and a narrow d band with bandwidth W centered at the equilibrium Fermi level $\mu_0 = 0$. (a) $\varepsilon_0 = -2.6$, (b) $\varepsilon_0 = -2$, (c) $\varepsilon_0 = 0$. The transmission coefficients at the Fermi level are $T = 0.006, 0.01, 1$, respectively. (d) Contour plot of the spectrum, normalized such that for each given ε_0, the height of the largest peak or dip is 1. Parameters in unit of the vibration energy $\hbar\omega_0$: $t' = 2t = W = 2$, $\Gamma_0 = 0.1$, $k_B T = 0.02$. Here, t is the hopping matrix element of the d band, and t' is its coupling to the electronic level.

The result above are obtained from Eq. (4.18) and Eq. (4.23), by pure algebra and using that the retarded Greens function is a simple complex scalar function given by:

$$G^r = \frac{1}{\varepsilon - \varepsilon_0 - i\frac{\Gamma_L(\varepsilon)+\Gamma_R(\varepsilon)}{2}}. \tag{4.39}$$

In the typical case of transition metal electrodes the coupling can contain contributions both from a wide s-band as well as from a narrow d-band leading to a significant $\delta\Gamma$ and finite κ, resulting in a peak-dip feature in the IETS signal.

To model the s-band we use a constant Γ_0, and to mimic the coupling (hopping t') to a d-band we add the self-energy of a semi-infinite 1D chain, with bandwidth $2W$ centered at $\mu_0 = 0$, as illustrated in Fig. 4.3. Thus the following coupling is used

$$\Gamma_\alpha(\varepsilon) = \Gamma_0 + \Theta(2|t| - \varepsilon)\frac{2t'^2}{t}\sqrt{1 - \left(\frac{\varepsilon}{2t}\right)^2}. \tag{4.40}$$

The Figures 4.4(a-c) compare the signal obtained by the model above to the WBA results where $\mu_L = \mu_R = \mu_0$, for different ε_0. Both the LOE and the LOE-WBA gives a peak in the off-resonance regime and dip on-resonance. However, only in the LOE the two regimes are separated by a peak-dip structure close to resonance, due to the "asymmetric" κ, which is enhanced at the onset of the coupling with the d-band in one of the electrodes. The IETS signal for a range of gate-potentials(ε_0) is shown in Fig. 4.4. The one level model clearly illustrates how a symmetric coupled system can experience peak-dip features in the IETS signal driven by an energy dependent coupling.

4.4 DFT Example

In the experimental reports of Song *et al.*[118], they showed how the transport through a BDT molecule could be tuned from off-resonance, ($G \sim 0.01G_0$), to near the HOMO resonance, thereby increasing the conductance by more than a order of magnitude. Gating from off resonance towards the HOMO resonance they observe three peaks in the IETS, around 95, 130 and 200 meV, evolve into peak-dip features as shown in Fig. 4.1.

The observed peak-dip features were analyzed by applying a model developed by Persson and Baratoff [95], which they fitted to reproduce the peak-dip fea-

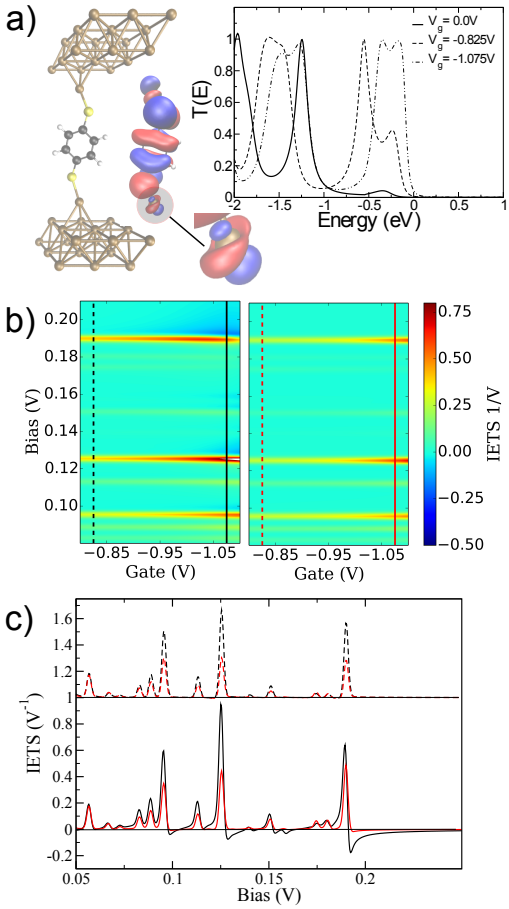

Figure 4.5: Adopted from Lü *et al.*[75]. BDT between two adatoms on Au(111) together with transmission for off resonance (zero gate) and close to resonance. (b) IETS as a function of gate voltage from LOE (left) and LOE-WBA (right). (c) IETS for fixed gate voltage off-resonance (dashed lines, offset for clarity) and close-to-resonance (solid lines). Black: LOE, Red: LOE-WBA. $k_BT = 4.2$ K and $V_{\mathrm{rms}} = 1$ mV

tures. However, the model by Persson and Baratoff were developed for a STM-setup and rely on the assumption off an asymmetric system, where $\Gamma_R >> \Gamma_L$, and the potential drop is only over the right electrode. But, the assumption of a strongly asymmetric system are contradicted by the observed symmetric I–V curves shown in Fig. 4.1.

However, the symmetric one-level model above suggest, that the peak-dip feature instead originates from in an energy dependent coupling. Thus, below the IETS signal for a Au-BDT-Au junction are simulated within the DFT-NEGF framework presented in this chapter. In the experiment the exact atomic structure is unknown; however, they were able to gate the BDT molecule indicating a quite open junction. In order to emulate this, we model the BDT bonded between adatoms on Au(111) surfaces, see Fig. 4.5(a), and only apply the gamma point in the transport calculation giving sharp features in the electronic structure. A normal DFT treatment of BDT in a gold junction is known to underestimate the HOMO-LUMO gap[121, 34]; therefore, the HOMO-LUMO gap is corrected by the so called SAINT scheme[34], which amounts to shifting the occupied(unoccupied) molecular orbitals down(up) in energy, the resulting transmission can be seen if Fig. 4.5. likewise, the gating of the BDT molecule is modeled by a rigid shift of the molecular energies relative to the gold electrodes. The IETS signal computed for a range of gate values is shown in Fig. 4.5 (b) both for the LOE (left) and for the LOE-WBA (right). Both for the LOE and LOE-WBA three signals are observed, around 95, 130 and 200 meV, off-resonance in agreement with the experiment. However, only the LOE captures the peak-dip feature for close to resonance transport, as predicted by the one-level model.

The peak-dip feature appear due to sharp resonances i the transmission around the Fermi-energy as seen from Fig. 4.5 (a). These resonances involve the d-orbitals on the contacting gold atoms as seen from the eigenchannel[89] plot i Fig. 4.5 (a).

The asymmetric feature is most prominent for the vibrational mode with the highest energy, as can be seen from Fig. 4.5 (c) , in contrast to the experimental findings.

4.5 Summary

In this chapter we have generalized the LOE scheme for IETS simulations formulated in terms of NEGF and quantities obtained from DFT. The LOE scheme extend the LOE-WBA, by taking variations of the electronic structure, on the scale of a vibrational frequency ($\hbar\omega$), into account, while, retaining both the

transparency and computational efficiency of the LOE-WBA.

This improvement is important to capture correctly the IETS line shape for systems where the electronic structure varies appreciably on the scale of the vibration energies, such as near sharp resonances or band edges.

The improved LOE was applied to an analytical one-level model revealing how a symmetric system can give rise to peak-dip features in the IETS. The computational efficiency of the LOE enabled DFT-NEGF calculations explaining the intricate experimental line shape of a gated BDT without the need to assume asymmetric bonding of the molecule to the electrodes.

Chapter 5

Graphene Nanoribbons

5.1 Introduction

In the previous chapter an efficient method for calculating the inelastic signal was developed. The use of the so-called lowest order expansion (LOE) without resorting to the wide-band approximation (WBA), facilitates the investigation of the effect of gating or doping.

Graphene as the basis of a new generation of electronics[98] has been the center of much attention over the last years, and devices based on nanostructured graphene have been put forward. The most generic form of nanostructured graphene is graphene nanoribbons (GNR)[24]. Other structures such as graphene anti-dot lattices[93, 6] can be viewed as consisting of a network of GNRs. GNRs are a potential candidate for molecular wires with tailored conductance properties. For graphene-based nanostructures the edges and their passivation, as well as defects inside the structure, can play a crucial role for the transport properties[130], and it is thus of interest to characterize this in well controlled experiments. However, characterization of edge passivation or structural/chemical defects is challenging especially after device fabrication. Raman spectroscopy[27] can give information about defects on large areas of the sample but does not yield local information or the importance for transport. On the other hand inelastic electron tunneling spectroscopy (IETS) serves as a way of

performing non-destructive characterization yielding vibrational/phonon fingerprints of a range of defects. Thus, in this chapter theoretical modeling of the inelastic signals, as a consequence of electron-phonon scattering, in the electronic current of GNRs is investigated.

GNRs have been fabricated using different strategies including lithographic techniques[41], chemical synthesis[68, 133], epitaxial growth[7], and longitudinal unzipping of carbon nanotubes[62]. Furthermore, several groups have succeeded in atomically precise bottom-up fabrication of armchair GNRs (AGNR)[16, 9] on metal surfaces. Experimentally, the vibrational properties have been investigated by Raman spectroscopy[16, 48] and the electronic structure has been mapped out by STM, angle-resolved (two photon) photo-emission and high-resolution electron energy loss spectroscopy(HREELS)[14, 101], for the AGNRs on metal surfaces. Further, for AGNRs on a Au(111) surfaec, signatures of phonon excitation was observed by STM in the differential conductance spectroscopy at the zigzag termini state.[126] These signatures were furthermore shown to be sensitive to modifications in the local atomic geometry.

Interestingly, one group has been able to lift the AGNR from the weakly bonding Au(111) surface by a STM tip and have reported voltage-dependent conductance measurements for AGNRs suspended between a substrate and a STM tip[59].

From the theoretical side density-functional theory (DFT) has been used to investigate the stability of structural and chemical reconstructions of GNR edges,[132, 67, 131] together with the transport and band-gap engineering[45, 37, 139, 4, 130]. The vibrational properties and phonon band structure have been calculated both using an empirical potential[136] and DFT[128, 36]. In addition, there have been theoretical predictions[140, 102] of the Raman spectrum, in good agreement with the experiments. For a finite AGNR the role of zigzag termini states have been studied theoretically, comparing DFT to the many-body Hubbard model[49].

The chapter is organized as follows. First, as motivation, the lifting experiments by Koch *et al.*,[59] and the investigation of the vibrational structure of graphene nanoribbons investigated in the Doktorarbeit of M. Koch [58] are reviewed. Then the lifting' experiment is modeled in a simplified manner as a gold-chain AGNR junction. Followed, by a more thorough treatment of the IETS originating from the bulk GNRs. The results for pristine AGNR and ZGNR are presented and discussed comparing transport and IETS with their band structures. Then we turn to the defective systems where we consider examples of defects in the passivation, atomic structure, or by the presence of adatoms. Finally, we summarize and conclude.

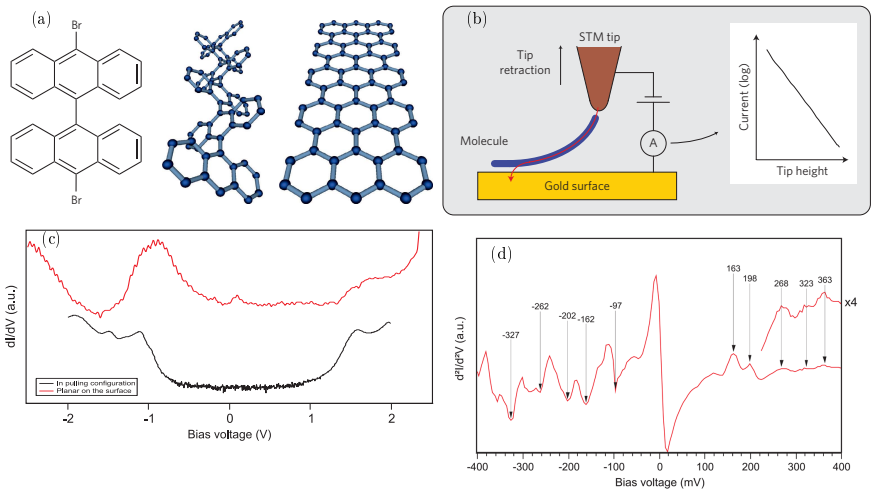

Figure 5.1: (a-b) Adopted from Koch *et al.*[59], (c-d) adopted from the Doktorarbeit of M. Koch [58]. (a) Chemical synthesis of an armchair GNR from 10,10′-dibromo-9,9′-bianthryl molecules, which are connected to oligomers in the first heating step and to GNRs in the second heating step. (b) Schematic of the STM pulling experiment (arrow indicates tunnelling current). A characteristic current signal during the pulling sequence is shown in the right panel. (c) Experimental dI /dV conductance curves for two different confgurations of the GNRs. Red: The ribbon is adsorbed planar on the surface. Black: The ribbon is in pulling geometry between STM tip and surface. The red curve is shifted upwards for better visibility. (d) Averaged d^2I/dV^2 from 12 different GNRs which have been pulled up. The pulling spectrum of each GNR was averaged over five sweeps from −400 to +400 mV.

5.2 Lifting Experiments

We start by considering the recent lifting experiments by Koch *et al.*,[59]. In the experiments armchair GNRs were synthesized, from 10,10′-dibromo-9,9′-bianthryl molecules, on an Au(111) surface, as illustrated in Fig. 5.1 (a). Then the AGNRs were lifted up from the weakly bonding Au(111) surface with the tip of a STM, as shown in Fig. 5.1 (b), enabling measurements of the voltage-dependent conductance in suspended configurations, see Fig. 5.1 (c).

Further, in the Doktorarbeit of M. Koch [58], the vibrational structure of graphene

nanoribbons were investigated in terms of the second derivative of the current dI^2/dV^2. In the work of M. Koch five features appear, in dI^2/dV^2, for negative bias polarity at -97, -162, -202, -262, and -327 mV. If the dips observed at negative bias are due to excitations of vibrations in the nanoribbon, corresponding peaks should be expected at positive bias. However, for positive bias polarity only two clear features appear at $+163$ and $+198$ mV, while there are three small features at $+268$, $+323$ and 363 mV. Thus, a signal around $+97$ mV is missing and a new weak signal at $+363$ mV emerges.

The suppression of features at positive bias voltages can be due to the asymmetric system setup and thus asymmetric coupling from the left/right-leads to the nanoribbon. The asymmetric coupling gives an asymmetric current which in itself can suppress the signal at the positive side due to less intensity. Furthermore, the asymmetric coupling can cause a non-trivial voltage drop where the nanoribbon follows the Fermi-energy of one of the leads.

In the Doktorarbeit of M. Koch [58] the signals are related to to the signals found by Raman spectroscopy on AGNRs on a metal surfaces. The signals around ± 200 and ± 163 are identified as the G-mode and D-mode, measured by Raman to be at 166/167meV[16, 48] and 198/200meV[16, 48], respectable. The weak feature at -262 mV is related to the $C \equiv C$ vibration of the dehydrogenated edges measured to 245 meV by Huang *et al.*[48] The feature at -327 mV is assigned to the 2D-mode which is shifted compared to 323 eV reported by Raman[48] and the signal at -97 mV is said to be due to the C-H bending mode observed by HREELS[14] at 98 eV.

The discrepancy between the Raman measurements and the signals in $\frac{d^2I}{dV^2}$ can be due to the substrate or the curvature and/or the strain of the AGNR in the lifting experiment. Further, the selection rules for Raman and IETS need not be the same, resulting in the detection of different modes.

5.3 Gold-chain Armchair Graphene Nanoribbon Junction

Inspired by the experiment by Koch *et al.*[59], described above, the signals of electron-phonon scattering in the conductance is investigated theoretically, in a simplified setup explained below, using the LOE presented in Chapter 4.

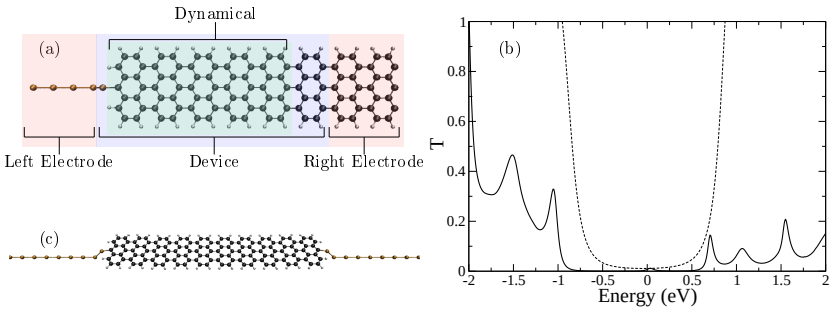

Figure 5.2: (a) Structure of the transport setup. (b) Solid line Transmission for the structure in (a), dashed line Transmission for a infinite ribbon. An electrode broadening of $\eta = 1$ eV was used, see text . (c) Periodic structure for the SIESTA calculation

5.3.1 System setup

The experiment is modeled in a simplified manner, as a gold chain connected to a half infinite GNR, as shown in Fig. 5.2(a). The transport system is obtained by first making a SIESTA calculation relaxing the AGNR unit-cells closest to the Au-chain (6 cells left, 2 cells right), in the periodic structure shown in Fig. 5.2 (c), and then treating the 5 first gold-atoms to the left and the 10 gold atoms and 2 unit-cells of AGNR to the right as buffer atoms.

For all the atoms a single-zeta polarized basis set is used, together with a cut-off energy of 400-500 Ry for the real-space grid.

Using a gold chain as electrode has the disadvantage of the d-band being pushed close to the Fermi-energy. Thus to break the symmetry of the d-electrons on the last Au atom, to make a better connection between the gold d-orbitals and the p-orbitals of the AGNR, the last Au atom in the chain is lifted to make an angle, (here $\pi/4$), relative to the gold chain while keeping the bond length constant.

In the experiment the AGNR is suspended between a STM-tip and a gold-surface, both with a more flat DOS than the electrodes used here (gold-chain and AGNR). Thus, to broaden the sharp 1-D features in the gold-chain and smear out the energy gap in the AGNR electrode, a finite numerical imaginary part in the electrode recursion calculation,[103] $\eta = 1$ eV, is used to broaden all states in the semi-infinite electrodes. The resulting Transmission, see Fig. 5.2 (b), exhibits a gap from -1 eV to 0.5 eV with a small peak at the Fermi-energy due to the zigzag termini state. Despite the smearing of the electrodes the

transmission yields sharp features outside the gap due to the gold-chain part of the system.

When calculating the IETS signal, the voltage drop is assumed to be across the gold AGNR interface, because, the contact area between the substrate and AGNR is much lager than the contact area between the STM-tip and the AGNR, which only consists of a single bond. In the experiment charge transfer between the gold substrate and the AGNR will occur. Thus, to simulate the effect of charge transfer we assume that the chemical potentials can be shifted by an applied gate voltage V_G. Therefore, due to the asymmetric voltage drop and the charge transfer the IETS signal, i.e. κ and γ in Eq. (4.33) , is evaluated at $\mu_L = E_F + \hbar\omega_\lambda + V_G$, $\mu_R = E_F + V_G$.

5.3.2 IETS

The use of the approximate but computationally efficient LOE scheme, allows for evaluations of IETS on a fine V_G grid of relevant values between valence and conduction bands of the GNRs. The IETS signal is shown for a range of gate values in Fig. 5.3. The IETS is found to be asymmetric as a result of the asymmetric system setup. Thus, explaining the suppression of the IETS signal for positive bias polarities, as is seen in Fig. 5.1. Furthermore, an overall suppression of the IETS signal is observed at energies close to the resonance of the zigzag termini state around $V_G = 0$ V [126]. Three robust features are seen for a range of gate values at $\mp$196 meV, $\mp$169 meV and $\mp$159 meV. Figure 5.3(c) shows the IETS signal at a gate of 0.3 meV, besides the three features mentioned above two small signals appear, for negative bias polarity, at -366 meV and -350 meV, and one highly asymmetric signal, for positive bias polarity at 366 meV.

We have calculated the individual IETS signal for 6 of the GNR unit cells closest to the zigzag edge, indicated by the dashed lines in Fig. 5.3 (a), to further investigate the effect of the zigzag edge and how much of the "bulk" ribbon we are probing. The result are displayed in Fig. 5.3(d), going from edge at the bottom to the 6. unit cell at the top. Figure 5.3(d) shows how the signal at -350 meV originates from the zigzag edge and that the asymmetric signal at 366 meV is due to the unit cells away from the edge.

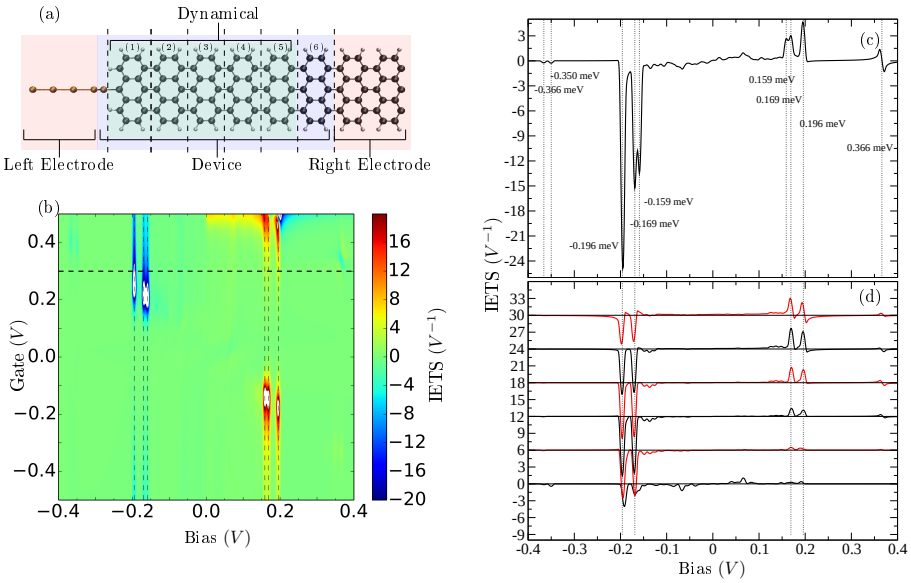

Figure 5.3: (a) Setup for the calculations showing different regions, the dashed lines indicate the dynamical regions used in (c). (b) IETS signal for the large dynamical region shown in (a). The IETS signal is calculated for a number of gate values. The thin dashed vertical lines are guides to the eye indicating the energy of the most contributing vibrational modes. The thick dashed horizontal line indicates the position of the cut shown i (c). (c) IETS signal for $V_G = 0.3$ V. (d) IETS signal for the small dynamical regions indicated by dashed lines in (a). (b-c) Broadening originates from lock-in modulation $V_{\mathrm{rms}} = 5$ mV and temperature $T = 4.2$ K.

5.3.2.1 Comparing to experiment

The two features around 200 and 160 meV observed in Fig. 5.1 (b) seem likely to originate in inelastic tunneling and correspond to the calculated signal at ∓ 196 meV and ∓ 169 meV and ∓ 159 meV. Further, in Fig. 5.3 (c) signals due to hydrogen vibrations are observed. The signals at $+97$, -262, and -327 meV, is not observed. The experimental observed signals not found in Fig. 5.3 (b) can originate in defects or in the latter case be a 2 phonon process which is not included in the LOE.

To circumvent the sharp features in the gold-chain and to address the signal of defects in the bulk , the next section takes another approach to IETS in GNRS. To make the study more general both armchair and zig-zag GNRs are studied.

5.4 Bulk GNRs

In the previous section, the IETS signal for a gold-chain AGNR junction was considered. Here we investigate theoretically the signals of electron-phonon scattering in the conductance of long GNRs between metal electrodes. Our aim is two-fold. First, we address how the phonons can give rise to signals in pristine GNRs. Second, we consider how the IETS signals change when defects are present in the GNRs in order to establish to what extent we might expect transport spectroscopy and IETS, in particular to give information about which defects are present and how they impact the transport. The focus is on the two most generic edge-types, namely armchair(AGNR) and zig-zag(ZGNR). For the pristine ZGNR we wish to examine the role of spin polarization. In experiments the substrate or an applied gate potential can change the actual Fermi level in the ribbons. To address this we scan the Fermi level using the numerically effective scheme, precented in Chap. 4, enabling fast calculations of the IETS[75].

5.4.1 Setup

As for the gold-chain AGNR junction, a single-zeta polarized basis set for the carbon and hydrogen atoms is used together with a cut-off energy of 400-500 Ry for the real-space grid. In the case of chemical defects, a double-zeta polarized basis set is used. These choices, balancing accuracy and computational cost, provide a good description to investigate trends and general behavior of a substantial number of systems.

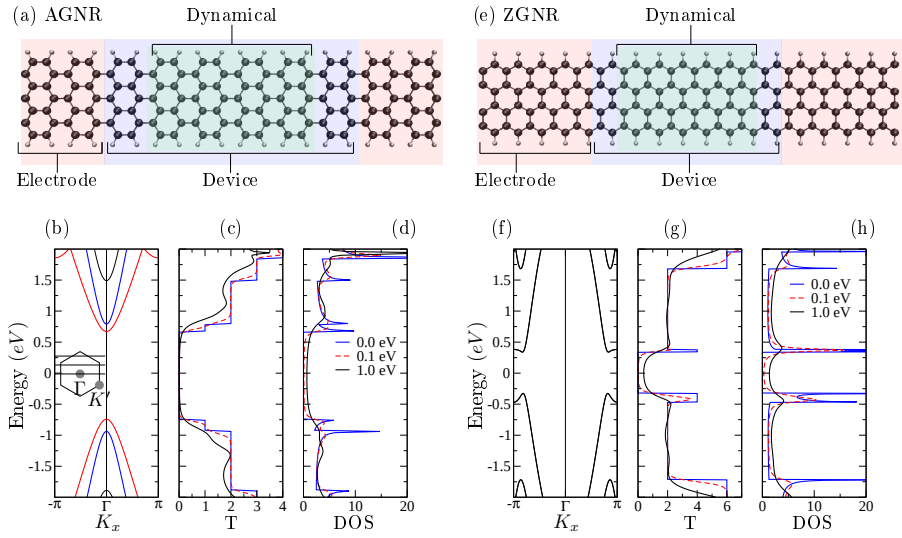

Figure 5.4: (a) Computational setup for a pristine AGNR showing electrode, device and dynamical regions. (b) Electronic band structure (K_x is in units of inverse unit cell length). The different bands are colored according to symmetry of the electronic states. Red: symmetric, corresponding to Fig. 5.5(a-b). Blue: anti-symmetric, corresponding to Fig. 5.5(c-d). The insert is a illustration of the zone folding leading to the gap. (c) Electronic transmission for varying electrode broadening describing the coupling to the metal contacts, $\eta = 0, 0.1, 1$ eV, see text. (d) Electronic DOS projected onto the dynamical region. Panels (e)-(h) show the similar entities for the pristine ZGNR case.

The generic armchair and zig-zag GNRs considered here are shown in Fig. 5.4. We adopt the usual two probe setup defining left (L) and right (R) electrodes, with electronic matrix elements defined in a local basis set in the devise region (D). A subset of the atoms in the device are allowed to vibrate. This dynamical region is restricted by the condition that the electron-phonon coupling is fully included inside D. The electrode coupling $\mathbf{\Gamma}_{L/R}$ is obtained from TranSIESTA[13] and exists on the symmetric L/R electrode parts of the system, see Fig. 5.4(a,e). The primitive unit cell of the AGNR (ZGNR) consist of 18 (10) atoms and in our calculations this unit cell is repeated 10 (18) times in the transport direction. The self-energy from the infinite electrodes is included on the two (five) first/last unit cells. The dynamical region where atoms are allowed to vibrate is restricted to the center 4 and 6 unit-cell for the AGNR and ZGNR, respectively. The corresponding electron-phonon couplings used to calculate the inelastic electron transport are included in the center 6 unit-cells for the AGNR and 8 unit-cells for the ZGNR.

5.4.1.1 Model for the broadening by metal leads

In the experimental setup we will address here the nanoribbons is suspended between two metallic leads. In the case of the lifting experiments[59] described in 5.2, these will be the Au(111) sample surface and Au STM tip, respectively. Here the focus is on the action inside the GNRs, to put aside the possible complications due to the detailed electronic structure of the metal, and the metal-GNR interface in particular.

To this end, a simple model of the metal electrodes, without substantial electronic features, is introduced. We choose semi-infinite GNR with highly broadened states effectively smearing out the energy gap. In this way, we mimic the experimental setup by a more generic description of the metal. In practice this is done by choosing an finite numerical imaginary part in the electrode recursion calculation,[103] η, broadening all states in the semi-infinite electrodes. The scheme above ensures that the phonon effects originates from inside the AGNR, and are not artifacts of the coupling to the metal electrode, which is unknown in the STM experiments. The electronic band structures for the infinite ribbons, along with the transmission and DOS, are shown for $\eta = 0, 0.1, 1$ eV in Fig. 5.4(b,c,d) and Fig. 5.4(f,g,h) for AGNR and ZGNR, respectively. We note that the broadened transmission resemble the smearing seen in the experimental differential conductance curves[59] shown in Fig. 5.1 (c) The electronic states involved in the transport are shown in Fig. 5.5, where we depict the transmission eigenchannels[89] for states in the valence and conduction bands of the AGNR and ZGNR. Their spatial symmetry play a significant role for the selection rules involved in the inelastic scattering.

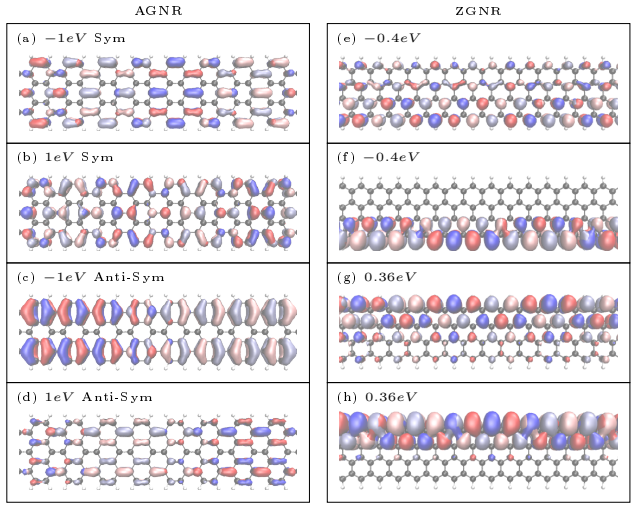

Figure 5.5: (a)-(d) Electron transmission eigenchannels for the clean AGNR for the valence bands at $E - E_F = -1$ eV and for the conduction bands at $E - E_F = 1$ eV. (e)-(h) Electron transmission eigenchannels for the clean ZGNR in the valence bands at $E - E_F = -0.4$ eV and in the conduction bands at $E - E_F = 0.4$ eV for one spin component. The eigenchannels for the other spin component are simply mirror images around the middle of the ZGNR (not shown). The red/blue (pink/gray) isosurfaces represent the real (imaginary) part and sign of the scattering state wave function. For all eigenchannel calculations the electrode broadening was set to zero ($\eta = 0$ eV)

5.4.1.2 Convergence of IETS with cell-size

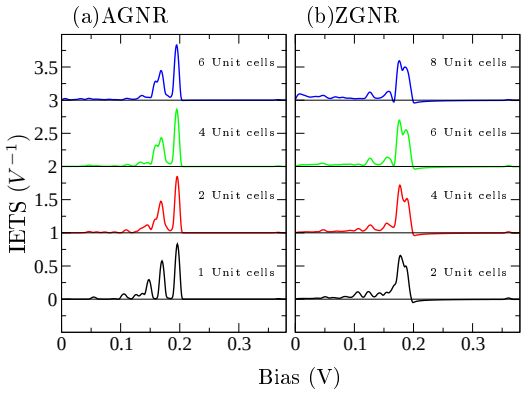

Figure 5.6: The convergence w.r.t. number of dynamical cell size for the clean GNR. (a) IETS signals for the AGNR. (b)IETS signals for the ZGNR. (a-b) normalized with respect to the number of unit cells in the dynamical region (4H14C in AGNR, 2H8C in ZGNR)

The convergence of the IETS with the size of the dynamical region is addressed, by investigating the effect of the finite size of the dynamical region. The IETS signal, for the AGNR, is shown in Fig. 5.6(a), for a fixed gate value of $V_G = 0.0$V, for four different sizes of the dynamical region ranging from 1 to 6 unit-cells. In order to compare the signals they are normalized by the number of unit-cells. The signal scales linearly with the active electron-phonon coupling region. If the dynamical region consists of more than one unit-cell a third peak appears at 159 meV corresponding to the edge phonon mode, the blue band in Fig. 5.8. The convergence for the ZGNR, shown in Fig. 5.6(b) is approximately of the same range as for the AGNR.

5.4.1.3 Gate and voltage-drop

In principle, the electronic structure should be evaluated at finite bias. However, since we wish to avoid using a detailed model of the connection to the metal electrodes, where an important part of the voltage drop will take place, and since the systems are rather long such that the relevant electric fields will be small, we use the zero-voltage electronic structure in the following and use a symmetric voltage drop for these symmetric setups.

Experiments on graphene nanostructures typically include the possibility of ap-

plying a gate potential and thereby change the carrier density. Moreover, in the lifting experiments[59] the charge transfer from the metals electrodes was not clarified. In order to simulate the effect of doping or a gate we further consider that the chemical potentials can be shifted by an applied gate voltage V_G, i.e., $\mu_L = E_F + \hbar\omega_\lambda/2 + V_G$, $\mu_R = E_F - \hbar\omega_\lambda/2 + V_G$. Combined with the LOE, this gives an approximate but computationally efficient scheme, allowing for the evaluation of IETS on a fine V_G grid of relevant values between valence and conduction bands of the GNRs.

5.5 Pristine graphene nanoribbons

In this section, we turn to the IETS results of the two clean ribbons. First we focus on the AGNR systems directly relevant for the lifting experiments[59]. The results for the ZGNR are provided as comparison and to look into the role of chirality and in particular effects rooted in spin polarization, and thus we now discuss these separately.

5.5.1 Pristine armchair nanoribbon

The pristine("Clean") AGNR shown in Fig. 5.4(a) has a width of $W = 7$ dimers (7-AGNR) corresponding to a C-C width of 7.5Å. It presents a direct semiconducting band gap due to the lateral confinement. It is in the class of "large" gaps for ribbons of comparable width since $W = 3p+1$ where p is integer.[98] We obtain $E_g \approx 1.3$ eV at the present level of approximation (DFT-GGA and small basis-set), as seen from the electronic band structure shown in Fig. 5.4. The obtained band gap is below the one observed experimentally, for an AGNR on a Au(111) surface which is around[101, 14] 2.3-2.6 eV or the AGNR suspended between surface and STM-tip[59] $\sim$ 2.7 eV. This is due to the underestimation of the electron-electron interaction,[137] which play an more important role in quasi one-dimensional GNRs compared to pristine graphene. The dielectric screening from the substrate also play a significant role of the gap. Even a weak coupling to a substrate can affect the gap substantially. For a 7-AGNR a band-gap of 3.2 eV was found to be lowered to 2.7 eV on a hBN substrate using GW calculations,[52] similar to the lowering calculated for a 7-AGNR on Au(111).[69] In general we expect that the effect of the underestimation of band-gaps amounts to a scaling of the gate-voltage which shifts the Fermi energy inside the band-gap.

All calculated IETS signals for different gate voltages are shown in Fig. 5.7(a) as

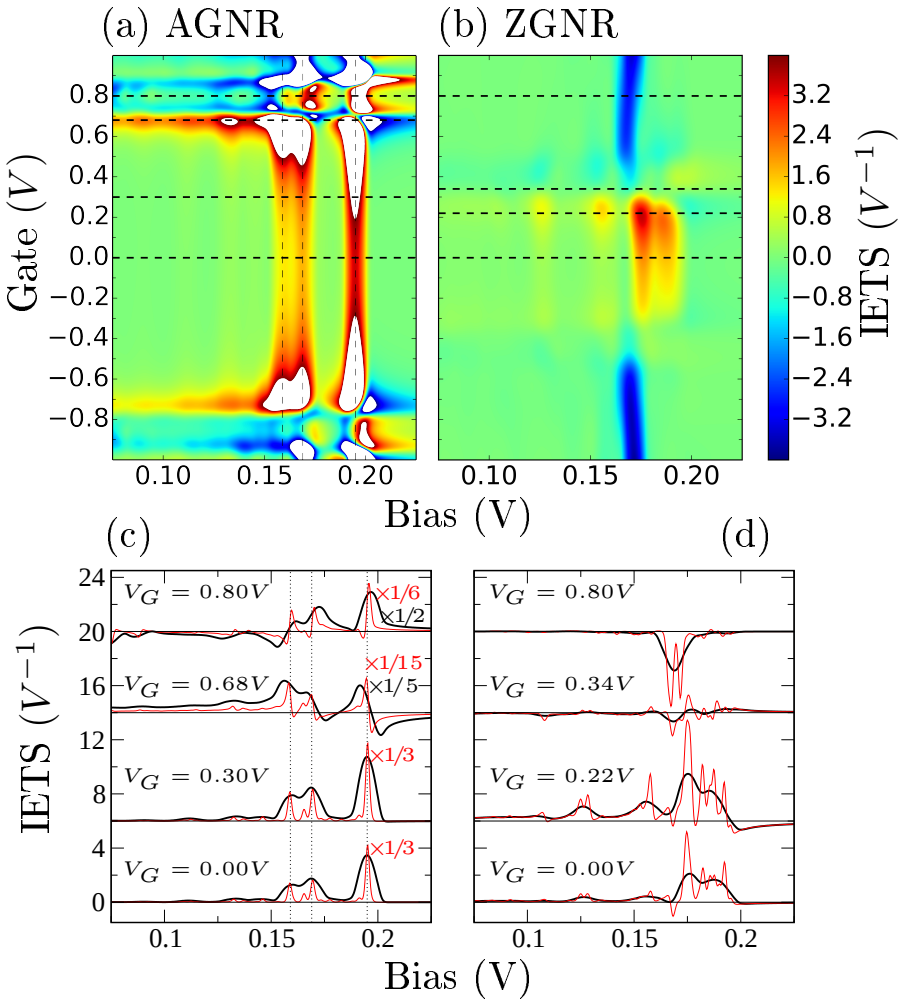

Figure 5.7: IETS signals as a function of gate voltage for (a) pristine AGNR (4 vibrating unit cells) and (b) pristine ZGNR (6 vibrating unit cells). Vertical dashed lines are guides to the eye indicating the energy of the most contributing vibrational modes. Specific IETS signals for the (c) AGNR and (d) ZGNR at selected gate voltages marked with horizontal dashed lines in panels (a) and (b). Broadening originates from temperature $T = 4.2$ K and a lock-in modulation voltage $V_{\mathrm{rms}} = 5$ mV (except for the thin red lines in the lower panels with $V_{\mathrm{rms}} = 0$ mV).

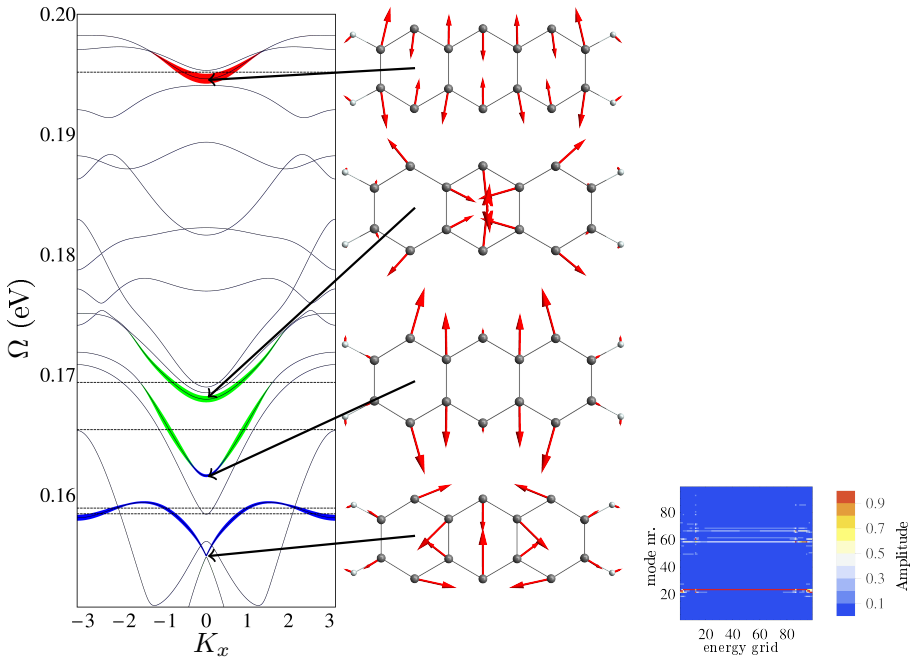

Figure 5.8: Left: The phonon band structure of the AGNR. The size of the fat red, green and blue bands are proportional with the overlap between the repeated band vector and the modes contributing to the IETS signal, ($P_n k$ in Eq. (5.1)). Middle: The band modes evaluated at Γ for the bands which contribute to the IETS signal. Right: The Amplitude $|\gamma_\lambda| + |\kappa_\lambda|$ given in Eqs. (4.34)-(4.35).

a density plot, while selected IETS spectra at selected gate voltages are shown in Fig. 5.7(c). When calculating the IETS we can apply a broadening to take into account the lock-in modulation voltage, $V_{rms} = 5$ mV, which is typically used in experiments, besides the broadening from temperature, which we take here as $T = 4.2$ K. The results in Fig. 5.7(c) are shown both with and without the V_{rms}-broadening.

The results in Fig. 5.7(a,c) correspond to a dynamical region consisting of 4 unit cells. Fig. 5.6 shows how the size of the IETS signals scale linearly with number of cells. Importantly, the shape of the IETS signal is basically converged with 4 dynamical primitive cells, which is what we will apply from here on. We note that in principle comparing the calculated magnitude of the IETS signal directly with experiments might be used to estimate the size of the active interaction region when comparing to experiments.

We find that for all sizes of the dynamical region two IETS signals appear at 196 meV and 169 corresponding to the G-mode and D-mode(ring breathing), respectively, observed in Raman spectroscopy.[41, 27]. Shifting the gate voltage inside the gap region does not affect the IETS signal appreciably. However, when the gate potential shift the equilibrium Fermi level close to the conduction band of the AGNR, the signal increases by a factor of five and a small peak-dip feature appears similar to the one reported for experiments[118] and theory[75] of gated Benzene-Di-Thiol molecular contacts, discussed in chapter Chap. 4. If the system is gated further into the conduction band the signals shift from peaks to dips as the transmission increases beyond approximately 0.5 for the involved channels.[91] The signals for gate voltages corresponding to E_F close to the valence band result in approximately the same signals although the electronic states here differ as seen in Fig. 5.5(a-d).

We can identify the mode vectors (indices λ), v_λ, of the most important vibrational modes inside the dynamical region contributing to the IETS signal by taking the sum of the absolute value of the amplitudes $|\gamma_\lambda|$ and $|\kappa_\lambda|$ given in Eqs. (4.34)-(4.35). According to the right panel in Fig. 5.8 only four modes contributes to the IETS. These can be analyzed further in terms of the phonons in the infinite AGNR by projecting the contributing IETS modes in the finite dynamical cell onto the phonon band modes (band index n, k-point k) defined in the primitive cell u_{nk}, but expanded into the dynamical region consisting of 4 primitive cells using their Bloch form,

$$P_{nk} = \left| u_{nk} \left(1, e^{ik}, e^{i2k}, e^{i3k}\right) \cdot v_\lambda \right|^2 . \tag{5.1}$$

The projections are depicted as widths of the bands in Fig. 5.8, where we also show the corresponding Γ-point phonon modes inside the primitive cell for the infinite ribbon. Besides the two highest energy modes corresponding to the G and D Raman modes, we also get contributions from modes at lower energies in the IETS.

5.5.2 Pristine zig-zag nanoribbon

The ZGNR shown in Fig. 5.4(e) has a width of 4 zig-zag chains (4-ZGNR) corresponding to 7.26 Å(C-C). The breaking of sublattice symmetry for the ZGNR and lack of pseudo-phase result in different selection rules for matrix elements and difference in for example Raman signals from different edges[102]. The ZGNR present spin polarized edge states which are metallic in simpler tight-binding descriptions but present a small gap in DFT[98]. These play a major role for the conduction. Inside the band-gap the conduction takes place in spin polarized channels close to the edge, see Fig. 5.5(e-h). Since the edge

states break the mirror symmetry with respect to the middle of the ribbon, there will be no symmetry forbidden transition between scattering states. Thus we expect a wider range of modes to contribute to the IETS signal compared to the AGNR case which indeed is in agreement with the findings shown in Fig. 5.7(b,d). The greater number of modes contributing to the IETS for the ZGNR result in broader signals with similar magnitude as for the AGNR.

5.5.2.1 Comparison between spin- and non-spin- polarized ZGNR

This difference suggests a way to indirectly observe spin polarized edge states by considering the width or number of IETS signals. Therefore in Fig. 5.9 we compare the IETS signal obtained from a non-spin polarized and a spin polarized calculation. In the undoped case, the IETS signal have opposite signs due to the spin induced gap. Only a single peak contributes to the non-spin polarized IETS signal while several peaks contribute to the spin polarized IETS signal. Even if the ZGNR is doped corresponding to $V_G = 0.5$V, were the spin polarized edge state decays into the ribbon and spin polarized and non-spin polarized IETS signal have the same sign, the spin polarized IETS persist to have several peaks opposed to a single peak in the non-spin polarized IETS.

Projecting the modes contributing to the IETS onto the phonon band modes further underlines how several bands with different symmetries contribute to the spin polarized IETS, while only a couple of bands contribute to the non-spin polarized IETS.

In order to visualize the important phonon band modes taking part in the inelastic scattering we introduce the overlap between modes in the finite dynamical cell and the phonon band modes weighted by the size of the IETS signal

$$F_{nk}(V_G) = \sum_{\lambda} |\gamma_\lambda(V_G)| \left| u_{nk}\left(1, e^{ik}, e^{i2k}, \ldots, e^{i5k}\right) \cdot v_\lambda \right|^2, \tag{5.2}$$

where u_{nk} is the phonon band mode indexed by n, and v_λ is the modes in finite 4 primitive cell long dynamical region index by λ. The results are shown in Fig. 5.9. It is clear that the spin-polarization leads to contributions to IETS from new modes.

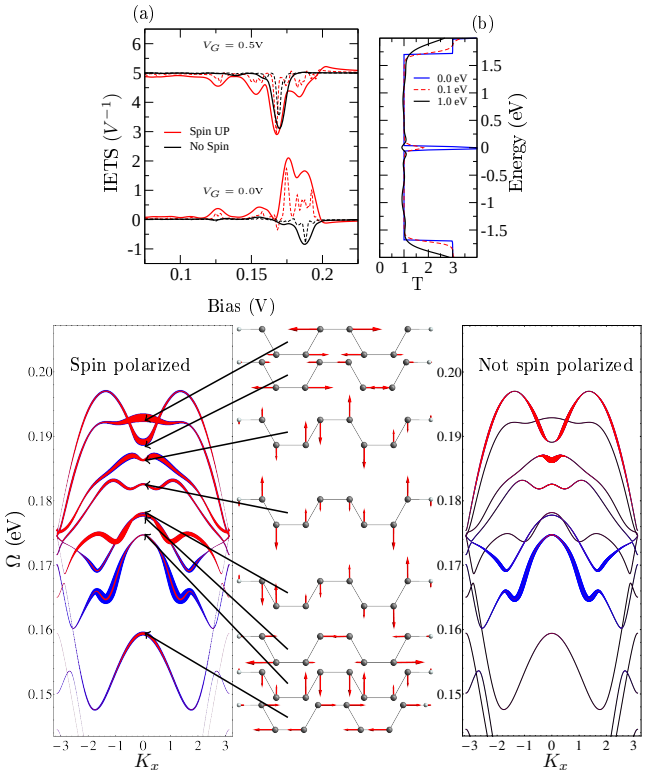

Figure 5.9: Upper panel: (a) IETS signal for the pristine ZGNR. The black lines are without spin polarization, and the red lines are the spin-up component from a spinpolarized calculation. Solid line: Broadening using $V_{rms} = 5$ mV and $T = 4.2$ K. Stippled line: $V_{rms} = 0$ mV and $T = 4.2$ K. (b) Electronic transmission, from a non-spinpolarized calculation, for varying electrode broadening describing the coupling to the metal contacts, $\eta = 0, 0.1, 1$ eV. Lower panel: The phonon band structure of the ZGNR together with the Γ-point modes. The widths of the red bands are proportional to the weight function $F(0.0)$ (Eq. (5.2)), while the widths of the blue bands are proportional to $F(0.0) + F(0.5)$.

5.6 Defective graphene nanoribbons

5.6.1 Defects in AGNRs

Now we turn to the signals due to defects. Regardless of the fabrication method, defects will inevitable occur. For example, if the AGNRs are synthesized from a precursor molecule, involving heating and dehydrogenation, as reported by Cai *et al.*[16] and Blankenburg *et al.*,[9] there is a chance that the reaction is incomplete and some of the carbon-carbon bonds between the precursor molecules do not form. Also there is a chance that a part of the final AGNR will have dehydrogenated edges or edges passivated by two hydrogen atoms. Finally, defects may be introduced on purpose locally by applying a high current in the STM.[126]

In Fig. 5.10 we show the structures of pristine AGNR along with 8 different defect configurations which we have considered. These include four defects in the edge passivation as follows: A single edge side with an extra hydrogen atom [`1H-edge`, Fig. 5.10(b)], two edge sides with each an extra hydrogen atom [`2H-edge`, Fig. 5.10(c)], one hydrogen replaced by a fluorine atom [`1F-edge`, Fig. 5.10(d)], and a dehydrogenated edge with 4 hydrogen atoms removed from each side [`8H-free`, Fig. 5.10(e)]. We have also considered defects in the atomic structure in the form of one, two, or four broken C-C bonds [`1C-broken`, `2C-broken`, `4C-broken`, Fig. 5.10(f)-(h)] as well as a Cu adatom on the AGNR [`Cu-adatom`, Fig. 5.10(i)]. For all these systems the entire dynamical region was relaxed, i.e., the parts of the AGNRs shown in Fig. 5.10.

The defects can influence the IETS signal in two ways. First, they can have a direct impact by changing the vibrational degrees of freedom. In order for the change in the vibrational spectrum to give a signal in the IETS, the "new" vibration must couple to the current, and preferably have a frequency which do not coincide with one of the "clean" signals obtained for pristine ribbons. Second, they can change the electronic structure, and thereby have a direct effect by changing the electron-phonon coupling, or have a more indirect effect by changing the transmission channels, *e. g.* shifting a peak in the IETS to a dip or giving rise to an asymmetric contribution from the term in Eq. (4.31).

The effect of the defects on the elastic electronic properties are investigated in Fig. 5.11. The carbon density of states are shown projected to the Device region together with the total transmission T as a function of energy. The clean AGNR has two bands and contributing transmission channels close to E_F. Thus, we also show $\frac{T}{T_1}$, where T_1 is the transmission of the dominating eigenchannel, as a measure of the minimum number of contributing channels. Measurements

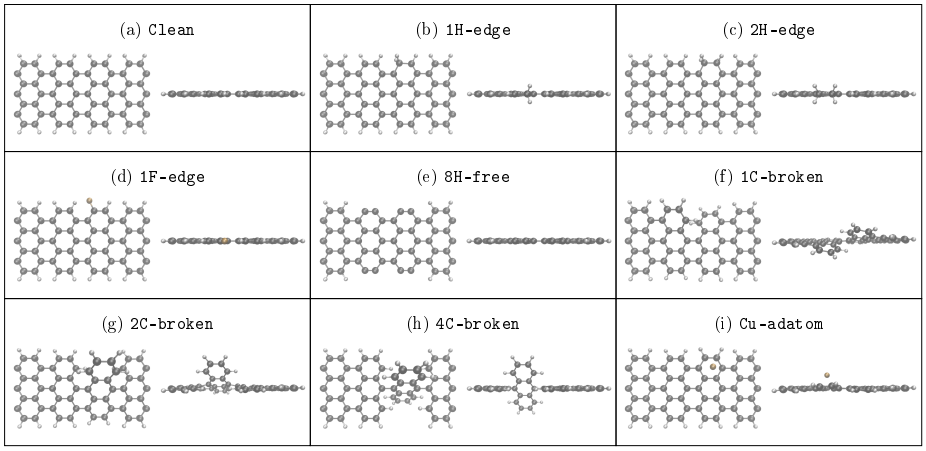

Figure 5.10: Top and side views of the dynamical region describing the various AGNR defect structures. (a) Pristine AGNR. (b) One extra H atom on one of the edges. (c) Two extra H atoms on one of the edges. (d) One H atom replaced by a F atom. (e) Dehydrogenated edge where 4 H atoms have been removed from each side. (f) One broken C-C bond. (g) Two broken C-C bonds. (h) Four broken C-C bonds. (i) Cu adatom in a hollow site on the edge.

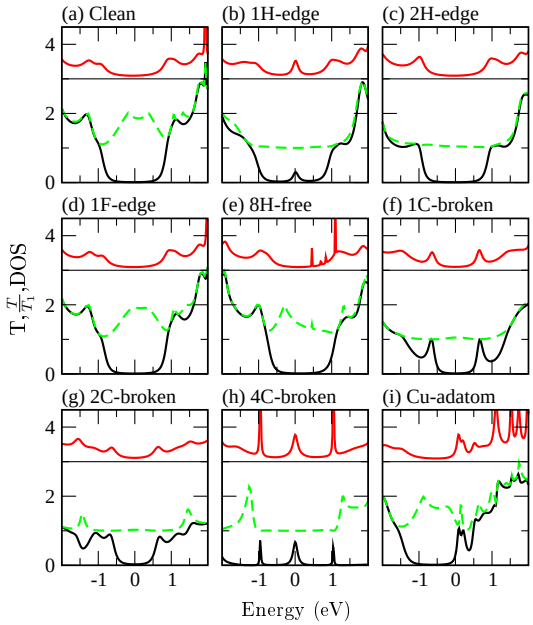

Figure 5.11: Electronic properties of the AGNR structures shown in Fig. 5.10. The total transmission is shown with black lines. The ratio T/T_1, where T_1 is the transmission originating from the most transmitting eigenchannel is shown with green dashed lines (this ratio gives a lower bound to the number of contributing eigenchannels). The DOS for the C atoms in the dynamical region is shown with red lines (offset by 3 units).

of shot-noise may provide insights into this effective number of conductance eigenchannels.[22, 107] For the clean system, the carbon DOS exhibit a gap as expected from the band structure in Fig. 5.4, which is broadened due to the coupling to metallic electrodes. Inside the gap we find T/T_1 around 2 close to E_F corresponding to channels derived from the valence and conduction bands.

Not all defects change the elastic transmission, and furthermore, a change in elastic transmission needs not be unique for a specific defect. The addition of IETS may provide a better fingerprint of the defect type in the current. Thus, we again calculate the IETS for various positions of the Fermi level corresponding to doping or applying a gate potential. The resulting plots are shown in Fig. 5.12. As for the clean structures, the two peaks at 196 meV and 169 meV, corresponding to the Raman G-mode and D-mode, are dominating for a range of gate values for all the structures. Another feature, which is present in all the systems, is the appearance of several signals close to a band onset. The most contributing modes can be identified by considering the value of the amplitudes, γ_λ and κ_λ given in Eq. (4.34) and Eq. (4.35).

5.6.1.1 Edge passivation

Considering defects in the edge-passivation, structure (b-e) in Fig. 5.10, the gap in the transmission is unchanged, see Fig. 5.11(b-e), except for the `1H-edge` structure were a peak appears at the Fermi level in the DOS and in the transmission. The extra peak can be attributed to tunneling via a mid-gap state which appears due to the local breaking of sub-lattice symmetry.[98] Thus, if a hydrogen is added to the neighboring carbon atom, as in `2H-edge`, the peak disappears. The addition of one or two hydrogen atoms on the side also results in the closing of one transmission channel as shown in Fig. 5.11(b,c). Concerning the vibrational degrees of freedom, the addition of extra hydrogen to the edge results in new vibrational modes outside the frequency range of the pristine ribbon, around 330 meV for the `1H-edge` and around 343 meV and 353 meV for the `2H-edge`.

However, only the `1H-edge` gives a IETS signal which differs significantly from the pristine case, as can be seen by comparing Fig. 5.12(a-c). Considering the top curve in Fig. 5.12(k) showing the IETS signal for `1H-edge` at $V_G = 0.2$V, we see how new signals appear above 300 meV. For positive bias polarity two signals appear at 330 meV and 365 meV, respectively. However, for negative bias polarity only a asymmetric signal around 365 meV is present. The signal at 330 meV is due to vibrations of the H_2, while the signal at 365 meV is due to the hydrogen sitting on the neighboring atom, as shown in Fig. 5.13 (a-b). Furthermore, the size of the signals around 196 meV and 169 meV also depend

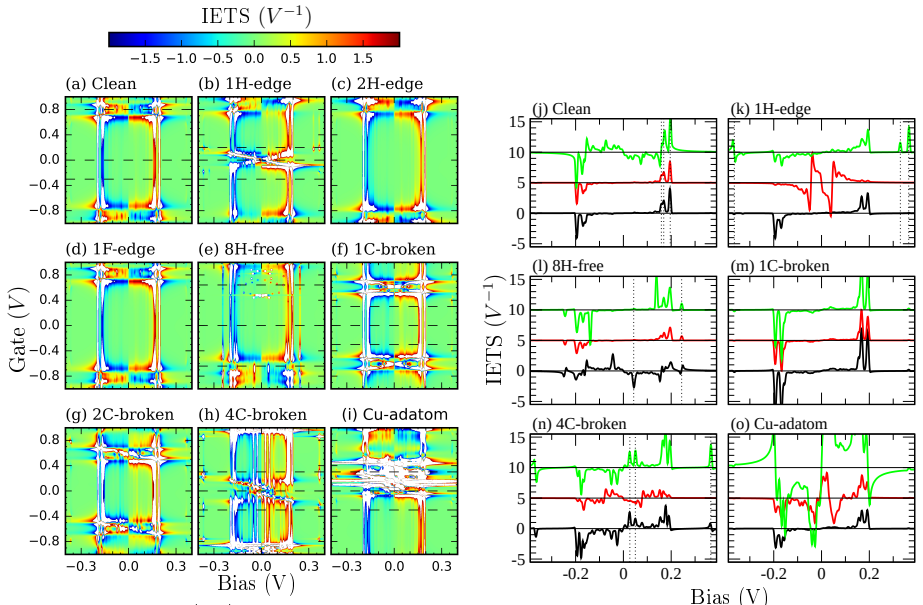

Figure 5.12: (a-i) IETS as a function of gate voltage V_G for the pristine and defective AGNR structures shown in Fig. 5.10 . (j-o) IETS for six selected structures at three specific gate values (dashed horizontal lines in panels a-i). The curves are offset with the most negative gate value at the bottom (black curves) and the most positive at the top (green curves). (j) Clean AGNR at gate values $V_G = -0.3$, 0.0, and 0.8 V. (k) `1H-edge` at $V_G = -0.3$, 0.0, and 0.2 V. (l) `8H-free` at $V_G = -0.3$, 0.0, and 0.6 V. (m) `1C-broken` at $V_G = -0.3$, 0.0, and 0.3 V. (n) `4C-broken` at $V_G = -0.3$, 0,0, and 0.3 V. (o) `Cu-adatom` at $V_G = -0.3$, 0.0, and 0.3 V. Dotted vertical lines are guides to the eye of characteristic IETS signals corresponding to the modes in Fig. 5.13

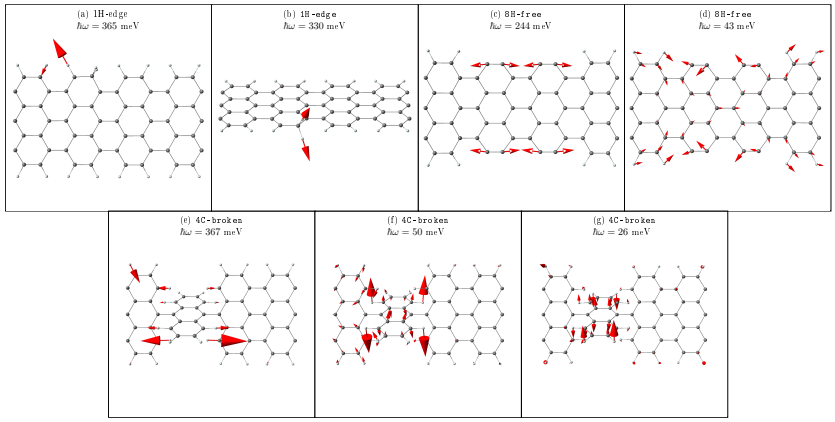

Figure 5.13: Visualization of the most contributing defect-induced vibrational modes to the IETS signals indicated by vertical lines in Fig. 5.12(j-o). (a-b) The two hydrogen signals for `1H-edge`. (c) Localized edge mode at the carbon dimers for the `8H-free`. (d) Delocalized edge mode for the `8H-free`. (e) Hydrogen mode from the zigzag edge of `4C-broken`. (f-g) Defect modes for `4C-broken`.

on the bias polarity.

Gating onto the zero-energy resonance for `1H-edge` the IETS signal are dominated by large asymmetric signals for low energy vibrations given by the asymmetric function in Eq. (4.31). Note that the amplitude κ_λ changes sign with the bias polarity for this approximately left-right symmetric structure, as can be seen from the red IETS curve in Fig. 5.12(k) which is roughly an odd function. In close proximity of the resonance the frequency of the contributing modes increase giving the X-shape in Fig. 5.12(b). Gating further away from the zero-energy resonance, the IETS signal approaches the pristine signal.

The results for IETS when substituting a hydrogen with a fluorine atom, shown in Fig. 5.11(d), is seen to have virtually no effect. This indicates that a significant change in the chemical and electronic structure is required in order to obtain a signal although the vibrations are influenced by the heavier passivation.

Significantly changing the passivation by removing four hydrogen atoms on each side, as in `8H-free`, give rise to four very narrow peaks in the unoccupied band part of the carbon DOS in Fig. 5.11(e). These correspond to very localized dangling-bond states on the dehydrogenated dimers, and does not show up in the transmission. However, the dehydrogenated edges give rise to localized vibrations around 245 meV outside the range of the pristine vibrational spec-

trum [26]. The in-phase vibration of the dehydrogenated carbon dimers at the armchair edges, see Fig. 5.13(c), gives rise to an extra IETS peak at 244 meV matching the H-free mode measured by Raman.[48] We find that this signal is robust against gating and appears in the whole range of gate values. When gating into to the valence band a new signal appears around 43 meV originating from a low energy edge vibration shown in Fig. 5.13(d).

5.6.1.2 Structural defects

The electronic transmission is mediated by the carbon π system. Thus if a carbon-carbon bond fails to be formed during the GNR synthesis or is broken afterwards, a large effect can be expected for the electronic properties as also evident from Fig. 5.11(f-h). Breaking one or two bonds results in the formation of two in-gap peaks which are broadened by the electrodes making the gap to appear smaller. However, for a longer ribbon the gap would remain unchanged. The IETS signal for the 1C-C and 2C-C have the same two signals, at 196 meV and 169 meV, as the Clean ribbon. However the relative size of the peaks are shifted making the "D-peak" slightly larger than the "G-peak".

Breaking four carbon-carbon bonds so only that a single bond is left results in a totally altered DOS which now is dominated by three sharp peaks. The IETS signals for the `4C-broken` are shown in Fig. 5.12(h) and Fig. 5.12(n). In the proximity of the resonance, at $V_G = 0.0$ V, a broad range of signals at low vibrational energies appear. Gating away from the broad zero-energy transmission resonance we observe two robust IETS signals at 27 meV and 50 meV resulting from vibrations, shown in Fig. 5.13(f-g), localized at the defect.

5.6.1.3 Adatom

Transition metals are typically used for growth of graphene or as a substrate for the bottom-up synthesis of GNRs. Thus it is of interest to consider the effect of this type of adatom on the GNR. Here we consider a Cu adatom which for bulk graphene have a lowest energy adsorption site in the on-top position.[71] For the AGNR we here consider the stable position breaking the axial symmetry in Fig. 5.10(i) which is at a hexagon center at the edge. The DOS and transmission reveal a n-type doping effect shifting E_F close to the conduction band while leaving the two transmission channels inside the gap relatively intact.

For the pristine ribbon the electron-phonon coupling involving the out-of-plane vibrations are suppressed due to the symmetry of the π-orbitals. However,

around the onset of the conduction band the IETS signal shown in Fig. 5.12(i,o) is dominated by large asymmetric signals with a significant contribution from out-of-plane phonons. The appearance of these are due to the breaking of the planar symmetry of the GNR by the adatom. However, when gating into the gap these signatures of the adatom disappear, cf. lower curve in Fig. 5.12(o).

5.6.2 Defects in ZGNRs

Now we consider defects in a zigzag graphene nanoribbons. As was the case for the pristine zigzag ribbon we do a spinpolarized calculation. The spin degrees of freedom $\sigma = \uparrow, \downarrow$ generalizes γ_λ^σ and κ_λ^σ [Eqs.(4.34)-(4.35)] corresponding to two independent spin channels, which in general can have quite different amplitudes and even opposite sign. The observable IETS would simply be the sum of these two components $(\partial_V^2 I_\uparrow + \partial_V^2 I_\downarrow)/(\partial_V I_\uparrow + \partial_V I_\downarrow)$.

As for the AGNR we study eight different defect configurations, shown in Fig. 5.14. We consider the following defects in the edge-passivation: A single edge with an extra hydrogen [`1H-edge`, Fig. 5.14(b)], one hydrogen is replaced by either a F atom [`1F-edge`, Fig. 5.14(c)], an OH group [`1OH-edge`, Fig. 5.14(f)], or a NO_2 group [`1NO2-edge`, Fig. 5.14(g)]. We also consider defects in the form of a Cu adatom [`Cu-adatom`, Fig. 5.14(d)] or a Li adatom [`Li-adatom`, Fig. 5.14(e)]. Finally, we also study the effect of a structural defect in form of a 57 reconstruction [`R57`, Fig. 5.14(h)] and a substitutional defect where a C atom next to the edge is replaced by a Si atom [`Si-substitute`, Fig. 5.14(i)]. For all these systems the entire dynamical region was relaxed, i.e., the parts of the ZGNRs shown in Fig. 5.14 using spin-polarized treatments.

In the same way as for the AGNR case we first characterize the electronic properties in the device region, but now spin resolved, showing the electronic properties of the different impurity configurations for spin up/down in the left/right parts of Fig. 5.15.

5.6.2.1 Edge passivation

The broad IETS signals in the ZGNR resulting from the breaking of the axial mirror symmetry makes signals originating from the defects more difficult to identify. Inside the gap the `1H-edge` IETS signal resembles the pristine ZGNR signal, however, gating into the valance band the edge states starts to decay into the ribbon and some of the mirror symmetry is restored resulting in part of the pristine ZGNR signals to disappear. Here an extra signal appears due to edge-

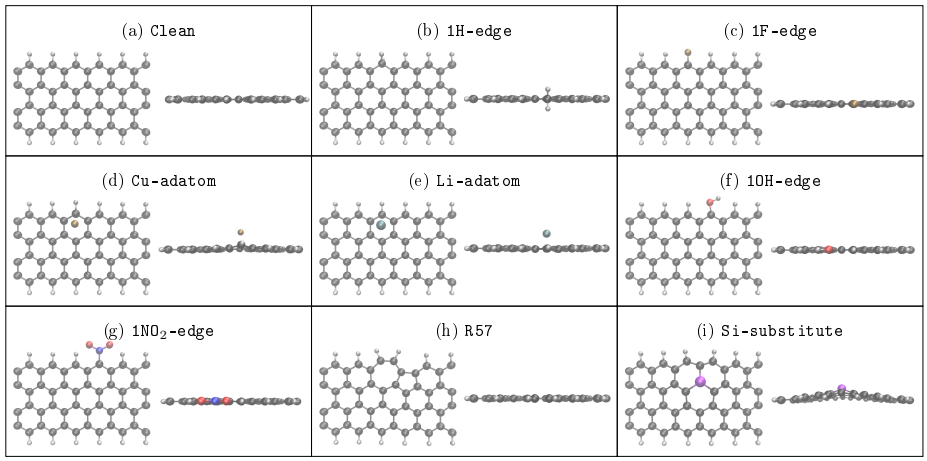

Figure 5.14: Top and side views of the dynamical region describing the various ZGNR defect structures. (a) Pristine ZGNR. (b) One extra H atom on one of the edges. (c) One H atom replaced by a F atom. (d) Cu adatom in a hollow site on the edge. (e) Li adatom in a hollow site on the edge. (f) One H replaced by a OH group. (g) One H replaced by a NO_2 group. (h) Structural defect (R57). (i) Substitutional Si defect next to the edge.

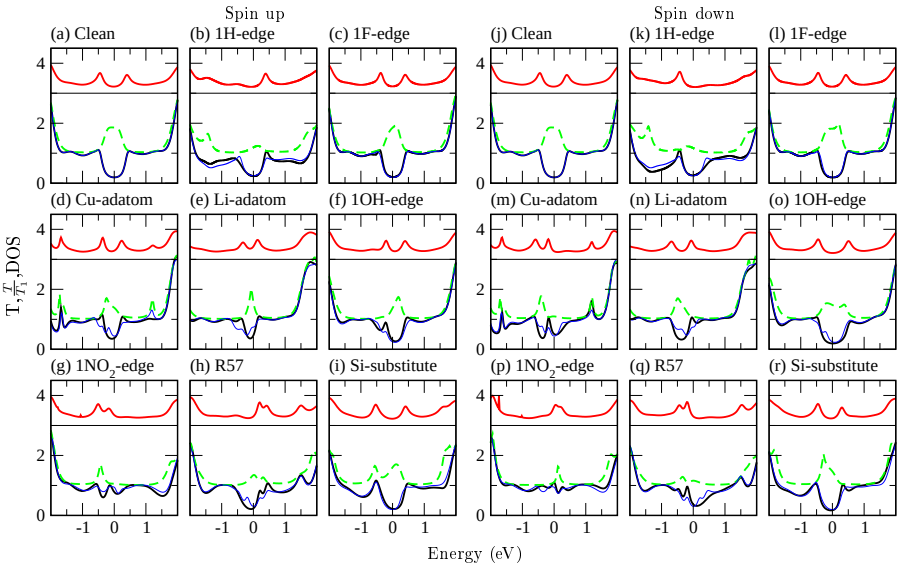

Figure 5.15: Electronic properties of the ZGNR structures shown in Fig. 5.14 with the spin-up/down components in the left/right panel. The spin-resolved total transmission is shown with black lines while spin-averaged total transmission is shown with thin blue lines. The ratio T^σ/T_1^σ, where T_1^σ is the transmission originating from the most transmitting spin eigenchannel, is shown with green dashed lines (this ratio gives a lower bound to the number of contributing eigenchannels with spin σ). The spin-resolved DOS for the C atoms in the dynamical region is shown with red lines (offset by 3 units).

modes in the frequency range 194 to 199 meV with the most contributing mode at 196 meV as shown in Fig. 5.17(a). The resulting IETS signal can clearly be seen in the bottom curve in Fig. 5.16(k). As for the AGNR substituting a hydrogen with a flourine atom has a very limited effect on the electronic properties and the IETS signal.

Substituting a hydrogen with an OH group, according to Fig. 5.15(f) and (o), have only a small effect on the spin down electrons, while it shrinks and add additional structure to the gap for the spin up electrons. For the spin up electrons there is a small peak inside the gap which give rise to a large asymmetric IETS signal around $V_G = -0.2$V in Fig. 5.15(o) lower curve, compared to the pristine case. The mode having the largest contribution to the asymmetric signal is shown in Fig. 5.17(b). However, there is no clear signature of the OH group itself. In the same manner the substitution with a NO_2 group removes the gap in the electronic properties without leaving any direct fingerprint of the NO_2 group in the IETS signal.

5.6.2.2 Adtoms

As for the armchair we consider the effect of adatoms. For the Cu adatom the transport gap shrinks for the spin up electrons while there is an in-gap peak for the spin down electrons, cf. Fig. 5.15(m). Thus, for some gate values the IETS signals reflect that the spin down electrons will back scatter while the spin up electrons will be forward scattered, and the observed signal is then the sum of these contributions. For a gate value of $V_g = -0.2$V, the IETS signal is dominated by spin down electrons. Due to the finite width of the in-gap peak, in the spin down transmission, the low frequency phonons ($\hbar\omega < 0.1$ meV) give rise to back scattering while the high frequency phonons ($\hbar\omega > 0.1$ meV) result in forward scattering. Thus, the low and high energy signals have different signs as can be seen from Fig. 5.16(l). Interestingly, the low energy signal primarily consists of symmetric contributions from out of plane modes as the one shown in Fig. 5.17(b) . Gating by $V_g = -0.32$ V, the spin down transmission is about 0.4 while the spin up transmission is about 0.85. Thus, in Fig. 5.18 we see how this give rise to comparable spin resolved signals with opposite signs in the $\frac{d^2I}{dV^2}$.

Replacing the Cu adatom with Li, the transmission and DOS, shown in Fig. 5.15(e) and Fig. 5.15(n), reveals a spin dependent n-type doping effect, where E_F is shifted the most for spin down. However, no in-gap peak is seen as for Cu and the IETS show no clear signature of the lithium atom.

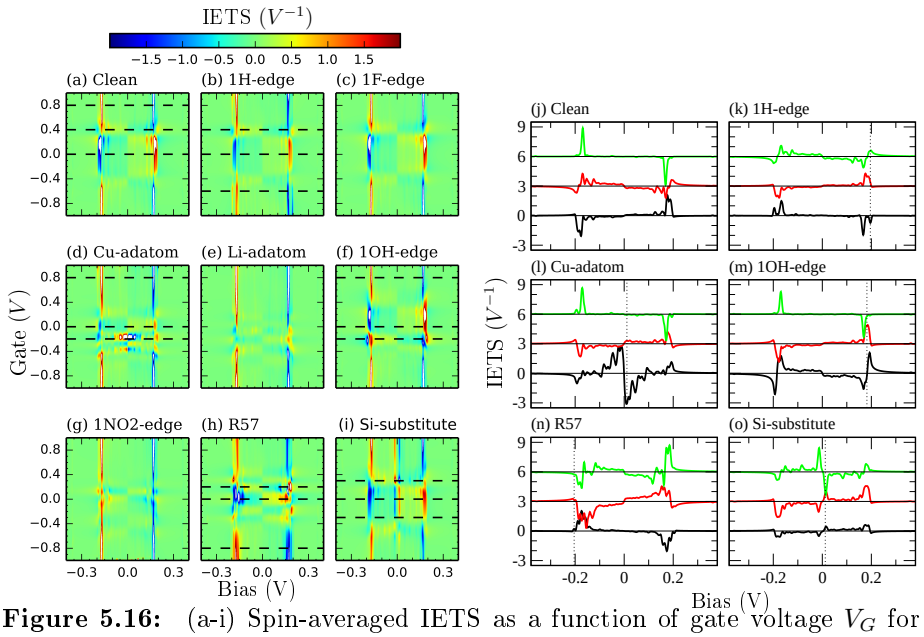

Figure 5.16: (a-i) Spin-averaged IETS as a function of gate voltage V_G for the pristine and defective ZGNR structures shown in Fig. 5.14. (j-o) IETS for six selected structures at three specific gate values (dashed horizontal lines in panels a-i). The curves are offset with the most negative gate value at the bottom (black curves) and the most positive at the top (green curves). (j) Clean ZGNR for gate values $V_G = 0.0$, 0.4, and 0.8 V. (k) `1H-edge` at $V_G = -0.6$, 0.0, and 0.4 V. (l) `Cu-adatom` at $V_G = -0.2$, 0.0, and 0.8 V. (m) `1OH-edge` at $V_G = -0.2$, 0.0, and 0.8 V. (n) `R57` at $V_G = -0.8$, 0.0, and 0.2 V. (o) `Si-substitute` at $V_G = -0.3$, 0.0, and 0.3 V. Dotted vertical lines are guides to the eye of characteristic IETS signals corresponding to the modes shown in Fig. 5.17.

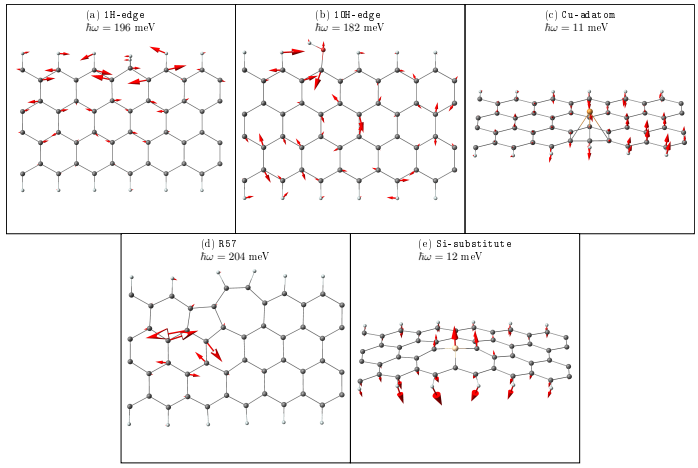

Figure 5.17: Visualization of the most contributing modes to the IETS signals indicated by vertical lines in Fig. 5.16(j-o). (a) Edge mode at the edge with the extra hydrogen in `1H-edge`. (b) Mode contributing to the asymmetric signal in Fig. 5.16 (m) for the `10H-edge`. (c) Out-of-plane mode for `Cu-adatom`. (d) Localized mode for `R57`. (e) Out o plane mode for `Si-substitute`.

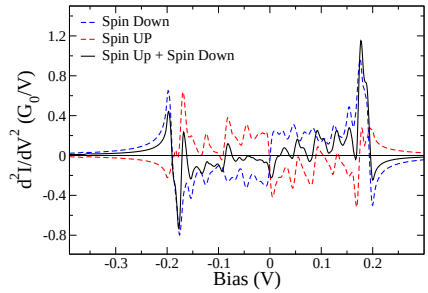

Figure 5.18: Spin resolved $\frac{d^2I}{dV^2}$ for the `Cu-adatom` system for gate value $V_g = -0.32$ V.

5.6.2.3 Structural defect

The formation of a R57 reconstruction results in a peak in the DOS in the device region, just below/above the Fermi-energy for the spin down/up electrons . The R57 breaks the symmetry both in the vibrational and electronic structure allowing for IETS signals from a wider range of vibrations, resulting in broader peaks, as seen from Fig. 5.16(h) and Fig. 5.16(n). One of the contributing modes, shown in Fig. 5.17(d) is localized at the border between the pentagon-ring and middle of the ribbon at $\hbar\omega = 204$meV. This localized mode yield a relatively small signal compared to the other signals, however, contrary to the other modes the localized mode is not expected to be broadened if the coupling to phonons away from the dynamical region is taken into account. The breaking of symmetry in the electronic structure also give rise to different signals for the two bias polarities.

5.6.2.4 Substitutional impurity

Substituting a carbon with a silicon atom leads to an out-of-plane buckling, see Fig. 5.14. However, both silicon and carbon have an s^2p^2 electronic structure, and the electronic transmission is basically similar to the pristine case. On the other hand, the buckling give rise to low energy peaks in the IETS signal originating from the e-ph coupling to the out-of-plane modes. The most contributing out-of-plane mode is shown in Fig. 5.17(e). Gating close to the band-edge of the conduction band give rise to different sign of the signals at low and high vibrational energies, as seen from the top curve in Fig. 5.16(o).

5.7 Summary and Conclusions

In conclusion, we have investigated the gate dependent IETS signal for a gold-chain AGNR junction and for symmetrically contacted pristine as well as a selection of defective armchair and zigzag graphene nanoribbons.

The gold-chain AGNR junction experiences three peaks at 196, 169 and 159 mV. The peak at 196 mV corresponds to the G-mode and the two peaks at 169 and 159 mV are merged to give the D-peak, observed around 200 and 163 mV experimentally[58]. Furthermore, signals due to hydrogen are observed, for a gate value of $V_G = 0.3$ V. Two symmetric signals at -350 mV and -366 mV and an asymmetric signal at 366 mV. The signal at -350 mV is shown to originate

from the zigzag edge while the asymmetric signal at 366 mV is due to the "bulk" part of the ribbon.

Considering the symmetrically contacted pristine AGNR the inelastic tunneling give rise to two peaks in the IETS spectrum at 196 mV and 169 mV corresponding to the G-mode and D-mode, also seen in the gold-chain AGNR junction. By connecting the IETS signals to the phonon band structure, we have clarified how only four bands contribute. Concerning defects in AGNRs we have shown how some defects leave the IETS spectra unchanged while others give a clear signal. We have shown how adding an extra hydrogen atom to a single edge side gives a clear signal for some gate values and how adding one more hydrogen atom to the neighboring edge side, restoring the sub-lattice symmetry, removes the IETS signal due to the hydrogens. For the `1H-edge` structure a signal at 330 mV is observed for some gate values, offering an alternative explanation of the "2D-peak", observed in Fig. 5.1. Furthermore, exchanging a single hydrogen atom with a fluorine atom in the passivation does not result in any change in both the elastic and inelastic tunneling. However removing 8 hydrogen atoms leaving part of the edge on each side without passivation, gives a clear robust signal throughout the investigated gate values. The signal is due to the carbon dimers at the edge and have a frequency around 245 meV making it easy to detect since it is outside the vibrational spectrum of the pristine ribbon. Thus, this confirmes that the dehydrogenated edge mode measured by Raman ay 245 meV by Huang *et al.*[48] also give rise to a signal in the IETS and is a possible explanation for the peak observed at -262 mV in Fig. 5.1. The breaking of one or two carbon-carbon bonds turns out to shift the size of the peaks due to the "G-mode" and "D-mode" making the "D-signal" slightly larger. Breaking 4 carbon-carbon bonds give rise to signals caused by the defect tilted out of plane. Lifting the symmetry of the π-electrons by adding a `Cu-adatom` allows the out-of plane modes to contribute.

For the ZGNR we find broad signals especially close to the Fermi-energy. Importantly, the broad signals are a consequence of the breaking of the axial mirror symmetry in the ribbon due to the presence of spin-polarized edges. Thus, by comparing to non-spin polarized calculations, we suggest that IETS can give an indirect proof of spin-polarization in zigzag ribbons.

In contrast to the AGNR the broad signals for the ZGNR makes it difficult to identify clear signals for the defect investigated in this chapter. However, the presence of a `R57`-reconstruction broadens the signal further, by breaking both the electronic and vibrational symmetry. Substituting a carbon atom with a silicon atom makes the ribbon buckle, breaking the planar symmetry, allowing the out-of-plane modes to contribute to the IETS.

Therefore, we suggest that in the future studies IETS can be used to gain

information of the curvature of GNRs and other graphene structures.

Chapter 6

Heating in Nanostructures

The preceding two chapters was concerned with the influence of vibrations on the electronic current, quantified by the IETS signal. The IETS signal is due to the coupling between the current and vibrations. When the electrons scatter inelastically on a phonon, energy is transferred between the electrons and phonons. The heating due to random scattering with electrons is called Joule heating. Joule heating is an non-equilibrium effect, and is thought to be the activation mechanism for electromigration[119]. Scaling down our electronic devices while keeping the voltage constant results in an increased current density which enhances the Joule heating and electromigration in the device, potentially leading to contact disrupture and thereby malfunction. M. Engelund *et al.*[26] explained how Joule heating of localized edge vibrations could explain the edge reconstruction, due to the current, observed in graphene nanostructures by X. Jia *et al.*[50]. Thus, understanding of the mechanism behind heating on the nano-scale is an important issue in nano-scale electronics. While Joule heating is a random process, alternative deterministic current-induced forces have been suggested as an alternative/addition to Joule heating responsible for the heating on the nano-scale. The deterministic force have four contributions: The non-conservative "wind" force (NC), a Lorentz-type force originating in the quantum-mechanical Berry phase (BP), the electronic friction force due to electron hole pair excitations, and finally the renormalization force (RN) which acts as correction to the confining potential[23, 73, 11, 74].

The deterministic nature of the forces can in principle be utilized to make molecular scaled devices. Dundas *et al.*[23] have suggested how the NC force can be used to drive a molecular motor. However, a maybe more imminent/simple question is understanding the mechanisms behind the breaking of an metallic-chain[115]. If the nuclei performs a closed loop through regions of varying current density, the NC force can continuously pump energy into the system increasing the kinetic energy of the nuclei leading to "runaway modes"[74]. Runaway modes can also be obtained through the non-equilibrium part of the electronic friction, which can turn positive if the probability of exiting an phonon exceeds the probability of absorbing a phonon[78, 39].

This chapter presents the preliminary work on the role of the current-induced deterministic forces on graphene nanoribbons.

6.1 The Equation of Motion

To describe the dynamics of the system in question an equation of motion is needed. For an isolated system the equation of motion is, in the harmonic approximation, given as:

$$F(U(t)) = -\mathbf{W}U(t), \tag{6.1}$$

where $F(U(t))$ is the force vector from the potential of the isolated system, given by the mass-normalized displacements of the ions U, with elements ($U_i = \sqrt{m_i} \cdot (x_i - x_i^0)$), and the dynamical matrix $\mathbf{W}$.

6.1.1 The Langevin equation

Considering a standard transport setup described in Chap. 2, the system is both in contact with the phonon bath of the left/right leads and the bath consisting of electron hole-pair excitations in the electronic system. If the baths can be described by harmonic degrees of freedom, (a set of coupled harmonic-oscillators), then the dynamics of the system can be described by the semi-classical generalized Langevin equation(SGLE)[74, 97, 17, 106], derived in Appendix B:

$$\ddot{U}(t) - F(U(t)) = -\int^t \Pi^r(t-t')U(t')dt' + f(t). \tag{6.2}$$

Here Π^r describes the time-delayed back action of the bath on the system due

to the motion of the system, and $f(t)$ is a random force due to quantum and thermal fluctuations. Thus, Π^r has three contributions,

$$\Pi^r = \Pi^r_L + \Pi^r_R + \Pi^r_e. \tag{6.3}$$

The Π^r_L and Π^r_R are the phonon self-energies, while the Π^r_e describes the coupling to the electrons. In equilibrium Π^r_e was related to the interaction-weighted electron hole-pair density of states, Λ, by Head-Gordon and Tully[44]

6.1.1.1 Non-equilibrium

The Langevin equation can be extended to include the non-equilibrium effects in the electronic system due to the current, as shown by J. T. Lü *et al.*[74]. Including the non-equilibrium effects the contribution from the electron degrees of freedom becomes:

$$\Pi^r_e(t-t') = \theta(t-t')\tilde{\Pi}_e(t-t') \tag{6.4}$$

$$\tilde{\Pi}_e(t-t') = \int \frac{d\omega}{2\pi} e^{-i\omega'(t-t')}\Lambda(\omega), \tag{6.5}$$

where the interaction-weighted electron-hole pair density of states, (including spin), is defined as:

$$\Lambda(\omega) = \sum_{\alpha,\beta} \Lambda^{\alpha\beta}(\omega) \tag{6.6}$$

$$\Lambda^{\alpha\beta}_{kl}(\omega) = 2\int \frac{d\epsilon_1}{2\pi} \int \frac{d\epsilon_2}{2\pi} \delta(\hbar\omega - \epsilon_1 - \epsilon_2)\, \mathrm{Tr}\left[M^k A_\alpha(\epsilon_1) M^l A_\beta(\epsilon_2)\right] \left(n_F(\epsilon_l - \mu_\alpha) - n_F(\epsilon_2 - \mu_\beta)\right) \tag{6.7}$$

where the indices α and β runs over the left and right electrodes and k and l are the phonon indices.

The SGLE, in Eq. (6.2), is given in the time domain, however, since we are considering steady state, it is convenient to work in the frequency domain. Thus, by Fourier transformation we obtain:

$$\Pi_e^r(\omega) = \int d\tau e^{-i\omega'(t-t')}\Pi_e^r(t-t') \tag{6.8}$$

$$=\theta(t-t')\tilde{\Pi}_e(t-t') \tag{6.9}$$

$$= \int_0^\infty \frac{d\omega}{2\pi}\frac{\Lambda(\omega)}{\omega'-\omega-i\eta} \tag{6.10}$$

By applying the Sokhatsky-Weiestrass theorem $\Pi^r(\omega)$ can be split into four contributions giving rise to the four forces mentioned in the beginning of the chapter.

$$\mathbf{\Pi}_e^r(\omega) = \underbrace{i\pi \operatorname{Re}\Lambda(\omega)}_{FR} - \underbrace{\pi \operatorname{Im}\Lambda(\omega)}_{NC} + \underbrace{\pi\mathcal{H}\left[\operatorname{Re}\Lambda(\omega')\right](\omega)}_{RN} + \underbrace{i\pi\mathcal{H}\left[\operatorname{Im}\Lambda(\omega')\right](\omega)}_{BP} \tag{6.11}$$

6.1.1.2 Wide-band approximation

To simplify the equations the wide-band approximation can be applied to Eq. (6.7), reducing the equation of motion to (neglecting the phonon bath):

$$\ddot{U}(t) = -\mathbf{W}U(t) - \eta_0\dot{U}(t) + \mathcal{N}_0U(t) - \zeta_0U(t) - \mathcal{B}_0\dot{U}(t) + f(t), \tag{6.12}$$

with matrices in phonon index describing FR, NC, RN and BP, respectively, given by,

$$\eta_0 = 2\frac{\hbar}{4\pi}\operatorname{Tr}\left[\boldsymbol{M}\boldsymbol{A}(\mu_0)\boldsymbol{M}\boldsymbol{A}(\mu_0)\right] \tag{6.13}$$

$$\mathcal{N}_0 = eV2\frac{\hbar}{2\pi}\operatorname{Im}\operatorname{Tr}\left[\boldsymbol{M}\boldsymbol{A}_L(\mu_0)\boldsymbol{M}\boldsymbol{A}_R(\mu_0)\right] \tag{6.14}$$

$$\zeta_0 = eV2\frac{1}{2\pi}\operatorname{Tr}\left[\boldsymbol{M}\Delta\boldsymbol{A}(\mu_0)\boldsymbol{M}\operatorname{Re}\boldsymbol{G}(\mu_0)\right] \tag{6.15}$$

$$\mathcal{B}_0 = eV2\frac{\hbar}{2\pi}\operatorname{Tr}\left[\boldsymbol{M}\Delta\boldsymbol{A}(\mu_0)\boldsymbol{M}\partial_\varepsilon\operatorname{Re}\boldsymbol{G}(\mu_0)\right] \tag{6.16}$$

where $\Delta\boldsymbol{A} = \boldsymbol{A}_L - \boldsymbol{A}_R$.

The simplest way of solving Eq. (6.12) is by Fourier transformation:

$$-\omega^2U(\omega) = -\mathbf{W}U(\omega) - \eta_0 i\omega U(\omega) + \mathcal{N}_0U(\omega) - \zeta_0U(\omega) - \mathcal{B}_0 i\omega U(\omega) + f(\omega). \tag{6.17}$$

In order for Eq. (6.17) to give an accurate description the electronic properties needs to be constant, not only on the scale of the phonon energy, but throughout the entire bias window. Alternatively, when calculating Λ in Eq. (6.7), one can relax the WBA and only demand a constant self-energy, Σ, and expand the spectral function in Lorentzians[72, 38]. This procedure retain some of the energy dependence in $\Pi_e^r(\omega)$, however it does not provide the eigenmodes , since the problem now is nonlinear.

6.2 ZGNR

We start by considering the clean zigzag nanoribbon also discussed in Chap. 5, where the electronic properties are shown in Fig. 5.4. The phononic transmission and band-structure are shown in Fig. 6.1 Ideally, translation in the three spatial directions and rotation around the longitudinal direction of the GNR should lead to zero energy modes at the gamma point. Thus, one should expect four bands starting at $\hbar\omega = 0.0$ eV at the gamma point leading to four open transmission channels. However, as seen from Fig. 6.1, this is not the case, indicating the limitations of the calculations and the difficulty in describing the long range elastic forces. The low energy/long wave length modes are important for heat transport, but, in this chapter we will consider high energy modes, where the calculation is expected to be accurate.

6.2.0.3 Run-away modes

In order to analyze the influence of the current we define the nonequilibrium phonon density of states as:

$$DOS(\omega) = -\frac{2}{\pi\omega}\,\mathrm{Im}\,\mathrm{Tr}\left[\boldsymbol{D}^r(\omega)\right], \tag{6.18}$$

where $\boldsymbol{D}^r(\omega)$ is the nonequilibrium phonon Greens function obtained from the SCLE:

$$\boldsymbol{D}^r(\omega) = \frac{1}{(\omega + i\eta)^2 - \mathbf{W} - \boldsymbol{\Pi}^r(\omega)}. \tag{6.19}$$

Contrary to equilibrium, the DOS given in Eq. (6.18) can take negative values. A negative DOS is interpreted as modes with a negative lifetime, *i. e.* growing in population as a function of time.

Applying the WBA, evaluating the spectral function at $E_F = 0.6$ eV gives the DOS shown in Fig. 6.2. The DOS is calculated for a bias voltage of $V_b = 0.0$

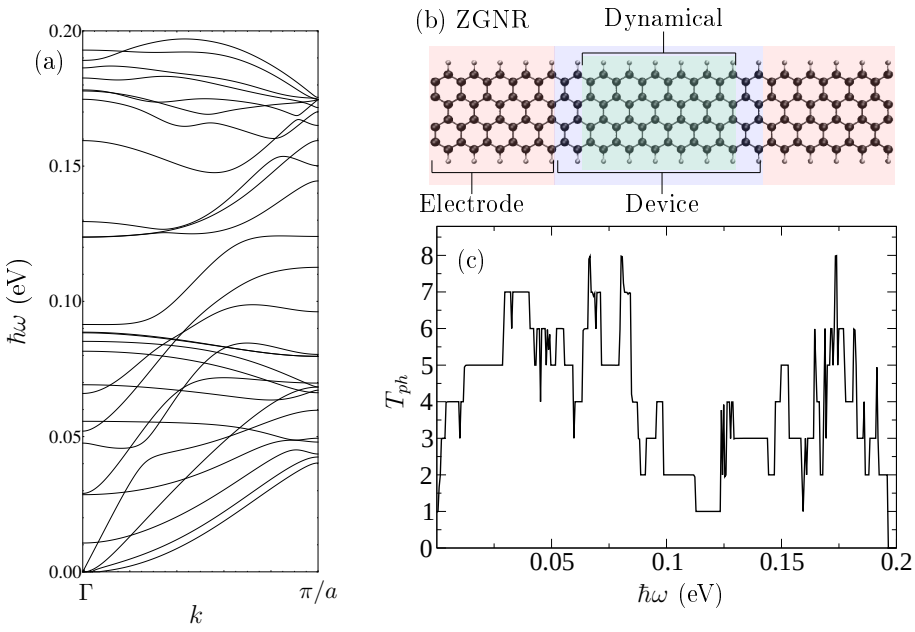

Figure 6.1: (a) The Phononic band-structure for the structure in (b). (b) Structure of the transport setup. (c) The phononic transmission for the structure in (b)

V,$V_b = 0.5$ V and $V_b = 0.85$ V, showing how the current induced forces can give rise to negative values in the DOS. Already for a bias of $V_b = 0.5$ V we see two small dips below zero. Increasing the bias to $V_b = 0.85$ gives two other dips below zero.

6.2.0.4 Mode analysis

To identify the modes which can show run-away behavior, we need to find the solutions to Eq. (6.17), where we have set the noise force, $f(\omega)$, to zero. This is done by treating the velocity and displacement as independent variables and use the relation $-i\omega U(\omega) = \dot{U}(\omega)$ to obtain the double eigenvalue problem:

$$\begin{bmatrix} 0 & -I \\ \mathbf{W} + \zeta_0 + R_{ph} + \mathcal{N}_0 & \eta_{ph} + \eta_0 - \mathcal{B}_0 \end{bmatrix} \begin{bmatrix} U(\omega) \\ \dot{U}(\omega) \end{bmatrix} = i\omega \begin{bmatrix} U(\omega) \\ \dot{U}(\omega) \end{bmatrix}. \tag{6.20}$$

Here, R_{ph} and η_{ph}, is the renormalization of the dynamical matrix and friction,

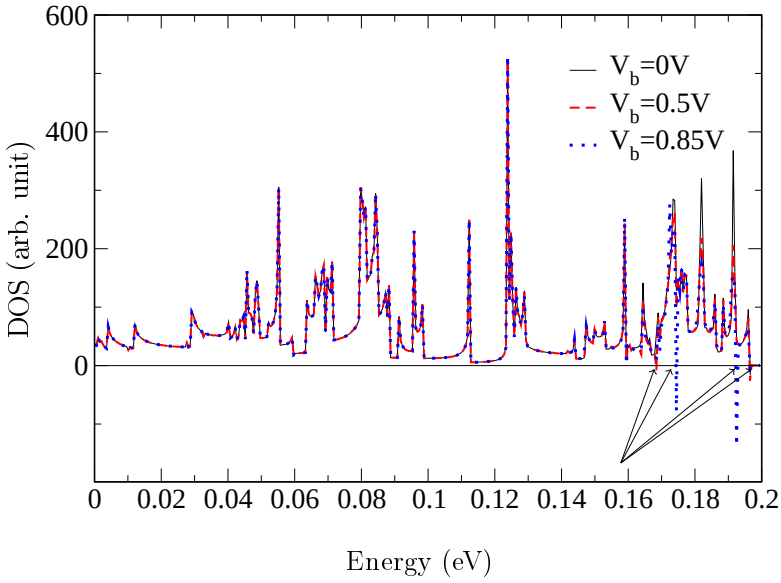

Figure 6.2: The total density of states for the phonons including current for the structure in Fig. 6.1 (b). The current induced forces are included in the WBA evaluating the electronic properties at $e_F = 0.6$ eV. The arrows indicate the dips below zero.

respectively, due to the phonon bath. However, even if the electronic degrees of freedom are treated in the wide band approximation, the phonon bath self-energy is not. Thus, to solve Eq. (6.20), the most natural approach is to evaluate $\mathbf{\Pi}^r_{ph}(\omega)$ at the frequency of the dip.

Solving Eq. (6.20) gives the eigenmodes and complex eigenfrequencies. For a given eigenmode a corresponding positive imaginary part of the eigenfrequency means that the mode is a run-away mode, while if the imaginary part is negative the modes is damped. The damping can be quantized by the inverse Q-factor giving the change in energy per unit time $\frac{1}{Q} = \left(2\pi \frac{\Delta E}{E_{tot}}\right)^{-1} = -\frac{2\,\mathrm{Re}\,\omega_i}{\mathrm{Im}\,\omega_i}$.

Thus, the run-away modes can be identified as the modes where $\mathrm{Im}\,\omega > 0$. However solving Eq. (6.20) evaluating the phonon bath self-energy at the dip position in Fig. 6.2 give rise to a range of run-away modes with frequencies which differ from the one obtained from the DOS. Therefore, Fig. 6.3 (a) shows run-away frequencies as a function of the energy where $\mathbf{\Pi}^r_e$ is evaluated. The blue oblige line indicate the self consistent solutions. The run-away modes are a linear combination of the non-perturbed modes. the unperturbed modes which contributes to the run-away modes can be seen from Fig. 6.3 (b). The modes indexed as 48 and 49 are seen to contribute. The two modes are shown in Fig. 6.4 together with the linear combination illustrating the runaway. We can see how some of the atoms in the runaway mode depicted in Fig. 6.4 (c) makes closed lopes. Thus, the NC force allows the mode to pick up energy every time a loop is completed, eventualy leading to break down of the harmonic approximation, ending with e.g. rupture or damping by anharmonic effects.

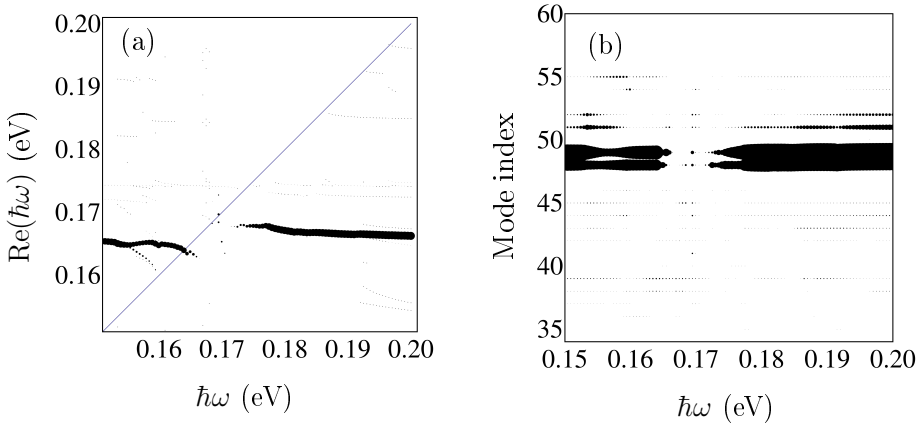

Figure 6.3: (a)The frequency of the runaway modes as a function of the frequency where the phonon selfenergy is evaluated. The point size is proportional to the imaginary part of the mode frequency. (b) The Y-axis is the unperturbed mode coordinate (j) of the runaway modes. and the X-axis is the frequency where the phonon selfenergy is evaluated. The point size is proportional $|Q|$ defined in the text.

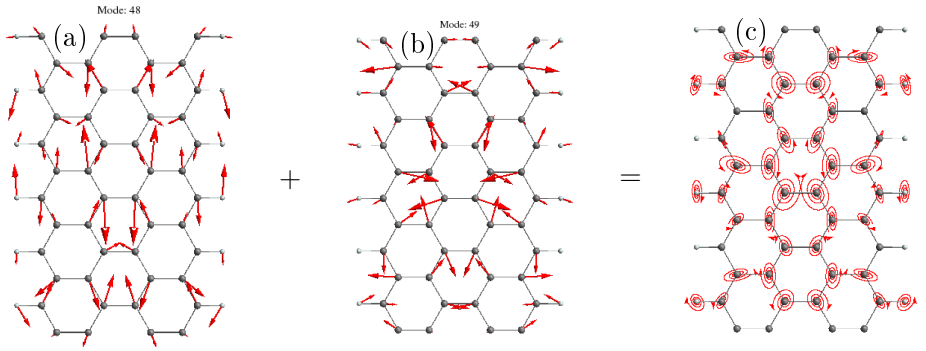

Figure 6.4: (a-b) Unperturbed modes contributing to one of the run-away modes. (c) Combination of the modes in (a) and (b) illustrating how the individual atoms a run-away mode can preform closed loops.

6.3 Asymmetric heating

In the above we have focused on the deterministic forces and ignored the random force (noise) due to the thermal, or current-induced fluctuation of the bath variables. Now we will focus on the heating due to the current and examine the combined effect of the deterministic and random forces.

The second quantum term $f(t)$, in Eq. (6.2), is characterized by the correlation matrix $\langle f_\alpha(t) f_\alpha^T(t')\rangle = S_\alpha(t-t')$. We will assume the two phonon baths to be in thermal equilibrium. Thus, their noise correlation S_{ph} is related to the phonon self energy Π_{ph}^r through the fluctuation-dissipation theorem, $S_{ph}(\omega) = \hbar\,(n_B(\omega,T)+\frac{1}{2})\Gamma_{ph}(\omega)$ with $\Gamma_{ph}(\omega) = -2\mathrm{Im}\Pi_{ph}^r(\omega)$, and n_B is the Bose distribution function. However, due to the electrical current, the electronic bath is not in equilibrium. The noise correlation term of the electron bath can now be written as[76],

$$S_e(\omega) = -2\pi \sum_{\alpha\beta} n_B(\omega - (\mu_\alpha - \mu_\beta))\Lambda^{\alpha\beta}(\omega). \tag{6.21}$$

In the absence of electrical current, the electrons serve as an equilibrium thermal bath, similar to phonons. However, in the presence of current, the term ($\sim \mathrm{Im}\Lambda_{kl}^{RL}, k \neq l$) becomes important. It may coherently couple two vibrational modes (kl) inside the system leading to non-zero NC and BP forces. Generally, NC and BP forces will depend on the direction of electronic current. Furthermore, the coherent coupling breaks time-reversal symmetry of the noise correlation function, $S_e(t-t') \neq S_e(t'-t)$. Hereafter, we denote these forces by *asymmetric CIF*, and focus on their role for the excess heat distribution.

We will consider the case where all baths are at the same temperature (T), and the electron bath is subject to a nonzero voltage bias ($eV = \mu_L - \mu_R$). To look at the excess heating, we calculate the kinetic energy of atom n from its local displacement correlation function, and obtain

$$E_n = \langle \dot{U}\dot{U}^*\rangle = \sum_{\sigma=x,y,z}\int_0^{+\infty} d\omega\,\omega^2\langle U_{n,\sigma}U_{n,\sigma}\rangle = \sum_{\sigma=x,y,z}\int_0^{+\infty}\frac{d\omega}{2\pi}\omega^2\mathrm{diag}\{D^r S D^a\}_{n,\sigma}(\omega). \tag{6.22}$$

Here D^r (D^a) is the eV-dependent phonon retarded (advanced) Greens functions, S is the sum of noise correlation function from all the baths, and $\mathrm{diag}\{A\}_{n,\sigma}$ means the diagonal matrix element of A, corresponding to the n-th atom's σ degrees of freedom e.g. (x,y,z).

In the next section we will illustrate the role of the current-induced forces for the heating and its spatial variation/symmetry.

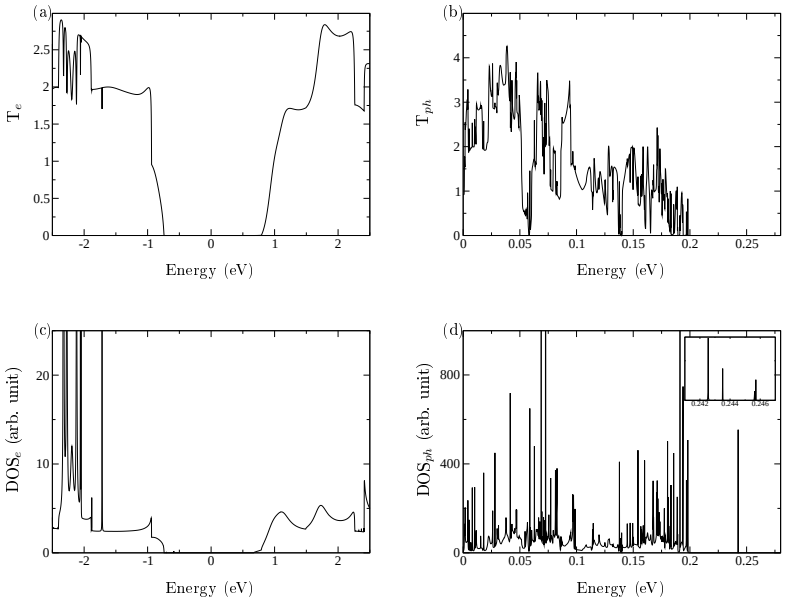

Figure 6.5: (a) Electronic transmission. (b) Phononic transmission. (c) Electronic density of states projected to the device region. (d) Phononic density of states projected to the device region (Insert: Zoom on the dimer-vibrations). In the SIESTA/TRANSIESTA DFT-calculation the following settings was used. Exchange-correlation functional: GGA-PBE. Basis-set: Single-zeta polarized. Real space mesh cutoff: 400 Rydberg. The structure was relaxed until the forces on the atoms in the device region was below 0.01 eV/Ang

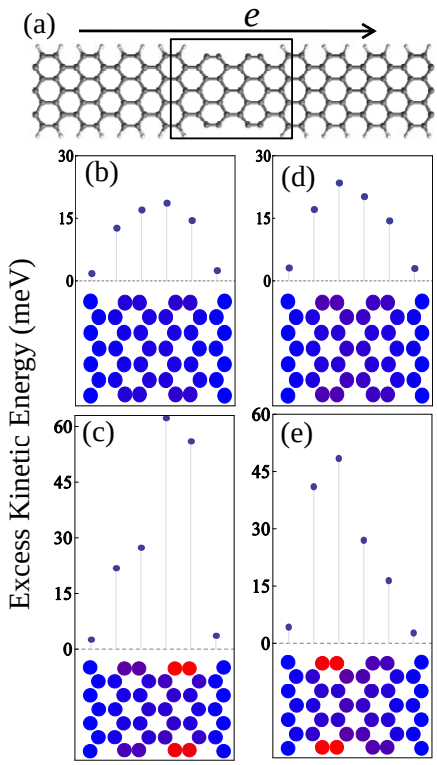

Figure 6.6: (a) Structure of a partially passivated armchair graphene ribbon considered. The two sides of the ribbon is hydrogen passivated except in the device region, enclosed by the solid lines. (b)-(c) The excess kinetic energy of each atom without and with the asymmetric CIF, at $V = 0.4$ V, $T = 300$ K, $E_F = 1.4$ eV. The dots show the average over atoms belonging to each zigzag column. (d)-(e) Same with (b)-(c) with $E_F = -1.0$ eV.

6.3.1 Partially passivated AGNR

In the last chapter we learned how an armchair graphene nanoribbon (AGNR) with partial hydrogen passivation(8H-free), gave rise to IETS signals due to the dehydrogenated carbon dimers at the edge, (see Fig. 5.12 (e) and (l)), suggesting that the localized high-frequency edge vibrations interact strongly with electrical current. Further, the (8H-free) system is also relevant for experiments showing current-induced edge-reconstructions in graphene[50] where the physical mechanism was attributed to Joule heating[26]. The unperturbed electronic and phononic properties are collected in Fig. 6.5. The phononic DOS in Fig. 6.5 (d) experience four peaks outside the bulk AGNR spectrum, due to vibrations of the four pairs of dehydrogenated carbon dimers in Fig. 6.6 (a). The vibrations are localized and are therefore not present in the phononic transmission shown in Fig. 6.5 (d). Consequently, the excess energy is mainly stored in the dimers and nearby atoms Fig. 6.6 (b),(d). Including the asymmetric CIF leads to symmetry breaking of the heating profile along the current direction.

To investigate the difference between electron and hole dominated transport we calculate the excess heating for the Fermi-energy tuned into the conduction band at $E_F = 1.4$ eV in Fig. 6.6 (b),(c), and into the valance band at $E_F = -1.0$ eV in Fig. 6.6 (d),(e). From comparing Fig. 6.6 (b-c) to Fig. 6.6 (c-e) we see how including the asymmetric CIF leads to symmetry breaking of the heating profile along the current direction with heat accumulation at hot-spots. Going from conduction to valence band results in the motion of the hot-spot from "down-stream" to "up-stream" w.r.t. the electron current when tuning from $E_F = 1.4$ eV to $E_F = -1.0$ eV cf. Fig. 6.6 (c),(e). Thus, the hot-spot moves from one side to the other because, when E_F crosses the electron-hole symmetric point, and the dominant current-carriers contributing to inelastic transport change from electrons to holes, or vice versa. Interestingly, similar effect at the micrometer scale has been observed experimentally in graphene transistors[31, 5] and electrodes of molecular junctions[66]. Here we show that it is equally important at atomic scale, and related to the asymmetric CIF.

6.4 Summary and Discussion

In this chapter we have introduced the forces due to the current on the atoms. We have seen how the deterministic part can give rise to run-away modes, and how, when calculating the excess heat, the current breaks the symmetry of the heating profile via the CIF. The main obstacle in calculating the current-induced forces for the graphene nanoribbons is the energy dependence of the interaction-

weighted electron-hole pair density of states, Λ, given in Eq. (6.7). The function Λ can be calculated efficiently in the WBA, however, the results differ from what is obtained by the constant self energy approximation (not shown). However, calculating single matrix element of Λ without resorting to any approximations disagree with both the WBA and the constant Γ calculation. The reason for the discrepancy between the different levels of approximation is probably the sharp bond onset both in the electrodes and the device. Thus, one way of getting the same result for the full calculation and constant self-energy is to include an η in the electrode recursion as done in the previous chapter. Alternatively a full calculation has to be preformed. However, calculating Λ without resorting to any approximations is a numerical heavy task, and if not done carefully enough the numerically error will exceed the error of assuming a constant Γ.

Chapter 7

Summary and Outlook

Current in nanostructures give rise to different excitations which can be used to gain insigt into the electronic structure and transport.

In this thesis we have shown how measuring the **noise** can give information about the quantum nature of the device and how the high frequency noise can be correlated to **light-emission**. A first principle method was presented for calculating the light-emission and was utilized to calculate the light-emission from two STM experiments: An adatom on a Ag(111) surface and a C_{60} on a Cu(111) surface. The calculated photon yield was found to agree with experiments for photons with energies below the applied bias ($\hbar\omega < eV$). However, in the experiments[110, 112] above-threshold phonon emission, ($\hbar\omega > eV$), was also observed. The mechanism behind emission of phonons with energy exceeding the applied bias is still debated[134, 46, 124, 108, 56]. It can be attributed to hot electrons due to direct electron-electron interaction[108, 112], or alternative due to higher-order electron-plasmon scattering[56, 134]. Plasmons are not well understood in the atomic limit. Thus, in the work presented in this thesis the coupling to the plasmon was treated in the simplest possible way. A better understating of of the electron-plasmon coupling, would be required if the observed light-emission should be utilized in device application.

Inelastic electron tunneling spectroscopy(**IETS**) serves as a powerful tool for non-destructive characterization. A new fast method for calculating the **en-**

ergy dependent IETS signal was presented, and applied to a one-level model revealing how a symmetric system can give rise to peak-dip features in the IETS. The new method was used to explain the IETS signal obtained for a BDT molecule in a symmetric gold junction[118] as a function of gate voltage.

Gating molecules in 3D metal junctions is difficult due to screening effects. On the other hand, graphene devices are routinely gated. Thus, we have studied the IETS signal from gated **graphene nanoribbons** (GNR). We have studied pristine GNRs with both zigzag and armchair chirality, and related the IETS signal to the phononic band structure. For the spin-polarized zigzag GNRs the role of the spin-polarization was investigated, and IETS was suggested as an indirect measurement of spin-polarization. Further, the role of impurities was explored, revealing the possibility of detecting defects in the hydrogen passivisation by IETS.

The effect of the length of dynamical region was studied and found to converge quickly. However, the role of the width is still to be investigated, if the results are to be generalized to other graphene nano-structures. On the theoretically side, the effect of sharp band-onsets was neglected, including this effect might be important for some systems. Another extension is to relax the lowest order approximation taking into account the higher-order diagrams. For graphene materials, this will allow the out of plane modes to contribute.

Lastly a preliminary study of the **heating** due to the electrical current was described, investigating the effect of the **deterministic current-induced forces**, treated within the framework of the semi-classical generalized Langevin equation(SGLE). For a pristine zigzag ribbon the non-conservative and Berry forces was seen to give rise to runaway modes. For an armchair ribbon with partly dehydrogenated edges the non-conservative and Berry forces was seen to break the symmetry and increase the excess heating.

Appendix A

IETS

In this appendix we derive the IETS signal using the lowest order expansion.

A.1 General equations

The system is divided into three parts, the left(L) and right(R) leads and the device(D) region. The current is given by the Meir-Wingreen expression; thus, in the left lead the current is given by:

$$I_L = 2\int dE\ \frac{1}{2\pi} Tr\left[\mathbf{\Sigma}_L^{<}(E)\mathbf{G}^{>}(E) - \mathbf{\Sigma}_L^{>}(E)\mathbf{G}^{<}(E)\right]. \tag{A.1}$$

Atomic units are used in the above expression and in the rest of the appendix, so $e = 1$ and $\hbar = 1$.
The Electrode self-energies are:

$$\mathbf{\Sigma}_\alpha^{<}(E) = i n_F^\alpha \mathbf{\Gamma}_\alpha(E), \tag{A.2}$$
$$\mathbf{\Sigma}_\alpha^{>}(E) = -i(1 - n_F^\alpha)\mathbf{\Gamma}_\alpha(E), \tag{A.3}$$

where $\mathbf{\Gamma}_\alpha(E) = i(\mathbf{\Sigma}^r_\alpha(E) - \mathbf{\Sigma}^{r\dagger}_\alpha(E))$
The unperturbed electronic Green's functions are given by:

$$\mathbf{G}^<_0(E) = \mathbf{G}_0(E)[\mathbf{\Sigma}^<_L(E) + \mathbf{\Sigma}^<_R(E)]\mathbf{G}^\dagger_0(E), \tag{A.4}$$
$$= i(n^L_F\mathbf{A}_L(E) + n^R_F\mathbf{A}_R(E)) \tag{A.5}$$
$$\mathbf{G}^>_0(E) = \mathbf{G}_0(E)[\mathbf{\Sigma}^>_L(E) + \mathbf{\Sigma}^>_R(E)]\mathbf{G}^\dagger_0(E), \tag{A.6}$$
$$= -i((1-n^L_F)\mathbf{A}_L(E) + (1-n^R_F)\mathbf{A}_R(E)), \tag{A.7}$$

where we have defined the spectral function as: $\mathbf{A}_\alpha(E) = \mathbf{G}_0(E)\mathbf{\Gamma}_\alpha(E)\mathbf{G}^\dagger_0(E)$, and the time reversed spectral function as $\tilde{\mathbf{A}}_\alpha = \mathbf{G}^\dagger_0\mathbf{\Gamma}_\alpha\mathbf{G}_0$ The unperturbed phonon Green's functions are given by:

$$\mathbf{D}^<_0(\omega) = -2\pi i[n_b(\Omega)\delta(\omega-\Omega) + (1+n_b(\Omega))\delta(\omega+\Omega)], \tag{A.8}$$
$$\mathbf{D}^>_0(\omega) = -2\pi i[n_b(\Omega)\delta(\omega+\Omega) + (1+n_b(\Omega))\delta(\omega-\Omega)]. \tag{A.9}$$

The relation between the full Green's functions and the unperturbed is given by Dyson and Keldysh equations:

$$\mathbf{G}(E) = \mathbf{G}_0(E) + \mathbf{G}_0(E)\mathbf{\Sigma}^r_{\rm ph}(E)\mathbf{G}(E), \tag{A.10}$$
$$\mathbf{G}^<(E) = \mathbf{G}(E)[\mathbf{\Sigma}^<_L(E) + \mathbf{\Sigma}^<_R(E) + \mathbf{\Sigma}^<_{\rm ph}(E)]\mathbf{G}^\dagger(E), \tag{A.11}$$
$$\mathbf{G}^>(E) = \mathbf{G}(E)[\mathbf{\Sigma}^>_L(E) + \mathbf{\Sigma}^>_R(E) + \mathbf{\Sigma}^>_{\rm ph}(E)]\mathbf{G}^\dagger(E). \tag{A.12}$$
$$\tag{A.13}$$

The phonon contribution to the self-energies of the electrons are:

$$\mathbf{\Sigma}^<_{\rm ph}(E) = i\int\frac{d\omega}{2\pi}\mathbf{M}\mathbf{D}^<_0(\omega)\mathbf{G}^<_0(E-\omega)\mathbf{M} \tag{A.14}$$
$$= \mathbf{M}\left[(1+n_b(\Omega))\mathbf{G}^<_0(E+\Omega) + n_b(\Omega)\mathbf{G}^<_0(E-\Omega)\right]\mathbf{M}, \tag{A.15}$$
$$\mathbf{\Sigma}^>_{\rm ph}(E) = i\int\frac{d\omega}{2\pi}\mathbf{M}\mathbf{D}^>_0(\omega)\mathbf{G}^>_0(E-\omega)\mathbf{M} \tag{A.16}$$
$$= \mathbf{M}\left[(1+n_b(\Omega))\mathbf{G}^>_0(E-\Omega) + n_b(\Omega)\mathbf{G}^>_0(E+\Omega)\right]\mathbf{M}, \tag{A.17}$$
$$\mathbf{\Sigma}^r_{\rm ph}(E) = \frac{1}{2}\left(\mathbf{\Sigma}^>_{\rm ph}(E) - \mathbf{\Sigma}^<_{\rm ph}(E)\right) - \frac{i}{2}H\left\{\mathbf{\Sigma}^>_{\rm ph}(E) - \mathbf{\Sigma}^<_{\rm ph}(E)\right\}. \tag{A.18}$$

In the rest of the note the explicit energy dependence is omitted, however, to keep track of shifts by a phonon frequency $\pm\Omega$, the following notation convention is used:

$$\mathbf{G}_0 \equiv \mathbf{G}_0(E) \tag{A.19}$$
$$\mathbf{G}^\pm_0 \equiv \mathbf{G}_0(E\pm\Omega) \tag{A.20}$$

for $\mathbf{G}_0$ and similar for the other energy-dependent quantities.

A.2 Expansion of current expression

The current is treated to second order in the e-ph coupling matrix $\mathbf{M}$, leading to the following expression for the current:

$$I_L \approx I_L^{(0)} + I_L^{(1)} + I_L^{(2)} + I_L^{(3)} \tag{A.21}$$

$$I_L^{(0)} = \int dE\, Tr\left[\mathbf{\Sigma}_L^{<}\mathbf{G}_0^{>} - \mathbf{\Sigma}_L^{>}\mathbf{G}_0^{<}\right] \tag{A.22}$$

$$I_L^{(1)} = \int dE\, Tr\left[\mathbf{\Sigma}_L^{<}\mathbf{G}_0\mathbf{\Sigma}_{\mathrm{ph}}^{r}\mathbf{G}_0^{>} - \mathbf{\Sigma}_L^{>}\mathbf{G}_0\mathbf{\Sigma}_{\mathrm{ph}}^{r}\mathbf{G}_0^{<}\right] \tag{A.23}$$

$$I_L^{(2)} = \int dE\, Tr\left[\mathbf{\Sigma}_L^{<}\mathbf{G}_0^{>}\mathbf{\Sigma}_{\mathrm{ph}}^{\dagger}\mathbf{G}_0^{\dagger} - \mathbf{\Sigma}_L^{>}\mathbf{G}_0^{<}\mathbf{\Sigma}_{\mathrm{ph}}^{\dagger}\mathbf{G}_0^{\dagger}\right] \tag{A.24}$$

$$I_L^{(3)} = \int dE\, Tr\left[\mathbf{\Sigma}_L^{<}\mathbf{G}_0\mathbf{\Sigma}_{\mathrm{ph}}^{>}\mathbf{G}_0^{\dagger} - \mathbf{\Sigma}_L^{>}\mathbf{G}_0\mathbf{\Sigma}_{\mathrm{ph}}^{<}\mathbf{G}_0^{\dagger}\right] \tag{A.25}$$

$I_L^{(0)}$ is the unperturbed current and carry no signal of the phonons. Therefore, to get an expression for the IETS signal we develop the rest of the expressions further. First we take a closer look at $I_L^{(3)}$:

A.2.1 $I^{(3)}$

For $I_L^{(3)}$ we have:

$$I_L^{(3)} = \int dE\ \boldsymbol{\Sigma}_L^{<}\mathbf{G}_0\boldsymbol{\Sigma}_{\mathrm{ph}}^{>}\mathbf{G}_0^{\dagger} - \boldsymbol{\Sigma}_L^{>}\mathbf{G}_0\boldsymbol{\Sigma}_{\mathrm{ph}}^{<}\mathbf{G}_0^{\dagger} \tag{A.26}$$

$$= \int dE\ \boldsymbol{\Sigma}_L^{<}\mathbf{G}_0\mathbf{M}\left((1+n_b)\mathbf{G}_0^{>,-} + n_b\mathbf{G}_0^{>,+}\right)\mathbf{M}\mathbf{G}_0^{\dagger} - \boldsymbol{\Sigma}_L^{>}\mathbf{G}_0\mathbf{M}\left((1+n_b)\mathbf{G}_0^{<,+} + n_b\mathbf{G}_0^{<,-}\right)\mathbf{M}\mathbf{G}_0^{\dagger} \tag{A.27}$$

$$= \int dE\ \tilde{\mathbf{A}}_L\mathbf{M}\Big[\left(n_F^L(1-n_L^{L,-}+n_b) - n_b n_F^{L,-}\right)\mathbf{A}_L^{-} + \left(n_F^L(1-n_F^{R,-}+n_b) - n_b n_F^{R,-}\right)\mathbf{A}_R^{-}\Big]\mathbf{M} - \tilde{\mathbf{A}}_L\mathbf{M}\Big[\left(n_L^{L,+}(1-n_F^{L}+n_b) - n_b n_F^{L}\right)\mathbf{A}_L^{+} + \left(n_F^{R,+}(1-n_F^{L}+n_b) - n_b n_F^{L}\right)\mathbf{A}_R^{+}\Big]\mathbf{M} \tag{A.28}$$

$$= \int dE\ \tilde{\mathbf{A}}_L\mathbf{M}\Big[\left(n_F^L(1-n_F^{R,-}+n_b) - n_b n_F^{R,-}\right)\mathbf{A}_R^{-} - \left(n_F^{R,+}(1-n_F^{L}+n_b) - n_b n_F^{L}\right)\mathbf{A}_R^{+}\Big]\mathbf{M}. \tag{A.29}$$

$$= \int dE\ \Big[\left(\coth(\frac{\Omega}{2k_bT}) - \coth(\frac{\Omega-eV}{2k_bT})\right)(n_F^L - n_F^{R,-})\tilde{\mathbf{A}}_L\mathbf{M}\mathbf{A}_R^{-}\mathbf{M} + \left(\coth(\frac{\Omega}{2k_bT}) - \coth(\frac{\Omega+eV}{2k_bT})\right)(n_F^L - n_F^{R,+})\tilde{\mathbf{A}}_L\mathbf{M}\mathbf{A}_R^{+}\mathbf{M}.\Big] \tag{A.30}$$

$$= \sum_{\sigma=\pm}\left(\coth(\frac{\Omega}{2k_bT}) - \coth(\frac{\Omega+\sigma eV}{2k_bT})\right)\int dE\ (n_F^L - n_F^{R,\sigma})\tilde{\mathbf{A}}_L\mathbf{M}\mathbf{A}_R^{\sigma}\mathbf{M} \tag{A.31}$$

Where we in the fifth line have used the the fact we are integrating from $-\infty$ to ∞, and therefore are allowed to shift the integrated variable with a constant.Assuming $T = 0$, then $n_b = 0$, $n_f^{\alpha} = \Theta(\mu_\alpha - E)$, $1 - n_f^{\alpha} = \Theta(E - \mu_\alpha)$ and $\frac{d}{dV}\Theta(\mu_\alpha - E) = \delta(\mu_\alpha - E)$. Thus, for $\mu_L = -\mu_R = 1/2V$ Eq. (A.29) becomes:

$$I_L^{(3)} = \int dE \ \left[\left(n_F^L(1-n_F^{R,-})\right)\tilde{\mathbf{A}}_L\mathbf{M}\mathbf{A}_R^-\mathbf{M} - \left(n_F^{R,+}(1-n_F^L)\right)\tilde{\mathbf{A}}_L\mathbf{M}\mathbf{A}_R^+\mathbf{M}\right]. \tag{A.32}$$

$$\begin{aligned}\frac{d}{dV}I_L^{(3)} = \int dE \ \Big[&\frac{1}{2}\Theta(V-\Omega)\left(\delta(V/2-E)+\delta(E+V/2-\Omega)\right)\tilde{\mathbf{A}}_L\mathbf{M}\mathbf{A}_R^-\mathbf{M} \\ &+\frac{1}{2}\Theta(-V-\Omega)\left(\delta(-V/2-E-\Omega)+\delta(E-V/2)\right)\tilde{\mathbf{A}}_L\mathbf{M}\mathbf{A}_R^+\mathbf{M}\Big].\end{aligned} \tag{A.33}$$

For $V > 0$:

$$\begin{aligned}\frac{d}{dV}I_L^{(3)} = \frac{1}{2}\Theta(V-\Omega)\Big(&\tilde{\mathbf{A}}_L(V/2)\mathbf{M}\mathbf{A}_R(V/2-\Omega)\mathbf{M} \\ &+\tilde{\mathbf{A}}_L(\Omega-V/2)\mathbf{M}\mathbf{A}_R(-V/2)\mathbf{M}\Big)\end{aligned} \tag{A.34}$$

$$\frac{d^2}{dV^2}I_L^{(3)} = \delta(V-\Omega)\tilde{\mathbf{A}}_L(\Omega/2)\mathbf{M}\mathbf{A}_R(-\Omega/2)\mathbf{M} \tag{A.35}$$

Reinstating the energy-dependence of the Fermi-functions:

$$\begin{aligned}\frac{d}{dV}I_L^{(3)} = \frac{d}{dV}(\mathcal{I}^{\mathrm{sym}})\frac{1}{2}\Big(&\tilde{\mathbf{A}}_L(V/2)\mathbf{M}\mathbf{A}_R(V/2-\Omega)\mathbf{M} \\ &+\tilde{\mathbf{A}}_L(\Omega-V/2)\mathcal{I}^{\mathrm{sym}}\mathbf{M}\mathbf{A}_R(-V/2)\mathbf{M}\Big)\end{aligned} \tag{A.36}$$

$$\frac{d^2}{dV^2}I_L^{(3)} = \frac{d^2}{dV^2}\mathcal{I}^{\mathrm{sym}}\tilde{\mathbf{A}}_L(\Omega/2)\mathbf{M}\mathbf{A}_R(-\Omega/2)\mathbf{M} \tag{A.37}$$

where

$$\mathcal{I}^{\mathrm{sym}}(V,\Omega) \equiv \sum_{\sigma=\pm}\sigma(\Omega+\sigma V)\left(\coth\frac{\Omega}{2T} - \coth\frac{\Omega+\sigma V}{2T}\right).$$

A.2.2 $I_L^{(1)}$ and $I_L^{(2)}$

$I_L^{(1)}$ reads

$$I_L^{(1)} = \int dE\ \mathbf{\Sigma}_L^{<}\mathbf{G}_0\mathbf{\Sigma}_{\rm ph}^{r}\mathbf{G}_0^{>} - \mathbf{\Sigma}_L^{>}\mathbf{G}_0\mathbf{\Sigma}_{\rm ph}^{r}\mathbf{G}_0^{<} \tag{A.38}$$

$$= \int dE\ n_F^L\mathbf{\Gamma}_L\mathbf{G}_0\mathbf{\Sigma}_{\rm ph}^{r}\mathbf{G}_0[(1-n_F^L)\mathbf{\Gamma}_L + (1-n_F^R)\mathbf{\Gamma}_R]\mathbf{G}_0^{\dagger}$$
$$- (1-n_F^L)\mathbf{\Gamma}_L\mathbf{G}_0\mathbf{\Sigma}_{\rm ph}^{r}\mathbf{G}_0[n_F^L\mathbf{\Gamma}_L + n_F^R\mathbf{\Gamma}_R]\mathbf{G}_0^{\dagger} \tag{A.39}$$

$$= \int dE\ n_F^L(1-n_F^R)\mathbf{\Gamma}_L\mathbf{G}_0\mathbf{\Sigma}_{\rm ph}^{r}\mathbf{G}_0\mathbf{\Gamma}_R\mathbf{G}_0^{\dagger}$$
$$- (1-n_F^L)n_F^R\mathbf{\Gamma}_L\mathbf{G}_0\mathbf{\Sigma}_{\rm ph}^{r}\mathbf{G}_0\mathbf{\Gamma}_R\mathbf{G}_0^{\dagger} \tag{A.40}$$

and similar for $I_L^{(2)}$

$$I_L^{(2)} = \int dE\ \mathbf{\Sigma}_L^{<}\mathbf{G}_0^{>}\mathbf{\Sigma}_{\rm ph}^{\dagger}\mathbf{G}_0^{\dagger} - \mathbf{\Sigma}_L^{>}\mathbf{G}_0^{<}\mathbf{\Sigma}_{\rm ph}^{\dagger}\mathbf{G}_0^{\dagger} \tag{A.41}$$

$$= \int dE\ n_F^L\mathbf{\Gamma}_L\mathbf{G}_0[(1-n_F^L)\mathbf{\Gamma}_L + (1-n_F^R)\mathbf{\Gamma}_R]\mathbf{G}_0^{\dagger}\mathbf{\Sigma}_{\rm ph}^{\dagger}\mathbf{G}_0^{\dagger}$$
$$- (1-n_F^L)\mathbf{\Gamma}_L\mathbf{G}_0[n_F^L\mathbf{\Gamma}_L + n_F^R\mathbf{\Gamma}_R]\mathbf{G}_0^{\dagger}\mathbf{\Sigma}_{\rm ph}^{\dagger}\mathbf{G}_0^{\dagger} \tag{A.42}$$

$$= \int dE\ n_F^L(1-n_F^R)\mathbf{\Gamma}_L\mathbf{G}_0\mathbf{\Gamma}_R\mathbf{G}_0^{\dagger}\mathbf{\Sigma}_{\rm ph}^{\dagger}\mathbf{G}_0^{\dagger}$$
$$- (1-n_F^L)n_F^R\mathbf{\Gamma}_L\mathbf{G}_0\mathbf{\Gamma}_R\mathbf{G}_0^{\dagger}\mathbf{\Sigma}_{\rm ph}^{\dagger}\mathbf{G}_0^{\dagger} \tag{A.43}$$

The sum of $I_L^{(1)}$ and $I_L^{(2)}$ gives:

$$I_L^{(1+2)} = \int dE\ \tilde{\mathbf{A}}_L\Big[n_F^L(1-n_F^R)\left(\mathbf{\Sigma}_{\rm ph}^{r}\mathbf{G}_0\mathbf{\Gamma}_R + h.c.\right)$$
$$- (1-n_F^L)n_F^R\left(\mathbf{\Sigma}_{\rm ph}^{r}\mathbf{G}_0\mathbf{\Gamma}_R + h.c.\right)\Big] \tag{A.44}$$

$$= \int dE\ (n_f^L - n_f^R)\tilde{\mathbf{A}}_L\left(\mathbf{\Sigma}_{\rm ph}^{r}\mathbf{G}_0\mathbf{\Gamma}_R + h.c.\right) \tag{A.45}$$

A.2.2.1 phonon self-energy

The effect of the phonons enter eq. A.45 through the retarded phonon self-energy . Thus, to investigate $\mathbf{\Sigma}_{\rm ph}^{r}$ further it is convenient to define the quantity

$\mathbf{X}$ as:

$$\mathbf{X} \equiv \frac{1}{2}(\mathbf{\Sigma}^{>}_{\mathrm{ph}} - \mathbf{\Sigma}^{<}_{\mathrm{ph}}) \tag{A.46}$$

$$= \frac{1}{2}\mathbf{M}((1+n_b)(\mathbf{G}_0^{>,-} - \mathbf{G}_0^{<,+}) + n_b(\mathbf{G}_0^{>,+} - \mathbf{G}_0^{<,-}))\mathbf{M} \tag{A.47}$$

$$= -\frac{i}{2}\mathbf{M}\Big\{(1+n_b-n_f^{L,-})\mathbf{A}_L^- + (1+n_b-n_f^{R,-})\mathbf{A}_R^- + (n_f^{L,+}+n_b)\mathbf{A}_L^+ + (n_f^{R,+}+n_b)\mathbf{A}_R^+\Big\}\mathbf{M} \tag{A.48}$$

Note that $\mathbf{X}^\dagger = -\mathbf{X}$.

In this notation the retarded self-energy and it's complex conjugate becomes:

$$\mathbf{\Sigma}^r_{\mathrm{ph}} = \mathrm{Re}(\mathbf{\Sigma}^r_{\mathrm{ph}}) + i\,\mathrm{Im}(\mathbf{\Sigma}^r_{\mathrm{ph}}) \tag{A.49}$$

$$= \mathbf{X} - i\mathcal{H}[\mathbf{X}] \tag{A.50}$$

$$\left(\mathbf{\Sigma}^r_{\mathrm{ph}}\right)^\dagger = -\mathbf{X} - i\mathcal{H}[\mathbf{X}] \tag{A.51}$$

Thus, $\mathbf{X}$ gives a Symmetric contribution and $\mathcal{H}[\mathbf{X}]$ gives a antisymmetric contribution to the differential conductance.

A.2.2.2 The Symmetric Contribution

The symmetric part gives

$$I_L^{(1+2)S} = \int dE\,(n_f^L - n_f^R)\tilde{\mathbf{A}}_L\,(\mathbf{X}\mathbf{G}_0\mathbf{\Gamma}_R + h.c.) \tag{A.52}$$

$$= \int dE\,(n_f^L - n_f^R)\tilde{\mathbf{A}}_L\Big(-\frac{i}{2}\mathbf{M}\Big\{(1+n_b-n_f^{L,-})\mathbf{A}_L^- + (1+n_b-n_f^{R,-})\mathbf{A}_R^- + (n_f^{L,+}+n_b)\mathbf{A}_L^+ + (n_f^{R,+}+n_b)\mathbf{A}_R^+\Big\}\mathbf{M}\mathbf{G}_0\mathbf{\Gamma}_R + h.c.\Big) \tag{A.53}$$

To calculated the differential conductance we still need to evaluate the integral in eq. A.53. However, in the limit $T \to 0$ we can take advantages of the facts, that $n_F = \theta(kV)$, $\frac{d}{dV}n_f(\mu = kV) = k\delta(kV)$ and $n_b = 0$, (were we have defined: $\mu_\alpha = k_\alpha V$, demanding that $k_L - k_R = 1$).Thus, the symmetric part of the differential conductance becomes:

$$\frac{dI_L^{(1+2)S}}{dV} = \int dE\ \tilde{\mathbf{A}}_L\Big(-\frac{i}{2}\mathbf{M}\Big\{(k_L\delta(k_LV)\theta(V-\Omega) - k_R\delta(k_RV+\Omega)\theta(V-\Omega))\mathbf{A}_R^- + (k_L\delta(k_L-\Omega)\theta(V-\Omega) - k_R\delta(k_R)\theta(V-\Omega))\mathbf{A}_L^+\Big\}\mathbf{M}\mathbf{G}_0\mathbf{\Gamma}_R + h.c.\Big) \tag{A.54}$$

$$= \theta(V-\Omega)\tilde{\mathbf{A}}_L\Big(-\frac{i}{2}\mathbf{M}\Big\{(k_L\delta(k_LV) - k_R\delta(k_RV+\Omega))\mathbf{A}_R^- + (k_L\delta(k_L-\Omega) - k_R\delta(k_R))\mathbf{A}_L^+\Big\}\mathbf{M}\mathbf{G}_0\mathbf{\Gamma}_R + h.c.\Big), \tag{A.55}$$

and for $k_L = -k_R = \frac{1}{2}$

$$\frac{dI_L^{(1+2)S}}{dV} = -\frac{i}{4}\theta(V-\Omega)\Big(\Big[\tilde{\mathbf{A}}_L(\mathbf{M}\mathbf{A}_R^-\mathbf{M}\mathbf{G}_0\mathbf{\Gamma}_R - h.c.)\Big]\Big|_{\frac{V}{2},\Omega-\frac{V}{2}} + \Big[\tilde{\mathbf{A}}_L(\mathbf{M}\mathbf{A}_L^+\mathbf{M}\mathbf{G}_0\mathbf{\Gamma}_R - h.c.)\Big]\Big|_{-\frac{V}{2},\frac{V}{2}-\Omega}\Big) \tag{A.56}$$

$$= -\frac{i}{4}\theta(V-\Omega)\Big(\Big[\tilde{\mathbf{A}}_L(\mathbf{M}\mathbf{A}_R^-\mathbf{M}\mathbf{G}_0\mathbf{\Gamma}_R - h.c.)\Big]\Big|_{\frac{V}{2}} + \Big[\tilde{\mathbf{A}}_L^-(\mathbf{M}\mathbf{A}_L\mathbf{M}\mathbf{G}_0^-\mathbf{\Gamma}_R^- - h.c.)\Big]\Big|_{\frac{V}{2}} \Big[\tilde{\mathbf{A}}_L^+(\mathbf{M}\mathbf{A}_R\mathbf{M}\mathbf{G}_0^+\mathbf{\Gamma}_R^+ - h.c.)\Big]\Big|_{-\frac{V}{2}} + \Big[\tilde{\mathbf{A}}_L(\mathbf{M}\mathbf{A}_L^+\mathbf{M}\mathbf{G}_0\mathbf{\Gamma}_R - h.c.)\Big]\Big|_{-\frac{V}{2}}\Big) \tag{A.57}$$

If we just are interested in the height of the step we can evaluate eq. A.57 for $V = \Omega$

$$\frac{dI_L^{(1+2)S}}{dV} = \theta(V-\Omega)\,\mathrm{Im}\Big(Tr\Big[\tilde{\mathbf{A}}_L(\Omega/2)(\mathbf{M}\mathbf{A}_R(-\Omega/2)\mathbf{M}\mathbf{G}_0(\Omega/2)\mathbf{\Gamma}_R(\Omega/2)\Big] \tag{A.58}$$

$$+Tr\Big[\tilde{\mathbf{A}}_L(-\Omega/2)(\mathbf{M}\mathbf{A}_L(\Omega/2)\mathbf{M}\mathbf{G}_0(-\Omega/2)\mathbf{\Gamma}_R(-\Omega/2)\Big]\Big) \tag{A.59}$$

To include the broadening of the temperature the step function is replaced by the first derivative of the so called universal symmetric function $\mathcal{I}_{sym}(V,\Omega)$ know

from the normal LOE.

$$\frac{dI_L^{(1+2)S}}{dV} = \partial_{eV}\mathcal{I}_{sym}(V,\Omega)\,\mathrm{Im}\Big(\mathrm{Tr}\left[\tilde{\mathbf{A}}_L(\Omega/2)(\mathbf{M}\mathbf{A}_R(-\Omega/2)\mathbf{M}\mathbf{G}_0(\Omega/2)\mathbf{\Gamma}_R(\Omega/2)\right] + \mathrm{Tr}\left[\tilde{\mathbf{A}}_L(-\Omega/2)(\mathbf{M}\mathbf{A}_L(\Omega/2)\mathbf{M}\mathbf{G}_0(-\Omega/2)\mathbf{\Gamma}_R(-\Omega/2)\right]\Big) \tag{A.60}$$

A.2.2.3 The antisymmetric part

The antisymmetric contribution is given by:

$$I_L^{(1+2)A} = \int dE\,(n_f^L - n_f^R)\tilde{\mathbf{A}}_L\,(-i\mathcal{H}\left[\mathbf{X}\right]\mathbf{G}_0\mathbf{\Gamma}_R + h.c.) \tag{A.61}$$

Thus to calculate the the antisymmetric part of the conductance the Hilbert-transform of $\mathbf{X}$ is needed

$$\mathcal{H}\left[\mathbf{X}\right] = \frac{1}{2}\left(\mathcal{H}\left[\mathbf{\Sigma}_{ph}^{>}\right] - \mathcal{H}\left[\mathbf{\Sigma}_{ph}^{<}\right]\right) \tag{A.62}$$

$$= -\frac{1}{2}\mathbf{M}\mathcal{H}\Big[(1+n_b-n_f^{L,-})\mathbf{A}_L^- + (1+n_b-n_f^{R,-})\mathbf{A}_R^- + (n_f^{L,+}+n_b)\mathbf{A}_L^+ + (n_f^{R,+}+n_b)\mathbf{A}_R^+\Big]\mathbf{M} \tag{A.63}$$

$$= \frac{1}{2}\mathbf{M}\left(2(1+n_b)\,\mathrm{Re}(\mathbf{G}_0^-) + 2n_b\,\mathrm{Re}(\mathbf{G}_0^+) - \sum_{\alpha\in\{L,R\},\sigma\in\{+,-\}}\mathcal{H}\left[\sigma n_f^{\alpha,\sigma}\mathbf{A}_\alpha^\sigma\right]\right)\mathbf{M} \tag{A.64}$$

where we have used: $\mathcal{H}\left[\mathbf{A}_L^- + \mathbf{A}_R^-\right] \approx -2\,\mathrm{Re}(\mathbf{G}_0^-)$ (This is only exact at equilibrium).

A.2.2.4 Taylor-expansion of the Spectral-function

If the spectral-function vary on the scale of the phonon-frequencies then Eq. (A.64) becomes numerical difficult to solve. Thus, to proceed we choose to Taylor-expand the Spectral-function in Eq. (A.64).
We start by considering $\mathcal{H}\left[n_f\mathbf{A}\right]$:

$$\mathcal{H}\left[n_f(\epsilon')\mathbf{A}(\epsilon')\right](\epsilon) = \frac{1}{\pi}\lim_{\delta\to 0}\int_{-\infty}^{\mu} d\epsilon'\,\frac{\mathbf{A}(\epsilon')(\epsilon'-\epsilon)}{(\epsilon'-\epsilon)^2+\delta^2} \tag{A.65}$$

Taylor expanding $\mathbf{A}(\epsilon')$ around ϵ gives:

$$\mathbf{A}(\epsilon') = \mathbf{A}(\epsilon) + \mathbf{A}'(\epsilon)(\epsilon' - \epsilon) + \frac{1}{2}\mathbf{A}''(\epsilon)(\epsilon' - \epsilon)^2 + \dots \tag{A.66}$$

Only the zero-order term is considered since only this term gives a divergent contribution. Thus we get:

$$\mathcal{H}\left[n_f(\epsilon')\mathbf{A}(\epsilon')\right](\epsilon) = \frac{1}{\pi}\mathrm{P}\int_{-\infty}^{\mu} d\epsilon' \, \frac{\mathbf{A}(\epsilon)}{(\epsilon' - \epsilon)} \tag{A.67}$$

$$= \frac{1}{\pi}\mathbf{A}(\epsilon)(\log(\mu - \epsilon) - B), \tag{A.68}$$

where B is a boundary term stemming from the lower cutoff of $\mathbf{A}$, which is independent of the voltage and will therefore not give a contribution to the IETS. To include the broadening, due to the temperature we now write

$$\mathcal{H}\left[n_f(\epsilon')\mathbf{A}(\epsilon')\right](\epsilon) = \mathbf{A}(\epsilon)\mathcal{H}\left[n_f(\epsilon')\right](\epsilon) \tag{A.69}$$

Thus we get:

$$\frac{1}{2}\left(H\left\{\mathbf{\Sigma}_{ph}^{>}\right\} - H\left\{\mathbf{\Sigma}_{ph}^{<}\right\}\right) =$$
$$\frac{1}{2}\mathbf{M}\left(2(1+n_b)\,\mathrm{Re}(\mathbf{G}_0^-) + 2n_b\,\mathrm{Re}(\mathbf{G}_0^+) - \sum_{\alpha\in\{L,R\}}^{\sigma\in\{+,-\}} \mathbf{A}_\alpha^\sigma \mathcal{H}\left[\sigma n_f^{\alpha,\sigma}\right]\right)\mathbf{M} \tag{A.70}$$

Thus the Hilbert part of I^{1+2} is:

$$I^{(1+2)asym} = \frac{1}{2}\int d\epsilon\, (n_f^L - n_f^R)\tilde{\mathbf{A}}_L\left[\mathbf{\Gamma}_R\mathbf{G}_0^\dagger\mathbf{M}\left(2(1+n_b)\,\mathrm{Re}(\mathbf{G}_0^-) + 2n_b\,\mathrm{Re}(\mathbf{G}_0^+)\right.\right.$$
$$\left.\left. - \sum_{\alpha\in\{L,R\}}^{\sigma\in\{+,-\}} \mathbf{A}_\alpha^\sigma \mathcal{H}\left[\sigma n_f^{\alpha,\sigma}\right]\right)\mathbf{M} + h.c.\right] \tag{A.71}$$

We assume that the Fermi functions vary much faster than the spectral function; thus, we can omit the terms $2(1+n_b)\,\mathrm{Re}(\mathbf{G}_0^-)$ and $2n_b\,\mathrm{Re}(\mathbf{G}_0^+)$.(In the case of

a bond onset this is a bad assumption). Thus we are left with

$$I^{(1+2)asym} = -\frac{1}{2}\int d\epsilon\,(n_f^L - n_f^R)\tilde{\mathbf{A}}_L\left[\mathbf{\Gamma}_R\mathbf{G}_0^\dagger\mathbf{M}\left(\sum_{\alpha\in\{L,R\}}^{\sigma\in\{+,-\}}\mathbf{A}_\alpha^\sigma\mathcal{H}\left[\sigma n_f^{\alpha,\sigma}\right]\right)\mathbf{M} + h.c.\right] \tag{A.72}$$

$$= -\frac{1}{2}\int d\epsilon\,(n_f^L - n_f^R)\mathcal{H}\left[n_f^{L,+}\right]\tilde{\mathbf{A}}_L\left[\mathbf{\Gamma}_R\mathbf{G}_0^\dagger\mathbf{M}\left(\mathbf{A}_L^+\right)\mathbf{M} + h.c.\right] \tag{A.73}$$

$$-\frac{1}{2}\int d\epsilon\,(n_f^L - n_f^R)\mathcal{H}\left[-n_f^{L,-}\right]\tilde{\mathbf{A}}_L\left[\mathbf{\Gamma}_R\mathbf{G}_0^\dagger\mathbf{M}\left(\mathbf{A}_L^-\right)\mathbf{M} + h.c.\right] \tag{A.74}$$

$$-\frac{1}{2}\int d\epsilon\,(n_f^L - n_f^R)\mathcal{H}\left[n_f^{R,+}\right]\tilde{\mathbf{A}}_L\left[\mathbf{\Gamma}_R\mathbf{G}_0^\dagger\mathbf{M}\left(\mathbf{A}_R^+\right)\mathbf{M} + h.c.\right] \tag{A.75}$$

$$-\frac{1}{2}\int d\epsilon\,(n_f^L - n_f^R)\mathcal{H}\left[-n_f^{R,-}\right]\tilde{\mathbf{A}}_L\left[\mathbf{\Gamma}_R\mathbf{G}_0^\dagger\mathbf{M}\left(\mathbf{A}_R^-\right)\mathbf{M} + h.c.\right] \tag{A.76}$$

All the four term above are divergent; however, only to of the terms (A.73 and A.76) take infinite values inside the bias window set by $(n_f^L - n_f^R)$ at zero temperature($\log(\mu_L - \Omega - \epsilon)$ and $\log(\mu_R + \Omega - \epsilon)$); thus, we ascribe the signals to these two terms. To make connections to the wide-band LOE result the terms (A.74 and A.75) are also kept; however we assume $A_L^- = A_L^+$ and $A_R^+ = A_R^-$, since the don't contribute to the signal. We evaluate all the the electronic structure functions (**G**,**Γ**,**A**), at the peak values, keeping only the energy dependence of the Fermi-functions inside the integral.

$$I^{(1+2)asym} = \int d\epsilon\,(n_f^L - n_f^R)\mathcal{H}\left[n_f^{L,-} - n_f^{L,+}\right]\mathrm{Re}\left[\tilde{\mathbf{A}}_L\mathbf{\Gamma}_R\mathbf{G}_0^\dagger\mathbf{M}\left(\mathbf{A}_L^+\right)\mathbf{M}\right]\Big|_{\mu_L-\Omega} \tag{A.77}$$

$$+\int d\epsilon\,(n_f^L - n_f^R)\mathcal{H}\left[n_f^{R,-} - n_f^{R,+}\right]\mathrm{Re}\left[\tilde{\mathbf{A}}_L\mathbf{\Gamma}_R\mathbf{G}_0^\dagger\mathbf{M}\left(\mathbf{A}_R^-\right)\mathbf{M}\right]\Big|_{\mu_R+\Omega} \tag{A.78}$$

Thus, around the phonon threshold we get:

$$\frac{d^2I^{(1+2)asym}}{dV^2} = 2\frac{d^2\mathcal{I}^{asym}}{dV^2}\,\mathrm{Re}\,\mathrm{Tr}\left[\tilde{\mathbf{A}}_L(-\Omega/2)\mathbf{\Gamma}_R(-\Omega/2)\mathbf{G}_0^\dagger(-\Omega/2)\mathbf{M}\mathbf{A}_L(\Omega/2)\mathbf{M}\right. \tag{A.79}$$

$$\left. + \tilde{\mathbf{A}}_L(\Omega/2)\mathbf{\Gamma}_R(\Omega/2)\mathbf{G}_0^\dagger(\Omega/2)\mathbf{M}\mathbf{A}_R(-\Omega/2)\mathbf{M}\right] \tag{A.80}$$

Where $\mathcal{I}^{asym}$ is the universal asymmetric function known from the ordinary

LOE and given by:

$$I^{asym} = \int d\epsilon \, (n_f^L - n_f^R)\mathcal{H}\left[n_f^{R,-} - n_f^{R,+}\right] \tag{A.81}$$

$$= \quad -\frac{e}{\pi}k_bT\left(h(\frac{eV+\Omega}{2\pi k_bT}) - h(\frac{eV-\Omega}{2\pi k_bT}) - 2h(\frac{\Omega}{2\pi k_bT})\right) \tag{A.82}$$

where $h(x) \equiv x\,\mathrm{Re}\,\Psi(ix)$, and $\Psi(x)$ is the digamma function.

A.3 Relations between the Fermi and Bose-Einstion distribution

The Fermi distribution function is defined by:

$$n_f(\mu, \epsilon) = \frac{1}{e^{\frac{\epsilon-\mu}{k_b T}} + 1} \tag{A.83}$$

The Bose-Einstein distribution function is defined by:

$$n_b(\mu = 0, \Omega) = \frac{1}{e^{\frac{\Omega}{k_b T}} - 1} \tag{A.84}$$

Useful relations: the Bose-Einstein distribution function can be rewritten in themes of the coth function:

$$n_b(\Omega) = \frac{1}{2}(\coth(\frac{\Omega}{2k_b T}) - 1) \tag{A.85}$$

the product of two Fermi functions can be rewritten as minus the sum with Bose for factors:

$$n_F(\epsilon - \mu_L) n_F(\epsilon - \mu_R) = -n_b(\mu_L - \mu_R) n_F(\epsilon - \mu_L) - n_b(\mu_R - \mu_L) n_F(\epsilon - \mu_R) \tag{A.86}$$

The Bose function has the following probity

$$n_b(\Omega) + n_b(-\Omega) = -1 \tag{A.87}$$

Thus

$$n_F^L(1 - n_F^R) = n_F(\epsilon - \mu_L) + n_b(\mu_L - \mu_R) n_F(\epsilon - \mu_L) + n_b(\mu_R - \mu_L) n_F(\epsilon - \mu_R) \tag{A.88}$$

$$= n_b(\mu_R - \mu_L) \left(n_F^R - n_F^L\right) \tag{A.89}$$

$$= \frac{1}{2}(\coth(\frac{\mu_R - \mu_L}{2k_b T}) - 1)(n_F^R - n_F^L) \tag{A.90}$$

Appendix B

The Langevin Equation

In this note the semi classical Langevin equation is derived. Consider a system of atoms coupled by "springs" i.e. the assumption is that the system can be described as a set of coupled harmonic-oscillators. The system is divided into two parts: devise (d) and bath(B). Now the system is described by the following Hamiltonian:

$$H = \sum_{d,B} \frac{1}{2} \left(\dot{u}_\alpha^\dagger \dot{u}_\alpha + u_\alpha^\dagger K^\alpha u_\alpha \right) + u_d^\dagger V^{dB} u_B + u_d^\dagger V^{dB} u_B \tag{B.1}$$

u_α is the mass scaled coordinate vector given by: $u_\alpha = \sqrt{m_\alpha} x_\alpha$, where m_α is the mass vector and x_α is the coordinate operator; furthermore K^α is the dynamical matrix describing the coupling inside the devise/bath and V^{dB} describe the coupling between devise and bath.

The equation of motion for the devise and bath atoms are given by:

$$\ddot{u}_d = \frac{\partial H}{\partial u_d} = -K^d u_d - V^{dB} u_B \tag{B.2}$$

$$\ddot{u}_B = \frac{\partial H}{\partial u_B} = -K^B u_B - V^{Bd} u_d \tag{B.3}$$

$$\tag{B.4}$$

To solve the equation of motion for the devise region, the following green function is defined:

$$-\frac{\partial^2}{\partial t'^2}g(t,t') = K^B g(t,t') + \delta(t,t') \tag{B.5}$$

with the initial condition that $g(t,t') = 0$ for $t < t'$. To solve for u_d in eq. B.2 requires u_B to be expressed in themes of u_d and the initial conditions for the bath. This is reached by first applying $g(t,t')$ from the left on each side in eq B.3 and integrate over t' from t_0 to ∞:

$$\int_{t_0}^{\infty} dt' g(t,t')\ddot{u}_B = \int_{t_0}^{\infty} dt' g(t,t') \left(-K^B u_B - V^{BD} u_d\right) \tag{B.6}$$

$\Downarrow$ (integration by parts)

$$\left[g(t,t')\dot{u}_B\right]_{t_0}^{\infty} - \int_{t_0}^{\infty} dt' \dot{g}(t,t')\dot{u}_B = \int_{t_0}^{\infty} dt' g(t,t') \left(-K^B u_B - V^{Bd} u_d\right) \tag{B.7}$$

and then applying $u_B(t)$ from the right in eq. B.5 and again integrate over t' from t_0 to ∞:

$$\int_{t_0}^{\infty} dt' \left(-\frac{\partial^2}{\partial t'^2}g(t,t')\right) u_B(t') = \int_{t_0}^{\infty} dt' \left(K^d g(t,t') + \delta(t,t')\right) u_B(t')$$

$\Downarrow$ (integration by parts)

$$-\left[\dot{g}(t,t')u_B(t')\right]_{t_0}^{\infty} + \int_{t_0}^{\infty} dt' \dot{g}(t,t')\dot{u}_B(t') = \int_{t_0}^{\infty} dt' \left(K^B g(t,t') + \delta(t,t')\right) u_B(t') \tag{B.8}$$

finally adding eq. B.7 and eq. B.8, and using $g(t,\infty) = \dot{g}(t,\infty) = 0$ gives:

$$\dot{g}(t,t_0)u_B(t_0) - g(t,t_0)\dot{u}_B(t_0) = \left(\int_{t_0}^{\infty} dt' g(t,t')V^{Bd}u_d(t')\right) + u_B(t) \tag{B.9}$$

$\Downarrow$ (isolating $u_b(t)$)

$$u_B(t) = \dot{g}(t,t_0)u_B(t_0) - g(t,t_0)\dot{u}_B(t_0) - \int_{t_0}^{\infty} dt' g(t,t')V^{Bd}u_d(t') \tag{B.10}$$

Inserting eq. B.10 into the equation of motion of u_d (eq. B.2) gives:

$$\begin{aligned}\ddot{u}_d(t) =& -K^d u_d - V^{dB}\left(\dot{g(t,t_0)}u_B(t_0) - g(t,t_0)\dot{u}_B(t_0) - \int_{t_0}^{\infty} dt' g(t,t')V^{Bd}u_d(t')\right) \\ =& -K^d u_d - \left(\int_{t_0}^{\infty} dt' \Pi^r(t,t')u_d(t')\right) + \xi(t,t')\end{aligned} \tag{B.11}$$

where $\Pi^r(t,t') = V^{dB}g(t,t')V^{Bd}$ and $\xi(t,t') = -V^{dB}\left(g(t,t_0)\dot{u}_B(t_0) - g(t,t_0\dot{u}_B(t_0))\right)$

B.1 Noise Correlations

So far, the only assumption has been that the system is described by harmonic oscillators, and the above derivation is valid both if the system is considered to be classical but also in the case of quantum mechanical harmonic oscillators. However, eq. B.11 is considered an classical equation, but retaining some QM correlations in the leads. $\xi(t)$ depend on the initial conditions of the bath. The initial time t_0 is set to $-\infty$. Following the concept of adiabatic switch-on at time $-\infty$ the devise and bath are decoupled, and the bath is in thermal equilibrium and described by the Bose distribution n_B. The initial condition is considered unknown, and hence $u_B(t_0)$ and $\dot{u}_B(t_0)$ are considered random variables. Thus $\xi(t)$ is a random vector with zero mean, $\langle \xi(t) \rangle = 0$, and furthermore the correlation between $\xi(t)$ for different times is given by:

$$\begin{aligned}\left\langle \xi(t)\xi(t')^\dagger \right\rangle = \\ \Big\langle V^{dB} \big[& g(t,t_0)\dot{u}_B(t_0)\dot{u}_B(t_0)^\dagger g(t',t_0)^\dagger \; - g(t,t_0)\dot{u}_B(t_0)u_B(t_0)^\dagger \dot{g}(t',t_0)^\dagger \\ & + \dot{g}(t,t_0)u_B(t_0)u_B(t_0)^\dagger \dot{g}(t',t_0)^\dagger \; - \dot{g}(t,t_0)u_B(t_0)\dot{u}_B(t_0)^\dagger g(t',t_0)^\dagger \big] \Big\rangle\end{aligned} \tag{B.12}$$

The basis where K^B is, diagonal is used to simplify the problem; i.e the eigenmode representation for the matrix g; thus eq. B.5 can easily be solved:

$$g(t,t') = S^T g^{diago} S \tag{B.13}$$

$$g^{diago} = -\theta(t-t')\frac{\sin\omega(t-t')}{\omega_j} \tag{B.14}$$

$$\frac{\partial}{\partial t'} g^{diago} = \qquad \delta(t-t')\frac{\sin\omega(t-t')}{\omega_j} + \theta(t-t')\cos\omega_j(t-t_0) \tag{B.15}$$

$$= \theta(t-t')\cos\omega_j(t-t_0) \tag{B.16}$$

The system is much smaller than the bath region, thus the bath is only weakly affected by the devise, u_B is therefore also diagonal in the basis mentioned above. Hence u_B can be written as a set of uncoupled harmonic oscillators. This means that u_B can be written as:

$$\begin{aligned} u_B &= \frac{l}{2}(a^\dagger + a) \\ \dot{u}_B &= \frac{i\hbar}{l\sqrt{2}}(a^\dagger - a) \end{aligned} \tag{B.17}$$

The QM expectation values in eq. B.12 can be calculated using eq. B.17.

$$\langle \dot{u}_B \dot{u}_B \rangle = \frac{-\hbar^2}{2l^2}\langle a^\dagger a^\dagger + aa - a^\dagger a - aa^\dagger \rangle \frac{\hbar^2}{2l^2}\langle 2a^\dagger a + 1 \rangle \tag{B.18}$$

$$= \frac{\hbar^2}{2l^2}(n_B + \frac{1}{2}) \tag{B.19}$$

$$\langle u_B u_B \rangle = \frac{l^2}{2}\langle 2a^\dagger a + 1 \rangle = \frac{l^2}{2}(n_B + \frac{1}{2}) \tag{B.20}$$

$$\langle \dot{u}_B u_B \rangle = \frac{1}{2}\hbar i \langle a^\dagger a - aa^\dagger \rangle = -\frac{1}{2}\hbar i \tag{B.21}$$

$$\langle u_B \dot{u}_B \rangle = \frac{1}{2}\hbar i \langle -a^\dagger a + aa^\dagger \rangle = \frac{1}{2}\hbar i \tag{B.22}$$

Thus the terms in eq. B.12 become:

$$\dot{g}(t,t_0)\langle u_B u_B \rangle \dot{g}(t',t_0) = \frac{l^2}{2}(n_B + \frac{1}{2})\cos\omega_j(t-t_0)\cos\omega_j(t'-t_0) \tag{B.23}$$

$$g(t,t_0)\langle \dot{u}_B \dot{u}_B \rangle g(t',t_0) = \left(\frac{\hbar}{l}\right)^2 (n_B + \frac{1}{2})\frac{\sin\omega_j(t-t_0)\sin\omega_j(t'-t_0)}{\omega_j} \tag{B.24}$$

where $l = \sqrt{\frac{\hbar}{\omega}}$. Adding eq. B.23 and eq. B.24, using the the relation: $\cos(x - y) = \cos(x)\cos(y) + \sin(x)\sin(y)$, gives:

$$\frac{\hbar}{\omega_j}(n_B + \frac{1}{2})\cos(t - t_0 - t' + t_0) = \frac{\hbar}{\omega_j}(n_B + \frac{1}{2})\cos(t - t') \tag{B.25}$$

Similarly

$$g(t,t_0)\langle \dot{u}_B u_B \rangle \dot{g}(t',t_0) = \frac{1}{2}i\hbar\theta(t-t_0)\frac{\sin\omega_j(t-t_0)}{\omega_j}\theta(t'-t_0)cos(t'-t_0) \tag{B.26}$$

$$\dot{g}(t,t_0)\langle u_B \dot{u}_B \rangle g(t',t_0) = \frac{1}{2}i\hbar\theta(t'-t_0)\frac{\sin\omega_j(t'-t_0)}{\omega_j}\theta(t-t_0)cos(t-t_0) \tag{B.27}$$

Adding eq. B.26 and eq. B.27, using the relation $\sin(x - y) = \sin(x)\cos(y) - \cos(x)\sin(y)$ gives:

$$\frac{1}{2}\frac{\hbar i}{\omega}\sin(t' - t_0 - t + t_0) = \frac{1}{2}\frac{\hbar i}{\omega}\sin(t' - t) \tag{B.28}$$

Finally the noise-correlation is expressed as:

$$\langle \xi(t)\xi(t')^\dagger \rangle = V^{dB}\left(\frac{\hbar}{\omega_j}(n_B + \frac{1}{2})\cos(t - t') + \frac{1}{2}\frac{\hbar i}{\omega}\sin(t' - t)\right)V^{Bd} \tag{B.29}$$

The correlation of the heat bath, as expressed in eq. B.29, is time translationally invariant and independent of t_0 as expected. Eq. B.29 has a complex component,

originating from the fact that in QM $\xi(t)$ and $\xi(t')$ are noncommuting, and the product of the two is not a Hermitian operator; hence the correlation in eq. B.29 is not an observable and therefore a classical noise spectrum cannot be constructed to fulfill eq. B.29. Instead the symmetrized correlation can be used:

$$\frac{1}{2}\left\langle \xi(t)\xi(t')^{\dagger} + \xi(t')\xi(t)^{\dagger} \right\rangle = \left\langle V^{dB}\left(\frac{\hbar}{\omega_j}(n_B + \frac{1}{2})\cos(t-t')\right) V^{Bd} \right\rangle \quad \text{(B.30)}$$

Appendix C

Publications

Paper 1

Jing-Tao Lü Rasmus Bjerregaard Christensen and Mads Brandbyge

Light emission and finite-frequency shot noise in molecular junctions: From tunneling to contact

PHYSICAL REVIEW B 88, 045413 (2013)

Light emission and finite-frequency shot noise in molecular junctions: From tunneling to contact

Jing-Tao Lü,[1,2,3,*] Rasmus Bjerregaard Christensen,[2] and Mads Brandbyge[2]

[1]*School of Physics, Huazhong University of Science and Technology, 1037 Luoyu Road, Wuhan, China*

[2]*DTU-Nanotech, Department of Micro- and Nanotechnology, Technical University of Denmark, Ørsteds Plads, Bldg. 345E, DK-2800 Kongens Lyngby, Denmark*

[3]*Niels-Bohr Institute, Nano-Science Center, University of Copenhagen, Universitetsparken 5, 2100 Copenhagen Ø, Denmark*

(Received 5 April 2013; revised manuscript received 9 June 2013; published 8 July 2013)

Scanning tunneling microscope induced light emission from an atomic or molecular junction has been probed from the tunneling to contact regime in recent experiments. There, the measured light emission yields suggest a strong correlation with the high-frequency current/charge fluctuations. We show that this is consistent with the established theory in the tunneling regime, by writing the finite-frequency shot noise as a sum of inelastic transitions between different electronic states. Based on this, we develop a practical scheme to perform calculations on realistic structures using nonequilibrium Green's functions. The photon emission yields obtained reproduce the essential feature of the experiments.

DOI: 10.1103/PhysRevB.88.045413 PACS number(s): 72.70.+m, 68.37.Ef, 73.20.Mf, 73.63.Rt

I. INTRODUCTION

When a scanning tunneling microscope (STM) tip is brought towards a metal surface, strong localized plasmon modes develop between the tip and surface, in addition to the propagating surface mode at the metal interface. Under an electric field, the plasmon modes interact with the electrons traversing the gap. This provides an efficient way to excite the plasmon modes electrically, and has become an important topic bridging nanoelectronics and plasmonics.[1–21] Radiative damping of the excited plasmons results in light emission, which can be detected experimentally in the far field at the same or opposite side of the STM tip.[5–13,20] Analyzing the emitted light can provide information about the nanogap. The dependence of light emission on the type of metal, the shape of tip and surface, and on the inserted molecular layer between tip and surface, have all been explored.[14–19,22] Different types of plasmon modes have been detected.[20,21] Most of these experiments are done in the tunneling regime, where the coupling between STM tip and metal surface is weak. Theoretically, it has been established that the excitation of plasmon modes is due to the inelastic electronic transitions taken place near the gap.[23,24]

Recently, STM-induced light emission has been probed during the transition from the tunneling to the contact regime, both for single atom contacts and a C_{60} molecular junction.[25–27] The experimental results suggest a strong correlation between the light emission intensity and the current/charge fluctuations at optical frequencies, and furthermore, show the possibility of controlling light emission by engineering the electronic structure. The established theory in the weak coupling, tunneling regime seems to be inadequate for explaining the experimental results in the strong coupling, contact regime.

A detailed modeling of such experiments needs to take into account the plasmon field distribution near the STM tip, the nonequilibrium electronic structure at high bias, the coupling of the plasmonic field with electrical current, and the propagation of light to the far field.[23,24,28] In this paper, instead of developing a full theory, we focus on the electronic part of the problem. In particular, we study how the change of the electronic structure with tip-position and voltage bias influences the efficiency of plasmonic excitation. To this end, we derive a Fermi-golden-rule like expression for the finite frequency shot noise, and relate it to the theory of STM-induced light emission in the tunneling regime. We then express the result in terms of nonequilibrium Green's functions (NEGF) and develop a practical scheme to perform calculations on realistic structures, using information available from density functional theory based NEGF (DFT-NEGF) transport calculations. We demonstrate how this scheme manage to capture the essential feature of the atomic metal and molecular contact experiments.

II. THEORY

In this section, we briefly summarize the theory of STM-induced light emission in the tunneling regime.[23,24] Then, following Refs. 29 and 30, we introduce an approach to express the finite frequency shot noise in a coherent conductor as a sum of inelastic electronic transitions. We demonstrate how the shot-noise explanation of the light emission in a molecular contact is consistent with the theory in the tunneling regime.

A. Inelastic transition due to electron-plasmon interaction

Following the theory of light emission from STM[23,24] and point contacts,[31] the interaction of the electrical current with the plasmon field in the tip-surface cavity is described by the following Hamiltonian,

$$H_{\rm int} = \frac{1}{c}\int j(r)A(r)d^3r\,, \tag{1}$$

where $j(r)$ is the electron current density operator at position r. The plasmon mode, with frequency, Ω, and spatial distribution, $\xi(r)$, is represented by a vector potential,

$$A(r) = \sqrt{\frac{2\pi\hbar c^2}{V\Omega}}\xi(r)(a+a^\dagger)\,. \tag{2}$$

Here, $a(a^\dagger)$ is the annihilation (creation) operator of the plasmon mode, c is the speed of the light, $\hbar$ is the reduced Planck constant, and V is the normalization volume. In

principle, we may calculate the plasmon mode frequency and field distribution for a given a tip-surface distance. However, this is a daunting task for atomistic first principles theory and we do not consider this problem here. Instead, we focus only on the source of the light emission, and investigate the effect of the nonequilibrium electronic structure on the emission rate. We ignore the spatial distribution of the mode in the xy plane transverse to the current, $\xi(r) = \xi(z)$, and perform the integration over these directions in Eq. (1) and get

$$H_{\rm int} = \frac{1}{c}\int I(z)A(z)dz, \\ = M(a + a^{\dagger}), \tag{3}$$

where $I(z)$ is the surface current evaluated at z, integrated over the transverse surface. The emitted power from the junction is proportional to the inelastic transition probability due to the interaction between initial(ψ_i) and final(ψ_f) states originating from the tip or surface electrode,

$$P(\Omega) \sim \sum_{i,f}\iint |\langle\psi_f|M|\psi_i\rangle|^2\delta(\varepsilon_i - \varepsilon_f - \hbar\Omega) \\ \times n_F(\varepsilon_i - \mu_i)[1 - n_F(\varepsilon_f - \mu_f)]d\varepsilon_i d\varepsilon_f\,. \tag{4}$$

We employ the normalization, $\langle\psi_i|\psi_j\rangle = \delta_{ij}\delta(\varepsilon_i - \varepsilon_j)$, and filling given by the Fermi-Dirac distributions n_F, corresponding to the initial and final electrodes with Fermi energies given by μ_i and μ_f, respectively. Finally, we will assume that the "diagonal" contributions in the z direction capture the main dependence of the emitted power on the electronic structure of the junction. Thus we get,

$$P(\Omega) \sim \int dz|\xi(z)|^2\sum_{i,f}\iint |\langle\psi_f|I(z)|\psi_i\rangle|^2\delta(\varepsilon_i - \varepsilon_f - \hbar\Omega) \\ \times n_F(\varepsilon_i - \mu_i)[1 - n_F(\varepsilon_f - \mu_f)]d\varepsilon_i d\varepsilon_f. \tag{5}$$

This "diagonal" assumption can clearly not be justified *per se* without concrete knowledge about the spatial distribution of the mode along with the local current operator. However, below we will use a first-principles method in order to calculate without any fitting parameters the light emission using this approximation and compare with the experimental trends.

B. Current, charge fluctuations, and emission rate

Now we show that the Fermi's golden-rule rate in Eq. (5) is closely related to the finite frequency shot noise of the electrical current, which is defined as

$$\langle\langle I_z(0)I_{z'}(t)\rangle\rangle \equiv \langle(I_z(0) - \langle I_z(0)\rangle)(I_{z'}(t) - \langle I_{z'}(t)\rangle)\rangle, \tag{6}$$

where $I(t) = e^{iHt/\hbar}Ie^{-iHt/\hbar}$ is the surface current operator along z in the Heisenberg representation and z/z' are two positions along the transport direction. The positive direction of I_z is defined to be from the surface electrode towards the tip. Since we are dealing with the time dependence explicitly, we put the position variables z, z' as the subindices. The Fourier transform of Eq. (6) gives the noise spectrum,

$$S_{zz'}(\omega) = \int_{-\infty}^{+\infty}\langle\langle I_z(0)I_{z'}(t)\rangle\rangle e^{i\omega t}dt\,. \tag{7}$$

Following Refs. 29 and 30, inserting a complete set of eigenstates into Eq. (7), and doing the Fourier transform, we obtain a golden-rule-type expression for the current noise,

$$S_{zz'}(\omega) = 2\pi\hbar\sum_{\substack{i,f\\ i\neq f}}\iint\langle\psi_i|I_z|\psi_f\rangle\langle\psi_f|I_{z'}|\psi_i\rangle\delta(\varepsilon_i - \varepsilon_f - \hbar\omega) \\ \times n_F(\varepsilon_i - \mu_i)[1 - n_F(\varepsilon_f - \mu_f)]d\varepsilon_i d\varepsilon_f\,. \tag{8}$$

The initial and final states are summed over scattering states from both electrodes. Equation (8) includes both the Nyquist-Johnson (thermal) and shot noise contributions. Since the energy of the emitted light is much larger than the thermal energy ($\hbar\omega \gg k_BT$), only the zero-temperature limit is considered. In this case, besides the zero-point fluctuations, the only contribution is the shot noise,

$$S_{zz'}(\omega) = 2\pi\hbar\sum_{s,t}\int_{\mu_s+\hbar\omega}^{\mu_t}\langle\psi_t|I_z|\psi_s\rangle\langle\psi_s|I_{z'}|\psi_t\rangle d\varepsilon_t\,, \tag{9}$$

with $\varepsilon_s = \varepsilon_t - \hbar\omega$ for positive sample bias $V = V_s - V_t > 0$. We define the upper and lower Fermi levels are at $|eV|/2$ and $-|eV|/2$, respectively. The "diagonal" correlation S_{zz} gives the sum of the transition rates between the initial filled tip scattering states ψ_t, and the final empty surface scattering states ψ_s, with energies ε_t and ε_s, respectively. This illustrates how the finite frequency shot noise can be viewed as inelastic electronic transitions between the tip and surface scattering states. The positive frequency/energy part of the noise spectrum corresponds to the photon emission, relevant to the experiment, and the negative part to the absorption process. We notice that if z and z' are located at the surface and tip electrode, respectively, then according to charge conservation,

$$I_d \equiv \dot{Q}_d = I_z - I_{z'}\,, \tag{10}$$

and therefore, the charge fluctuation in the central molecule/"device" region(d) is given by

$$S_{dd} = S_{zz} + S_{z'z'} - S_{zz'} - S_{z'z}\,. \tag{11}$$

Similarly the fluctuation of the average current $I_a = \frac{1}{2}(I_z + I_{z'})$ is

$$S_{aa} = \tfrac{1}{4}(S_{zz} + S_{z'z'} + S_{zz'} + S_{z'z}). \tag{12}$$

Using the result in this subsection, we can write Eq. (5) as

$$P(\Omega) \sim \int dz\,|\xi(z)|^2 S_{zz}(\Omega), \tag{13}$$

which makes connection between the "old" theory for STM-induced light emission in the tunneling regime and the "new" shot noise argument.

III. NUMERICAL SCHEME

We aim at a formulation targeting the DFT-NEGF approach to atomistic electron transport, such as the SIESTA/TRANSIESTA method[32] and similar methods employing a localized basis set. In these the whole system is separated into a central device region(d), and two electrode regions, here the tip (t) and surface (s) electrodes. The electrodes are represented by the self-energies. In order to directly employ the DFT-NEGF

formalism, we will rewrite Eq. (9) in terms of the device Green's functions and the self-energies (Σ_s,Σ_t) folded into the same device region representing the coupling of the device region to tip and surface electrodes, respectively. By our choice of device region, we effectively define separating surfaces between the regions.

As an example, we now consider the current evaluated at the surface electrode. In order to calculate the surface electrode current fluctuations, $S_{ss}(\omega)$, an explicit expression for the surface current is needed in terms of quantities readily available in the DFT-NEGF calculation. The current matrix I_s, can be written as,[33]

$$I_s = -\frac{ie}{\hbar}[P_s,H] = \frac{ie}{\hbar}(V_{ds} - V_{sd}), \tag{14}$$

where P_s denotes projection into the surface electrode subspace, H is the total Hamiltonian, V_{ds} is the coupling matrix between the device and surface electrode, V_{sd} is its complex conjugate, and e is the electron charge. We ignore electron spin throughout the paper, since it is not relevant. We assume an orthogonal basis set; however, a generalization to the non-orthogonal case is straightforward by a Löwdin transformation.

Next, we evaluate the current matrix element between different scattering states. We start from the Lippmann-Schwinger equation connecting the scattering states and the retarded Green's functions of the whole system $G(\varepsilon)$,

$$|\psi_s(\varepsilon)\rangle = |\phi_s(\varepsilon)\rangle + G(\varepsilon)V_T|\phi_s(\varepsilon)\rangle\,. \tag{15}$$

Here, $|\psi_s(\varepsilon)\rangle$ and $|\phi_s(\varepsilon)\rangle$ are the scattering states from the semi-infinite surface electrode with and without coupling to the device, respectively. Note that ϕ_s is nonzero only in the surface electrode, but ψ_s spans over the whole region including both electrodes and the device. The coupling matrix V_T represent the coupling between the device and the two electrodes, localized near the device-electrode interfaces. Here, $G(\varepsilon)$ is the retarded Green's function of the whole system including the effect of V_T.

Using the projection matrices, $P_t + P_d + P_s = I$, and the fact that $V_T|\phi_s\rangle$ is only nonzero in the device region, it is possible to write the current matrix element $\langle\psi_t(\varepsilon)|I_s|\psi_s(\varepsilon_-)\rangle$ in terms of the device Green's functions and self-energies, where $\varepsilon_- = \varepsilon - \hbar\omega$. Firstly, using $V_{ds} = P_dV_{ds}P_s$, and Eq. (15), we have

$$P_s|\psi_s(\varepsilon_-)\rangle = (I + G_{sd}(\varepsilon_-)V_{ds})|\phi_s(\varepsilon_-)\rangle. \tag{16}$$

Here, $G_{sd} \equiv P_sGP_d$ is a submatrix of the full Green's function G, and G_{dd} is defined correspondingly. Using the relations

$$G_{sd} = g_{ss}V_{sd}G_{dd}, \tag{17}$$

$$|\psi_s^d\rangle = P_d|\psi_s\rangle = G_{dd}V_{ds}|\phi_s\rangle, \tag{18}$$

$$\Sigma_s = V_{ds}g_{ss}V_{sd}, \tag{19}$$

we get

$$\langle\psi_t(\varepsilon)|V_{ds}|\psi_s(\varepsilon_-)\rangle = \langle\psi_t^d(\varepsilon)|G_{dd}^{-1}(\varepsilon_-) + \Sigma_s(\varepsilon_-)|\psi_s^d(\varepsilon_-)\rangle. \tag{20}$$

Note that here g_{ss} is the retarded Green's function of the isolated surface electrode. Similarly, for the second term in Eq. (14), we have

$$\begin{aligned}\langle\psi_t(\varepsilon)|V_{sd}|\psi_s(\varepsilon_-)\rangle &= \langle\psi_t(\varepsilon)|P_sV_{sd}P_d|\psi_s(\varepsilon_-)\rangle\\ &= \langle\psi_t(\varepsilon)|V_{td}G_{dd}^\dagger V_{ds}g_{ss}^\dagger V_{sd}P_d|\psi_s(\varepsilon_-)\rangle\\ &= \langle\psi_t^d(\varepsilon)|\Sigma_s^\dagger(\varepsilon)|\psi_s^d(\varepsilon_-)\rangle.\end{aligned} \tag{21}$$

Defining

$$W_i(\varepsilon_-,\varepsilon) \equiv G_d^{-1}(\varepsilon_-) + \Sigma_i(\varepsilon_-) - \Sigma_i^\dagger(\varepsilon), \tag{22}$$

we finally obtain the desired matrix element

$$\langle\psi_t(\varepsilon)|I_s|\psi_s(\varepsilon_-)\rangle = \frac{ie}{\hbar}\langle\psi_t^d(\varepsilon)|W_s(\varepsilon_-,\varepsilon)|\psi_s^d(\varepsilon_-)\rangle. \tag{23}$$

Note that all quantities are projected to the device region and thus depend on the actual splitting into regions.

Using the current matrix element, we can now write the surface current shot noise at zero temperature as

$$S_{ss}(\omega) = \int_\theta \mathrm{Tr}[W_s(\varepsilon_-,\varepsilon)A_s(\varepsilon_-)W_s^\dagger(\varepsilon_-,\varepsilon)A_t(\varepsilon)]d\varepsilon\,, \tag{24}$$

where the integral is defined as

$$\int_\theta \cdot\, d\varepsilon = \theta(|eV| - \hbar\omega)\frac{e^2}{2\pi\hbar}\int_{\hbar\omega-|eV|/2}^{|eV|/2} \cdot\, d\varepsilon, \tag{25}$$

with $\theta(x)$ being the Heaviside step function, $A_s(\varepsilon) = G_d(\varepsilon)\Gamma_s(\varepsilon)G_d^\dagger(\varepsilon) = 2\pi\sum_{i=s}|\psi_i^d(\varepsilon)\rangle\langle\psi_i^d(\varepsilon)|$ is the device spectral function due to scattering states from the surface electrode, similarly for A_t, and $\Gamma_s = i(\Sigma_s - \Sigma_s^\dagger)$. In the same way, we get the tip current noise,

$$S_{tt}(\omega) = \int_\theta \mathrm{Tr}[W_t^\dagger(\varepsilon,\varepsilon_-)A_s(\varepsilon_-)W_t(\varepsilon,\varepsilon_-)A_t(\varepsilon)]d\varepsilon\,, \tag{26}$$

and their cross correlation,

$$\begin{aligned}S_{st}(\omega) &= S_{ts}^*(\omega)\\ &= -\int_\theta \mathrm{Tr}\,[W_s(\varepsilon_-,\varepsilon)A_s(\varepsilon_-)W_t(\varepsilon,\varepsilon_-)A_t(\varepsilon)]\,d\varepsilon\,.\end{aligned} \tag{27}$$

Equations (24)–(27) are our main formal results, where we have written the finite frequency shot noise in terms of the Green's functions and self-energies, readily available from DFT-NEGF calculations. The difference between Eqs. (24) and (26) reveals the position dependence of finite frequency noise. Importantly, they both yield the standard result in the zero-frequency limit.[34]

Assuming constant self-energies (Σ_s,Σ_t), and decoupled eigenchannel transmissions[33] at different energies, $T_n(\varepsilon)$, we arrive at more physically transparent expressions,

$$S_{ss}(\omega) = \sum_n \int_\theta T_n(\varepsilon)[1 - T_n(\varepsilon_-)]\,d\varepsilon\,, \tag{28}$$

$$S_{tt}(\omega) = \sum_n \int_\theta T_n(\varepsilon_-)[1 - T_n(\varepsilon)]\,d\varepsilon\,, \tag{29}$$

valid for positive sample voltages, $V > 0$. The two expressions are exchanged for negative bias. Note that T_n are the channel transmissions calculated for the particular bias, V. We refer to Appendix for the full result of $S_{ss}(\omega)$ at finite temperature. Unfortunately, we are not able to write the cross correlations S_{st} and S_{ts} in terms of the eigentransmissions T_n.

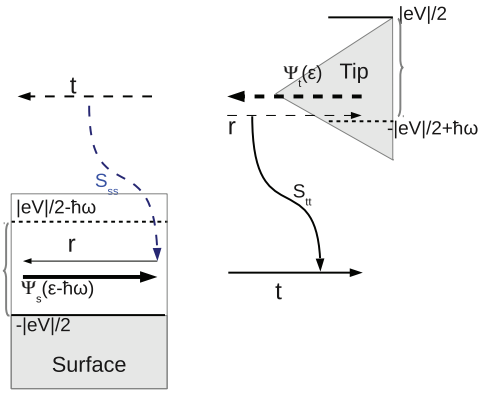

FIG. 1. (Color online) Schematic diagrams showing the two processes contributing to S_{tt} (solid black) and S_{ss} (dashed blue) for positive sample bias, $V > 0$. The curly brackets show two active energy windows for inelastic transitions.

Equations (28) and (29) show that the finite frequency noise is related to the eigenchannel transmission and reflection coefficients at two energy windows. The first energy window corresponds to transmission in the energy range $[\hbar\omega - (eV/2); eV/2]$, the other window is shifted downwards by $\hbar\omega$, $[-eV/2; eV/2 - \hbar\omega]$. We denote these as the active energy windows. The correlation, S_{ss}, corresponds to inelastic transitions taking place at the device-surface interface. For positive sample voltage, $V > 0$, it is proportional to the transmission coefficient of the tip scattering state in the high energy window, and the reflection coefficient of the surface scattering state in the low energy window. The reverse is the case for S_{tt}. Schematic diagrams of these two processes are shown in Fig. 1.

IV. RESULTS

Now we apply the method outlined above to calculate the light emission from the STM resembling two recent experiments where the tip is brought into contact with (i)a Ag adatom on a Ag(111) surface,[26] and (ii) a C_{60} molecule a Cu(111) surface.[27] In the experiments, two type of photons with energy smaller and larger than the applied bias are detected. They are attributed to one- and two-electron process, respectively. Here, we focus only on the former. We used the SIESTA/TRANSIESTA code[32,35] with the generalized gradient approximation (GGA-PBE) for exchange and correlation.[36] For the Ag system, we use a single-ζ polarized basis-set for the Ag atoms. For the C_{60} system, we use a double-ζ basis-set for the carbon atoms, and a single-ζ basis set for the bulk electrode Cu atoms. For both systems, to accurately describe the surface and/or the chemical bonding with the C_{60}, an optimized diffuse basis set was applied for surface layer atoms and the tip.[37]

A. Ag adatom on Ag(111)

In Ref. 26, STM-induced light emission from a Ag-Ag(111) junction has been probed from tunneling to contact regime. The photon yield (roughly emission probability per electron) develops a plateau in the tunneling regime, and has a kink near the conductance quantum upon contact. These results

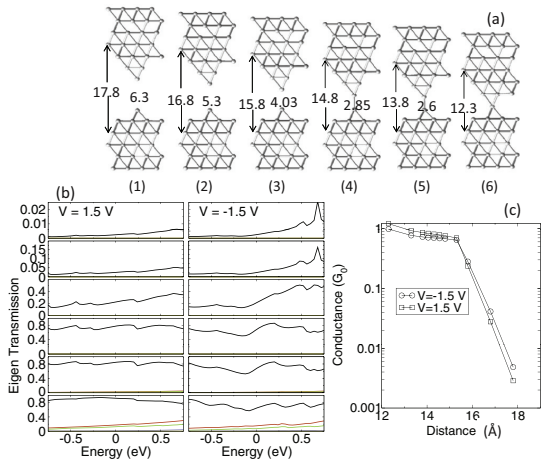

FIG. 2. (Color online) (a) A subset of structures used in the calculation, going from tunneling to contact. In the final structure, one tip atom is pushed aside when forming contact. The two surface layers, the tip and the adatom are relaxed at zero bias for each structure. The numbers show the distance between the two fixed layers and between the tip-adatom in units of Å. (b) Transmission eigenchannels at $V = V_s - V_t = \pm 1.5$ V, going from tunneling to contact (top to bottom), for the structures shown in (a). (c) The average conductance as a function of surface layer separation, showing the transition from tunneling to contact.

suggest possible correlation between photon emission and current shot noise.

To simulate this experiment, we have studied a similar setup: Ag adatom on Ag(111) surface. Figure 2(a) shows a subset of the structures used in the calculations, going from tunneling to contact regime. A 4×4 surface unit cell were used, together with $2 \times 2/5 \times 5$ surface k points to sample electronic structure/transmission. We relaxed the two surface layers, the tip and the adatom at zero bias. After the relaxation, transport calculations were done for a bias of $V = \pm 1.5$ V. Figure 2(b) shows the transmission eigenchannels for the structures in Fig. 2(a). From Fig. 2(b), it is evident that, (i) there is only one dominate transmission eigenchannel, and (ii) there is a small asymmetry in the transmission for the two bias polarities. Figure 2(c) shows the change of the average conductance when going from tunneling to contact on a logarithmic scale. In the tunneling regime, the conductance depends exponentially on the tip-atom distance, while it develops to a plateau upon contact as typically seen in experiments.[26]

The emission rate (proportional to the shot noise power) was evaluated for a plasmon energy of $\hbar\Omega = 1.2$ eV using Eq. (9), or equivalently Eqs. (24)–(26). In order to map out the spatial distribution, the emission rate were calculated for the surface current defined at 6 different interfaces, shown in Figs. 3(a) and 3(b). From these calculations, we observe that the emission rate does not change significantly for interfaces in the same electrode, while they are quite different for the two electrodes, and for the tip-adatom interface.

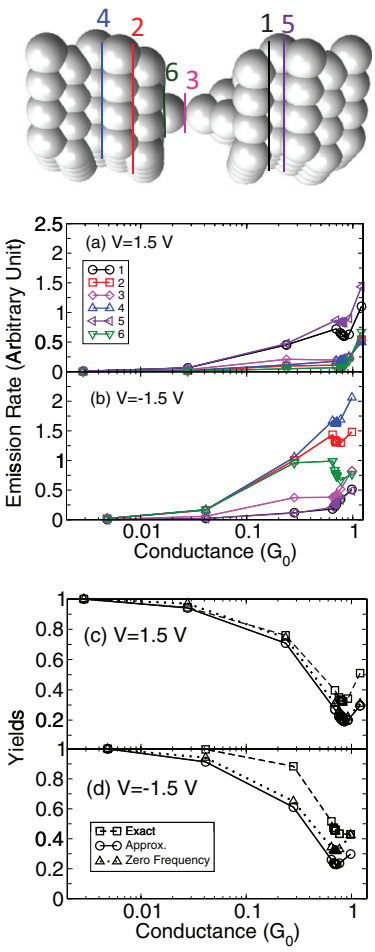

FIG. 3. (Color online) (a) and (b) Calculated noise power (or emission rate) S_{zz} from Eq. (9) for I_z defined through six different surfaces, shown above, for plasmon energy $\hbar\Omega = 1.2$ eV. (c) and (d): Calculated yields $Y = P/\langle I\rangle$, normalized with respect to the first point. The power P is the averaged noise power over the 6 different surfaces (squares). Also shown are the results from average of S_{ss} and S_{tt} using the approximated expressions Eqs. (28) and (29) (circles), and from the zero-frequency noise calculation used in Ref. 26 (triangles). All of them give qualitatively similar results.

To relate the emission rates to the intensity of light emission, we need to do an average of the surface currents, taking into account the spatial distribution of the plasmon mode, $\xi(z)$. Since we do not have specific knowledge about the mode we will choose to do it in the simplest possible way here. Firstly, we take the equally weighted average of all the surface layers [e.g., $\xi(z) =$ constant]. Secondly, as mentioned above, we will use Eq. (5) instead of Eq. (4), so we ignore the cross terms involving surface current at different positions.

We have two comments regarding the approximations. (i) In reality, the plasmon field distribution may change with the tip-surface distance. In the tunneling regime, we expect a high weighting-factor in the region between the tip-surface gap. On the other hand, upon contact, due to the high conductance, we expect the field distribution to spread out into both electrodes.[38,39] Study of this distance-dependent field distribution is an interesting problem by itself, and is beyond the scope of present paper. (ii) We actually tried to include some of the cross terms using Eq. (27), and only see slight change of the final results. But it is computationally too expensive to include all of them.

The final results for the photon yields $Y = P/\langle I\rangle$, normalized over the first point, for the two bias polarities are shown in Figs. 3(c) and 3(d). Here the power P is proportional to the emission rate averaged over six different surfaces. $\langle I\rangle$ is the average current. In Figs. 3(c) and 3(d), we also show results from the approximate calculation using Eqs. (28) and (29), and from the zero-frequency noise employed in Ref. 26. We see that the qualitatively trends are similar for all these calculations: a plateau in the tunneling regime, and the development of a dip at contact around the fully transmitting single channel for $G = 1G_0$, consistent with the experiments.[26]

The agreement between different approximations can be understood from the eigentransmission plotted in Fig. 2(b): (i) in the tunneling regime, there is only one eigenchannel. The eigentransmission is rather small and scales logarithmically with the distance in the whole energy range. Consequently, the distance dependence of the photon yields is encoded in the reflection coefficient $R = 1 - T \approx 1$. As a result, the photon yields show a rather weak dependence on the distance. (ii) In the contact regime, the eigentransmission is rather flat in the whole bias window. From Eqs. (28) and (29), we expect that the finite frequency shot noise shows weak position dependence, and becomes similar to the zero-frequency one.

B. C_{60} on Cu(111)

In Ref. 27, STM-induced light emission from a C_{60} molecule sitting on the reconstructed Cu(111) surface was studied in the tunneling and contact regime. It was found that the C_{60} molecule modifies the photon yields drastically. Especially, a strong bias polarity dependence is observed, indicating the effect of localized molecular resonance on the light emission property.

To simulate this experiment, we used a 4×4 surface unit cell and $2 \times 2/10 \times 10$ surface k points in order to sample the electronic structure/transmission. Due to the surface reconstruction in the experiments[27,40] the two first surface layers and tip were relaxed at zero bias to 0.02 eV/Å at different tip positions. Thus, we do not capture the abrupt jump-to-contact observed in the experiment at finite negative bias in our calculations. Figure 4 shows the five different structures considered in the calculations, together with the transmission eigenchannels at $V = \pm 1.5$ V. Different from the Ag system, when making the contact, there are now mainly three contributing eigenchannels.

As in the experiment, we observe different emission rates for the two bias polarities [see Figs. 5(a) and 5(b)]. For positive sample bias, the magnitude at four different surfaces is comparable. But for the negative bias, the fluctuations near the surface electrode are four times larger than that of the tip

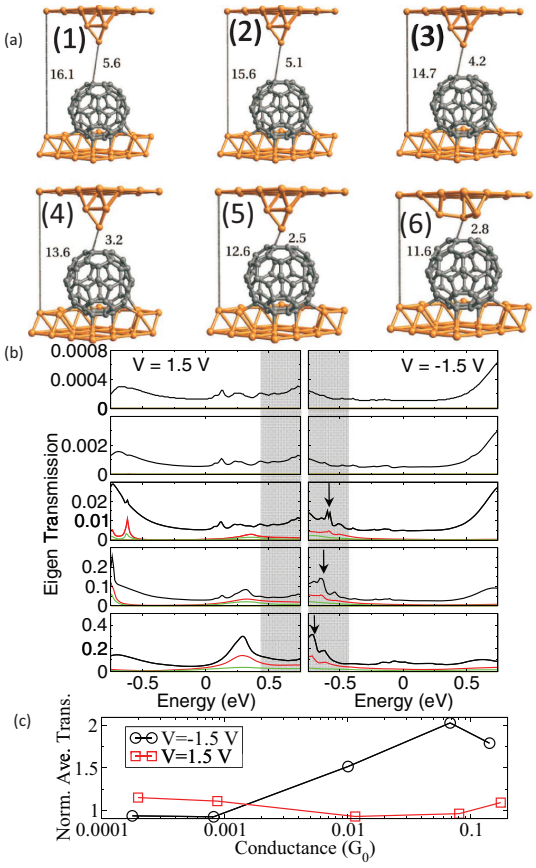

FIG. 4. (Color online) (a) All structures considered in the calculation. In structure 6 a deformation of the tip occurred and has been disregarded in the following. The two surface layers, C_{60} and the tip were relaxed at zero bias for each electrode separation. (b) Transmission eigenchannels at $V = \pm 1.5$ V for the structures shown above. The shaded areas are the active energy windows contributing to S_{ss}. (c) The average transmission in the active energy window [shaded areas in (b)], normalized over that in the whole bias window [−0.75–0.75] eV. The increase from tunneling to contact at $V = -1.5$ V is due to the appearance of HOMO level (peak in the shaded region).

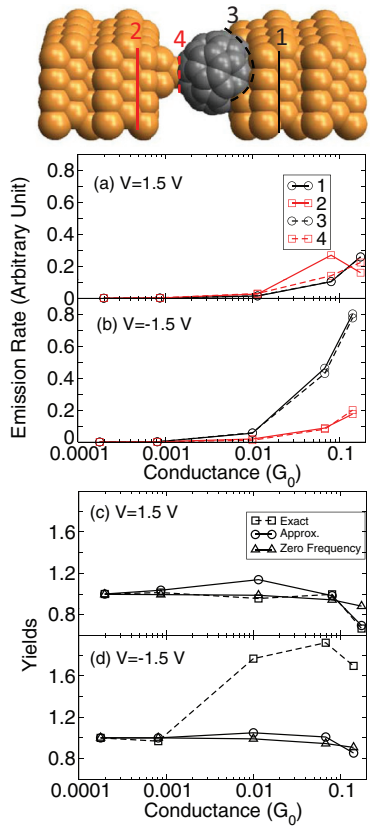

FIG. 5. (Color online) (a) and (b) Similar to Figs. 3(a) and 3(b), calculated emission rates at four different surfaces for the C_{60} system using $\hbar\Omega = 1.2$ eV at $V = \pm 1.5$ V. (c) and (d) Similar to Figs. 3(c) and 3(d).

electrode. Consequently, the calculated yields show different trends at negative and positive bias when going from tunneling to contact, as shown in Figs. 5(c) and 5(d). These results can be explained as a consequence of the appearance of the HOMO level in the bias window, as discussed in Ref. 27. When the HOMO level enters the bias window, the occupied charge begins to fluctuate. This generates new available final states for inelastic transitions, which contribute to high-frequency noise at the plasmon frequency. Since the molecule couples better to the surface than the tip, the charge fluctuations are compensated mainly by the surface-current fluctuations. This allows us to understand the results qualitatively by looking at the surface current fluctuations. In the single channel, small transmission case, we can ignore the $1 - T$ term in Eqs. (28) and (29). So the photon yield due to surface current fluctuation can be characterised by the ratio of the average transmission in the active window (shaded region in Fig. 4) to that in the whole bias window. We plotted this normalized average transmission in Fig. 4(c) and observed a sudden increase upon contact.

Comparing the two systems, we can see that the main difference between them is whether spatially localized molecular resonance participates in the light emission process or not. (1) For the Ag system there are no such localized resonances and the transmission spectrum is weakly energy dependent. The behavior of the finite frequency noise is similar to that at zero-frequency. So the experimental results can basically be understood by looking at the zero-frequency noise, as has been done in Ref. 26. (2) On the other hand for the C_{60} system, at negative bias, the C_{60}-HOMO level enters into the active window upon contact, modifies the transmission in there, and enhances the shot noise power. From this study, we can see that molecular level engineering provides an efficient way to control the light emission property of STM junctions. Along these lines we note that very recent STM

experiments using the photon-map technique indicate that individual molecular resonances can play a determining role ("gate") for the emission process.[22]

V. CONCLUSIONS

We have developed a practical scheme to calculate the finite-frequency shot noise of the electrical current through a coherent molecular conductor within a DFT-NEGF approach. By a spatial average, we re-produce qualitatively the essential features of two recent experiments, confirming the hypothesis that the current/charge fluctuations are the energy source of STM-induced light emission from molecular junctions, going from tunneling to contact. Furthermore, by writing the shot noise expression into a Fermi-golden-rule form, we have established a connection with the theory of light emission in the tunneling regime, based on inelastic electronic transitions. The relation between shot noise power and light emission intensity makes it possible to understand qualitatively the light emission property of atomic/molecular junctions with the help of its eigentransmission spectrum.

Here, we have focused on the source of the light emission, which is the inelastic electronic transitions induced by current. However, to get a quantitative understanding of the experimental results, in a semiclassical model of the electron-plasmon coupling, the following questions have to be addressed: (1) the spatial field distribution of different plasmon modes near the STM tip and (2) their detailed coupling with the current. These questions are also important if we want to distinguish the localized gap mode from the propagating surface mode. Recent experiments showed that the tunneling electrons can couple to both types. An alternative way to proceed is to perform time dependent DFT calculations. So far, model structures have been considered[41] with this approach. However, it is very challenging to perform calculations on realistic structures involving coupling to the metallic surfaces in order to approach the experiments.

ACKNOWLEDGMENTS

We thank R. Berndt and N. Schneider for insightful discussions and the Danish Center for Scientific Computing (DCSC) for providing computer resources. J. T. Lü is supported by the Fundamental Research Funds for the Central Universities, HUST:2013TS032.

APPENDIX: FREQUENCY DEPENDENT NOISE AT FINITE TEMPERATURE

At finite temperature, to evaluate the surface current correlation, we need all the matrix elements. The other three read

$$\langle\psi_s(\varepsilon)|I_s|\psi_t(\varepsilon_-)\rangle = -\frac{ie}{\hbar}\langle\psi_s(\varepsilon)|W_s^\dagger(\varepsilon,\varepsilon_-)|\psi_t(\varepsilon_-)\rangle,$$

$$\langle\psi_t(\varepsilon)|I_s|\psi_t(\varepsilon_-)\rangle = \frac{ie}{\hbar}\langle\psi_t(\varepsilon)|\Sigma_s(\varepsilon_-) - \Sigma_s^\dagger(\varepsilon)|\psi_t(\varepsilon_-)\rangle,$$

$$\langle\psi_s(\varepsilon)|I_s|\psi_s(\varepsilon_-)\rangle = \frac{ie}{\hbar}\langle\psi_s(\varepsilon)|\Sigma_t^\dagger(\varepsilon) - \Sigma_t(\varepsilon_-) - \omega I|\psi_s(\varepsilon_-)\rangle.$$

Assuming a constant self-energy, for positive sample bias, we have the full result for surface current noise at finite temperature

$$S_{ss}(\omega) = \frac{e^2}{2\pi\hbar}\sum_{\alpha\beta} C_{\alpha\beta}(\omega)\Delta n_F^{\alpha\beta},$$

with

$$C_{tt}(\omega) = \int \mathrm{Tr}\left[T(\varepsilon)T(\varepsilon_-)\right]\Delta n_F^{tt}d\varepsilon,$$

$$C_{ss}(\omega) = \int \mathrm{Tr}\left[(\omega I - i\Gamma_t)A_s(\varepsilon_-)(\omega I + i\Gamma_t)A_s(\varepsilon)\right]\Delta n_F^{ss}d\varepsilon,$$

$$C_{st} = \int \mathrm{Tr}\left[(I - T(\varepsilon))T(\varepsilon_-)\right]\Delta n_F^{ts}d\varepsilon,$$

$$C_{ts} = \int \mathrm{Tr}\left[(I - T(\varepsilon_-))T(\varepsilon)\right]\Delta n_F^{ts}d\varepsilon,$$

where

$$\Delta n_F^{\alpha\beta} = n_F(\varepsilon,\mu_\alpha)[1 - n_F(\varepsilon_-,\mu_\beta)].$$

The above result includes both the Nyquist-Johnson (thermal) and the shot noise. Notice the different form of C_{ss} from C_{tt}. It is related to the complex reflection coefficients in the scattering approach discussed by Büttiker.[42] Physically, it means that even when the transmission is zero, there still could be fluctuations at the surface electrode at finite temperature.

*jtlu@hust.edu.cn

[1] A. Nitzan and M. Galperin, Phys. Chem. Chem. Phys. **14**, 9421 (2012).
[2] C. Chen, C. A. Bobisch, and W. Ho, Science **325**, 981 (2009).
[3] D. R. Ward, F. Huser, F. Pauly, J. C. Cuevas, and D. Natelson, Nat. Nanotechnology **5**, 732 (2010).
[4] J. Kern, S. Gromann, N. V. Tarakina, T. Hckel, M. Emmerling, M. Kamp, J.-S. Huang, P. Biagioni, J. C. Prangsma, and B. Hecht, Nano Lett. **12**, 5504 (2012).
[5] J. K. Gimzewski, J. K. Sass, R. R. Schlitter, and J. Schott, Europhys. Lett. **8**, 435 (1989).
[6] X. H. Qiu, G. V. Nazin, and W. Ho, Science **299**, 542 (2003).
[7] Z.-C. Dong, X.-L. Guo, A. S. Trifonov, P. S. Dorozhkin, K. Miki, K. Kimura, S. Yokoyama, and S. Mashiko, Phys. Rev. Lett. **92**, 086801 (2004).
[8] E. Cavar, M. C. Blum, M. Pivetta, F. Patthey, M. Chergui, and W.-D. Schneider, Phys. Rev. Lett. **95**, 196102 (2005).
[9] T. Uemura, M. Furumoto, T. Nakano, M. Akai-Kasaya, A. Salto, M. Aono, and Y. Kuwahara, Chem. Phys. Lett. **448**, 232 (2007).
[10] C. W. Marquardt, S. Grunder, A. Blaszczyk, S. Dehm, F. Hennrich, H. von Lohneysen, M. Mayor, and R. Krupke, Nat. Nanotechnology **5**, 863 (2010).

[11]G. Hoffmann, L. Libioulle, and R. Berndt, Phys. Rev. B **65**, 212107 (2002).
[12]X. Tao, Z.-C. Dong, J. L. Yang, Y. Luo, J. G. Hou, and J. Aizpurua, J. Chem. Phys. **130**, 084706 (2009).
[13]N. L. Schneider, F. Matino, G. Schull, S. Gabutti, M. Mayor, and R. Berndt, Phys. Rev. B **84**, 153403 (2011).
[14]R. Berndt, J. K. Gimzewski, and P. Johansson, Phys. Rev. Lett. **67**, 3796 (1991).
[15]R. Berndt and J. K. Gimzewski, Phys. Rev. B **48**, 4746 (1993).
[16]R. Berndt, R. Gaisch, J. K. Gimzewski, B. Reihl, R. R. Schlittler, W.-D. Schneider, and M. Tschudy, Science **262**, 1425 (1993).
[17]J. Aizpurua, S. P. Apell, and R. Berndt, Phys. Rev. B **62**, 2065 (2000).
[18]Y. Zhang, X. Tao, H. Y. Gao, Z.-C. Dong, J. G. Hou, and T. Okamoto, Phys. Rev. B **79**, 075406 (2009).
[19]F. Geng, Y. Zhang, Y. Yu, Y. Kuang, Y. Liao, Z. Dong, and J. Hou, Opt. Express **20**, 26725 (2012).
[20]T. Wang, E. Boer-Duchemin, Y. Zhang, G. Comtet, and G. Dujardin, Nanotechnology **22**, 175201 (2011).
[21]P. Bharadwaj, A. Bouhelier, and L. Novotny, Phys. Rev. Lett. **106**, 226802 (2011).
[22]T. Lutz, C. Große, C. Dette, A. Kabakchiev, F. Schramm, M. Ruben, R. Gutzler, K. Kuhnke, U. Schlickum, and K. Kern, Nano Lett. **13**, 2846 (2013).
[23]P. Johansson, R. Monreal, and P. Apell, Phys. Rev. B **42**, 9210 (1990).
[24]B. N. J. Persson and A. Baratoff, Phys. Rev. Lett. **68**, 3224 (1992).
[25]G. Schull, N. Neel, P. Johansson, and R. Berndt, Phys. Rev. Lett. **102**, 057401 (2009).
[26]N. L. Schneider, G. Schull, and R. Berndt, Phys. Rev. Lett. **105**, 026601 (2010).
[27]N. L. Schneider, J. T. Lü, M. Brandbyge, and R. Berndt, Phys. Rev. Lett. **109**, 186601 (2012).
[28]R. Marty, C. Girard, A. Arbouet, and G. Colas des Francs, Chem. Phys. Lett. **532**, 100 (2012).
[29]U. Gavish, Y. Levinson, and Y. Imry, Phys. Rev. B **62**, R10637 (2000).
[30]R. Aguado and L. P. Kouwenhoven, Phys. Rev. Lett. **84**, 1986 (2000).
[31]A. V. Lebedev, G. B. Lesovik, and G. Blatter, Phys. Rev. B **81**, 155421 (2010).
[32]M. Brandbyge, J.-L. Mozos, P. Ordejon, J. Taylor, and K. Stokbro, Phys. Rev. B **65**, 165401 (2002).
[33]M. Paulsson and M. Brandbyge, Phys. Rev. B **76**, 115117 (2007).
[34]Y. Blanter and M. Buttiker, Phys. Rep. **336**, 1 (2000).
[35]J. M. Soler, E. Artacho, J. D. Gale, A. Garcia, J. Junquera, P. Ordejon, and D. Sanchez-Portal, J. Phys.: Condens. Matter **14**, 2745 (2002).
[36]J. P. Perdew, K. Burke, and M. Ernzerhof, Phys. Rev. Lett. **77**, 3865 (1996).
[37]S. Garcia-Gil, A. Garcia, N. Lorente, and P. Ordejon, Phys. Rev. B **79**, 075441 (2009).
[38]J. A. Scholl, A. Garca-Etxarri, A. L. Koh, and J. A. Dionne, Nano Lett. **13**, 564 (2013).
[39]K. J. Savage, M. M. Hawkeye, R. Esteban, A. G. Borisov, J. Aizpurua, and J. J. Baumberg, Nature (London) **491**, 574 (2012).
[40]W. W. Pai, H. T. Jeng, C. M. Cheng, C. H. Lin, X. D. Xiao, A. D. Zhao, X. Q. Zhang, G. Xu, X. Q. Shi, M. A. Van Hove *et al.*, Phys. Rev. Lett. **104**, 036103 (2010).
[41]P. Song, P. Nordlander, and S. Gao, J. Chem. Phys. **134**, 074701 (2011).
[42]M. Büttiker, Phys. Rev. B **45**, 3807 (1992).

C.1 Paper 2

Jing-Tao Lü, Rasmus B. Christensen, Giuseppe Foti, Thomas Frederiksen, Tue Gunst and Mads Brandbyge

Efficient calculation of inelastic vibration signals in electron transport: Beyond the wide-band approximation

PHYSICAL REVIEW B 89, 081405(R) (2014)

PHYSICAL REVIEW B **89**, 081405(R) (2014)

Efficient calculation of inelastic vibration signals in electron transport: Beyond the wide-band approximation

Jing-Tao Lü,[1,2] Rasmus B. Christensen,[2] Giuseppe Foti,[3,4] Thomas Frederiksen,[4,5] Tue Gunst,[2] and Mads Brandbyge[2,*]

[1]*School of Physics, Huazhong University of Science and Technology, Wuhan, China*

[2]*Department of Micro- and Nanotechnology, Technical University of Denmark, Ørsteds Plads, Bldg. 345E, DK-2800 Kongens Lyngby, Denmark*

[3]*Centro de Física de Materiales, Centro Mixto CSIC-UPV, Donostia-San Sebastián, Spain*

[4]*Donostia International Physics Center (DIPC) – UPV/EHU, Donostia-San Sebastián, Spain*

[5]*IKERBASQUE, Basque Foundation for Science, Bilbao, Spain*

(Received 24 December 2013; revised manuscript received 24 January 2014; published 21 February 2014)

We extend the simple and efficient lowest order expansion (LOE) for inelastic electron tunneling spectroscopy (IETS) to include variations in the electronic structure on the scale of the vibration energies. This enables first-principles calculations of IETS line shapes for molecular junctions close to resonances and band edges. We demonstrate how this is relevant for the interpretation of experimental IETS using both a simple model and first-principles simulations.

DOI: 10.1103/PhysRevB.89.081405 PACS number(s): 73.63.−b, 68.37.Ef, 61.48.−c

The inelastic scattering of electronic current on atomic vibrations is a powerful tool for investigations of conductive atomic-scale junctions. Inelastic electron tunneling spectroscopy (IETS) has been used to probe molecules on surfaces with scanning tunneling microscopy (STM) [1], and for junctions more symmetrically bonded between the electrodes [2–7]. Typical IETS signals show up as dips or peaks in the second derivative of the current-voltage (I-V) curve [8]. In many cases the bonding geometry is unknown in the experiments. Therefore, first-principles transport calculations at the level of density functional theory (DFT) in combination with nonequilibrium Green's functions (NEGF) [9–14] can provide valuable insights into the atomistic structure and IETS. For systems where the electron-vibration (e-vib) coupling is sufficiently weak and the density of states (DOS) varies slowly with energy (compared to typical vibration energies) one can greatly simplify calculations with the lowest order expansion (LOE) in terms of the e-vib coupling together with the wide-band approximation (LOE-WBA) [10,15]. The LOE-WBA yields simple expressions for the inelastic signal in terms of quantities readily available in DFT-NEGF calculations. Importantly, the LOE-WBA can be applied to systems of considerable size.

However, the use of the WBA cannot account for IETS signals close to electronic resonances or band edges, which often contains crucial information [16,17]. For example, a change in IETS signal *from peak to peak-dip* shape was recently reported by Song *et al.* [6] for single-molecule benzene-dithiol (BDT) junctions, where an external gate enabled tuning of the transport from off-resonance to close-to-resonance. Also, high-frequency vibrations involving hydrogen appear problematic since the LOE-WBA is reported to underestimate the IETS intensity [18].

Here we show how the energy dependence can be included in the LOE description without changing significantly the transparency of the formulas or the computational cost. We describe how the generalized LOE differs from the original LOE-WBA, and demonstrate that it captures the IETS line shape close to a resonance. We apply it to DFT-NEGF calculations on the resonant BDT system and to off-resonant alkane-dithiol junctions, and show how the improved LOE is necessary to explain the experimental data.

Method. We adopt the usual two-probe setup with quantities defined in a local basis set in the central region (C) coupled to left/right electrodes ($\alpha = L, R$). We consider only interactions with vibrations (indexed by λ with energies $\hbar\omega_\lambda$ and e-vib coupling matrices $\mathbf{M}_\lambda$) inside C. To lowest order in the e-vib self-energies $\mathbf{\Sigma}_\lambda$ (second order in $\mathbf{M}_\lambda$) the current can be expressed as a sum of two terms $I(V) = I_e + I_i$, using unperturbed Green's functions $\mathbf{G}^a = \mathbf{G}^{r\dagger}$ defined in region C [10,15],

$$I_e = \frac{\mathrm{G}_0}{e}\int_{-\infty}^{\infty} d\varepsilon\,\{f_L(\varepsilon) - f_R(\varepsilon)\}\left\{\mathrm{Tr}[\mathbf{G}^r\mathbf{\Gamma}_L\mathbf{G}^a\mathbf{\Gamma}_R](\varepsilon) + 2\mathrm{Re}\,\mathrm{Tr}\left[\mathbf{G}^r\mathbf{\Sigma}_\lambda^r\mathbf{G}^r\mathbf{\Gamma}_L\mathbf{G}^a\mathbf{\Gamma}_R\right](\varepsilon)\right\}, \quad (1)$$

$$I_i = \frac{\mathrm{G}_0}{e}\int_{-\infty}^{\infty} d\varepsilon \mathrm{Tr}[\mathbf{\Sigma}_\lambda^<\mathbf{G}^r\mathbf{\Sigma}_L^>\mathbf{G}^a - \mathbf{\Sigma}_\lambda^>\mathbf{G}^r\mathbf{\Sigma}_L^<\mathbf{G}^a](\varepsilon), \quad (2)$$

where $\mathrm{G}_0 = 2e^2/h$ is the conductance quantum and summation over the vibration index λ is assumed. The e-vib self-energies $\mathbf{\Sigma}_\lambda$ are expressed as

$$\mathbf{\Sigma}_\lambda^{\gtrless}(\varepsilon) = \mathbf{M}_\lambda\{(N_\lambda + 1)\mathbf{G}^{\gtrless}(\varepsilon_+) + N_\lambda\mathbf{G}^{\gtrless}(\varepsilon_-)\}\mathbf{M}_\lambda, \quad (3)$$

$$\mathbf{\Sigma}_\lambda^{r,a}(\varepsilon) = \pm\tfrac{1}{2}\{\mathbf{\Sigma}_\lambda^>(\varepsilon) - \mathbf{\Sigma}_\lambda^<(\varepsilon)\} - \frac{i}{2}\mathcal{H}[\mathbf{\Sigma}_\lambda^> - \mathbf{\Sigma}_\lambda^<](\varepsilon), \quad (4)$$

with $\varepsilon_\pm = \varepsilon \pm \hbar\omega_\lambda$, bosonic occupations N_λ, and $\mathcal{H}$ denoting the Hilbert transform. Finally, the lesser/greater Green's functions $\mathbf{G}^{\lessgtr}$ describing the occupied/unoccupied states

$$\mathbf{G}^{\gtrless}(\varepsilon) = \mp i\,\{f_L(\mp\varepsilon)\mathbf{A}_L(\varepsilon) + f_R(\mp\varepsilon)\mathbf{A}_R(\varepsilon)\} \quad (5)$$

are given by the spectral density matrices $\mathbf{A}_\alpha = \mathbf{G}^r\mathbf{\Gamma}_\alpha\mathbf{G}^a$ for left/right moving states with fillings according to the reservoir Fermi functions $f_\alpha(\varepsilon) = n_F(\varepsilon - \mu_\alpha)$.

*mads.brandbyge@nanotech.dtu.dk

The above equations are numerically demanding because of the energy integration over *voltage-dependent* traces. In the following we describe how further simplifications are possible without resorting to the WBA. Here we are interested in the "vibration signal" that is the change in the current close to the excitation threshold $|eV| \approx \hbar\omega_\lambda$, with $eV = \mu_L - \mu_R$. As IETS signals are obtained at low temperatures, we assume that this is the smallest energy scale $k_BT \ll \hbar\omega_\lambda, \Gamma$, where Γ is the typical electronic resonance broadening. The inelastic term I_i [Eq. (2)] then reduces to

$$I_i \approx \frac{G_0}{2e}\sum_{\sigma=\pm}\left(\coth\frac{\hbar\omega_\lambda}{2k_BT} - \coth\frac{\hbar\omega_\lambda+\sigma eV}{2k_BT}\right)\int_{-\infty}^{\infty} d\varepsilon \mathrm{Tr} \times [\mathbf{M}_\lambda \tilde{\mathbf{A}}_L(\varepsilon)\mathbf{M}_\lambda \mathbf{A}_R(\varepsilon_\sigma)]\{f_L(\varepsilon) - f_R(\varepsilon_\sigma)\}, \quad (6)$$

where $\tilde{\mathbf{A}}_\alpha = \mathbf{G}^a\boldsymbol{\Gamma}_\alpha\mathbf{G}^r$ is the time-reversed version of $\mathbf{A}_\alpha$. In the second derivative of I_i with respect to voltage V, the coth parts give rise to a sharply peaked signal around $|eV| = \hbar\omega_\lambda$, with width of the order of k_BT. If the electronic structure ($\mathbf{A}_\alpha$) varies slowly on the k_BT scale, it can be replaced by a constant using $\varepsilon \approx \mu_L$ and $\varepsilon_\sigma \approx \mu_R = \mu_L + \sigma\hbar\omega_\lambda$. Thus, around the vibration threshold we get

$$\partial_V^2 I_i \approx \gamma_{i,\lambda}\,\partial_V^2 \mathcal{I}^{\mathrm{sym}}, \quad (7)$$

$$\gamma_{i,\lambda} = \mathrm{Tr}[\mathbf{M}_\lambda \tilde{\mathbf{A}}_L(\mu_L)\mathbf{M}_\lambda \mathbf{A}_R(\mu_R)], \quad (8)$$

where we, as in the LOE-WBA, define the "universal" function

$$\mathcal{I}^{\mathrm{sym}} \equiv \frac{G_0}{2e}\sum_{\sigma=\pm}\sigma(\hbar\omega_\lambda+\sigma eV) \times\left(\coth\frac{\hbar\omega_\lambda}{2k_BT} - \coth\frac{\hbar\omega_\lambda+\sigma eV}{2k_BT}\right). \quad (9)$$

The elastic term I_e [Eq. (1)] can be divided into two parts, $I_e = I_e^n + I_e^h$, where the first (latter) represents all terms without (with) the Hilbert transformation originating in Eq. (4). The "non-Hilbert" part I_e^n yields a coth factor and integral of similar in form to the one for I_i. Both I_i and I_e^n thus yield an inelastic signal with a line shape given by the function $\partial_V^2\mathcal{I}^{\mathrm{sym}}$ and the sign/intensity governed by $\gamma_\lambda = \gamma_{i,\lambda} + \gamma_{e,\lambda}$, with $\gamma_{e,\lambda} \approx \mathrm{Im}B_\lambda$, and

$$B_\lambda \equiv \mathrm{Tr}[\mathbf{M}_\lambda\mathbf{A}_R(\mu_L)\boldsymbol{\Gamma}_L(\mu_L)\mathbf{G}^r(\mu_L)\mathbf{M}_\lambda\mathbf{A}_R(\mu_R) - \mathbf{M}_\lambda\mathbf{G}^a(\mu_R)\boldsymbol{\Gamma}_L(\mu_R)\mathbf{A}_R(\mu_R)\mathbf{M}_\lambda\mathbf{A}_L(\mu_L)]. \quad (10)$$

The "Hilbert" part I_e^h requires a bit more consideration. Besides terms which do not result in threshold signals [19], we have terms involving $\mathcal{H}[\mathbf{A}_\alpha f_\alpha]$. Again, if $\mathbf{A}_\alpha$ varies slowly around the step in f_α we may approximate

$$\mathcal{H}[\mathbf{A}_\alpha(\varepsilon')f_\alpha(\varepsilon')](\varepsilon) \approx \mathbf{A}_\alpha(\varepsilon)\mathcal{H}[f_\alpha(\varepsilon')](\varepsilon)\,. \quad (11)$$

The Hilbert transformation of the Fermi function is strongly peaked at the chemical potential, and again we evaluate the energy integral by evaluating all electronic structure functions ($\mathbf{A}_\alpha, \mathbf{G}^r, \boldsymbol{\Gamma}_\alpha$) at the peak values, keeping only the energy dependence of the functions related to f_α inside the integral. The result is

$$\partial_V^2 I_e^h \approx \kappa_\lambda\,\partial_V^2\mathcal{I}^{\mathrm{asym}}, \quad (12)$$

with $\kappa_\lambda = 2\mathrm{Re}B_\lambda$ and, again as in the LOE-WBA, the universal function

$$\mathcal{I}^{\mathrm{asym}} \equiv \frac{G_0}{2e}\int_{-\infty}^{+\infty} d\varepsilon \mathcal{H}\{f(\varepsilon'_-) - f(\varepsilon'_+)\}(\varepsilon)[f(\varepsilon - eV) - f(\varepsilon)] \approx -\frac{G_0}{2e\pi}\sum_{\sigma=\pm}\sigma(eV+\sigma\hbar\omega_\lambda)\ln\left|\frac{eV+\sigma\hbar\omega_\lambda}{\hbar\omega_\lambda}\right|. \quad (13)$$

Here the latter is for $k_BT = 0$, while it can be expressed using the digamma function for finite k_BT [20]. In total we have written the IETS as a sum of individual vibration signals [10],

$$\partial_V^2 I(V) = \gamma_\lambda\,\partial_V^2\mathcal{I}^{\mathrm{sym}}(V,\hbar\omega_\lambda,T,N_\lambda) + \kappa_\lambda\,\partial_V^2\mathcal{I}^{\mathrm{asym}}(V,\hbar\omega_\lambda,T). \quad (14)$$

Equation (14) is our main formal result. As for the LOE-WBA we have expressed the vibration signals from the universal functions, and structure factors containing quantities readily obtained from DFT-NEGF. However, importantly, here we have generalized these to include the effect of *finite* $\hbar\omega_\lambda$, and thus the change in electronic structure over the excitation energy. Our LOE expressions for γ_λ and κ_λ above simply reduce to the LOE-WBA when $\mu_L = \mu_R = \mu_0$. We will now demonstrate some situations where the LOE expression Eq. (14) is crucial for detailed interpretation of experimental IETS line shapes.

Simple model. First we use a single-level model to illustrate how the "asymmetric" term contains important information about the energy dependence of the electrode couplings. In the LOE-WBA one always has $\kappa_\lambda = 0$ for symmetric junctions. This is *not* the case for the LOE expression Eq. (10). We therefore consider a *symmetric junction* containing a single electronic level at ε_0 (with $\mu_0 = 0$), coupled to a local vibration (ω_0), and with energy-dependent electrode coupling rates. Assuming symmetrical potential drop, and using the notations $\Gamma_l = \Gamma_L(\mu_L) + \Gamma_R(\mu_L)$ and $\Gamma_r = \Gamma_L(\mu_R) + \Gamma_R(\mu_R)$ we can write the "symmetric,"

$$\gamma = -C\left\{\Gamma_l^2\Gamma_r^2 - \left(4\varepsilon_0^2 - \hbar^2\omega_0^2\right)^2\right\}, \quad (15)$$

and "asymmetric" coefficients,

$$\kappa = 4C(\delta\Gamma\,\varepsilon_0 + \bar{\Gamma}\,\hbar\omega_0)\left\{\Gamma_l\Gamma_r - \left(4\varepsilon_0^2 - \hbar^2\omega_0^2\right)\right\}, \quad (16)$$

where $\delta\Gamma = \Gamma_l - \Gamma_r$, $\bar{\Gamma} = (\Gamma_l + \Gamma_r)/2$, and C is a constant common to γ and κ. In the typical case of transition metal electrodes the coupling can contain contributions both from a wide s band as well as from a narrow d band leading to a significant $\delta\Gamma$ and finite κ. To model the s band we use a constant Γ_0, and to mimic the coupling (hopping t') to a d band we add the self-energy of a semi-infinite 1D chain, with bandwidth $2W$ centered at $\mu_0 = 0$. Figures 1(a)–1(c) compare the signals calculated from LOE-WBA and LOE for different ε_0. For both treatments we observe that the peak in the off-resonance IETS evolves into a dip on-resonance. However, only in the LOE the two regimes are separated by a peak-dip structure close to resonance due to the asymmetric κ, which is enhanced at the onset of the coupling with d band in one electrode. The change in IETS signal with a gate-potential (ε_0) is shown in Fig. 1(d). The features observed at $\varepsilon_0 = \pm\hbar\omega/2 - W$ is associated with the level being resonant with the left/right d-band onset, respectively, see Fig. 1(e).

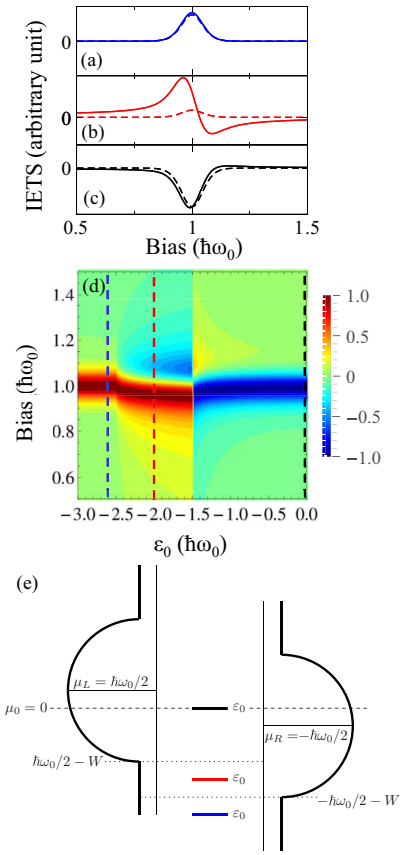

FIG. 1. (Color online) (a)–(c) IETS spectrum from LOE (solid) and LOE-WBA (dashed) for three different position of an electronic level, coupling with a wide s band with constant density of states, and a narrow d band with bandwidth W centered at the equilibrium Fermi level $\mu_0 = 0$. (a) $\varepsilon_0 = -2.6$, (b) $\varepsilon_0 = -2$, and (c) $\varepsilon_0 = 0$. The transmission coefficients at the Fermi level are $T = 0.006, 0.01, 1$, respectively. (d) Contour plot of the IETS spectrum for different level positions. The signal is normalized such that for each given ε_0, the height of the largest peak or dip is 1. Parameters in unit of the vibration energy $\hbar\omega_0$: $t' = 2t = W = 2$, $\Gamma_0 = 0.1$, $k_B T = 0.02$. Here t is the hopping matrix element of the d band, and t' is its coupling to the electronic level. (e) Schematics of the one-level model (shown for the three different level positions) biased at the emission threshold $V = \hbar\omega_0$.

IETS of benzene-dithiol. It has been possible to apply an external gate potential to junctions with small molecules between metallic electrodes [5,6]. Under these conditions IETS have been recorded for gated octane-dithiol (ODT) and benzene-dithiol (BDT) molecules between gold electrodes [6]. For both ODT and BDT the quite symmetric I-V characteristics indicates a symmetric bonding to the electrodes. For the π-conjugated BDT it was shown how the transport can be tuned from far off-resonance ($G \sim 0.01 G_0$) to close to the HOMO resonance increasing the conductance by more than an order of magnitude. As in the simple symmetric model above, this was reflected in the shape of the IETS signal for BDT going from a peak for off-resonance, to a peak-dip close to resonance, with the peaks appearing at the same voltages. However, the analysis by Song *et al*. [6] was based on a model assuming asymmetric electrode couplings at zero bias (STM regime) [16]. Our simple model [Fig. 1(b)] instead suggests that the observed peak-dip line shape originates solely from the Γ_l, Γ_r asymmetry driven by the bias voltage near resonance rather than from asymmetric electrode couplings in equilibrium (Γ_L, Γ_R at μ_0).

Next, we turn to our DFT-NEGF calculations [21]. The importance of an efficient scheme is underlined by the fact that an IETS calculation is required for each gate value. In the break-junction experiments the atomic structure of the junction is unknown. We anticipate that the gap between the electrodes is quite open and involves sharp asperities with low-coordinated gold atoms in order to allow for the external gating to be effective. In order to emulate this we consider BDT bonded between adatoms on Au(111) surfaces [Fig. 2(a)], and employ only the Γ point in the transport calculations yielding sharper features in the electronic structure. We correct the HOMO-LUMO gap [22] and model the electrostatic gating simply by a rigid shift of the molecular orbital energies relative to the gold energies. In Figs. 2(b) and 2(c) we compare IETS calculated with LOE and LOE-WBA as a function of gating. As in the experiment, we observe three clear signals around $\hbar\omega = 95, 130, 200$ meV due to benzene vibrational modes. Off-resonance the LOE and LOE-WBA are in agreement as expected. But when the gate voltage is tuned to around $V_g \approx -1$ V the methods deviate because of the appearance of sharp resonances in the transmission around the Fermi energy [Fig. 2(a)]. These resonances involve the d orbitals on the contacting gold atoms, as seen in the eigenchannel [23] plot in Fig. 2(a), and result in a peak-dip structure as seen in the experiment and anticipated by the simple model. Thus it is important to go beyond LOE-WBA in order to reproduce the peak to peak-dip transition taken as evidence for close-to-resonance transport.

IETS of alkane-dithiol. As another demonstration of the improvement of LOE over LOE-WBA, we consider molecular junctions formed by straight or tilted butane-dithiol (C4DT) molecules linked via low-coordinated Au adatoms to Au(111) electrodes, see inset to Fig. 3. Based on DFT-NEGF [21] we calculate elastic transmission and IETS for the periodic structure averaged over electron momentum $k_{||}$ [24]. As shown in Figs. 3(a) and 3(b), transport around the Fermi level is off-resonance but dominated by the tail of a sulfur-derived peak centered at approximately 0.25 eV below the Fermi level. This feature introduces a relatively strong energy dependence into the electronic structure which makes the WBA questionable. Indeed, as shown in Fig. 3(c), LOE-WBA gives a smaller IETS intensity compared to the LOE for the energetic CH_2 stretch modes ($\hbar\omega \sim 375$ meV). The WBA may thus be the reason why LOE-WBA calculations were reported to underestimate the IETS intensity for these energetic modes in comparison with experiments [18]. We note that the intensity enhancement is found to be more pronounced for the straight configuration, which we speculate may be related to the change in the sulfur density of states as a function of tilt (for the tilted geometry

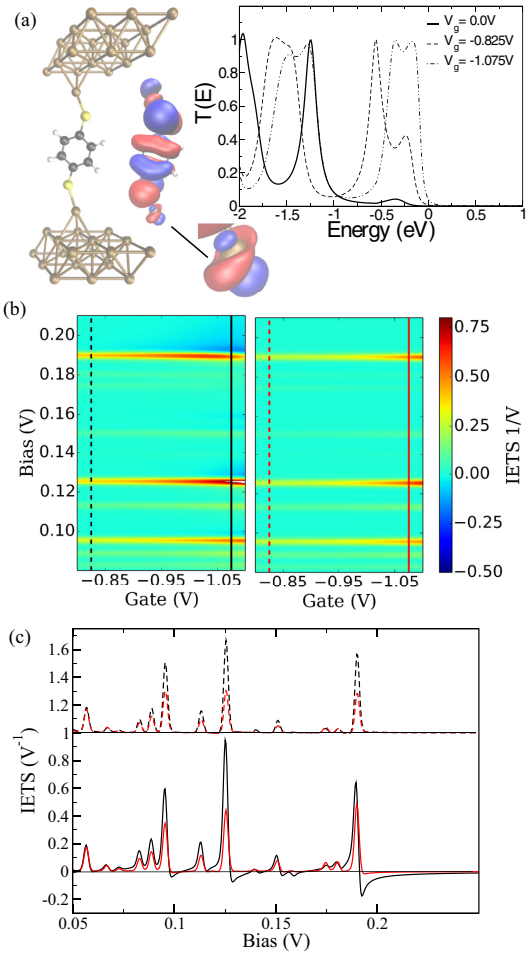

FIG. 2. (Color online) (a) BDT between two adatoms on Au(111) together with transmission for off-resonance (zero gate) and close-to-resonance. (b) IETS as a function of gate voltage from LOE (left) and LOE-WBA (right). (c) IETS for fixed gate voltage off-resonance (dashed lines, offset for clarity) and close-to-resonance (solid lines). Black: LOE, red: LOE-WBA. The IETS signals are calculated for $T = 4.2$ K and processed to mimic the experimental broadening arising from the lock-in technique with a harmonic voltage modulation of $V_{\text{rms}} = 1$ mV [13].

the slope of the PDOS close to the Fermi level decreases). The intensity change reported in Fig. 3 thus suggests the relevance of going beyond LOE-WBA for simulations involving high-energy vibrational modes.

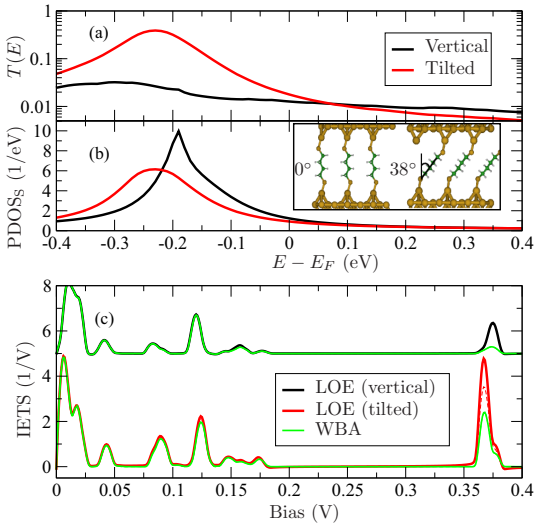

FIG. 3. (Color online) (a) Transmission and (b) projected density of states over S for vertical and tilted C4DT in a 2×2 supercell of Au(111). (c) IETS within LOE and LOE-WBA (averaged over $k_{||}$) using $T = 4.2$ K and $V_{\text{rms}} = 5$ mV [13]. Thin dashed lines represent the reverse bias polarity.

Conclusions. A generalized LOE scheme for IETS simulations with the DFT-NEGF method has been described. Without introducing the WBA, our formulation retains both the transparency and computational efficiency of the LOE-WBA. This improvement is important to capture correctly the IETS line shape in situations where the electronic structure varies appreciably on the scale of the vibration energies, such as near sharp resonances or band edges. Together with DFT-NEGF calculations we have discovered that the intricate experimental line shape of a gated BDT can be explained without the need to assume asymmetric bonding of the molecule to the electrodes. Also, simulations for C4DT junctions suggest that going beyond WBA is important to capture the IETS intensity related to energetic CH_2 stretch modes.

Acknowledgements. We acknowledge computer resources from the DCSC, and support from Center for Nano-structured Graphene (Project DNRF58). J.T.L. acknowledges support from the National Natural Science Foundation of China (Grants No. 11304107 and No. 61371015), and the Fundamental Research Funds for the Central Universities (HUST:2013TS032). G.F. and T.F. acknowledge support from the Basque Departamento de Educacíon and the UPV/EHU (Grant No. IT-756-13), the Spanish Ministerio de Economía y Competitividad (Grant No. FIS2010-19609-CO2-00), and the European Union Integrated Project PAMS.

[1] B. C. Stipe, M. A. Rezaei, and W. Ho, Science **280**, 1732 (1998).

[2] N. Agrait, C. Untiedt, G. Rubio-Bollinger, and S. Vieira, Phys. Rev. Lett. **88**, 216803 (2002).

[3] R. H. M. Smit, Y. Noat, C. Untiedt, N. D. Lang, M. C. van Hemert, and J. M. van Ruitenbeek, Nature (London) **419**, 906 (2002).
[4] J. G. Kushmerick, J. Lazorcik, C. H. Patterson, R. Shashidhar, D. S. Seferos, and G. C. Bazan, Nano Lett. **4**, 639 (2004).
[5] L. H. Yu, Z. K. Keane, J. W. Ciszek, L. Cheng, M. P. Stewart, J. M. Tour, and D. Natelson, Phys. Rev. Lett. **93**, 266802 (2004).
[6] H. Song, Y. Kim, Y. H. Jang, H. Jeong, M. A. Reed, and T. Lee, Nature (London) **462**, 1039 (2009).
[7] N. Okabayashi, M. Paulsson, and T. Komeda, Prog. Surf. Sci. **88**, 1 (2013).
[8] M. Galperin, M. A. Ratner, and A. Nitzan, J. Phys.: Condens. Matter **19**, 103201 (2007).
[9] N. Sergueev, D. Roubtsov, and H. Guo, Phys. Rev. Lett. **95**, 146803 (2005).
[10] M. Paulsson, T. Frederiksen, and M. Brandbyge, Phys. Rev. B **72**, 201101 (2005).
[11] J. Jiang, M. Kula, W. Lu, and Y. Luo, Nano Lett. **5**, 1551 (2005).
[12] G. C. Solomon, A. Gagliardi, A. Pecchia, T. Frauenheim, A. Di Carlo, J. R. Reimers, and H. S. Hush, J. Chem. Phys. **124**, 094704 (2006).
[13] T. Frederiksen, M. Paulsson, M. Brandbyge, and A.-P. Jauho, Phys. Rev. B **75**, 205413 (2007).
[14] E. T. R. Rossen, C. F. J. Flipse, and J. I. Cerdá, Phys. Rev. B **87**, 235412 (2013).
[15] J. K. Viljas, J. C. Cuevas, F. Pauly, and M. Hafner, Phys. Rev. B **72**, 245415 (2005).
[16] B. N. J. Persson and A. Baratoff, Phys. Rev. Lett. **59**, 339 (1987).
[17] R. Egger and A. O. Gogolin, Phys. Rev. B **77**, 113405 (2008).
[18] N. Okabayashi, M. Paulsson, H. Ueba, Y. Konda, and T. Komeda, Nano Lett. **10**, 2950 (2010).
[19] F. Haupt, T. Novotny, and W. Belzig, Phys. Rev. B **82**, 165441 (2010).
[20] G. Bevilacqua, arXiv:1303.6206.
[21] We employ the SIESTA [25]/TranSIESTA [26] method with the GGA-PBE [27] exchange-correlation functional. Electron-vibration couplings and IETS are calculated with Inelastica [13].
[22] V. M. García-Suárez and C. J. Lambert, New J. Phys. **13**, 053026 (2011).
[23] M. Paulsson and M. Brandbyge, Phys. Rev. B **76**, 115117 (2007).
[24] G. Foti, D. Sanchez-Portal, A. Arnau, and T. Frederiksen, J. Phys. Chem. C **117**, 14272 (2013).
[25] J. M. Soler, E. Artacho, J. D. Gale, A. Garcia, J. Junquera, P. Ordejon, and D. Sanchez-Portal, J. Phys.: Condens. Matter **14**, 2745 (2002).
[26] M. Brandbyge, J. L. Mozos, P. Ordejon, J. Taylor, and K. Stokbro, Phys. Rev. B **65**, 165401 (2002).
[27] J. P. Perdew, K. Burke, and M. Ernzerhof, Phys. Rev. Lett. **77**, 3865 (1996).

C.2 Paper 3

Rasmus B. Christensen, Thomas Frederiksen and Mads Brandbyge

Identication of pristine and defective graphene nanoribbons by phonon signatures in the electron transport characteristics

Accepted for PHYSICAL REVIEW B

Identification of pristine and defective graphene nanoribbons by phonon signatures in the electron transport characteristics

Rasmus B. Christensen,[1] Thomas Frederiksen,[2,3] and Mads Brandbyge[4]

[1] *Dept. of Micro- and Nanotechnology, Technical University of Denmark, Ørsteds Plads, Bldg. 345E, DK-2800 Kongens Lyngby, Denmark*
[2] *Donostia International Physics Center (DIPC) – UPV/EHU, Donostia-San Sebastián, Spain*
[3] *IKERBASQUE, Basque Foundation for Science, Bilbao, Spain*
[4] *Center for Nanostructured Graphene (CNG), Dept. of Micro- and Nanotechnology, Technical University of Denmark, Ørsteds Plads, Bldg. 345E, DK-2800 Kongens Lyngby, Denmark**

(Dated: February 12, 2015)

Inspired by recent experiments where electron transport was measured across graphene nanoribbons (GNR) suspended between a metal surface and the tip of a scanning tunneling microscope [Koch *et al.*, Nat. Nanotechnol. **7**, 713 (2012)], we present detailed first-principles simulations of inelastic electron tunneling spectroscopy (IETS) of long pristine and defective armchair and zigzag nanoribbons under a range of charge carrier conditions. For the armchair ribbons we find two robust IETS signals around 169 and 196 mV corresponding to the D- and G-modes of Raman spectroscopy as well as additional fingerprints due to various types of defects in the edge passivation. For the zigzag ribbons we show that the spin state strongly influences the spectrum and thus propose IETS as an indirect proof of spin polarization.

PACS numbers: 81.05.ue, 73.63.-b, 72.10.Di

I. INTRODUCTION

Graphene as the basis of a new generation of electronics[1,2] has been the center of much attention in the last years, and devices based on nanostructured graphene have been put forward. The most generic form of nanostructured graphene is graphene nanoribbons (GNR),[3] and other structures, such as graphene anti-dot lattices[4,5], can be viewed as networks of them. GNRs are potential candidates for molecular wires with tailored conductance properties. For graphene-based nanostructures the edges and their passivation, as well as defects inside the structure, can play crucial roles for the transport properties.[6] However, characterization of edge passivation or structural/chemical defects is challenging especially after device fabrication. Raman spectroscopy[7] can give information about defects on large areas of the sample, while tip-enhanced Raman spectroscopy (TERS)[8] have been used in combination with STM on GNRs. However, Raman studies involve averages over larger areas (> 10 nm), and does not yield information about the impact of vibrations on transport. In that aspect inelastic electron tunneling spectroscopy (IETS) serves as a way of performing non-destructive characterization yielding vibrational/phonon fingerprints of a range of defects. In order to interpret IETS experiments, theoretical modeling of the inelastic signals in the electronic current due to electron-phonon (e-ph) scattering is needed.

GNRs have been fabricated using different strategies including lithographic techniques,[9] chemical synthesis,[10,11] epitaxial growth[12], and longitudinal unzipping of carbon nanotubes.[13] Furthermore, several groups have succeeded in atomically precise bottom-up fabrication of armchair GNRs (AGNR)[14,15], chiral GNRs,[16] and AGNR hetero-junctions[17] grown on metal surfaces. Experimentally, the vibrational properties have been investigated by Raman spectroscopy and the electronic structure has been mapped out by STM, angle-resolved (two-photon) photo-emission and high-resolution electron energy loss spectroscopy.[8,18,19] Signatures of phonon excitation were observed by STM in the differential conductance spectroscopy performed at the zigzag termini state of AGNRs adsorbed on Au(111), and these signatures were shown to be sensitive to modifications in the local atomic geometry.[20] AGNRs have also been lifted up from the weakly bonding Au(111) surface with the tip of a STM enabling measurements of the voltage-dependent conductance in suspended configurations.[21]

From the theoretical side density-functional theory (DFT) has been used to investigate the stability of structural and chemical reconstructions of GNR edges,[22–24] together with the transport and band-gap engineering.[6,25–28] The vibrational properties and phonon band structure have been calculated with empirical potentials[29] and DFT.[30,31] In addition, there have been theoretical predictions[32,33] of the Raman spectrum, in good agreement with experiments.[14,34] For a finite AGNR the role of zigzag termini states have been studied theoretically, comparing DFT to the many-body Hubbard model.[35]

Inspired by the recent lifting experiments by Koch *et al.*,[21] we here investigate theoretically the signals of e-ph scattering in the conductance of long GNRs between metal electrodes. Our aim is two-fold. First, we want to address the role phonon scattering in the transport characteristics of pristine GNRs. Second, we wish to compute detailed IETS for different GNRs under varying charge

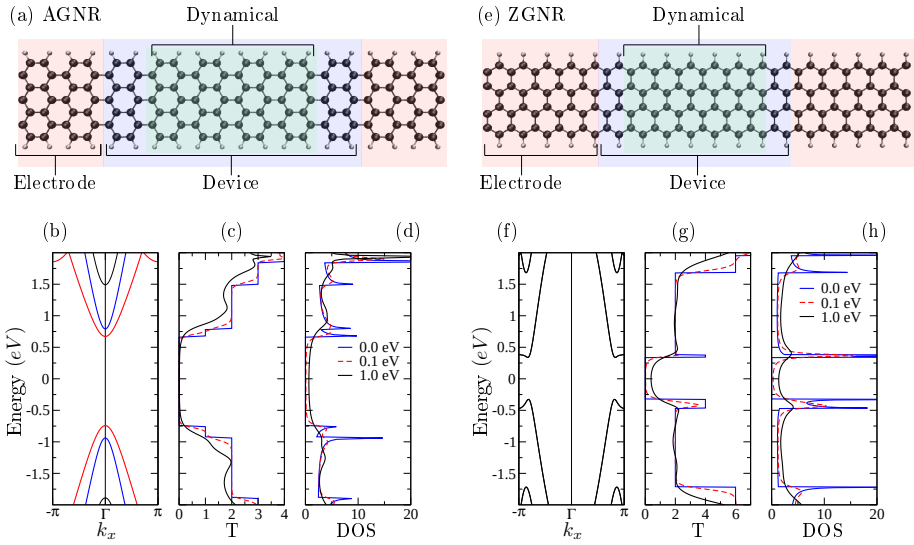

FIG. 1: (Color online) (a) Computational setup for a pristine AGNR showing electrode, device and dynamical regions. (b) Electronic band structure (k_x is in units of inverse unit cell length). The different bands are colored according to symmetry of the electronic states. Red: symmetric, corresponding to Fig. 2(a-b). Blue: anti-symmetric, corresponding to Fig. 2(c-d). (c) Electronic transmission for varying electrode broadening describing the coupling to the metal contacts, $\eta = 0, 0.1, 1$ eV, see text. (d) Electronic DOS projected onto the dynamical region. Panels (e)-(h) show the similar entities for the pristine ZGNR case.

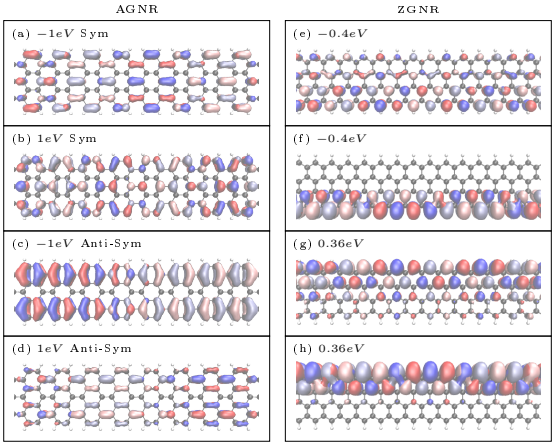

FIG. 2: (Color online) (a)-(d) Electron transmission eigenchannels for the clean AGNR for the valence bands at $E - E_F = -1$ eV and for the conduction bands at $E - E_F = 1$ eV. (e)-(h) Electron transmission eigenchannels for the clean ZGNR in the valence bands at $E - E_F = -0.4$ eV and in the conduction bands at $E - E_F = 0.4$ eV for one spin component. The eigenchannels for the other spin component are simply mirror images around the middle of the ZGNR (not shown). The red/blue (pink/gray) isosurfaces represent the real (imaginary) part and sign of the scattering state wave function. For all eigenchannel calculations the electrode broadening was set to zero ($\eta = 0$ eV).

carrier concentrations and explore how different types of realistic defects may modify the IETS and thus possibly be directly probed in transport measurements. We focus on the two most generic edge types, namely armchair (AGNR) and zigzag (ZGNR), and pay attention to the effects of spin polarization in the latter case. In actual experiments the substrate or an applied gate potential control the Fermi level E_F in the ribbons. To address this variability we scan E_F using a numerically effective scheme enabling fast calculations of the IETS.[36] We find that the AGNR generally display two robust IETS signals around 169 and 196 mV corresponding to the D- and G-modes of Raman spectroscopy and that a dehydrogenated dimer at the edge should further leave a clear defect signal at around 245 mV. For the ZGNR we find that the spin polarization breaks the mirror symmetry around the middle of the ribbon resulting in IETS signals from a range of modes around the D- and G-mode energies. For both AGNR and ZNGR defects which break the planar symmetry of ribbons allows for contributions to the IETS from out-of-plane phonon modes.

The paper is organized as follows. First we discuss our atomistic model setup for the density functional and electron transport calculations, and outline the approach for the IETS simulations. In Sec. III we present our results for pristine AGNR and ZGNR and relate their transport properties and IETS to the band structures. In Sec. IV we turn to the defective systems by considering realistic possibilities of defects in the edge passivation, backbone

bonding motifs, and presence of adatoms. Finally, a summary and our conclusions are presented in Sec. V.

II. METHODS

We calculate the electronic and vibrational structure from DFT using the academic codes SIESTA/TRANSIESTA.[37,38] We employ the generalized gradient approximation (GGA) for the exchange-correlation functional,[39] a single-zeta polarized (SZP) basis set for the carbon and hydrogen atoms, and use a cut-off energy of 400-500 Ry for the real-space grid. These choices, balancing accuracy and computational cost, provide a good description to investigate trends and general behavior of the substantial number of systems considered in this work.

The vibrational degrees of freedom, calculated by diagonalization of the dynamical matrix, and the e-ph couplings are extracted from finite differences as implemented in the INELASTICA code.[40–42] The armchair and zigzag GNRs considered here are shown in Fig. 1. We adopt the usual two-probe setup with the device region (D) coupled to left (L) and right (R) electrodes with all electronic matrix elements expressed in a local basis set. The primitive unit cell of the AGNR (ZGNR) consists of 18 (10) atoms and in our calculations this unit cell is repeated 10 (18) times in the transport direction to form the scattering regions illustrated in Fig. 1(a,e). The electrode couplings $\mathbf{\Gamma}_{L/R}$ are included on the two first/last unit cells before folding onto D. In our treatment a subset of atoms in D is allowed to vibrate. We fix this dynamical region, restricted by the condition that the e-ph couplings are fully included inside D, to the 4 and 6 central unit-cells for the AGNR and ZGNR, respectively. The corresponding e-ph couplings used to calculate the inelastic electron transport are thus expressed in the center 6 unit-cells for the AGNR and 8 unit-cells for the ZGNR. The convergence of our results with the size of the dynamical region is addressed below.

We generally consider nanoribbons that are suspended between two metallic leads. In the case of the lifting experiments,[21] these would correspond to the metal sample surface and the STM tip. We wish here to focus on the action inside the GNRs and put aside the possible complications due to the detailed electronic structure of the metals, and the metal-GNR interface in particular. To this end we introduce a simple model of the metal electrodes without substantial electronic features: we use semi-infinite GNRs with highly broadened states (effectively smearing out energy gaps). In practice this is done by adding a finite numerical imaginary part η to the energy argument in the electrode recursion calculation.[43] This scheme ensures that the phonon effects originate from the GNRs themselves and not from details of the metal-GNR interface, which is generally unknown in the STM experiments. The electronic band structures for the infinite ribbons, along with the transmission and density of states (DOS) are shown for $\eta = 0, 0.1, 1$ eV in Fig. 1(b,c,d) and Fig. 1(f,g,h) for AGNR and ZGNR, respectively. We note that the broadened transmission spectrum [Fig. 1(d)] is quite consistent with the experimentally reported differential conductance curves for AGNR.[21] The electronic states involved in the transport are shown in Fig. 2 in terms of the transmission eigenchannels[44] in the valence and conduction bands of the AGNR and ZGNR. Their spatial symmetry play a significant role for the selection rules involved in the inelastic scattering as discussed later.

In principle, the electronic structure should be evaluated at finite bias. However, without a detailed model of the connection to the metal electrodes (where an important part of the voltage drop will take place) and for sufficiently long systems (in which the electric field will be small), it is reasonable to use the zero-voltage electronic structure and to simply assume a symmetric voltage drop over the two identical, idealized device-electrode interfaces. More specifically, in the following we will treat the applied potentials non-self-consistently. An equal voltage drop (V) is used at the left and right electrodes for these left-right symmetric structures, and shift the electronic states and chemical potentials in the left/right electrodes by $\pm V/2$. We introduce the applied gate voltage V_G (mimicking actual doping or electrostatic gating that modify the charge carrier concentration in an experimental setup) as a shift in all energies. Thus close to the excitation threshold of a phonon λ we consider inelastic scattering between states at energies around the chemical potentials, $\mu_{L/R} = E_F \pm \hbar\omega_\lambda/2 + V_G$.

A. Computational scheme for IETS

For a device strongly coupled to the electrodes, a coupling between the electron current $I(V)$ and a phonon mode λ ideally shows up at zero temperature as a step discontinuity in the differential conductance when the inelastic phonon emission process becomes energetically allowed, that is, when the chemical potential difference exceeds the quantum of vibrational energy, $|\mu_L - \mu_R| = \hbar\omega_\lambda$. Thus, around the emission threshold the electronic states involved in the scattering process are those at μ_L and μ_R. The IETS signal, conventionally expressed as the ratio between the second and first derivatives of the current with respect to the voltage,

$$\mathrm{IETS} = \frac{\partial_V^2 I(V)}{\partial_V I(V)}, \tag{1}$$

is calculated by considering the e-ph coupling as the perturbation on the current, evaluated using the nonequilibrium Green's functions (NEGF). In the so-called lowest order expansion (LOE) the inelastic part of the differential conductance can be written as,[36]

$$\begin{aligned}\partial_V I(V) =& \gamma_\lambda\, \partial_V \mathcal{I}^{\mathrm{sym}}(V, \hbar\omega_\lambda, T) \\ &+ \kappa_\lambda\, \partial_V \mathcal{I}^{\mathrm{asym}}(V, \hbar\omega_\lambda, T),\end{aligned} \tag{2}$$

where summation over the vibration index λ is assumed. $\mathcal{I}^{\rm sym}$ and $\mathcal{I}^{\rm asym}$ are the "universal" (system-independent) functions that depend on the applied bias V, phonon energy $\hbar\omega_\lambda$ and the temperature T. Assuming the electronic and phononic distribution functions are given by the Fermi-Dirac and Bose-Einstein distributions, respectively, their analytical expressions can be written as:

$$\mathcal{I}^{\rm sym} \equiv \frac{\mathrm{G}_0}{2e}\sum_{s=\pm} s(\hbar\omega_\lambda + seV) \times \left(\coth\frac{\hbar\omega_\lambda}{2k_BT} - \coth\frac{\hbar\omega_\lambda + seV}{2k_BT}\right), \quad (3)$$

$$\mathcal{I}^{\rm asym} \equiv \frac{\mathrm{G}_0}{2e}\int_{-\infty}^{+\infty} d\varepsilon \mathcal{H}\{f(\varepsilon'_-) - f(\varepsilon'_+)\}(\varepsilon) \times \left[f(\varepsilon - eV) - f(\varepsilon)\right], \quad (4)$$

where $\mathrm{G}_0 = 2e^2/h$ is the conductance quantum, $f(\varepsilon)$ is the Fermi-Dirac function, $\varepsilon'_s \equiv \varepsilon' + s\hbar\omega_\lambda$, and $\mathcal{H}$ denotes the Hilbert transform.

The signal amplitudes γ_λ and κ_λ of the symmetric and antisymmetric signals in the differential conductance are even and odd in bias, respectively. For a symmetric structure the asymmetric signal vanishes in the wide-band approximation (LOE-WBA)[40]. However, this is not guaranteed in the more general treatment employed here,[36] where the energy dependence of the electronic structure is explicitly taken into account. The amplitudes γ_λ and κ_λ are expressed in terms of electronic structure quantities and e-ph couplings,[36]

$$\gamma_\lambda = \mathrm{Tr}[\mathbf{M}_\lambda \tilde{\mathbf{A}}_L(\mu_L)\mathbf{M}_\lambda \mathbf{A}_R(\mu_R)] + \mathrm{Im}B_\lambda, \quad (5)$$

$$\kappa_\lambda = 2\mathrm{Re}B_\lambda, \quad (6)$$

where B_λ is defined as

$$B_\lambda \equiv \mathrm{Tr}[\mathbf{M}_\lambda \mathbf{A}_R(\mu_L)\mathbf{\Gamma}_L(\mu_L)\mathbf{G}^r(\mu_L)\mathbf{M}_\lambda \mathbf{A}_R(\mu_R) - \mathbf{M}_\lambda \mathbf{G}^a(\mu_R)\mathbf{\Gamma}_L(\mu_R)\mathbf{A}_R(\mu_R)\mathbf{M}_\lambda \mathbf{A}_L(\mu_L)]. \quad (7)$$

In the above, $\mathbf{M}_\lambda$ denotes the e-ph coupling matrix for mode λ, $\mathbf{G}^{r/a}$ the retarded/advanced unperturbed Green's functions, and $\mathbf{A}_\alpha = \mathbf{G}^r\mathbf{\Gamma}_\alpha\mathbf{G}^a$ the spectral density matrices for left/right moving states with the time-reversed version $\tilde{\mathbf{A}}_\alpha = \mathbf{G}^a\mathbf{\Gamma}_\alpha\mathbf{G}^r$. The purely electronic quantities are thus being evaluated at the chemical potentials of the left/right electrodes corresponding to the excitation threshold for each vibration. We compute $\mathbf{M}_\lambda$ with the finite-difference scheme of Inelastica taking the vacuum energy as a common reference (in absence of real metal leads to pin the Fermi energy).[41]

In the localized atomic basis set of Siesta all the above quantities are matrices defined in the electronic space corresponding to region D. The second derivatives of the universal functions in Eqs. (3)-(4) are sharply peaked around the phonon threshold. For this reason the coefficients γ_λ and κ_λ can be considered voltage-independent with their values computed exactly at the threshold. Due to the computational efficiency of the LOE scheme described above we are able to evaluate the IETS on a fine grid of gate voltages V_G spanning a large range of relevant values between valence and conduction bands of the GNRs.

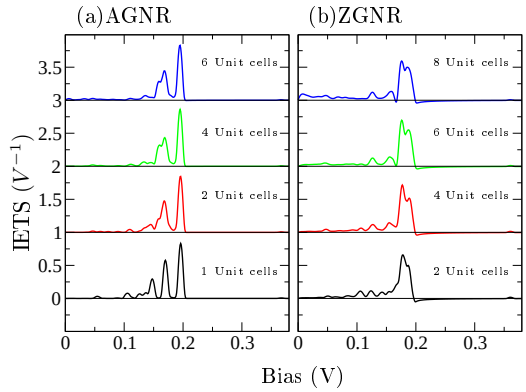

FIG. 3: (Color online) Convergence of the intrinsic IETS for pristine (a) AGNR and (b) ZGNR as a function of the size of the dynamical region (stated in the legends). The results are normalized with respect to the number of vibrating unit cells, i.e., we show the IETS amplitude per H_4C_{14} segment for AGNR and per H_2C_8 segment for ZGNR. No gate voltage is applied ($V_G = 0.0$ V).

III. PRISTINE GRAPHENE NANORIBBONS

Now we first turn to the IETS results of the two pristine (clean) ribbons, and in the following section to the impact of selected defects in the IETS. As our main system we focus on the AGNR systems directly relevant for the lifting experiments.[21] The results for the ZGNR are provided mainly as comparison and to look into the role of chirality and in particular effects rooted in spin polarization, and thus we now discuss these separately.

A. Pristine armchair nanoribbons

As representative of the AGNR class we have investigated a pristine AGNR with a width of $W = 7$ dimers (7-AGNR) corresponding to a C-C edge distance of 7.5 Å (see Fig. 1). It presents a direct semi-conducting band gap E_g due to the lateral confinement and can be classified as a "large-gap ribbons" since $p = 2$ is an integer in the relation $W = 3p + 1$.[1] We obtain $E_g \approx 1.3$ eV at the present level of approximation (DFT-GGA and SZP basis set), as seen from the electronic band structure shown in Fig. 1(b). This value is smaller than those estimated experimentally ($E_g \approx$ 2.3-2.6 eV for a flat AGNR on Au(111)[19,45] and $E_g \approx 2.7$ eV for an AGNR suspended between surface and STM-tip[21]) due to the underestimation of electron-electron interaction[46] which plays an

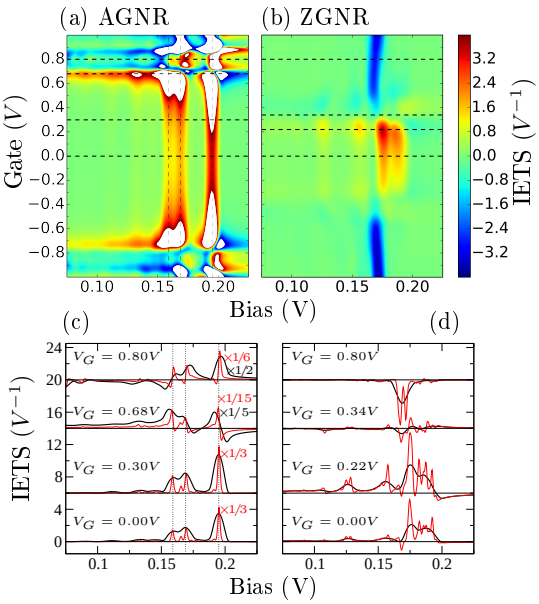

FIG. 4: (Color online) IETS signals as a function of gate voltage for (a) pristine AGNR (4 vibrating unit cells) and (b) pristine ZGNR (6 vibrating unit cells). Vertical dashed lines are guides to the eye indicating the energy of the most contributing vibrational modes. Specific IETS signals for the (c) AGNR and (d) ZGNR at selected gate voltages marked with horizontal dashed lines in panels (a) and (b). Broadening originates from temperature $T = 4.2$ K and a lock-in modulation voltage $V_{\rm rms} = 5$ mV (except for the thin red lines in the lower panels with $V_{\rm rms} = 0$ mV).

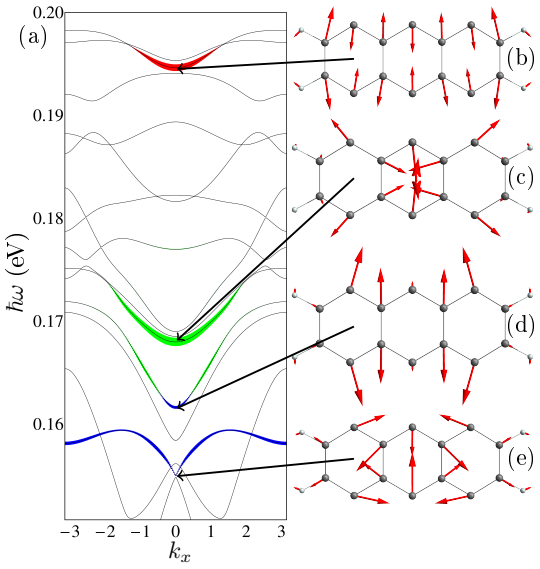

FIG. 5: (Color online) (a) Computed phonon band structure for the pristine, infinite AGNR (k_x is in units of inverse unit cell length). The magnitude of the red, green and blue bands (corresponding to the three vertical lines in Fig. 4(c)), is proportional to the signal size weighted overlap, ($F_{nk}(V_G = 0\text{V})$ in Eq. (8)), between the repeated band vector and modes with frequencies $\hbar\omega > 180$ meV, $180 > \hbar\omega > 162$ meV and $\hbar\omega < 162$ meV for red, green and blue, respectively. The red band is scaled by 0.2 compared to blue and green. (b-e) Selected phonon band modes at Γ for the infinite structure which, according to the projection, characterize the active IETS modes.

more important role in quasi one-dimensional GNRs compared to pristine graphene. Dielectric screening from the substrate also influences significantly the actual gap size: a band gap of 3.2 eV for a 7-AGNR was found to be lowered to 2.7 eV on a hexagonal boron-nitride (hBN) substrate using GW calculations,[47] similar to the lowering calculated for a 7-AGNR on Au(111).[48] In general we expect that underestimation of band gaps would mainly amount to a simple scaling the Fermi level position within the gap.

We first discuss the effect of the finite size of the dynamical region in our treatment. Figure 3(a) shows how the IETS signals for the AGNR (at fixed gate voltage $V_G = 0.0$ V) vary as a function of the size of the dynamical region, ranging from 1 to 6 unit cells. For easy comparison, the data are normalized by the number of vibrating unit cells. As the signal amplitudes in this representation are roughly constant we conclude that the absolute IETS simply scale linearly with the active e-ph coupling region. Consequently, the magnitudes in IETS may thus provide insight into the active scattering region in actual experiments. Further, as we find that both IETS amplitude and shape is well converged with 4 vibrating unit cells, we fix the dynamical region to this size in the following analysis.

The computed IETS signals for the AGNR as a function of varying gate voltage are shown in Fig. 4(a) as a density plot. Specific IETS spectra at selected gate voltages are shown in Fig. 4(c) for both the intrinsic part (temperature broadening at $T = 4.2$ K) as well as that one would observe employing the experimental lock-in technique (additional broadening due to a modulation voltage of $V_{\rm rms} = 5$ mV). We find that for the AGNR there are generally two well-defined IETS signals appearing around 169 and 196 meV, corresponding to the D- (ring breathing) and G- (E_{2g} phonon) modes, respectively, also observed in Raman spectroscopy.[7,9]. The D-signal also has a shoulder with a local maximum at 159 meV with contributions from several modes. These three distinct features are indicated with vertical lines in Fig. 4(a,c). Shifting E_F inside the gap region with a relatively small gate voltage $|V_G| \lesssim 0.5$ V does not affect the IETS appreciably. However, when E_F comes close to the conduction band of the AGNR the signal increases by a factor of five and a small peak-dip feature appear similar to the one reported for gated benzene-dithiol molec-

ular contacts.[36,49] Upon further gating into the conduction band the IETS signals undergo a sign reversal (from peaks to dips) as the transmission increases beyond approximately 0.5 for the involved channels.[50] This sign reversal can be traced back to the competition between inelastic and elastic scattering processes.[51–53] Similar effects are also found by gating into the valence band of the AGNR.

We can easily identify the most important vibrational mode vectors v_λ for the IETS from the two amplitudes $|\gamma_\lambda|$ and $|\kappa_\lambda|$ given in Eqs. (5)-(6). These modes can further be analyzed in terms of the phonons in the infinite AGNR. To do so we introduce the measure F_{nk} representing the overlap between modes in the finite dynamical cell and the phonon band modes weighted by the size of the IETS signal,

$$F_{nk}(V_G) = \sum_\lambda |\gamma_\lambda(V_G)| \left| u_{nk}\left(1, e^{ik}, \ldots, e^{i(N-1)k}\right) \cdot v_\lambda \right|^2, \tag{8}$$

where u_{nk} is the phonon band mode indexed by n, and v_λ is the modes in a finite N primitive cell long dynamical region index by λ.

The projections $F_{nk}(V_G = 0\text{V})$ are depicted as widths of the phonon bands in Fig. 5(a), where the red, green and blue colors refer to modes with frequencies in the ranges $\hbar\omega > 180$ meV, $180 > \hbar\omega > 162$ meV, and $\hbar\omega < 162$ meV, respectively. In total four bands contribute to the IETS signal corresponding to the four signals seen in the intrinsic part of the IETS spectrum in Fig. 4(c). The corresponding Γ-point phonon modes inside the primitive cell for the infinite ribbon are shown in Fig. 5(b-e).

In summary, the G-signal is due to the highest optical longitudinal mode shown in Fig. 5(b), corresponding to the red band in Fig. 5(a). The D-signal originates primarily from the ring breathing mode shown in Fig. 5(c), and has a small contribution from a longitudinal mode shown in Fig. 5(e) corresponding to the green bands in Fig. 5(a), while the shoulder in the D-band signal is due to the edge-phonon mode shown in Fig. 5(e) corresponding to the blue band in in Fig. 5(a).

B. Pristine zigzag nanoribbon

We next turn to our results for the pristine ZGNR shown in Fig. 1(e). It has a width of $W = 4$ zigzag "chains" (4-ZGNR) corresponding to a C-C edge distance of 7.26 Å. The breaking of sublattice symmetry for the ZGNR and lack of pseudo-phase result in different selection rules for the matrix elements and difference in for example Raman signals.[33] The ZGNR generally presents spin-polarized edge states exhibiting a small band gap at the DFT level,[1] in our case $E_g \approx 0.6$ eV (we note that this gap disappears in simpler tight-binding descriptions[1] or spin-degenerate DFT calculations). The spin-polarized edge states play the major role for the conduction, see the spin-down eigenchannels visualized in Fig. 2(e-h).

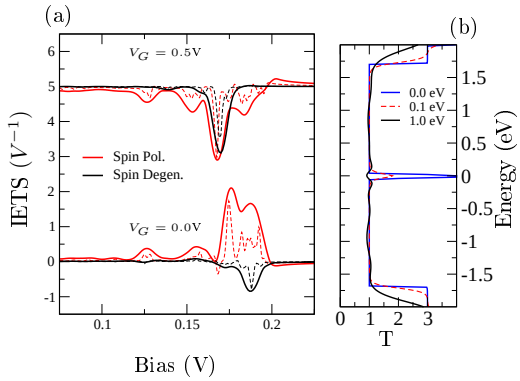

FIG. 6: (Color online) (a) IETS signals for the pristine ZGNR (6 vibrating unit cells). The black lines correspond to spin-degenerate calculations while the red lines are the spin-up components of spin-polarized calculations. Broadening originates from temperature $T = 4.2$ K and modulation voltage $V_{\rm rms} = 5$ mV (full lines) or $V_{\rm rms} = 0$ mV (dashed lines). (b) Electronic transmission from spin-degenerate calculations with varying electrode broadening describing the coupling to the metal contacts, $\eta = 0, 0.1, 1$ eV (see also Fig. 1(g) for the corresponding spin-polarized case).

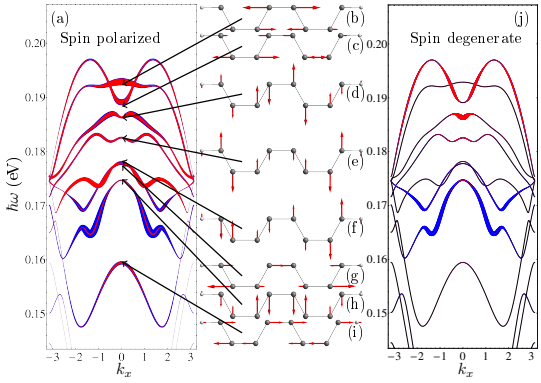

FIG. 7: (Color online) The phonon band structure of the ZGNR, (k_x is in units of inverse unit cell length), together with the Γ-point modes. The widths of the red bands are proportional to the weight function $F(0\text{V})$ (Eq. (8)), while the widths of the blue bands are proportional to $F(0\text{V})+F(0.5\text{V})$.

Since the edge states break the mirror symmetry with respect to the middle of the ribbon, there are fewer symmetry-forbidden inelastic transitions between the scattering states for the ZGNR. Thus, we expect a wider range of modes to contribute to the IETS signal as compared to the AGNR case. Indeed this is in agreement with the findings shown in Fig. 3(b) and Fig. 4(b,d). The greater number of modes contributing to the IETS for the ZGNR results in broader signals with similar magnitudes as compared to the IETS for AGNR. As for the AGNR

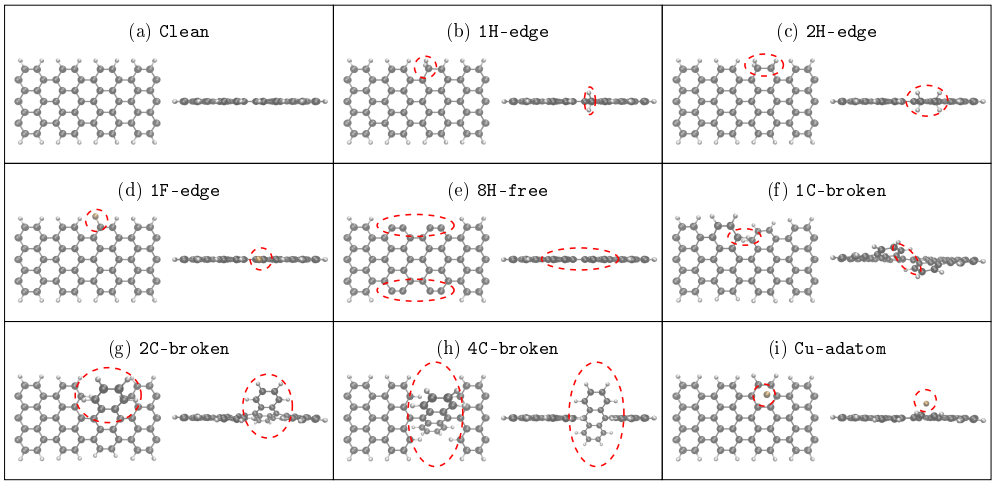

FIG. 8: (Color online) Top and side views of the dynamical region describing the various AGNR defect structures. The dashed red ellipses are guides to the eye highlighting the defect position. (a) Pristine AGNR. (b) One extra H atom on one of the edges. (c) Two extra H atoms on one of the edges. (d) One H atom replaced by a F atom. (e) Dehydrogenated edge where 4 H atoms have been removed from each side. (f) One broken C-C bond. (g) Two broken C-C bonds. (h) Four broken C-C bonds. (i) Cu adatom in a hollow site on the edge.

case the IETS signal is well converged with a dynamical region consisting of 6 vibrating unit cells [Fig. 3(b)].

For ZGNRs the ring breathing is forbidden by symmetry, thus the IETS is generally characterized by transverse and longitudinal modes. To explore the impact of spin-polarization on the ZGNR-IETS we compare in Fig. 6 the results from both spin-degenerate and spin-polarized calculations. Without gate voltage ($V_G = 0$ V) the IETS display opposite signs due to the spin-induced gap. Only a single peak contributes to the spin-degenerate IETS while several peaks contribute to the spin-polarized IETS. Even if the ZGNR is tuned by $V_G = 0.5$V to become metallic and the two treatments then show the same overall sign in IETS, the spin-polarized IETS persists to show a much richer structure. This difference suggests that IETS could be a way to indirectly observe spin-polarized edge states.

Projecting the modes contributing to the IETS onto the phonon band modes further underlines how several bands with different symmetries contribute to the spin-polarized IETS, while only a couple of bands contributes to the spin-degenerate IETS, see Fig. 7. Again we use Eq. (8) for this characterization, where the overlap for $V_G = 0.0$ V corresponds to the red color and the overlap for $V_G = 0.5$ V corresponds to the difference between the blue and red color in Fig. 7, respectively. It is clear that spin-polarization permits more modes to contribute to the IETS. In contrast to the spin-degenerate case, where the symmetric electronic states (with respect to the middle of the ribbon) only can couple to the symmetric vibration modes, the symmetry lowering of the electronic states by spin-polarization opens up also for scattering also via odd modes.

IV. DEFECTIVE GRAPHENE NANORIBBONS

In this section we address the modification and new signals in IETS that arise due to various defects in the GNR. Regardless of the fabrication method, defects will inevitable occur. For example, if the AGNRs are synthesized from a precursor molecule, involving heating and dehydrogenation, as reported by Cai *et al.*[14] and Blankenburg *et al.*,[15] there is a chance that the reaction is incomplete and some of the C-C bonds between the precursor molecules do not form. Also there is a chance that a part of the final AGNR will have dehydrogenated edges or are passivated by two hydrogen atoms. Finally, defects may be introduced on purpose by locally dosing a high current from the tip of a STM.[20]

A. Defects in AGNRs

In Fig. 8 we show the structures of pristine AGNR along with 8 different defect configurations which we have considered. These include four defects in the edge passivation as follows: A single edge side with an extra hydrogen atom [`1H-edge`, Fig. 8(b)], two edge sides with each an extra hydrogen atom [`2H-edge`, Fig. 8(c)], one hydrogen replaced by a fluorine atom [`1F-edge`, Fig. 8(d)], and a dehydrogenated edge with 4 hydrogen atoms removed from each side [`8H-free`, Fig. 8(e)]. We have also considered defects in the atomic structure in the form of one,

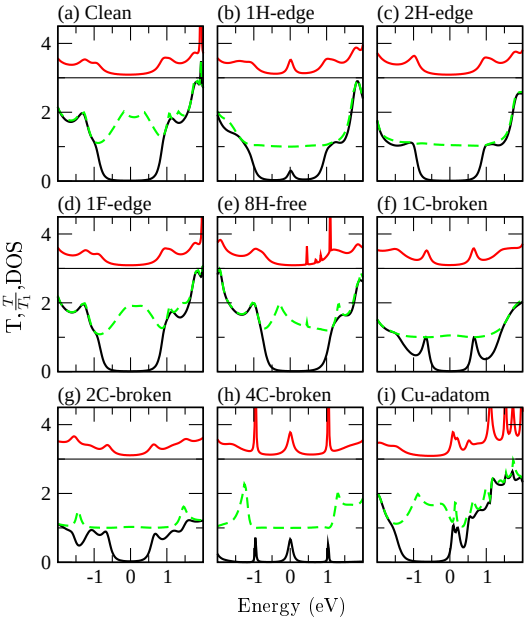

FIG. 9: (Color online) Electronic properties of the AGNR structures shown in Fig. 8. The total transmission is shown with black lines. The ratio T/T_1, where T_1 is the transmission originating from the most transmitting eigenchannel is shown with green dashed lines (this ratio gives a lower bound to the number of contributing eigenchannels). The DOS for the C atoms in the dynamical region is shown with red lines (offset by 3 units).

two, or four broken C-C bonds [`1C-broken`, `2C-broken`, `4C-broken`, Fig. 8(f)-(h)] as well as a Cu adatom on the AGNR [`Cu-adatom`, Fig. 8(i)]. For all these systems the entire dynamical region was relaxed, i.e., the parts of the AGNRs shown in Fig. 8.

Defects may influence the IETS signal in two ways. First, a defect can have a direct impact by changing the vibrational degrees of freedom. In order for the change in the vibrational spectrum to give a signal in the IETS, the new vibrations must couple to the current, and preferably have frequencies which do not coincide with ones already giving IETS signals for the pristine ribbons. Second, a defect can substantially change the electronic structure and thereby have an impact on the e-ph couplings associated with the active modes or even the transmission eigenchannels of the pristine ribbons, e.g., changing a peak in the IETS to a dip (and vice versa) or enhancing asymmetric contributions via Eq. (4).

The electronic properties of the pristine AGNR is shown in Fig. 9(a). The carbon DOS projected to the device region (red curve) reveals a gap as expected from the band structure [Fig. 1(b)], which is significantly broadened from the coupling to the metallic electrodes. The two valence and two conduction bands in the considered energy range naturally explain that the total transmission (black curve) is bound below a value of 2. Further, the ratio $T/T_1 < 2$ (green dashed line), measuring the minimum number of contributing channels where T_1 is the transmission of the most transmitting eigenchannel, shows that both channels play a role for the transport, at least away from the edges of the direct band gap. Measurements of shot noise may provide insights into this effective number of conductance eigenchannels.[54,55] We can now discuss how the different defects modify the electronic properties. From Fig. 9(b)-(i) we notice that not all defects change the elastic transmission, and furthermore, a change in elastic transmission needs not be unique for a specific defect.

Instead, IETS may provide a additional fingerprint in the current that can be used to identify the type of defect. Figure 10 shows the computed IETS as a function of gate voltage for the 8 different defects. As for the clean structure, the two peaks at 169 and 196 meV corresponding to the D- and G- Raman modes are dominant for a range of gate values for all the structures. Another feature, which is present in all the systems, is the appearance of several signals close to the band onsets. In the following subsections we discuss in more detail the transport characteristics with the different types of defects in AGNRs.

1. *Edge passivation*

Considering defects in the edge passivation [Fig. 8(b-e)] the gap in the transmission is essentially unchanged [Fig. 9(b-e)], except for the `1H-edge` structure where a zero-energy resonance appears in the DOS and transmission [Fig. 9(b)]. This new peak can be attributed to tunneling via a mid-gap state which appears due to the local breaking of sub-lattice symmetry.[1] Thus, if a H atom is added to the neighboring C atom [`2H-edge`, Fig. 8(c)] the peak disappears [Fig. 9(c)]. The addition of one or two H atoms on the same side also results in the closing of one transmission channel between the valence and conduction bands as shown in Fig. 9(b,c). Concerning the vibrational degrees of freedom, the addition of extra hydrogen to the edge results in new vibrational modes around 330 meV for `1H-edge` and around 343 and 353 meV for `2H-edge`, clearly outside the bulk phonon band (ranging up to ~ 200 meV) of pristine AGNR.[56]

Comparing the IETS in Fig. 10(a-c) we find that only `1H-edge` gives a signal which differs significantly from the pristine case. Figure 10(k) shows specific IETS for selected gate voltages for `1H-edge`. Here, at $V_G = 0.2$V (top green curve) we see how new signals appear at large voltages: For positive bias polarity two signals appear at 330 and 365 meV, respectively, while for negative bias polarity only an asymmetric signal around -365 meV is present. The signal at 330 meV is due to vibrations of the H_2 [Fig. 11(b)], while the signal at 365 meV [Fig. 11(a)] is

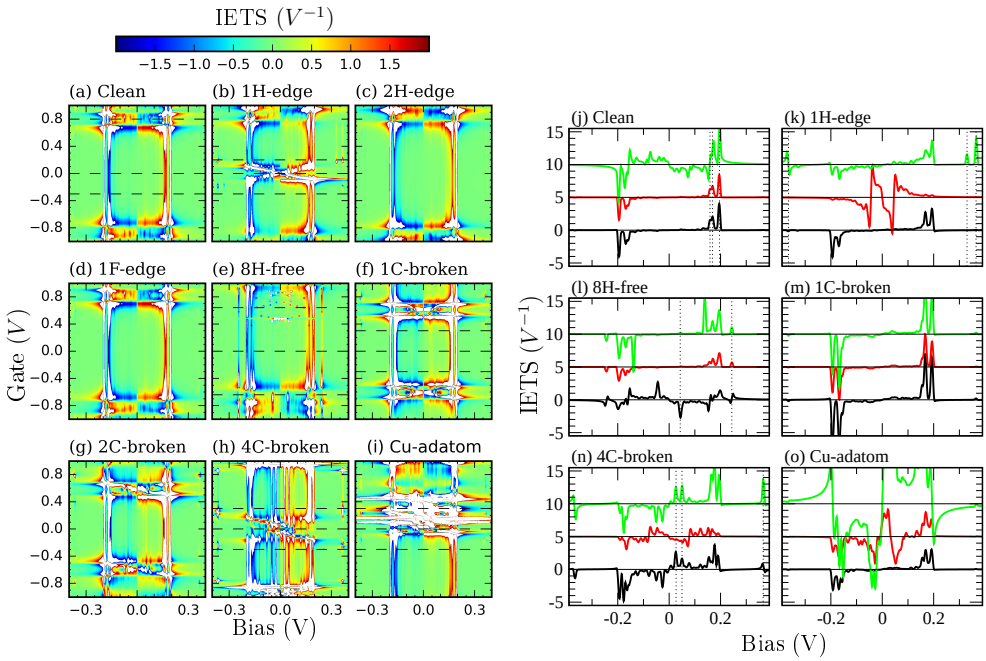

FIG. 10: (Color online) (a-i) IETS as a function of gate voltage V_G for the pristine and defective AGNR structures shown in Fig. 8 . (j-o) IETS for six selected structures at three specific gate values (dashed horizontal lines in panels a-i). The curves are offset with the most negative gate value at the bottom (black curves) and the most positive at the top (green curves). (j) Clean AGNR at gate values $V_G = -0.3$, 0.0, and 0.8 V. (k) `1H-edge` at $V_G = -0.3$, 0.0, and 0.2 V. (l) `8H-free` at $V_G = -0.3$, 0.0, and 0.6 V. (m) `1C-broken` at $V_G = -0.3$, 0.0, and 0.3 V. (n) `4C-broken` at $V_G = -0.3$, 0,0, and 0.3 V. (o) `Cu-adatom` at $V_G = -0.3$, 0.0, and 0.3 V. Dotted vertical lines are guides to the eye of characteristic IETS signals corresponding to the modes in Fig. 11

due to the H atom on the neighboring C atom. Further, the amplitude of the signals around 169 and 196 meV is also found to depend on bias polarity.

Gating onto the zero-energy resonance for `1H-edge` the IETS signal [middle red curve in Fig. 10(k)] is dominated by large asymmetric signals for low energy vibrations due to the contribution from κ_λ and Eq. (4). We note that κ_λ changes sign with bias polarity for this approximately left-right symmetric structure. This can be seen from the red IETS curve in Fig. 10(k) which is roughly an odd function of the bias voltage. In close proximity of the zero-energy resonance a characteristic "X-shape" is observed in the gate-dependent IETS, while away from it the signals approach that of the pristine AGNR [Fig. 10(b)].

Substituting a H atom with a F atom (`1F-edge`) is seen to have virtually no effect in the IETS of Fig. 10(d). This suggests that a significant change in the chemical composition directly involving the π-electronic system is required in order to obtain a signal although the vibrations are influenced by the heavier passivation.

Such a significant change in the passivation occurs for instance by removing four H atoms on each side (`8H-free`), giving rise to four very narrow peaks in the DOS around the conduction band, [Fig. 9(e)]. These correspond to very localized dangling-bond states on the dehydrogenated dimers and therefore do not show up in the transmission. However, the dehydrogenated edges give rise to localized vibrations outside the range of the pristine vibrational spectrum.[56] The in-phase vibration of the dehydrogenated C dimers at the armchair edges [Fig. 11(f)] gives rise to an extra IETS peak at 244 meV [Fig. 10(l)] matching the H-free mode measured by Raman.[34] We find that this signal is robust as it appears in the whole range of gate values. When gating into to the valence band a new signal appears around 43 meV [$V_G \approx -0.8$ V in Fig. 10(e)] originating from a low energy edge vibration [Fig. 11(g)].

2. *Structural defects*

The electronic transmission in GNRs is mediated by the carbon π system. Thus if a C-C bond fails to be formed during GNR synthesis or if it is broken again at a later stage, a large effect can be expected for the

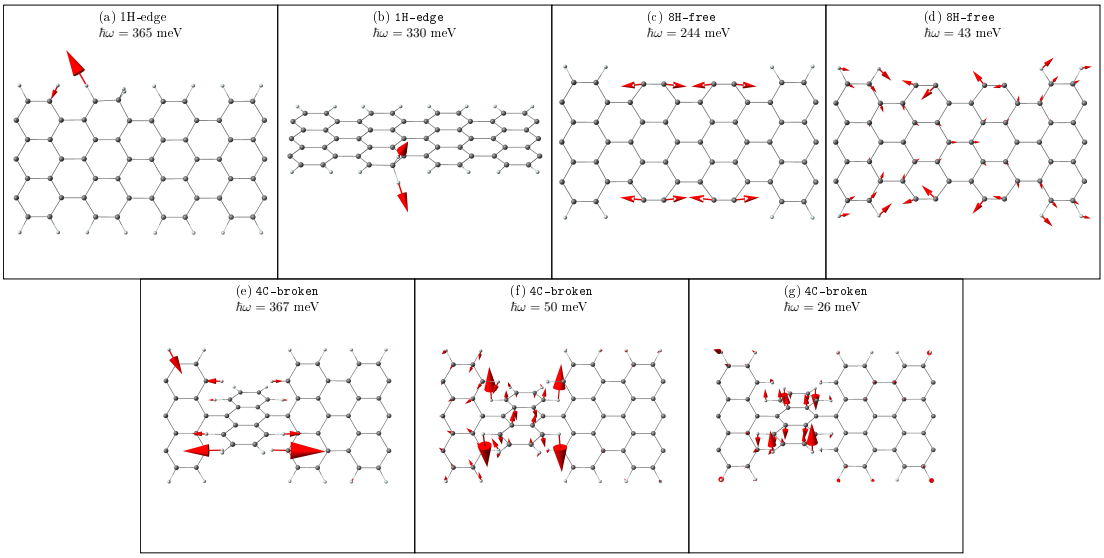

FIG. 11: (Color online) Visualization of the most contributing defect-induced vibrational modes to the IETS signals indicated by vertical lines in Fig. 10(j-o). (a-b) The two hydrogen signals for `1H-edge`. (c) Localized edge mode at the carbon dimers for the `8H-free`. (d) Delocalized edge mode for the `8H-free`. (e) Hydrogen mode from the zigzag edge of `4C-broken`. (f-g) Defect modes for `4C-broken`.

electronic conduction properties. This impact is indeed revealed in Fig. 9(f-h). Breaking one or two bonds results in the formation of two in-gap states which, broadened by the electrodes, make the gap appear smaller. The IETS signals for the `1C-broken` and `2C-broken` in Fig. 10(f,g,m) have the same two signals at 169 and 196 meV as for the clean ribbon. However, the relative amplitudes are interchanged such that the D-peak is now slightly more intense than the G-peak.

Breaking four C-C bonds [`4C-broken`, Fig. 8(h)], resulting in constrictions of single C-C bonds, totally alter the DOS which is now dominated by three sharp peaks as seen in Fig. 9(h). The corresponding IETS signals are shown in Fig. 10(h,n). In the proximity of the zero-energy resonance a broad range of signals at low vibrational energies appears (red curve in panel n) as well as a characteristic "X-shape" in the gate plot (panel h) similar to that of `1H-edge`. Gating away from the resonance we observe two additional robust IETS signals at 27 and 50 meV resulting from vibrations localized at the defect [Fig. 11(d,e)].

3. Adatom

Transition metals are typically used for growth of graphene or as a substrate for the bottom-up synthesis of GNRs. Thus it is of interest to consider the effect of adatoms of this type on GNRs. A Cu adatom on graphene adsorbs preferentially in the on-top position.[57] However, positioning Cu such that it breaks the axial symmetry of our AGNR, we find that it is most stable in a hollow site at the edge [`Cu-adatom`, Fig. 8(i)]. The DOS and transmission in Fig. 9(i) reveal a n-type doping effect shifting E_F close to the conduction band while leaving the two transmission channels inside the gap relatively intact.

For the pristine GNR the e-ph couplings of the out-of-plane vibrations are suppressed due to the symmetry of the π-orbitals. However, around the onset of the conduction band the IETS signals in Fig. 10(i,o) is dominated by large asymmetric signals with significant contributions from out-of-plane phonons. These modes come into play due to breaking of the planar symmetry by the adatom. Also note that by gating of E_F within the gap these signatures of the adatom disappear, cf. the lower black curve in Fig. 10(o).

B. Defects in ZGNRs

Let us next consider a series of defects for the zigzag graphene nanoribbon. Due to the different size and orientation of the AGNR and ZGNR unit cell their structural defects will generally differ. Thus, instead of the range of structural defects considered for the AGNR we investigate a number of chemical defects, both as adatoms, in the edge passivation and substituting a carbon atom. Lithium binding to carbon is of relevance to carbon-based Li-ion batteries[58] and DFT studies has

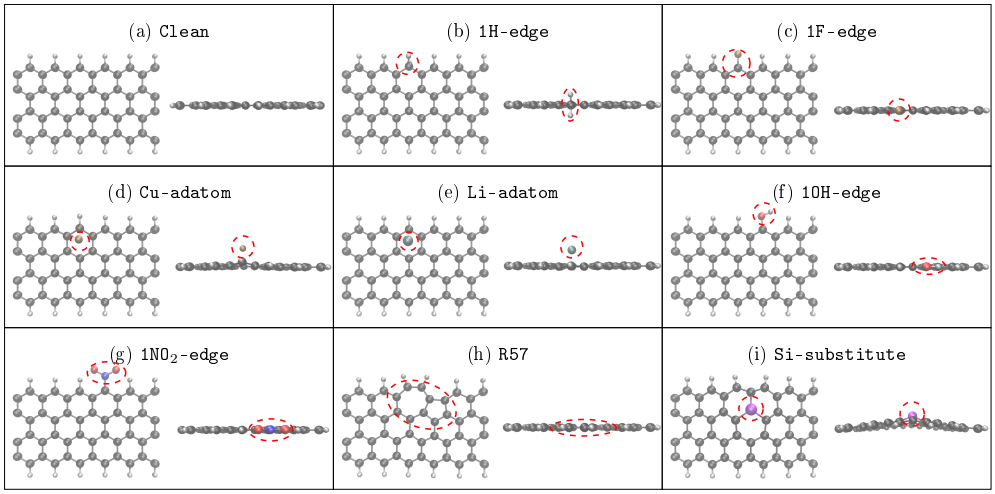

FIG. 12: (Color online) Top and side views of the dynamical region describing the various ZGNR defect structures. The dashed red ellipses are guides to the eye highlighting the defect position. (a) Pristine ZGNR. (b) One extra H atom on one of the edges. (c) One H atom replaced by a F atom. (d) Cu adatom in a hollow site on the edge. (e) Li adatom in a hollow site on the edge. (f) One H replaced by a OH group. (g) One H replaced by a NO_2 group. (h) Structural defect (R57). (i) Substitutional Si defect next to the edge.

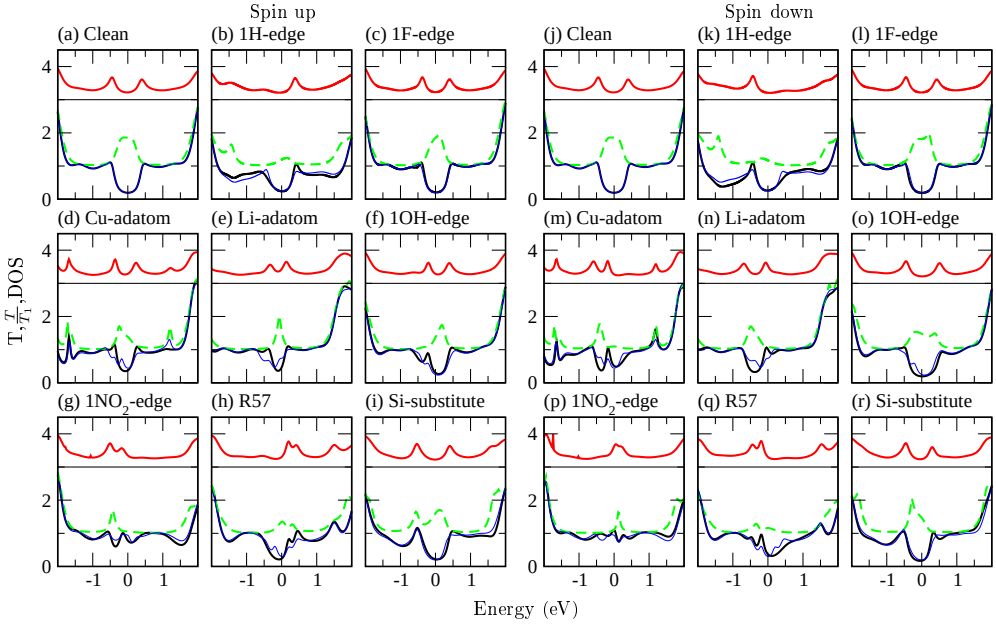

FIG. 13: (Color online) Electronic properties of the ZGNR structures shown in Fig. 12 with the spin-up/down components in the left/right panel. The spin-resolved total transmission is shown with black lines while spin-averaged total transmission is shown with thin blue lines. The ratio T^σ/T_1^σ, where T_1^σ is the transmission originating from the most transmitting spin eigenchannel, is shown with green dashed lines (this ratio gives a lower bound to the number of contributing eigenchannels with spin σ). The spin-resolved DOS for the C atoms in the dynamical region is shown with red lines (offset by 3 units).

shown edge-oxidized zigzag graphene to be more stable than hydrogen-terminated[6,25], further, NO_2 groups were shown to be Raman active.[59] Thus in Fig. 12 we show the atomic structures of pristine ZGNR along with 8 different defect configurations. We consider the following defects in the edge-passivation: A single edge with an extra hydrogen [`1H-edge`, Fig. 12(b)], one hydrogen is replaced by either a F atom [`1F-edge`, Fig. 12(c)], an OH group [`1OH-edge`, Fig. 12(f)], or a NO_2 group [`1NO2-edge`, Fig. 12(g)]. We also consider defects in the form of a Cu adatom [`Cu-adatom`, Fig. 12(d)] or a Li adatom [`Li-adatom`, Fig. 12(e)]. Finally, we also study the effect of a structural defect in form of a 57 reconstruction [`R57`, Fig. 12(h)] and a substitutional defect where a C atom next to the edge is replaced by a Si atom [`Si-substitute`, Fig. 12(i)]. For all these systems the entire dynamical region was relaxed, i.e., the parts of the ZGNRs shown in Fig. 12 using spin-polarized treatments. The spin degrees of freedom $\sigma = \uparrow, \downarrow$ generalizes γ_λ^σ and κ_λ^σ [Eqs.(5)-(6)] corresponding to two independent spin channels, which in general can have quite different amplitudes and even opposite sign. The observable IETS would simply be the sum of these two components $(\partial_V^2 I_\uparrow + \partial_V^2 I_\downarrow)/(\partial_V I_\uparrow + \partial_V I_\downarrow)$.

Similar to the AGNR case, the electronic properties in the device region with the different impurity configurations for the ZGNR, now spin resolved, are summarized in Fig. 13. The IETS of pristine ZGNR was already discussed in Sec. IIIB and below we continue describing the IETS fingerprints for the various defects.

1. *Edge passivation*

As commented above, the broader IETS signals of pristine ZGNR [Figs. 3-4] (as compared with AGNR) can be understood from the breaking of the axial mirror symmetry and hence fewer symmetry-forbidden inelastic transitions. These broader signals may in general make the detection of defect signatures more difficult. For `1H-edge` [Fig. 13(b)] the IETS resembles that of the pristine ZGNR [Fig. 13(a)] inside the gap. However, gating into the valance band [black curve in Fig. 13(k)] the edge states start to extend into the middle of the ribbon, partially restoring mirror symmetry, and thus resulting in part of the pristine ZGNR signals to disappear.

Here an extra signal appear due to edge-modes in the frequency range 194 to 199 meV with the most contributing mode at 196 meV as shown in [Fig. 15(a)]. The resulting IETS signal can clearly be seen in the bottom curve in Fig. 14(k). As for the AGNR substituting a hydrogen with a fluorine atom has a very limited effect on the electronic properties and the IETS signal.

Substituting a hydrogen with an OH group, according to Fig. 13(f) and (o), have only a small effect on the spin down electrons, while it shrinks and add additional structure to the gap for the spin up electrons. For the spin up electrons there is a small peak inside the gap which gives rise to a large asymmetric IETS signal around $V_G = -0.2$V in Fig. 13(o) lower curve, compared to the pristine case. The most contributing mode to the asymmetric IETS signal is shown in Fig. 15(b). However, there is no clear signature of the OH group itself. In the same manner the substitution with a NO_2 group removes the gap in the electronic properties without leaving any direct fingerprint of the NO_2 group in the IETS signal.

2. *Adatom*

As for the AGNR we consider the effect of adatoms. For the Cu adatom the transport gap shrinks for the spin up electrons while there is an in-gap peak for the spin down electrons, cf. Fig. 13(m). Thus, for some gate values the IETS signals reflect that the spin down electrons will back scatter while the spin up electrons will be forward scattered, and the observed signal is then the sum of these contributions. For a gate value of $V_G = -0.2$ V, the IETS signal is dominated by spin down electrons. Due to the finite width of the in-gap peak, in the spin down transmission, the low frequency phonons ($\hbar\omega < 0.1$ meV) give rise to back scattering while the high frequency phonons ($\hbar\omega > 0.1$ meV) result in forward scattering. Thus, the low and high energy signals have different signs as can be seen from Fig. 14(l). Interestingly, the low energy signal primarily consists of symmetric contributions from out-of-plane modes [Fig. 15(c)]. Replacing the Cu adatom with Li, the transmission and DOS, shown in Fig. 13(e,n), reveals a spin dependent n-type doping effect, where E_F is shifted the most for spin down. However, no in-gap peak is seen as for Cu and the IETS show no clear signature of the Li atom.

3. *Structural defect*

The formation of a `R57` reconstruction results in peaks in the DOS in the device region, just above E_F for spin up [Fig. 13(h)] and just below E_F for spin down [Fig. 13(q)]. The `R57` breaks the symmetry both in the vibrational and electronic structure allowing for IETS signals from a wider range of vibrations, resulting in broader peaks, as seen from Fig. 14(h) and Fig. 14(n). One of the contributing modes is localized at the border between the pentagon-ring and middle of the ribbon at $\hbar\omega = 204$meV [Fig. 15(d)]. This localized mode yield a relatively small signal compared to the other signals, however, contrary to the other modes the localized mode is not expected to be broadened if the coupling to phonons away from the dynamical region is taken into account. The breaking of symmetry in the electronic structure also give rise to difference signals for the two bias polarities.

4. Substitutional impurity

Substituting a carbon with a silicon atom leads to an out-of-plane buckling, see Fig. 12(i). However, both silicon and carbon have an s^2p^2 electronic structure, and the electron transmission is basically similar to the pristine. On the other hand, the buckling give rise to low energy peaks in the IETS signal originating from the e-ph coupling to the out-of-plane modes [Fig. 15(e)]. Gating close to the band edge of the conduction band gives rise to different sign of the signals at low and high vibrational energies, as seen from the top curve in Fig. 14(o).

V. CONCLUSIONS

In summary, we have investigated IETS signals in symmetrically contacted armchair and zigzag graphene nanoribbons, considering both pristine as well as a selection of defective configurations under varying charge carrier conditions. For the clean AGNR inelastic tunneling gives rise to two distinct peaks in the IETS spectrum at 169 mV and 196 mV corresponding to the D-and G-modes of Raman spectroscopy, respectively. By connecting the IETS signals to the phonon band structure, we have clarified how only a single band contributes to the G-mode while three bands contribute to the broader D-mode. Concerning defects in AGNRs we have shown how some leave IETS unchanged while others give clear signals. For instance, adding an extra hydrogen atom to a single edge side gives a clear signal for some gate values. This signal can be removed by adding another hydrogen atom to the neighboring edge side because the sub-lattice symmetry is restored. Further, exchanging a single hydrogen atom with a fluorine atom in the passivation does not result in any change in both the elastic and inelastic tunneling. However removing 8 hydrogen atoms leaving part of the edge on each side without passivation, gives a clear robust signal throughout the investigated gate values. The signal, due to the vibration of the carbon dimers at the edge, has an energy around 245 meV making it easy to detect since it is outside the vibrational spectrum of the pristine ribbon. Breaking of one or two C-C bonds turns out to interchange the relative intensity of the G- and D-peaks. Breaking 4 C-C bonds gives rise to signals caused by the defect tilted out of plane. Lifting the symmetry of the π-electrons by adding a Cu-adatom allows the out-of-plane modes to contribute.

For the ZGNR we find relatively broader IETS signals especially in the absense of a large gate voltage ($V_G \approx 0$ V). Importantly, this is a consequence of the breaking of the axial mirror symmetry in the ribbon due to the presence of spin-polarized edges. Thus, by comparing to spin-degenerate calculations, we suggest that IETS can give an indirect proof of spin-polarization in zigzag ribbons. On the other hand, the broader IETS features may make it difficult to identify the different defect signals reported in this paper.

The presence of a R57-reconstruction also broadens the IETS by breaking both the electronic and vibrational symmetry. Substituting a carbon atom with a silicon atom makes the ribbon buckle, breaking the planar symmetry, allowing the out-of-plane modes to contribute to the IETS. This suggests that IETS in principle could be used to gain information of the curvature of GNRs and other graphene-based structures.

Finally, as an outlook we note that here we presented calculations on long, symmetrically contacted systems where there is a significant overlap with both metallic electrodes. It would be interesting to extend such a study also to the asymmetric situation where a point tunnel contact is made to one end resembling, say, the coupling to a STM tip.[20]

Acknowledgments

TF thanks Center for Nanostructured Graphene (Project DNRF58) for hospitality during a visit supported by the Villum Foundation and acknowledges support from the Basque Departamento de Educación and the UPV/EHU (Grant No. IT-756-13), the Spanish Ministerio de Economía y Competitividad (Grant No. MAT2013-46593-C6-2-P), and the European Union FP7-ICT project PAMS (Contract No. 610446).

* Electronic address: mads.brandbyge@nanotech.dtu.dk

[1] H. Raza, *Graphene nanoelectronics : metrology, synthesis, properties and applications* (Springer, 2011).
[2] L. E. F. Foa Torres, S. Roche, and J.-C. Charlier, *Introduction to Graphene-Based Nanomaterials: From Electronic Structure to Quantum Transport* (Cambridge University Press, 2014).
[3] S. Dutta and S. K. Pati, "Novel properties of graphene nanoribbons: a review," J. Mater. Chem. **20**, 8207 (2010).
[4] T. G. Pedersen, C. Flindt, J. Pedersen, N. A. Mortensen, A. Jauho, and K. Pedersen, "Graphene antidot lattices: Designed defects and spin qubits," Phys. Rev. Lett. **100**, 136804 (2008).
[5] J. Bai, X. Zhong, S. Jiang, Y. Huang, and X. Duan, "Graphene nanomesh," Nat. Nanotechnol. **5**, 190 (2010).
[6] P. Wagner, C. P. Ewels, J.-J. Adjizian, L. Magaud, P. Pochet, S. Roche, A. Lopez-Bezanilla, V. V. Ivanovskaya, A. Yaya, M. Rayson, et al., "Band Gap Engineering via Edge-Functionalization of Graphene Nanoribbons," J. Phys. Chem. C **117**, 26790 (2013).
[7] A. C. Ferrari and D. M. Basko, "Raman spectroscopy as a versatile tool for studying the properties of graphene," Nat. Nanotechnol. **8**, 235 (2013).
[8] A. Shiotari, T. Kumagai, and M. Wolf, "Tip-Enhanced Ra-

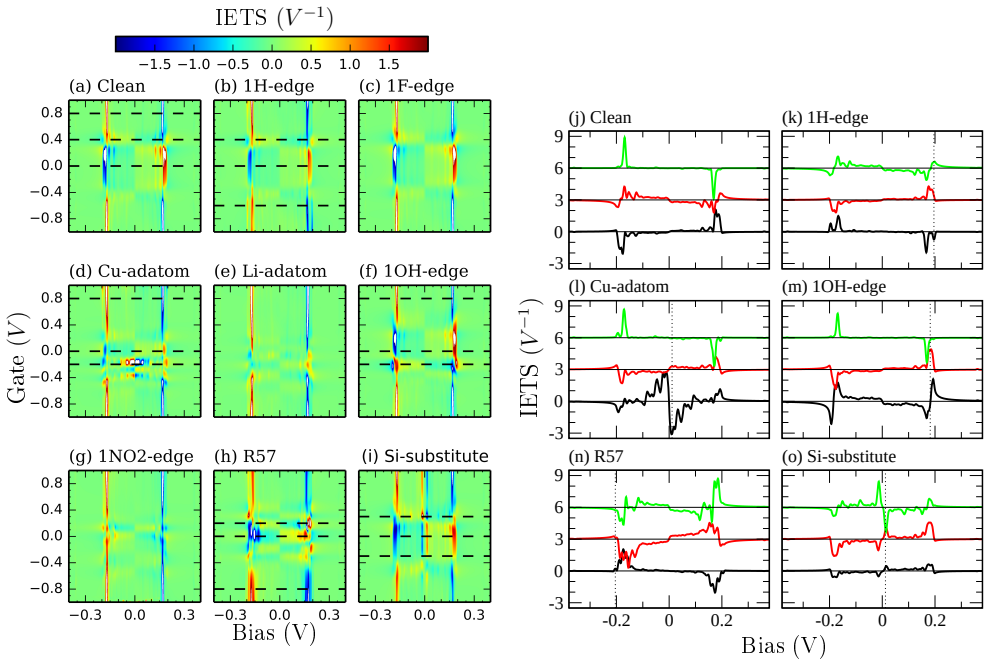

FIG. 14: (Color online) (a-i) Spin-averaged IETS as a function of gate voltage V_G for the pristine and defective ZGNR structures shown in Fig. 12. (j-o) IETS for six selected structures at three specific gate values (dashed horizontal lines in panels a-i). The curves are offset with the most negative gate value at the bottom (black curves) and the most positive at the top (green curves). (j) Clean ZGNR for gate values $V_G = 0.0$, 0.4, and 0.8 V. (k) `1H-edge` at $V_G = -0.6$, 0.0, and 0.4 V. (l) `Cu-adatom` at $V_G = -0.2$, 0.0, and 0.8 V. (m) `1OH-edge` at $V_G = -0.2$, 0.0, and 0.8 V. (n) `R57` at $V_G = -0.8$, 0.0, and 0.2 V. (o) `Si-substitute` at $V_G = -0.3$, 0.0, and 0.3 V. Dotted vertical lines are guides to the eye of characteristic IETS signals corresponding to the modes shown in Fig. 15.

man Spectroscopy of Graphene Nanoribbons on Au(111)," J. Phys. Chem. C **118**, 11806 (2014).

[9] M. Y. Han, B. Özyilmaz, Y. Zhang, and P. Kim, "Energy Band-Gap Engineering of Graphene Nanoribbons," Phys. Rev. Lett. **98**, 206805 (2007).

[10] X. Li, X. Wang, L. Zhang, S. Lee, and H. Dai, "Chemically derived, ultrasmooth graphene nanoribbon semiconductors," Science **319**, 1229 (2008).

[11] Z.-S. Wu, W. Ren, L. Gao, B. Liu, J. Zhao, and H.-M. Cheng, "Efficient synthesis of graphene nanoribbons sonochemically cut from graphene sheets," Nano Res. **3**, 16 (2010).

[12] J. Baringhaus, M. Ruan, F. Edler, A. Tejeda, M. Sicot, A. Taleb-Ibrahimi, A.-P. Li, Z. Jiang, E. H. Conrad, C. Berger, et al., "Exceptional ballistic transport in epitaxial graphene nanoribbons," Nature **506**, 349 (2014).

[13] D. V. Kosynkin, A. L. Higginbotham, A. Sinitskii, J. R. Lomeda, A. Dimiev, B. K. Price, and J. M. Tour, "Longitudinal unzipping of carbon nanotubes to form graphene nanoribbons.," Nature **458**, 872 (2009).

[14] J. Cai, P. Ruffieux, R. Jaafar, M. Bieri, T. Braun, S. Blankenburg, M. Muoth, A. P. Seitsonen, M. Saleh, X. Feng, et al., "Atomically precise bottom-up fabrication of graphene nanoribbons.," Nature **466**, 470 (2010).

[15] S. Blankenburg, J. Cai, P. Ruffieux, R. Jaafar, D. Passerone, X. Feng, K. Müllen, R. Fasel, and C. a. Pignedoli, "Intraribbon heterojunction formation in ultranarrow graphene nanoribbons.," ACS Nano **6**, 2020 (2012).

[16] P. Han, K. Akagi, F. Federici Canova, H. Mutoh, S. Shiraki, K. Iwaya, P. S. Weiss, N. Asao, and T. Hitosugi, "Bottom-up graphene-nanoribbon fabrication reveals chiral edges and enantioselectivity," ACS Nano **8**, 9181 (2014).

[17] J. Cai, C. A. Pignedoli, L. Talirz, P. Ruffieux, H. Söde, L. Liang, V. Meunier, R. Berger, R. Li, X. Feng, et al., "Graphene nanoribbon heterojunctions," Nat. Nanotechnol. **9**, 896 (2014).

[18] C. Bronner, F. Leyssner, S. Stremlau, M. Utecht, P. Saalfrank, T. Klamroth, and P. Tegeder, "Electronic structure of a subnanometer wide bottom-up fabricated graphene nanoribbon: End states, band gap, and dispersion," Phys. Rev. B **86**, 085444 (2012).

[19] P. Ruffieux, J. Cai, N. C. Plumb, L. Patthey, D. Prezzi, A. Ferretti, E. Molinari, X. Feng, K. Müllen, C. a. Pignedoli, et al., "Electronic structure of atomically precise graphene nanoribbons.," ACS Nano **6**, 6930 (2012).

[20] J. van der Lit, M. P. Boneschanscher, D. Vanmaekelbergh, M. Ijäs, A. Uppstu, M. Ervasti, A. Harju, P. Liljeroth, and I. Swart, "Suppression of electron-vibron coupling in graphene nanoribbons contacted via a single atom.," Nat. Commun. **4**, 2023 (2013).

[21] M. Koch, F. Ample, C. Joachim, and L. Grill, "Voltage-dependent conductance of a single graphene nanoribbon,"

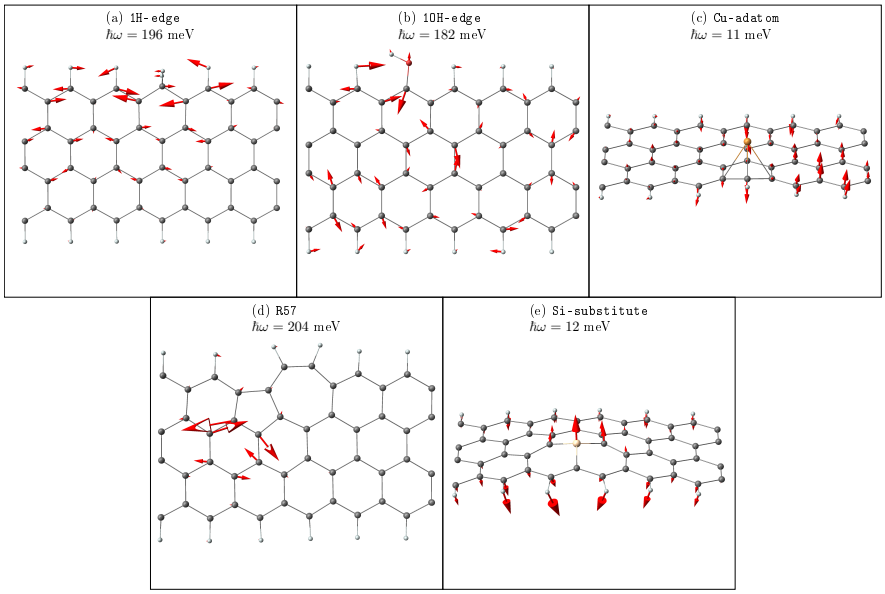

FIG. 15: (Color online) Visualization of the most contributing modes to the IETS signals indicated by vertical lines in Fig. 14(j-o). (a) Edge mode at the edge with the extra hydrogen in `1H-edge`. (b) Mode contributing to the asymmetric signal in Fig. 14 (m) for the `1OH-edge`. (c) Out-of-plane mode for `Cu-adatom`. (d) Localized mode for `R57`. (e) Out o plane mode for `Si-substitute`.

Nat. Nanotechnol. **7**, 713 (2012).

[22] T. Wassmann, A. P. Seitsonen, A. M. Saitta, M. Lazzeri, and F. Mauri, "Structure, Stability, Edge States, and Aromaticity of Graphene Ribbons," Phys. Rev. Lett. **101**, 096402 (2008).

[23] J. Li, Z. Li, G. Zhou, Z. Liu, J. Wu, B.-L. Gu, J. Ihm, and W. Duan, "Spontaneous edge-defect formation and defect-induced conductance suppression in graphene nanoribbons," Phys. Rev. B **82**, 115410 (2010).

[24] P. Wagner, V. V. Ivanovskaya, M. Melle-Franco, B. Humbert, J.-J. Adjizian, P. R. Briddon, and C. P. Ewels, "Stable hydrogenated graphene edge types: Normal and reconstructed Klein edges," Phys. Rev. B **88**, 094106 (2013).

[25] O. Hod, V. Barone, J. E. Peralta, and G. E. Scuseria, "Enhanced half-metallicity in edge-oxidized zigzag graphene nanoribbons.," Nano Lett. **7**, 2295 (2007).

[26] D. Gunlycke, J. Li, J. W. Mintmire, and C. T. White, "Altering low-bias transport in zigzag-edge graphene nanostrips with edge chemistry," Appl. Phys. Lett. **91**, 112108 (2007).

[27] C. Zhang, C. He, L. Xue, K. Zhang, L. Sun, and J. Zhong, "Transport properties of zigzag graphene nanoribbons with oxygen edge decoration," Org. Electron. **13**, 2494 (2012).

[28] N. Al-Aqtash, H. Li, L. Wang, W.-N. Mei, and R. Sabirianov, "Electromechanical switching in graphene nanoribbons," Carbon **51**, 102 (2013).

[29] T. Yamamoto, K. Watanabe, and K. Mii, "Empirical-potential study of phonon transport in graphitic ribbons," Phys. Rev. B **70**, 245402 (2004).

[30] M. Vandescuren, P. Hermet, V. Meunier, L. Henrard, and P. Lambin, "Theoretical study of the vibrational edge modes in graphene nanoribbons," Phys. Rev. B **78**, 195401 (2008).

[31] R. Gillen, M. Mohr, J. Maultzsch, and C. Thomsen, "Lattice vibrations in graphene nanoribbons from density functional theory," Phys. Status Solidi **246**, 2577 (2009).

[32] J. Zhou and J. Dong, "Vibrational property and Raman spectrum of carbon nanoribbon," Appl. Phys. Lett. **91**, 173108 (2007).

[33] R. Saito, M. Furukawa, G. Dresselhaus, and M. S. Dresselhaus, "Raman spectra of graphene ribbons.," J. Phys. Condens. Matter **22**, 334203 (2010).

[34] H. Huang, D. Wei, J. Sun, S. L. Wong, Y. P. Feng, a. H. C. Neto, and A. T. S. Wee, "Spatially resolved electronic structures of atomically precise armchair graphene nanoribbons.," Sci. Rep. **2**, 983 (2012).

[35] M. Ijäs, M. Ervasti, A. Uppstu, P. Liljeroth, J. van der Lit, I. Swart, and A. Harju, "Electronic states in finite graphene nanoribbons: Effect of charging and defects," Physical Review B **88**, 075429 (2013).

[36] J.-T. Lü, R. B. Christensen, G. Foti, T. Frederiksen, T. Gunst, and M. Brandbyge, "Efficient calculation of inelastic vibration signals in electron transport: Beyond the wide-band approximation," Phys. Rev. B **89**, 081405 (2014).

[37] J. M. Soler, E. Artacho, J. D. Gale, A. García, J. Junquera, P. Ordejón, and D. Sánchez-Portal, "The SIESTA method for ab initio order-N materials simulation," J. Phys.: Condens. Matter **14**, 2745 (2002).

[38] M. Brandbyge, J.-L. Mozos, P. Ordejón, J. Taylor, and K. Stokbro, "Density-functional method for nonequilibrium electron transport," Phys. Rev. B **65**, 165401 (2002).

[39] J. P. Perdew, K. Burke, and M. Ernzerhof, "Generalized gradient approximation made simple," Phys. Rev. Lett. **77**,

3865 (1996).
[40] M. Paulsson, T. Frederiksen, and M. Brandbyge, "Modeling inelastic phonon scattering in atomic- and molecular-wire junctions," Phys. Rev. B **72**, 201101 (2005).
[41] T. Frederiksen, M. Paulsson, M. Brandbyge, and A.-P. Jauho, "Inelastic transport theory from first principles: Methodology and application to nanoscale devices," Phys. Rev. B **75**, 205413 (2007).
[42] `http://sourceforge.net/projects/inelastica`.
[43] M. P. L. Sancho, J. M. L. Sancho, and J. Rubio, "Quick iterative scheme for the calculation of transfer matrices: application to Mo (100)," J. Phys. F: Met. Phys. **14**, 1205 (1984).
[44] M. Paulsson and M. Brandbyge, "Transmission eigenchannels from nonequilibrium Green's functions," Phys. Rev. B **76**, 115117 (2007).
[45] C. Bronner, M. Utecht, A. Haase, P. Saalfrank, T. Klamroth, and P. Tegeder, "Electronic structure changes during the surface-assisted formation of a graphene nanoribbon," J. Chem. Phys. **140**, 024701 (2014).
[46] L. Yang, C.-H. Park, Y.-W. Son, M. Cohen, and S. Louie, "Quasiparticle Energies and Band Gaps in Graphene Nanoribbons," Phys. Rev. Lett. **99**, 186801 (2007).
[47] X. Jiang, N. Kharche, P. Kohl, T. B. Boykin, G. Klimeck, M. Luisier, P. M. Ajayan, and S. K. Nayak, "Giant quasiparticle bandgap modulation in graphene nanoribbons supported on weakly interacting surfaces," Appl. Phys. Lett. **103**, 133107 (2013).
[48] L. Liang and V. Meunier, "Electronic structure of assembled graphene nanoribbons: Substrate and many-body effects," Phys. Rev. B **86**, 195404 (2012).
[49] H. Song, Y. Kim, Y. H. Jang, H. Jeong, M. A. Reed, and T. Lee, "Observation of molecular orbital gating," Nature **462**, 1039 (2009).
[50] M. Paulsson, T. Frederiksen, H. Ueba, N. Lorente, and M. Brandbyge, "Unified Description of Inelastic Propensity Rules for Electron Transport through Nanoscale Junctions," Phys. Rev. Lett. **100**, 226604 (2008).
[51] B. N. J. Persson and A. Baratoff, "Inelastic electron-tunneling from a metal tip - the contribution from resonant processes," Phys. Rev. Lett. **59**, 339 (1987).
[52] N. Lorente and M. Persson, "Theory of single molecule vibrational spectroscopy and microscopy," Phys. Rev. Lett. **85**, 2997 (2000).
[53] S. Kim and Y.-W. Son, "Scattering theory approach to inelastic transport in nanoscale systems," Phys. Rev. B **87**, 195423 (2013).
[54] D. Djukic and J. M. van Ruitenbeek, "Shot noise measurements on a single molecule," Nano Lett. **6**, 789 (2006).
[55] N. L. Schneider, J. T. Lü, M. Brandbyge, and R. Berndt, "Light emission probing quantum shot noise and charge fluctuations at a biased molecular junction," Phys. Rev. Lett. **109**, 186601 (2012).
[56] M. Engelund, J. A. Fürst, A. P. Jauho, and M. Brandbyge, "Localized Edge Vibrations and Edge Reconstruction by Joule Heating in Graphene Nanostructures," Phys. Rev. Lett. **104**, 36807 (2010).
[57] X. Liu, C. Z. Wang, M. Hupalo, W. C. Lu, M. C. Tringides, Y. X. Yao, and K. M. Ho, "Metals on graphene: correlation between adatom adsorption behavior and growth morphology.," Phys. Chem. Chem. Phys. **14**, 9157 (2012).
[58] Y. Liu, Y. M. Wang, B. I. Yakobson, and B. C. Wood, "Assessing carbon-based anodes for lithium-ion batteries: A universal description of charge-transfer binding," Phys. Rev. Lett. **113**, 028304 (2014).
[59] C. M. Berg and D. D. Dlott, "Picosecond dynamics of shock compressed and flash-heated nanometer thick films of δ-HMX," J. Physics: Conf. Ser. **500**, 142004 (2014).

C.3 Paper 4

Jing-Tao Lü Rasmus B. Christensen, Jian-Sheng Wang, Per Hedegåard and Mads Brandbyge

Current-induced forces and hot-spots in biased nano-junctions

Accepted for PHYSICAL REVIEW LETTERS

Current-induced forces and hot-spots in biased nano-junctions

Jing-Tao Lü,[1,2,3] Rasmus B. Christensen,[2] Jian-Sheng Wang,[4] Per Hedegård,[3] and Mads Brandbyge[5]

[1]*School of Physics, Huazhong University of Science and Technology, Wuhan, China*
[2]*Department of Micro- and Nanotechnology, Technical University of Denmark, Kongens Lyngby, Denmark*
[3]*Niels Bohr Institute, Nano-Science Center, University of Copenhagen, Copenhagen, Denmark*
[4]*Department of Physics, National University of Singapore, 117542 Singapore, Republic of Singapore*
[5]*Center for Nanostructured Graphene (CNG), Department of Micro- and Nanotechnology, Technical University of Denmark, Kongens Lyngby, Denmark*

We investigate theoretically the interplay of current-induced forces (CIF), Joule heating, and heat transport inside a current-carrying nano-conductor. We find that the CIF, due to the electron-phonon coherence, can control the spatial heat dissipation in the conductor. This yields a significant asymmetric concentration of excess heating (hot-spot) even for a symmetric conductor. When coupled to the electrode phonons, CIF drive different phonon heat flux into the two electrodes. First-principles calculations on realistic biased nano-junctions illustrate the importance of the effect.

PACS numbers: 85.75.-d, 85.65.+h,75.75.+a,73.63.Fg

Introduction– The effect of current-induced forces (CIF) on the dynamics of nano-scale conductors has gained renewed interest due to recent theoretical and experimental progress[1–9]. Several forces, present only in the nonequilibrium situation, have been discovered theoretically. Among them are the non-conservative (NC) "wind force", and the Berry-phase (BP) induced pseudo-magnetic force. Different from the stochastic Joule heating[10–21], the NC and BP forces can generate *deterministic* energy and momentum transfer between the current-carrying electrons and the vibrations in the conductor[1–5]. In carefully designed devices, this effect may be used to drive atomic motors[1, 6]. Meanwhile, it can also impact the stability of the device[2, 22, 23]. To this end, the vibrational/phononic[24] heat transport and heat distribution in the presence of current flow becomes an emergent problem to investigate.

The electrode phonons play an important role as heat sinks for the locally dissipated Joule heat in the conductor[14]. However, the effects on the heat transport of the deterministic CIF, and the momentum transfer from the current has so far not been explored. To address this question, we go beyond the previous treatments[2, 25] considering localized vibrations in the conductor, and include coupling to the phonons in the electrodes[26]. Employing the semi-classical generalized Langevin equation(SGLE),[25, 27–29], we find that, in addition to energy transfer, the CIF also influence how the excess vibrational energy is distributed in the junction and transported to the electrodes. Using first-principles calculations, we demonstrate how *symmetric* current-carrying nano-junctions typically possess a significant *asymmetric* excess heat distribution with heat accumulation at hot-spots in the junction. At the same time the phonon heat flow to the two electrodes differs. This behavior is governed by the phases of the electron and phonon wavefunctions, and is a result of electron-hole pair symmetry breaking in the electronic structure. It will have important implications for the description of how the junction ultimately will disrupt at high bias[22, 30].

Method – In the SGLE approach we adopt the two-probe transport setup, where a "bottleneck" nano-junction(system) is connected to left(L) and right(R) electrodes. We consider the case where the system region is characterized by a significant current density and deviation from equilibrium. The current-carrying electrons are treated as a nonequilibrium bath, coupling linearly with the system displacement, while the remaining atoms in L and R form two phonon baths interacting with the system also via a linear coupling. The electron-phonon (e-ph) coupling Hamiltonian can be written as

$$H_{eph} = \sum_{i,j,k} M_{ij}^{k}(c_i^{\dagger}c_j + h.c.)\hat{u}_k, \tag{1}$$

where $\hat{u}_k$ is the mass-normalized displacement away from the equilibrium position of the k-th atomic degrees of freedom, while $c_i^{\dagger}(c_j)$ is the electron creation(annihilation) operator for the i-(j-)th electronic state in the junction. The coupling matrix, M_{ij}^{k}, is local in real space, non-zero in the system and neglected in L, R. In order to focus on the effect of CIF, we will ignore the change of Hamiltonian due to the applied voltage.

The SGLE describing the dynamics of the system atoms reads,

$$\ddot{U}(t) - F(U(t)) \;=\; -\int^{t} \Pi^{r}(t-t')U(t')dt' + f(t), \tag{2}$$

where, U is a vector composed of the mass-normalized displacements of the system, and $F(U(t))$ is the force vector from the potential of the isolated system. We adopt the harmonic approximation, $F(U(t)) = -KU(t)$, with K being the dynamical matrix. The effect of all bath degrees of freedom is hidden in the terms on the right hand side of the SGLE. Each of them contains separate contributions from the L, R phonons, and the electron bath, such that $\Pi^{r} = \Pi_L^{r} + \Pi_R^{r} + \Pi_e^{r}$ and $f = f_L + f_R + f_e$. The Π^{r} describes the time-delayed backaction of the bath on the system due to its motion.

The second quantum term $f(t)$ is a random force (noise) due to the thermal, or current-induced fluctuation of the bath variables. It is characterized by the correlation matrix $\langle f_\alpha(t) f_\alpha^T(t')\rangle = S_\alpha(t-t')$. The two phonon baths are assumed to be in thermal equilibrium. Their noise correlation S_{ph} is related to the Π^r_{ph} through the fluctuation-dissipation theorem, $S_{ph}(\omega) = (n_B(\omega,T)+\frac{1}{2})\Gamma_{ph}(\omega)$ with $\Gamma_{ph}(\omega) = -2\mathrm{Im}\Pi^r_{ph}(\omega)$, n_B the Bose distribution function (using atomic units, $\hbar = 1$). Due to the electrical current, the electronic bath is not in equilibrium. We define the coupling-weighted electron-hole pair density of states as,[2, 25]

$$\Lambda^{\alpha\beta}_{kl}(\omega) \;=\; 2\sum_{m,n}\langle\psi_m|M^k|\psi_n\rangle\langle\psi_n|M^l|\psi_m\rangle(n_F(\varepsilon_n-\mu_\alpha)-n_F(\varepsilon_m-\mu_\beta))\delta(\varepsilon_n-\varepsilon_m-\omega), \tag{3}$$

with n_F the Fermi-Dirac distribution, and ψ_n the electron scattering state originating from the n-th channel of electrode α. The noise correlation and the backaction term of the electron bath can now be written as,

$$S_e(\omega) = -2\pi\sum_{\alpha\beta} n_B(\omega-(\mu_\alpha-\mu_\beta))\Lambda^{\alpha\beta}(\omega), \tag{4}$$

$$\Pi^r_e(\omega) = -\frac{1}{2}\left(\mathcal{H}\{\Gamma_e(\omega')\}(\omega) + i\Gamma_e(\omega)\right), \tag{5}$$

$$\Gamma_e(\omega) = -2\pi\sum_{\alpha\beta}\Lambda^{\alpha\beta}(\omega), \tag{6}$$

where $\mathcal{H}\{A\}$ is the Hilbert transform of A.

In the absence of electrical current, the electrons serve as an equilibrium thermal bath, similar to phonons. However, in the presence of current, the term ($\sim \mathrm{Im}\Lambda^{RL}_{kl}, k \neq l$) becomes important. It may coherently couple two vibrational modes (kl) inside the system leading to nonzero NC and BP forces. In Eq. (3) we observe that these effects depend on the phase of the electronic wavefunction, and thus the direction of electronic current. Furthermore, the coherent coupling breaks time-reversal symmetry of the noise correlation function, $S_e(t-t') \neq S_e(t'-t)$. Hereafter, we denote these forces by *asymmetric CIF*, and focus on their role for the excess heat distribution and heat transport in the junction.

We will consider the case where all baths are at the same temperature (T), and the electron bath is subject to a nonzero voltage bias ($eV = \mu_L - \mu_R$). To look at the excess heating, we calculate the kinetic energy of atom n from its local displacement correlation function, and obtain

$$E_n \;=\; \sum_{\sigma=x,y,z}\int_0^{+\infty}\omega^2\mathrm{diag}\{D^r S D^a\}_{n,\sigma}(\omega)\frac{d\omega}{2\pi}. \tag{7}$$

Here D^r (D^a) is the eV-dependent phonon retarded (advanced) Green's function, S is the sum of noise correlation function from all the baths, and $\mathrm{diag}\{A\}_{n,\sigma}$ means the diagonal matrix element of A, corresponding to the n-th atom's σ degrees of freedom.

To study heat transport, we calculate the phonon heat current flowing *into* the bath L as the product of the velocity of the system degrees of freedom, and the force exerted on them by bath L. Applying time average, using the solution of the SGLE, we arrive at a Landauer-like expression (Sec. I, Supplemental Materials (SM))

$$\begin{aligned} J_L \;=\; &-\int_{-\infty}^{+\infty}\omega\,\mathrm{tr}\left[\Gamma_L(\omega)D^r(\omega)\Lambda^{RL}(\omega)D^a(\omega)\right] \\ &\times\left(n_B(\omega+eV)-n_B(\omega)\right)d\omega, \end{aligned} \tag{8}$$

Defining the time-reversed phonon spectral function from the left bath $\tilde{\mathcal{A}}_L = D^a\Gamma_L D^r$, and similarly $\mathcal{A}_e = D^r\Lambda^{RL}D^a$, we can write the trace in Eq. (8) in different forms

$$\mathrm{tr}[\Gamma_L D^r\Lambda^{RL}D^a] = \mathrm{tr}[\Gamma_L\mathcal{A}_e] = \mathrm{tr}[\Lambda^{RL}\tilde{\mathcal{A}}_L]. \tag{9}$$

Equations (8) is analogous to the Landauer or non-equilibrium Green's function formula for electron/phonon transport. In our present case the energy current is driven by a non-thermal electron bath with the bias showing up in the Bose distributions and in the coupling function, Λ^{RL}, between phonons and electrical current. The two forms in Eq. (9) emphasize two aspects of the problem. In the first version emphasis is on the coupling, Γ_L of the system vibrations as described by $\mathcal{A}_e$, to the phonons of the leads. This is a general formula, which does not explicitly depend on the situation we are considering here, namely that the source of energy is the non-equilibrium electron bath. This aspect is emphasized in the second version. Here the coupling to the electrical current, Λ^{RL} is made explicit, and the complete phonon system including the coupling to leads are in the function $\tilde{\mathcal{A}}_L$. In both forms the asymmetric CIF show up in the different versions of the $\mathcal{A}$ functions. The forces are responsible for the build up of vibrational energy inside the junction, a fact that is present in the two phonon Green's functions D^r and D^a. Apart from this effect the non-equilibrium nature of the electron system shows up in the explicit factor Λ^{RL} in the second version of Eq. (9). This will develop an imaginary part which is not present in equilibrium.

Applying these formulas to a minimal model, in Sec. II of the SM, we have shown analytically that the asymmetric CIF, especially the NC force, generate an asymmetric

phonon heat flow and energy distribution, even for a left-right symmetric system.

First Principles calculations– Next we turn to numerical calculation for two concrete nano-junctions. We use SIESTA/TRANSIESTA[31, 32] to calculate the electronic transport, vibrational modes, e-ph coupling employing Ref. 33, and coupling to electrode phonons using Ref. 34, with similar parameters. The effect of current on the stability of gold single atomic junctions has been studied for more than a decade[30, 35]. Here we first consider a symmetric single atom gold chain between two Au(100) electrodes(Fig. 2 inset).[36, 37] We have previously[38] studied the asymmetric forces in this system neglecting the coupling to electrode phonons.

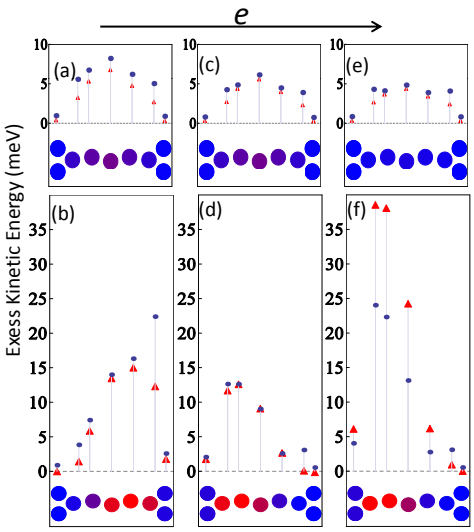

FIG. 1: Excess kinetic energy of each atom in a gold chain (inset of Fig. 2(a)) at $V = 1.0$ V, $T = 300$ K, with (bottom) and without (top) the asymmetric CIF. The total energy difference between the two cases is due to the non-conservative force contribution. The blue dots and the colored plot of each atom are from the full calculation. The asymmetric heating is qualitatively reproduced by only considering electron coupling with vibrational modes (1) and (2) in the inset of Fig. 2 (a), as shown by red triangles. (a)-(b)$E_F = -0.3$ eV, (c)-(d) $E_F = 0$, and (e)-(f) $E_F = 0.2$ eV. The arrow indicates the current direction.

Figure 1 shows the average excess kinetic energy ($\Delta E_n = E_n(eV) - E_n(0)$) of atoms along the chain for three different E_F. The structure is almost mirror symmetric. When we turn off the asymmetric CIF ($\mathrm{Im}\Lambda^{RL} = 0$) as in previous studies[13, 39], the heating profile is almost symmetric with respect to the center atom. However, once we include them, the kinetic energy of one side becomes many times higher than that of the other. Meanwhile, the total kinetic energy stored in the system increase significantly. Further analysis shows

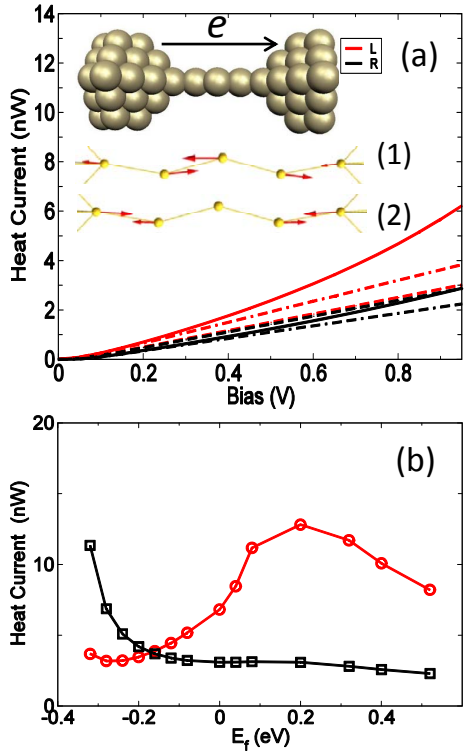

FIG. 2: (a) Bias dependence of the phonon heat current, going into the left and right phonon baths. Solid lines include the asymmetric CIF ($\sim \mathrm{Im}\Lambda^{RL}$), dashed lines do not, and the dash-dotted lines ignore the change of phonon spectral (D^r/D^a) due to NC and BP forces. In the inset, we show the two vibrational modes that couple most strongly with the electrical current, with vibrational energy at (1) 19 and (2) 18 meV. (b) Phonon heat current going into the left (red, circle) and right (black, square) baths at $V = 1$V, for different Fermi levels to illustrate the importance of the phase of the electron wavefunctions.

that both effects are due to the NC force (Fig. 2 in SM).

We now turn to the phonon heat current calculated using Eq. (8), shown in Fig 2 (a). The inclusion of the asymmetric CIF drives much larger heat current into the L bath. Intuitively, this is due to the asymmetric energy accumulation induced by the NC force, e.g., modifying D^r/D^a in Eqs. (8-9). However, there is another contribution at low bias. Ignoring the bias-induced change of $\tilde{\mathcal{A}}_L$, we get opposite heat flow into L and $R(J_L = -J_R)$ due to $\mathrm{tr}[\mathrm{Im}\Lambda^{RL}\mathrm{Im}\tilde{\mathcal{A}}^0_L]$. This term drives asymmetric heat flow even in the linear response regime, contributing with a correction to the thermoelectric Peltier coefficient (Sec. I(A) of SM). In the next section, we will show that it can be understood as asymmetric excitation of left- and right-travelling phonon waves.

From Fig. 1 (b)-(d) and 2 (b), we see that the phase of the electronic wavefunction, depending on the Fermi level, E_F, is controlling the direction and magnitude of the asymmetry. Thus we expect that the direction of electron flow is essential in the description of the atomic dynamics in the junction, as indicated in recent experiments[8].

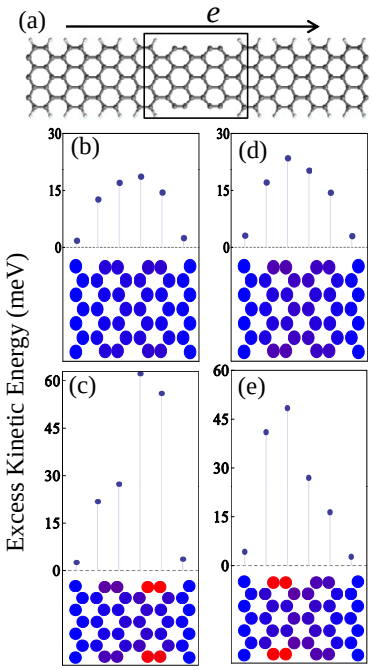

FIG. 3: (a) Structure of a partially passivated armchair graphene ribbon considered. The two sides of the ribbon is Hydrogen passivated except in the device region, enclosed by the solid lines. (b)-(c) The excess kinetic energy of each atom without and with the asymmetric CIF, at $V = 0.4$ V, $T = 300$ K, $E_F = 1.4$ eV. The dots show the average over atoms belonging to each zigzag column. (d)-(e) Same with (b)-(c) with $E_F = -1.0$ eV.

The second system we consider is an armchair graphene nanoribbon (a-GNR) with partial Hydrogen passivation, shown in Fig. 3 (a). This example is inspired by experiments showing current-induced edge-reconstructions in graphene[40] where the physical mechanism was attributed to Joule heating[41]. In Fig. 3 (a), the four pairs of unpassivated carbon dimers give rise to localized high-frequency vibrations interacting strongly with electrical current. Consequently, the excess energy is mainly stored in the dimers and nearby atoms (Fig. 3 (b),(d)). Including the asymmetric CIF leads to symmetry breaking of the heating profile along the current direction. Contrary to experiments on the gold chain E_F may in this case be tuned by gating. We predict the resulting hot-spot to move from "down-stream" to "up-stream" w.r.t. the electron current when tuning from $E_F = 1.4$ eV to $E_F = -1.0$ eV (Fig. 3 (c),(e), and Fig. 3 in SM).

The dependence of the hot-spot on E_F can be understood as follows (Sec. III of SM). For a mirror-symmetric system with electron-hole symmetry, the asymmetric heating and heat flow is absent. When E_F crosses the electron-hole symmetric point, the dominant current-carriers contributing to inelastic transport change from electrons to holes, or vice versa. Thus, the hot-spot moves from one side to the other. Interestingly enough, similar effect in micrometer scale has been observed experimentally in graphene transistors[42, 43] and electrodes of molecular junctions[21]. Here we show that it is equally important at atomic scale, and related to the asymmetric CIF.

Scattering analysis – The asymmetric heating and phonon heat flow at low bias can be qualitatively understood from the momentum transfer between electrons and phonons. To show this, we consider a simple 1D model with a local e-ph interaction which involve the displacement of the n- and $n+1$-th atoms (junction) (Sec. IV of SM),

$$H_{eph} = \sum_{j\in\{n,n+1\}} -m\hat{u}_j(c_j^\dagger c_{j+1} - c_j^\dagger c_{j-1} + h.c.). \quad (10)$$

For $eV > 0$, the important process is the inelastic electronic transition from the filled, left scattering states with momentum k_L to the empty, right states with k_R. It is straightforward to show that the emission probability of a right-travelling phonon with momentum q is different from that of a left-travelling mode, $-q$, due to the difference in matrix elements for the processes,

$$\Delta M_{LR} = |M_{LR}^q|^2 - |M_{LR}^{-q}|^2 \sim \sin(q)\sin(k_L - k_R). \quad (11)$$

Consequently, the left- and right-travelling steady state phonon populations become different, resulting in asymmetric heat flow.

In conclusion, we have presented a theory showing that CIF in nano-junctions lead to asymmetric distributions and transport of the excess heat. We derived a Landauer-like formula for the excess heat transport. Employing first-principles calculations, we demonstrate that the size of the asymmetry can be crucial for current-induced processes at the atomic scale.

We thank T. N. Todorov, D. Dundas, and T. Markussen for discussions and the Danish Center for Scientific Computing (DCSC) for computer resources. This work is supported by the Lundbeck Foundation (R49-A5454), National Natural Science Foundation of China (Grants No. 11304107, 61371015), and the Fundamental Research Funds for the Central Universities (HUST:2013TS032).

[1] D. Dundas, E. J. McEniry, and T. N. Todorov, Nature Nanotech. **4**, 99 (2009).
[2] J. T. Lü, M. Brandbyge, and P. Hedegård, Nano Lett. **10**, 1657 (2010).
[3] N. Bode, S. V. Kusminskiy, R. Egger, and F. von Oppen, Phys. Rev. Lett. **107**, 036804 (2011).
[4] T. N. Todorov, D. Dundas, A. T. Paxton, and A. P. Horsfield, Beilstein J. Nanotechnol. **2**, 727 (2011).
[5] I. A. Pshenichnyuk and M. Čížek, Phys. Rev. B **83**, 165446 (2011).
[6] R. Bustos-Marún, G. Refael, and F. von Oppen, Phys. Rev. Lett. **111**, 060802 (2013).
[7] F. Agostini, A. Abedi, and E. K. U. Gross, ArXiv:1406.5126, (2014).
[8] C. Schirm, M. Matt, F. Pauly, J. C. Cuevas, P. Nielaba, and E. Scheer, Nature Nano **8**, 645 (2013).
[9] P. J. Wheeler, R. Chen, and D. Natelson, Phys. Rev. B **87**, 155411 (2013).
[10] N. J. Tao, Nature Nanotech. **1**, 173 (2006).
[11] M. Galperin, M. A. Ratner, and A. Nitzan, J. Phys.:Condens. Matter **19**, 103201 (2007).
[12] M. Galperin, M. A. Ratner, A. Nitzan, and A. Troisi, Science **319**, 1056 (2008).
[13] Z. Huang, F. Chen, R. D'Agosta, P. A. Bennett, M. Di Ventra, and N. Tao, Nature Nanotech. **2**, 698 (2007).
[14] M. Tsutsui, M. Taniguchi, and T. Kawai, Nano Lett. **8**, 3293 (2008).
[15] Y. Asai, Phys. Rev. B **78**, 045434 (2008).
[16] R. H. M. Smit, Y. Noat, C. Untiedt, N. D. Lang, M. C. van Hemert, and J. M. van Ruitenbeek, Nature **419**, 906 (2002).
[17] W. Y. Wang, T. Lee, I. Kretzschmar, and M. A. Reed, Nano Lett. **4**, 643 (2004).
[18] J. G. Kushmerick, J. Lazorcik, C. H. Patterson, R. Shashidhar, D. S. Seferos, and G. C. Bazan, Nano Lett. **4**, 639 (2004).
[19] Z. Ioffe, T. Shamai, A. Ophir, G. Noy, I. Yutsis, K. Kfir, O. Cheshnovsky, and Y. Selzer, Nature Nanotech. **3**, 727 (2008).
[20] D. R. Ward, D. A. Corley, J. M. Tour, and D. Natelson, Nature Nanotech. **6**, 33 (2011).
[21] W. Lee, K. Kim, W. Jeong, L. A. Zotti, F. Pauly, J. C. Cuevas, and P. Reddy, Nature **498**, 209 (2013).
[22] R. H. M. Smit, C. Untiedt, and J. M. van Ruitenbeek, Nanotechnology **15**, S472 (2004).
[23] G. Schulze, K. J. Franke, A. Gagliardi, G. Romano, C. S. Lin, A. L. Rosa, T. A. Niehaus, T. Frauenheim, A. Di Carlo, A. Pecchia, et al., Phys. Rev. Lett. **100**, 136801 (2008).
[24] We use phonons and vibrations interchangably, although, strictly speaking, phonons are defined only in systems with translational invariance.
[25] J.-T. Lü, M. Brandbyge, P. Hedegård, T. N. Todorov, and D. Dundas, Phys. Rev. B **85**, 245444 (2012).
[26] J.-S. Wang, Phys. Rev. Lett. **99**, 160601 (2007).
[27] R. P. Feynman and F. L. Vernon, Ann. Phys. **24**, 118 (1963).
[28] A. Caldeira and A. Leggett, Physica A **121**, 587 (1983).
[29] A. Schmid, J. Low Temp. Phys. **49**, 609 (1982).
[30] Y. Oshima and Y. Kurui, Phys. Rev. B **87**, 081404 (2013).
[31] J. Soler, E. Artacho, J. Gale, A. Garcia, J. Junquera, P. Ordejon, and D. Sanchez-Portal, J. Phys.:Condens. Matter **14**, 2745 (2002).
[32] M. Brandbyge, J. L. Mozos, P. Ordejon, J. Taylor, and K. Stokbro, Phys. Rev. B **65**, 165401 (2002).
[33] T. Frederiksen, M. Paulsson, M. Brandbyge, and A.-P. Jauho, Phys. Rev. B **75**, 205413 (2007).
[34] M. Engelund, M. Brandbyge, and A. P. Jauho, Phys. Rev. B **80**, 045427 (2009).
[35] H. Yasuda and A. Sakai, Phys. Rev. B **56**, 1069 (1997).
[36] H. Ohnishi, Y. Kondo, and K. Takayanagi, Nature **395**, 780 (1998).
[37] A. I. Yanson, G. R. Bollinger, H. E. van den Brom, N. Agraït, and J. M. van Ruitenbeek, Nature **395**, 783 (1998).
[38] J. T. Lü, P. Hedegård, and M. Brandbyge, Phys. Rev. Lett. **107**, 046801 (2011).
[39] T. Frederiksen, M. Brandbyge, N. Lorente, and A.-P. Jauho, Phys. Rev. Lett. **93**, 256601 (2004).
[40] X. Jia, M. Hofmann, V. Meunier, B. G. Sumpter, J. Campos-Delgado, J. M. Romo-Herrera, H. Son, Y.-P. Hsieh, A. Reina, J. Kong, et al., Science **323**, 1701 (2009).
[41] M. Engelund, J. A. Fürst, A. P. Jauho, and M. Brandbyge, Phys. Rev. Lett. **104**, 036807 (2010).
[42] M. Freitag, H.-Y. Chiu, M. Steiner, V. Perebeinos, and P. Avouris, Nature Nanotech. **5**, 497 (2010).
[43] M.-H. Bae, Z.-Y. Ong, D. Estrada, and E. Pop, Nano Lett. **10**, 4787 (2010).

Bibliography

[1] IBM News room - 2014-07-10 IBM Announces $3 Billion Research Initiative to Tackle Chip Grand Challenges for Cloud and Big Data Systems - United States, July 2014.

[2] Nicolás Agraït, Carlos Untiedt, Gabino Rubio-Bollinger, and Vieira Sebastián. Onset of energy dissipation in ballistic atomic wires. *Phys. Rev. Lett*, 88(21):216803, 2002.

[3] Ramón Aguado and Leo P Kouwenhoven. Double Quantum Dots as Detectors of High-Frequency Quantum Noise in Mesoscopic Conductors. *Phys. Rev. Lett.*, 84(9):1986–1989, February 2000.

[4] Nabil Al-Aqtash, Hong Li, Lu Wang, Wai-Ning Mei, and R.F. Sabirianov. Electromechanical switching in graphene nanoribbons. *Carbon*, 51:102–109, January 2013.

[5] Myung-Ho Bae, Zhun-Yong Ong, David Estrada, and Eric Pop. Imaging, simulation, and electrostatic control of power dissipation in graphene devices. *Nano letters*, 10(12):4787–93, December 2010.

[6] Jingwei Bai, Xing Zhong, Shan Jiang, Yu Huang, and Xiangfeng Duan. Graphene nanomesh. *Nature Nanotechnology*, 5(3):190–194, 2010.

[7] Jens Baringhaus, Ming Ruan, Frederik Edler, Antonio Tejeda, Muriel Sicot, AminaTaleb-Ibrahimi, An-Ping Li, Zhigang Jiang, Edward H. Conrad, Claire Berger, Christoph Tegenkamp, Walt A. de Heer, and Amina Taleb-Ibrahimi. Exceptional ballistic transport in epitaxial graphene nanoribbons. *Nature*, 506(7488):349–354, February 2014.

[8] G Bevilacqua. Some integrals related to the Fermi function. *arXiv:1303.6206 [math-ph]*, 2013.

[9] Stephan Blankenburg, Jinming Cai, Pascal Ruffieux, Rached Jaafar, Daniele Passerone, Xinliang Feng, Klaus Müllen, Roman Fasel, and Carlo a Pignedoli. Intraribbon heterojunction formation in ultranarrow graphene nanoribbons. *ACS nano*, 6(3):2020–5, March 2012.

[10] Ya.M. M Blanter, M. Büttiker, and M Buttiker. Shot noise in mesoscopic conductors. *Physics Reports*, 336(1-2):1–166, September 2000.

[11] Niels Bode, Silvia Viola Kusminskiy, Reinhold Egger, and Felix von Oppen. Scattering Theory of Current-Induced Forces in Mesoscopic Systems. *Physical Review Letters*, 107(3):036804, July 2011.

[12] M. Born and R. Oppenheimer. Zur Quantentheorie der Molekeln. *Annalen der Physik*, 389(20):457–484, 1927.

[13] Mads Brandbyge, José-Luis Mozos, Pablo Ordejon, Jeremy Taylor, and Kurt Stokbro. Density-functional method for nonequilibrium electron transport. *Physical Review B*, 65(16):165401, March 2002.

[14] C. Bronner, F. Leyssner, S. Stremlau, M. Utecht, P. Saalfrank, T. Klamroth, and P. Tegeder. Electronic structure of a subnanometer wide bottom-up fabricated graphene nanoribbon: End states, band gap, and dispersion. *Physical Review B*, 86(8):085444, August 2012.

[15] M Büttiker. Scattering theory of thermal and excess noise in open conductors. *Phys. Rev. Lett.*, 65(23):2901–2904, December 1990.

[16] Jinming Cai, Pascal Ruffieux, Rached Jaafar, Marco Bieri, Thomas Braun, Stephan Blankenburg, Matthias Muoth, Ari P. Seitsonen, Moussa Saleh, Xinliang Feng, Klaus Müllen, and Roman Fasel. Atomically precise bottom-up fabrication of graphene nanoribbons. *Nature*, 466(7305):470–473, 2010.

[17] A.O. Caldeira and A.J. Leggett. Path integral approach to quantum Brownian motion. *Physica A: Statistical Mechanics and its Applications*, 121(3):587–616, September 1983.

[18] Ramon Carbó-Dorca. Symmetrical overlap transformations of function basis sets: the LCAO MO and quantum similarity practical cases. *Journal of Mathematical Chemistry*, 50(4):741–751, October 2011.

[19] Gianaurelio Cuniberti, Klaus Richter, and Giorgos Fagas, editors. *Introducing Molecular Electronics*, volume 680 of *Lecture Notes in Physics*. Springer Berlin Heidelberg, 2006.

[20] Pierre Darancet, Andrea Ferretti, Didier Mayou, and Valerio Olevano. Ab initio GW electron-electron interaction effects in quantum transport. *Physical Review B*, 75(7):075102, February 2007.

[21] P. Delaney and J. Greer. Correlated Electron Transport in Molecular Electronics. *Physical Review Letters*, 93(3):036805, July 2004.

[22] D Djukic and J M van Ruitenbeek. Shot noise measurements on a single molecule RID B-3783-2008. *Nano Lett.*, 6(4):789–793, April 2006.

[23] Daniel Dundas, Eunan J McEniry, and Tchavdar N Todorov. Current-driven atomic waterwheels. *Nature nanotechnology*, 4(2):99–102, February 2009.

[24] Sudipta Dutta and Swapan K. Pati. Novel properties of graphene nanoribbons: a review. *Journal of Materials Chemistry*, 20(38):8207, 2010.

[25] R. Egger and A. O. Gogolin. Vibration-induced correction to the current through a single molecule. *Physical Review B*, 77(11):113405, March 2008.

[26] M. Engelund, J. A. Fürst, A. P. Jauho, and M. Brandbyge. Localized Edge Vibrations and Edge Reconstruction by Joule Heating in Graphene Nanostructures. *Physical Review Letters*, 104(3):036807, January 2010.

[27] Andrea C. Ferrari and Denis M. Basko. Raman spectroscopy as a versatile tool for studying the properties of graphene. *Nature Nanotechnology*, 8(4):235–246, 2013.

[28] Thomas Frederiksen. *Inelastic transport theory for nanoscale systems.* Phd, DTU, 2007.

[29] Thomas Frederiksen, Mads Brandbyge, Nicolás Lorente, and Antti-Pekka Jauho. Inelastic Scattering and Local Heating in Atomic Gold Wires. *Phys. Rev. Lett.*, 93(25):256601, December 2004.

[30] Thomas Frederiksen, Magnus Paulsson, Mads Brandbyge, and Antti-Pekka A.-P. Jauho. Inelastic transport theory from first principles: Methodology and application to nanoscale devices. *Physical Review B*, 75(20):205413, May 2007.

[31] Marcus Freitag, Hsin-Ying Chiu, Mathias Steiner, Vasili Perebeinos, and Phaedon Avouris. Thermal infrared emission from biased graphene. *Nature nanotechnology*, 5(7):497–501, July 2010.

[32] Michael Galperin and Abraham Nitzan. Molecular optoelectronics: The interaction of molecular conduction junctions with light. *Physical Chemistry Chemical Physics*, 14(26):9421–9438, 2012.

[33] Michael Galperin, Mark A. Ratner, and Abraham Nitzan. Molecular transport junctions: vibrational effects. *Journal of Physics: Condensed Matter*, 19(10):103201, March 2007.

[34] Víctor M. García-Suárez and Colin J. Lambert. First-principles scheme for spectral adjustment in nanoscale transport. *New Journal of Physics*, 13(5):053026, May 2011.

[35] U. Gavish, Y. Levinson, and Y. Imry. Detection of quantum noise. *Physical Review B*, 62(16):R10637–R10640, October 2000.

[36] Roland Gillen, Marcel Mohr, Janina Maultzsch, and Christian Thomsen. Lattice vibrations in graphene nanoribbons from density functional theory. *Physica Status Solidi (B)*, 246(11-12):2577–2580, December 2009.

[37] D. Gunlycke, J. Li, J. W. Mintmire, and C. T. White. Altering low-bias transport in zigzag-edge graphene nanostrips with edge chemistry. *Applied Physics Letters*, 91(11):112108, 2007.

[38] Tue Gunst. *Transport and dynamics of nanostructured graphene*. PhD thesis, DTU, 2013.

[39] Tue Gunst, Jing-Tao Lü, Per Hedegård, and Mads Brandbyge. Phonon excitation and instabilities in biased graphene nanoconstrictions. *Physical Review B*, 88(16):161401, October 2013.

[40] D. Hamann, M. Schlüter, and C. Chiang. Norm-Conserving Pseudopotentials. *Physical Review Letters*, 43(20):1494–1497, November 1979.

[41] Melinda Y. Han, Barbaros Özyilmaz, Yuanbo Zhang, and Philip Kim. Energy Band-Gap Engineering of Graphene Nanoribbons. *Physical Review Letters*, 98(20):206805, May 2007.

[42] H Haug and A-P Jauho. *Quantum Kinetics in Transport and Optics of Semiconductors*. Springer-Verlag, 1996.

[43] Federica Haupt, T Novotny, Wolfgang Belzig, and Tomá šNovotný. Current noise in molecular junctions: Effects of the electron-phonon interaction. *PHYSICAL REVIEW B*, 82(16):165441, October 2010.

[44] Martin Head-Gordon and John C. Tully. Molecular dynamics with electronic frictions. *The Journal of Chemical Physics*, 103(23):10137, December 1995.

[45] Oded Hod, Verónica Barone, Juan E Peralta, and Gustavo E Scuseria. Enhanced half-metallicity in edge-oxidized zigzag graphene nanoribbons. *Nano letters*, 7(8):2295–9, August 2007.

[46] G Hoffmann, R Berndt, and P Johansson. Two-electron photon emission from metallic quantum wells. *Phys. Rev. Lett.*, 90(4):46803, 2003.

[47] P. Hohenberg. Inhomogeneous Electron Gas. *Physical Review*, 136(3B):B864–B871, November 1964.

[48] Han Huang, Dacheng Wei, Jiatao Sun, Swee Liang Wong, Yuan Ping Feng, a H Castro Neto, and Andrew Thye Shen Wee. Spatially resolved electronic structures of atomically precise armchair graphene nanoribbons. *Scientific reports*, 2:983, January 2012.

[49] M. Ijäs, M. Ervasti, A. Uppstu, P. Liljeroth, J. van der Lit, I. Swart, and A. Harju. Electronic states in finite graphene nanoribbons: Effect of charging and defects. *Physical Review B*, 88(7):075429, August 2013.

[50] Xiaoting Jia, Mario Hofmann, Vincent Meunier, Bobby G Sumpter, Jessica Campos-Delgado, José Manuel Romo-Herrera, Hyungbin Son, Ya-Ping Hsieh, Alfonso Reina, Jing Kong, Mauricio Terrones, and Mildred S Dresselhaus. Controlled Formation of Sharp. *Science (New York, N.Y.)*, 323(March):1701–1705, March 2009.

[51] J Jiang, M Kula, W Lu, and Y Luo. First-principles simulations of inelastic electron tunneling spectroscopy of molecular electronic devices. *Nano Lett.*, 5(8):1551–1555, 2005.

[52] Xueping Jiang, Neerav Kharche, Paul Kohl, Timothy B. Boykin, Gerhard Klimeck, Mathieu Luisier, Pulickel M. Ajayan, and Saroj K. Nayak. Giant quasiparticle bandgap modulation in graphene nanoribbons supported on weakly interacting surfaces. *Applied Physics Letters*, 103(13):133107, September 2013.

[53] Chengjun Jin, Mikkel Strange, Troels Markussen, Gemma C. Solomon, and Kristian S. Thygesen. Energy level alignment and quantum conductance of functionalized metal-molecule junctions: Density functional theory versus GW calculations. *The Journal of Chemical Physics*, 139(18):184307, November 2013.

[54] Peter Johansson, R. Monreal, and Peter Apell. Theory for light emission from a scanning tunneling microscope. *Phys. Rev. B*, 42(14):9210–9213, November 1990.

[55] J. Johnson. Thermal Agitation of Electricity in Conductors. *Physical Review*, 32(1):97–109, July 1928.

[56] Kristen Kaasbjerg and Abraham Nitzan. Theory of light emission from quantum noise in plasmonic contacts: above-threshold emission from higher-order electron-plasmon scattering. *arXiv:1412.1101 [cond-mat.mes-hall]*, page 6, December 2014.

[57] Youngsang Kim, Hyunwook Song, Florian Strigl, Hans-Fridtjof Pernau, Takhee Lee, and Elke Scheer. Conductance and Vibrational States of Single-Molecule Junctions Controlled by Mechanical Stretching and Material Variation. *Physical Review Letters*, 106(19):196804, May 2011.

[58] Matthias Koch. *Growth and Characterization of Single Molecular Wires on Metal Surfaces*. Phd, Freien Universität Berlin, 2013.

[59] Matthias Koch, Francisco Ample, Christian Joachim, and Leonhard Grill. Voltage-dependent conductance of a single graphene nanoribbon. *Nature Nanotechnology*, 7(11):713–717, November 2012.

[60] Jorge Kohanoff. *Electronic Structure Calculations for Solids and Molecules Theory and Computational Methods | Condensed matter physics, nanoscience and mesoscopic physics | Cambridge University Press*. Cambridge University Press, 2006.

[61] W. Kohn and L. J. Sham. Self-Consistent Equations Including Exchange and Correlation Effects. *Physical Review*, 140(4A):A1133–A1138, November 1965.

[62] Dmitry V Kosynkin, Amanda L Higginbotham, Alexander Sinitskii, Jay R Lomeda, Ayrat Dimiev, B Katherine Price, and James M Tour. Longitudinal unzipping of carbon nanotubes to form graphene nanoribbons. *Nature*, 458(7240):872–6, April 2009.

[63] S. Kurth, G. Stefanucci, C.-O. Almbladh, A. Rubio, and E. K. U. Gross. Time-dependent quantum transport: A practical scheme using density functional theory. *Physical Review B*, 72(3):035308, July 2005.

[64] J G Kushmerick, J Lazorcik, C H Patterson, R Shashidhar, D S Seferos, and G C Bazan. Vibronic contributions to charge transport across molecular junctions. *Nano Lett.*, 4(4):639–642, 2004.

[65] A V Lebedev, G B Lesovik, and G Blatter. Statistics of radiation emitted from a quantum point contact. *Phys. Rev. B*, 81(15):155421, April 2010.

[66] Woochul Lee, Kyeongtae Kim, Wonho Jeong, Linda Angela Zotti, Fabian Pauly, Juan Carlos Cuevas, and Pramod Reddy. Heat dissipation in atomic-scale junctions. *Nature*, 498(7453):209–212, June 2013.

[67] Jia Li, Zuanyi Li, Gang Zhou, Zhirong Liu, Jian Wu, Bing-Lin Gu, Jisoon Ihm, and Wenhui Duan. Spontaneous edge-defect formation and defect-induced conductance suppression in graphene nanoribbons. *Physical Review B*, 82(11):115410, September 2010.

[68] Xiaolin Li, Xinran Wang, Li Zhang, Sangwon Lee, and Hongjie Dai. Chemically derived, ultrasmooth graphene nanoribbon semiconductors. *Science (New York, N.Y.)*, 319(5867):1229–32, February 2008.

[69] Liangbo Liang and Vincent Meunier. Electronic structure of assembled graphene nanoribbons: Substrate and many-body effects. *Physical Review B*, 86(19):195404, November 2012.

[70] B. A. Lippmann and Julian Schwinger. Variational Principles for Scattering Processes. I. *Physical Review*, 79(3):469–480, August 1950.

[71] Xiaojie Liu, C Z Wang, M Hupalo, W C Lu, M C Tringides, Y X Yao, and K M Ho. Metals on graphene: correlation between adatom adsorption behavior and growth morphology. *Physical chemistry chemical physics : PCCP*, 14(25):9157–66, July 2012.

[72] Jing-Tao Lü. Unpublished note.

[73] Jing-Tao Lü, Mads Brandbyge, and Per Hedegå rd. Blowing the fuse: Berry's phase and runaway vibrations in molecular conductors. *Nano letters*, 10(5):1657–63, May 2010.

[74] Jing-Tao Lü, Mads Brandbyge, Per Hedegå rd, Tchavdar N. Todorov, and Daniel Dundas. Current-induced atomic dynamics, instabilities, and Raman signals: Quasiclassical Langevin equation approach. *Physical Review B*, 85(24):245444, June 2012.

[75] Jing-Tao Lü, Rasmus B. Christensen, Giuseppe Foti, Thomas Frederiksen, Tue Gunst, and Mads Brandbyge. Efficient calculation of inelastic vibration signals in electron transport: Beyond the wide-band approximation. *Physical Review B*, 89(8):081405, February 2014.

[76] Jing-Tao Lü, Rasmus B. Christensen, Jian-Sheng Wang, Per Hedegå rd, and Mads Brandbyge. Current-induced forces and hot-spots in biased nano-junctions. page 5, September 2014.

[77] Jing-Tao Lü, Rasmus Bjerregaard Christensen, and Mads Brandbyge. Light emission and finite-frequency shot noise in molecular junctions: From tunneling to contact. *Physical Review B*, 88(4):045413, July 2013.

[78] Jing-Tao Lü, Per Hedegå rd, and Mads Brandbyge. Laserlike Vibrational Instability in Rectifying Molecular Conductors. *Physical Review Letters*, 107(4):046801, July 2011.

[79] Theresa Lutz, Christoph Groß e, Christian Dette, Alexander Kabakchiev, Frank Schramm, Mario Ruben, Rico Gutzler, Klaus Kuhnke, Uta Schlickum, and Klaus Kern. Molecular Orbital Gates for Plasmon Excitation. *Nano Letters*, page in press., May 2013.

[80] Richard M. Martin. *Electronic Structure Basic Theory and Practical Methods / Condensed matter physics, nanoscience and mesoscopic physics / Cambridge University Press*. Cambridge University Press, 2008.

[81] Yigal Meir and Ned S. Wingreen. Landauer formula for the current through an interacting electron region. *Physical Review Letters*, 68(16):2512–2515, April 1992.

[82] G.E. Moore. Cramming More Components Onto Integrated Circuits. *Proceedings of the IEEE*, 86(1):82–85, January 1998.

[83] H. Nyquist. Thermal Agitation of Electric Charge in Conductors. *Physical Review*, 32(1):110–113, July 1928.

[84] Norio Okabayashi, Magnus Paulsson, and Tadahiro Komeda. Inelastic electron tunneling process for alkanethiol self-assembled monolayers. *Progress in Surface Science*, 88(1):1–38, February 2013.

[85] Norio Okabayashi, Magnus Paulsson, Hiromu Ueba, Youhei Konda, and Tadahiro Komeda. Inelastic Tunneling Spectroscopy of Alkanethiol Molecules: High-Resolution Spectroscopy and Theoretical Simulations. *Physical Review Letters*, 104(7):077801, February 2010.

[86] Norio Okabayashi, Magnus Paulsson, Hiromu Ueba, Youhei Konda, and Tadahiro Komeda. Site Selective Inelastic Electron Tunneling Spectroscopy Probed by Isotope Labeling. *Nano Lett.*, 10(8):2950–2955, August 2010.

[87] Woei Wu Pai, H. T. Jeng, C.-M. M Cheng, C.-H. H Lin, Xudong D Xiao, Aidi D Zhao, Xieqiu Q Zhang, Geng Xu, X. Q. Shi, M. A. Van Hove, C.-S. S Hsue, and K.-D. D Tsuei. Optimal Electron Doping of a C_{60} Monolayer on Cu(111) via Interface Reconstruction. *Physical Review Letters*, 104(3):036103, January 2010.

[88] M Paulsson, T Frederiksen, and M Brandbyge. Inelastic transport through molecules: Comparing first-principles calculations to experiments. *Nano Lett.*, 6(2):258–262, 2006.

[89] Magnus Paulsson and Mads Brandbyge. Transmission eigenchannels from nonequilibrium Green's functions. *Physical Review B*, 76(11):115117, September 2007.

[90] Magnus Paulsson, Thomas Frederiksen, and Mads Brandbyge. Modeling inelastic phonon scattering in atomic- and molecular-wire junctions. *Physical Review B*, 72(20):201101, November 2005.

[91] Magnus Paulsson, Thomas Frederiksen, Hiromu Ueba, Nicolás Lorente, and Mads Brandbyge. Unified Description of Inelastic Propensity Rules for Electron Transport through Nanoscale Junctions. *Physical Review Letters*, 100(22):226604, June 2008.

[92] Alessandro Pecchia and Aldo Di Carlo. Atomistic theory of transport in organic and inorganic nanostructures. *Reports on Progress in Physics*, 67(8):1497–1561, August 2004.

[93] Thomas G. Pedersen, Christian Flindt, Jesper Pedersen, Niels Asger Mortensen, Antti-Pekka Jauho, and Kjeld Pedersen. Graphene Antidot Lattices: Designed Defects and Spin Qubits. *Physical Review Letters*, 100(13):136804, April 2008.

[94] J P Perdew, K Burke, and M Ernzerhof. Generalized Gradient Approximation Made Simple. *Phys. Rev. Lett.*, 77:3865, 1996.

[95] B. N. J. Persson and A. Baratoff. Inelastic electron tunneling from a metal tip: The contribution from resonant processes. *Physical Review Letters*, 59(3):339, July 1987.

[96] B N J Persson and A Baratoff. Theory Of Photon-Emission In Electron-Tunneling To Metallic Particles. *Phys. Rev. Lett.*, 68(21):3224–3227, 1992.

[97] F. L. Vernon R. P. Feyman. The Theory of a General Quantum System Interacting with a Linear Dissipative System. *Annals of physicsSICS:*, 24:118, 1963.

[98] H. Raza. *Graphene Nanoelectronics - Metrology, Synthesis, Properties and Applications*. Springer, 2012.

[99] Gaël Reecht, Fabrice Scheurer, Virginie Speisser, Yannick J. Dappe, Fabrice Mathevet, and Guillaume Schull. Electroluminescence of a Polythiophene Molecular Wire Suspended between a Metallic Surface and the Tip of a Scanning Tunneling Microscope. *Physical Review Letters*, 112(4):047403, January 2014.

[100] E. T. R. Rossen, C. F. J. Flipse, and J. I. Cerdá. Lowest order in inelastic tunneling approximation: Efficient scheme for simulation of inelastic electron tunneling data. *Physical Review B*, 87(23):235412, June 2013.

[101] Pascal Ruffieux, Jinming Cai, Nicholas C Plumb, Luc Patthey, Deborah Prezzi, Andrea Ferretti, Elisa Molinari, Xinliang Feng, Klaus Müllen, Carlo a Pignedoli, and Roman Fasel. Electronic structure of atomically precise graphene nanoribbons. *ACS nano*, 6(8):6930–5, August 2012.

[102] R Saito, M Furukawa, G Dresselhaus, and M S Dresselhaus. Raman spectra of graphene ribbons. *Journal of physics. Condensed matter : an Institute of Physics journal*, 22(33):334203, August 2010.

[103] M P Lopez Sancho, J M Lopez Sancho, J M L Sancho, and J Rubio. Highly convergent schemes for the calculation of bulk and surface Green functions. *Journal of Physics F: Metal Physics*, 15(4):851–858, April 1985.

[104] Kevin J Savage, Matthew M Hawkeye, Rubén Esteban, Andrei G Borisov, Javier Aizpurua, and Jeremy J Baumberg. Revealing the quantum regime in tunnelling plasmonics. *Nature*, page 574, 2012.

[105] C. Schirm, M. Matt, F. Pauly, J. C. Cuevas, P. Nielaba, and E. Scheer. A current-driven single-atom memory. *Nature Nanotechnology*, 8(9):645–648, September 2013.

[106] Albert Schmid. On a quasiclassical Langevin equation. *Journal of Low Temperature Physics*, 49(5-6):609–626, December 1982.

[107] N. L. Schneider, J. T. Lü, M. Brandbyge, and R Berndt. Light Emission Probing Quantum Shot Noise and Charge Fluctuations at a Biased Molecular Junction. *Physical Review Letters*, 109(18):186601, October 2012.

[108] Natalia Schneider, Peter Johansson, and Richard Berndt. Hot electron cascades in the scanning tunneling microscope. *Physical Review B*, 87(4):045409, January 2013.

[109] Natalia L. Schneider. *Ballistic Electron Transport and Plasmon Excitation Studied by Scanning Tunneling Microscopy.* Doctor rerum naturalium, Christian-Albrecht-Universität zu Kiel, 2013.

[110] Natalia L. Schneider, Guillaume Schull, and Richard Berndt. Optical Probe of Quantum Shot-Noise Reduction at a Single-Atom Contact. *Phys. Rev. Lett.*, 105(2):26601, July 2010.

[111] Jonathan A Scholl, Aitzol García-Etxarri, Ai Leen Koh, and Jennifer A Dionne. Observation of Quantum Tunneling between Two Plasmonic Nanoparticles. *Nano Lett.*, 13(2):564–569, 2013.

[112] Guillaume Schull, Nicolas Néel, Peter Johansson, Richard Berndt, and Nicolas Neel. Electron-Plasmon and Electron-Electron Interactions at a Single Atom Contact. *Physical Review Letters*, 102(5):057401, February 2009.

[113] N Sergueev, D Roubtsov, and H Guo. Ab initio analysis of electron-phonon coupling in molecular devices. *Phys. Rev. Lett.*, 95(14):146803, September 2005.

[114] R H M Smit, Y Noat, C Untiedt, N D Lang, M C van Hemert, and J M van Ruitenbeek. Measurement of the conductance of a hydrogen molecule. *Nature (London)*, 419(6910):906–909, 2002.

[115] R H M Smit, C Untiedt, J M van Ruitenbeek, and J M Van Ruitenbeek. The high-bias stability of monatomic chains. *Nanotechnology*, 15(7):S472—-S478, July 2004.

[116] José M. Soler, Emilio Artacho, Julian D. Gale, Alberto García, Javier Junquera, Pablo Ordejón, and Daniel Sánchez-Portal. The SIESTA method for ab initio order- N materials. *Journal of Physics: Condensed Matter*, 2745(14):2745–2779, March 2002.

[117] G. C. Solomon, A. Gagliardi, A. Pecchia, T. Frauenheim, A. Di Carlo, J. R. Reimers, and H. S. Hush. Understanding the inelastic electron-tunneling spectra of alkanedithiols on gold. *J. Chem. Phys.*, 124:94704, 2006.

[118] Hyunwook Song, Youngsang Kim, Yun Hee Jang, Heejun Jeong, Mark A. Reed, and Takhee Lee. Observation of molecular orbital gating. *Nature*, 462(7276):1039–1043, December 2009.

[119] Richard S. Sorbello. Theory of Electromigration. *Solid State Physics*, 51:159–231, 1997.

[120] B C Stipe, M A Rezaei, and W Ho. Single-molecule vibrational spectroscopy and microscopy. *Science*, 280(5370):1732–1735, 1998.

[121] M. Strange, C. Rostgaard, H. Häkkinen, and K. S. Thygesen. Self-consistent GW calculations of electronic transport in thiol- and amine-linked molecular junctions. *Physical Review B*, 83(11):115108, March 2011.

[122] K. S. Thygesen. Impact of exchange-correlation effects on the IV characteristics of a molecula junction. *Physical Review Letters*, 100(16):166804, 2008.

[123] Kristian Thygesen and Angel Rubio. Conserving GW scheme for nonequilibrium quantum transport in molecular contacts. *Physical Review B*, 77(11):115333, March 2008.

[124] J. Tobiska, J. Danon, I. Snyman, and Yu. Nazarov. Quantum Tunneling Detection of Two-Photon and Two-Electron Processes. *Physical Review Letters*, 96(9):096801, March 2006.

[125] N. Troullier and José Luís Martins. A straightforward method for generating soft transferable pseudopotentials. *Solid State Communications*, 74(7):613–616, May 1990.

[126] Joost van der Lit, Mark P. Boneschanscher, Daniël Vanmaekelbergh, Mari Ijäs, Andreas Uppstu, Mikko Ervasti, Ari Harju, Peter Liljeroth, and Ingmar Swart. Suppression of electron-vibron coupling in graphene nanoribbons contacted via a single atom. *Nature communications*, 4(May):2023, January 2013.

[127] H. van Houten and C. W. J. Beenakker. Quantum Point Contacts. *arXiv:cond-mat/0512609*, December 2005.

[128] M. Vandescuren, P. Hermet, V. Meunier, L. Henrard, and Ph. Lambin. Theoretical study of the vibrational edge modes in graphene nanoribbons. *Physical Review B*, 78(19):195401, November 2008.

[129] J. K. Viljas, J. C. Cuevas, F. Pauly, M. Häfner, and M Hafner. Electron-vibration interaction in transport through atomic gold wires. *Physical Review B*, 72(24):245415, December 2005.

[130] Philipp Wagner, Christopher P. Ewels, Jean-Joseph Adjizian, Laurence Magaud, Pascal Pochet, Stephan Roche, Alejandro Lopez-Bezanilla, Viktoria V. Ivanovskaya, Abu Yaya, Mark Rayson, Patrick Briddon, and Bernard Humbert. Band Gap Engineering via Edge-Functionalization of Graphene Nanoribbons. *The Journal of Physical Chemistry C*, 117(50):26790–26796, December 2013.

[131] Philipp Wagner, Viktoria V. Ivanovskaya, Manuel Melle-Franco, Bernard Humbert, Jean-Joseph Adjizian, Patrick R. Briddon, and Christopher P. Ewels. Stable hydrogenated graphene edge types: Normal and reconstructed Klein edges. *Physical Review B*, 88(9):094106, September 2013.

[132] Tobias Wassmann, Ari P. Seitsonen, A. Marco Saitta, Michele Lazzeri, and Francesco Mauri. Structure, Stability, Edge States, and Aromaticity of Graphene Ribbons. *Physical Review Letters*, 101(9):096402, August 2008.

[133] Zhong-Shuai Wu, Wencai Ren, Libo Gao, Bilu Liu, Jinping Zhao, and Hui-Ming Cheng. Efficient synthesis of graphene nanoribbons sonochemically cut from graphene sheets. *Nano Research*, 3(1):16–22, March 2010.

[134] F. Xu, C. Holmqvist, and W. Belzig. Overbias Light Emission due to Higher-Order Quantum Noise in a Tunnel Junction. *Physical Review Letters*, 113(6):066801, August 2014.

[135] Yongqiang Xue, Supriyo Datta, and Mark A. Ratner. First-principles based matrix Green's function approach to molecular electronic devices: general formalism. *Chemical Physics*, 281(2-3):151–170, August 2002.

[136] Takahiro Yamamoto, Kazuyuki Watanabe, and Kazuaki Mii. Empirical-potential study of phonon transport in graphitic ribbons. *Physical Review B*, 70(24):245402, December 2004.

[137] Li Yang, Cheol-Hwan Park, Young-Woo Son, Marvin Cohen, and Steven Louie. Quasiparticle Energies and Band Gaps in Graphene Nanoribbons. *Physical Review Letters*, 99(18):186801, November 2007.

[138] L. H. Yu, Z. K. Keane, J. W. Ciszek, L. Cheng, M. P. Stewart, J. M. Tour, and D. Natelson. Inelastic Electron Tunneling via Molecular Vibrations

in Single-Molecule Transistors. *Physical Review Letters*, 93(26):266802, December 2004.

[139] C.X. Zhang, Chaoyu He, Lin Xue, K.W. Zhang, L.Z. Sun, and Jianxin Zhong. Transport properties of zigzag graphene nanoribbons with oxygen edge decoration. *Organic Electronics*, 13(11):2494–2501, November 2012.

[140] Jian Zhou and Jinming Dong. Vibrational property and Raman spectrum of carbon nanoribbon. *Applied Physics Letters*, 91(17):173108, 2007.

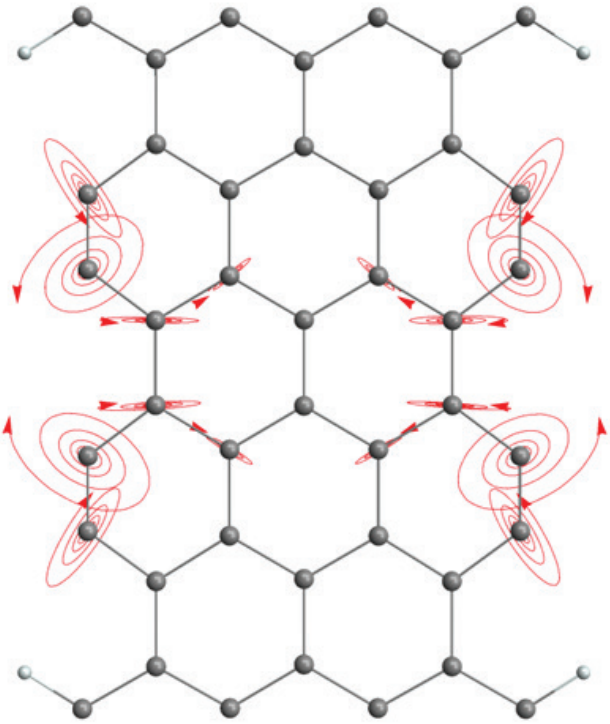

Published by:
DTU Nanotech
Department of Micro- and Nanotechnology
Technical University of Denmark
Ørsteds Plads, building 345B
DK-2800 Kgs. Lyngby